Deep levels in the zinc selenide

Paul Waite

DEEP LEVELS IN ZINC SELENIDE

by

P WAITE

Presented in candidature for the degree of Doctor of Philosophy in the University of Durham

For my wife, my parents, and my

friends and colleagues.

ACKNOWLEDGEMENTS

I would like to thank all my friends and colleagues for helping me during the course of this research project. In particular I wish to thank my supervisor Dr J Woods for all his advice and encouragement, and Dr K L Lewis for his many helpful discussions regarding the CVD material. Special thanks are due to Dr G J Russell for his expert help with the work done on the SEM, and for the many helfpul discussions relating to the project in general.

I would also like to thank Professor G G Roberts for allowing me the use of the departmental research facilities, and I am grateful to the workshop staff headed by Mr F Spence for their excellent work in the building of numerous items of apparatus. I am also grateful to Mr N F Thompson, both for the growth and the post-growth annealing treatments of the crystals used in this study.

Thanks are also due to Mr R L Rouse and Mr R M Wood for allowing me the use of the laser absorption equipment at the Hirst Research Centre, GEC Research Ltd., East Lane, Wembley, Middlesex, as part of the SRC CASE Studentship.

I would also like to thank my wife Pauline who patiently and expertly drew most of the diagrams, and Mrs L Ball, who typed the text. The production of this thesis would have been impossible without them.

Finally I would like to express my gratitude to both my wife and my parents for their constant support, without which this thesis would not be as tangible as it now is.

Science is always wrong: it never solves a problem without creating ten more.

George Bernard Shaw
1856-1950

ABSTRACT

The main purpose of the work reported in this thesis was to investigate and characterise the deep levels in zinc selenide crystals grown from the vapour phase at Durham, and by the CVD technique at AWRE, Aldermaston.

The methods of TSC, TSL and DLTS were applied to samples of Durham-grown and CVD ZnSe. The study revealed the presence of traps at 0.14-0.16, 0.23, 0.26, 0.30-0.31, 0.45, ~0.60 and 0.70 eV in Durham-grown material, whereas the CVD material was found to contain trapping levels at 0.10, 0.20 and 0.27-0.28 eV. The 0.10 eV level in CVD ZnSe is ascribed to the Na acceptor. The traps occurring at 0.26-0.31 eV in both materials are thought to be due to a vacancy-impurity complex.

Examination of the CVD material using the EBIC technique in an SEM revealed that the conductivity was limited by electrically-active grain boundaries which were shown to obey a simple potential barrier model. Cathodoluminescence studies showed that the emission bands at 465 nm (edge emission) and 630 nm (copper-red) were quenched at the grain boundaries. A relationship between the absorption coefficient at 10.6 μm and the intensity of the copper-red emission was demonstrated, which has important implications in the production of low absorption zinc selenide for laser optics.

DEEP LEVELS IN ZINC SELENIDE

CONTENTS

1 INTRODUCTION 1

1.1 DEEP LEVELS IN SEMICONDUCTORS 2
1.2 PROPERTIES OF ZINC SELENIDE 3
1.3 PURPOSE OF THE PRESENT WORK 7
1.4 THESIS ARRANGEMENT 8

2 BACKGROUND THEORY 12

2.1 ELECTRON-HOLE STATISTICS 13
2.2 TRAPS, RECOMBINATION CENTRES AND DEEP DEFECTS . . . 16
2.3 METAL-SEMICONDUCTOR CONTACTS 18

3 CRYSTAL GROWTH AND SAMPLE PREPARATION 23

3.1 INTRODUCTION 24
3.2 CRYSTAL STRUCTURE 24
3.3 CRYSTAL GROWTH 25
3.4 SAMPLE PREPARATION 29

4 THERMALLY STIMULATED LUMINESCENCE AND CONDUCTIVITY . . . 33

4.1 INTRODUCTION 34
4.2 THEORY 35
4.3 EXPERIMENTAL APPARATUS AND PROCEDURE 55
4.4 RESULTS 57
4.5 DISCUSSION 66

5 DEEP LEVEL TRANSIENT SPECTROSCOPY 72

5.1 INTRODUCTION 73
5.2 THEORY 73
5.3 EXPERIMENTAL APPARATUS AND PROCEDURE 84
5.4 EXPERIMENTAL RESULTS 87
5.5 DISCUSSION 92

6 SEM STUDIES AND LASER ABSORPTION MEASUREMENTS 98

6.1 INTRODUCTION 99
6.2 SEM INVESTIGATION 99
6.3 LASER ABSORPTION MEASUREMENTS 105

7 CONCLUSIONS 119

7.1 SUMMARY 120
7.2 SUGGESTIONS FOR FUTURE WORK 124

1 INTRODUCTION

1.1 DEEP LEVELS IN SEMICONDUCTORS

1.11 Introduction
1.12 Characterisation of deep level impurities

1.2 PROPERTIES OF ZINC SELENIDE

1.21 Electrical transport
1.22 Deep levels in zinc selenide

1.3 PURPOSE OF THE PRESENT WORK

1.4 THESIS ARRANGEMENT

1 INTRODUCTION

1.1 DEEP LEVELS IN SEMICONDUCTORS

1.11 Introduction

In semiconductors used in the fabrication of devices, defects caused by foreign atoms from groups of the periodic table close to that of the semiconductor are widely employed to control the electrical conductivity. These atoms usually introduce localised donor and acceptor states close to the band edge with binding energies less than about 50 meV. Historically such centres are called 'shallow' impurity levels.

Foreign atoms which do not belong to the adjacent group of the periodic table can generate defects within the crystal with binding energies much greater than 50 meV. These energy levels are hence often called 'deep' centres, and they seem to be present in all known semiconductors. The large binding energies of these states implies a strong potential which acts to localise the carrier wave function near the site of the defect. This is in contrast to the diffuse nature of shallow states where the binding energy is decreased proportionally to the square of the dielectric constant of the host semiconductor. One consequence of the localisation in real space is a corresponding delocalisation in k-space. This gives rise to two important properties of deep centres. The first is that they tend to be non-radiative recombination centres since the large extent in k-space allows the defect to couple to a large variety of momentum vectors or phonons. The second is that the entire band structure must be involved in any theoretical description of the defect, and not simply a minimum of a single band. As a result the deep state problem has remained largely unresolved in theoretical solid state physics which means that experimental techniques are of vital importance, and will probably remain so for the near future.

1.12 Characterisation of deep level impurities

Obviously from the discussion above, the energy position of the impurity level within the forbidden energy gap is of great importance. Furthermore, in order to describe recombination and excitation kinetics,

the probabilities of capture and emission processes must be known. However, the rates of recombination and excitation are proportional to the number of impurity levels, which means that a knowledge of their concentration within the material is desirable. Hence, to characterise the electrical and optical properties of deep level impurities at least ten quantities have to be known: thermal and optical capture constants of both electrons and holes, thermal and optical emission constants of electrons and holes, the energy position, and the concentration.

1.2 PROPERTIES OF ZINC SELENIDE

1.21 Electrical transport

One of the first studies of the transport properties of ZnSe was carried out by Aven and Woodbury [1], who showed that the resistivity of as-grown ZnSe crystals could be lowered by about 10 orders of magnitude by annealing them in liquid zinc. They attributed this to the removal of deep acceptors, particularly those associated with V_{Zn}, Cu and Ag. This explanation was later confirmed by the work of Jones and Woods [2] in a detailed study of the electrical properties of ZnSe doped with different shallow donor impurities.

Hall mobility measurements made on Zn-annealed ZnSe have shown that the electron mobility is limited by polar optical scattering above 150°K, and ionised impurity scattering at temperatures below 40°K, with a combination of both mechanisms operative in the intermediate region [2,3]. Some workers have found Hall mobilities decreasing exponentially with temperature below 50°K [4,5,6], and they have explained their results in terms of impurity conduction mechanisms.

For less conductive n-type ZnSe, with resistivities greater than 10^3 ohm-cm, the maximum mobilities reported are generally very small at about 100 $cm^2V^{-1}S^{-1}$. Heaton et al [7] and Yu and Park [8] made measurements on as-grown undoped ZnSe. The latter workers performed conductivity measurements between 320-380°K and found an activation energy of 0.92 eV which they associated with a deep donor level due to an intrinsic defect

such as selenium vacancies.

Several workers have claimed to have produced p-type ZnSe, but only with very low conductivity values. Aven (1962) [9], Haanstra and Dieleman (1965) [10] and Stringfellow and Bube (1968) [11] produced ZnSe:Cu with acceptor levels at about 0.7 and 0.9 eV above the valence band. Reinberg et al [12] (1971) found an acceptor level at 0.685 eV in ZnSe:P, and Park et al (1971) [13] obtained p-type ZnSe:Li by growth from the melt and the vapour phase. In 1973 Yu and Park [8] annealed ZnSe crystals in selenium. They reported levels at 0.65-0.75 eV above the valence band which was associated with intrinsic defects such as V_{Zn} or a zinc vacancy complex. The problems of self-compensation in p-type ZnSe were studied more recently by Bhargava et al (1979) [14], Neumark (1979) [15], Neumark et al (1980) [16] and Neumark (1980) [17]. The ZnSe was grown by liquid phase epitaxy, and shallow acceptors in the form of Li, Na, Cu and P impurities were incorporated. The main cause of self-compensation was thought to be due to the presence of accidental amphoteric impurities such as Li which can move out of Zn sites to form shallow donor levels as interstitials.

1.22 Deep levels in zinc selenide

Very little is to be found in the literature regarding trapping phenomena in ZnSe prior to about 1978. Since this date a relatively large number of publications have been produced. This may be due to the recent development of several new methods, such as capacitance transient spectroscopy, which make it possible to measure emission rates, capture rates, energy positions and impurity concentrations very accurately.

In 1968 Stringfellow and Bube [11] obtained values of 0.28 eV and 0.38 eV, using the methods of TSC and TSL, in ZnSe(SA) and ZnSe:Cu. In 1970 Wakim [18] observed two peaks from TSC and TSL at 118°K and 158°K in nominally undoped ZnSe which was known to contain traces of copper. He obtained a value of 0.38 eV for the largest peak at 158°K.

Grimmeiss et al (1976) [19] investigated the properties of ZnSe:Mn by

applying photocapacitance and photocurrent techniques to Schottky diodes. They found a level at 0.68 eV above the valence band which they suggested was either the self-activated centre, or a level associated with the manganese.

More recently in 1980, Satoh and Igaki [20] found three TSC peaks in undoped ZnSe which had been annealed in liquid zinc. The peaks were located at 120°K, 150°K and 180°K. Using a heating rate method, they found that the latter two peaks corresponded to traps at 0.19 eV and 0.31 eV respectively. They suggested that these traps were due to trace impurity defects such as Cl_{Se} or In_{Zn}, or an associated centre consisting of a native defect (V_{Se} or Zn_i) and some impurity.

Shirakawa and Kukimoto (1980) [21] carried out a DLTS study of a dominant electron trap at 0.29 eV in ZnS_xSe_{1-x}. Because the energy position of this level remained constant with respect to E_c with increasing x, the authors suggested that it was situated on the anion site. In addition, the level was found in low resistivity material doped with differing impurities, and grown by several different methods. On the strength of these facts they proposed that the defect was a Se/S vacancy. In a further publication [22] the same authors reported another electron trap at 0.33 eV. They suggested this level was due to a Zn vacancy-interstitial Ga complex.

Kosai [23] (1981) reported deep electron traps in LPE-grown ZnSe at 0.17, ~0.3, 0.64 and 1.4 eV below the conduction band. The author suggested that the traps at 0.17 and ~0.3 eV were the same as the 0.19 and 0.31 eV levels observed by Satoh and Igaki [20]. A comparison was made between the 0.3 eV trap data and the results reported by Shirakawa and Kukimoto [21]. Kosai then proposed that the defect reponsible could be a vacancy-impurity complex with a selenium vacancy as the unchanging member.

Besomi and Wessels (1980) [24] also found levels in the region 0.30-0.35 eV, however they attributed these to Cl, Al or In impurities. Verity et al (1982) [25] concluded that the commonly observed levels at between 0.30-0.35 eV must be due to native defects.

In a more recent publication Besomi and Wessels (1982) [26] observed seven electron traps at 0.24, 0.33, 0.35, 0.42, 0.54 and 0.71 and 0.86 eV. The trap concentrations ranged from 10^{11} to 10^{14} cm^{-3} depending on the growth conditions. The concentrations of the 0.33, 0.35 and 0.86 eV traps were plotted against the Zn/Se ratio used during growth. This resulted in the latter two levels both being ascribed to a selenium vacancy or a complex involving a single selenium vacancy, and the 0.33 eV trap being associated with a selenium divancy. The 0.86 eV level was also associated with gold derived from the Au Schottky contact.

Christianson and Wessels (1983) [27] found an electron trap at 0.33 eV below the conduction band, and a hole trap at 0.71 eV above the valence band which they tentatively suggested were due to native defects. They also observed a hole trap at 0.21 eV in Zn-annealed samples.

Using the ODLTS technique, Leigh and Wessels (1983) [28] studied nitrogen-doped ZnSe. They found acceptor levels at 0.085, 0.10 and 0.16 eV above the valence band, together with an electron trap at 0.35 eV below the conduction band. The authors compared these results with those of Fitzpatrick et al [29], Stutius [30] and Dean et al [31], and concluded that nitrogen associated levels may not only involve simple substitutional defects, but also complexes involving either native defects or impurities.

Qidwai and Woods (1983) [32] reported acceptor levels at 0.40, 0.55 and 0.67 eV above the valence band in ZnSe:Ga Schottky diodes. The 0.55 eV level, which was common to all samples, was ascribed to the self-activated centre, and the defect was suggested as being $(V_{Zn}\text{-}Ga_{Zn})'$. As the Ga doping was increased the 0.55 eV traps were observed to decrease in concentration, and a new level at 0.40 eV appeared. The 0.67 eV level was associated with copper.

More recently Ido and Okada (1985) [33] investigated levels in ZnSe epi-layers. Using the photocapacitance technique they found an electron trap at 0.14 eV and two hole traps at 0.10 and 0.57 eV which they ascribed

to an Na or Li acceptor, and the self-activated centre respectively. DLTS was also used to reveal an electron trap at 0.30 eV in an undoped sample which they attributed to an Se vacancy, and traps at 0.15, 0.29 and 0.52 eV in a Ga-doped sample. they also found a trap at 0.32 eV in a p-type sample, but they suggested that this level was not the same as the 0.30 eV trap discovered in the undoped material.

Finally Yoneda et al (1985) [34] studied deep electron traps in MBE-grown ZnSe using the DLTS technique. They observed two dominant traps at 0.34 and 0.54 eV. They attributed the 0.34 eV level to a native defect associated with the Se vacancy, and the 0.54 eV trap was thought to be due to a complex centre associated with donor impurities incorporated during growth.

1.3 PURPOSE OF THE PRESENT WORK

From Shockley-Read-Hall statistics [35,36] it is possible to show that the lifetime of a free carrier in a semiconductor is greatly reduced by deep crystal defect centres, and can be reduced still further if these levels have a large capture cross-section. The free carrier lifetime is usually the most critical parameter in semiconductor devices used in switching electronics and applications involving the use of photoconductive properties, radiative recombination etc. This in turn places an emphasis on the understanding of the role of deep centres in the semiconductors which are of interest in these fields.

Zinc selenide is a wide band-gap II-VI compound which is of interest as a material for the fabrication of electro-optic devices and other applications requiring the production of blue or green light. The characterisation of deep levels in this material is hence of prime importance for the reasons outlined above.

Great interest is also shown in ZnSe as an infra-red window material. The combination of a large band-gap (2.7 eV) and low lattice vibrational frequencies allows transmission over a wide wavelength range (0.5-22

microns), which covers most of the visible spectrum, the operating wavelengths of several IR lasers (HF, DF and CO_2), and two thermal imaging bands (3-5, and 8-12 microns). Typical IR windows are polished discs 25 mm diameter by 2 mm thick. The preferred growth method for the production of such material is the technique of chemical vapour deposition (CVD), which provides a polycrystalline wafer with a grain size of 50-100 microns [37]. The aim of producing material with a very low absorption coefficient means that attention must be paid to the effects of free-carrier scattering processes [38,39,40]. It was therefore thought that a study of the possible influence of deep levels on the free-carrier absorption of this material would prove useful.

The present work took the form of a CASE studentship between The University of Durham, and the Ministry of Defence (AWRE), who provided the CVD material. The overall aim was to characterise the deep centres present in both types of material, and to learn more about the effects they have on properties such as transparency.

1.4 THESIS ARRANGEMENT

The contents of this thesis can be found at two levels. At the front a general contents list is given for quick reference, and at the beginning of each chapter a more detailed contents page is provided, listing all the subsections.

The present chapter contains an introduction to the work, and the reasons for doing it, together with a survey of some of the relevant literature. Chapter two contains some elementary background theory to supplement that given in the results chapters. Chapter three contains details of the growth methods used to produce the Durham material, and the polycrystalline ZnSe grown by the CVD method at AWRE, Aldermaston. The results are presented in Chapters 4-6. Each of these chapters is self-contained, and holds the theory pertinent to the techniques used, the experimental details, the results, and a discussion section. Chapter seven contains a summary of all the work done.

References to the literature are appended to the end of the first chapter in which they are used. The format is [rr] where rr is the reference number. If a reference is made to a publication which has been referred to already in another chapter, the format is [c.rr] where c is the chapter number.

Equations are numbered in the format: c.ss-nn where c is the chapter number, ss the section number, and nn the number of the equation within that section. This makes equations easy to locate when referred to elsewhere.

Figures are numbered in a similar format: c.ss/nn where c and ss are as above, and nn is the number of the figure.

It is hoped that the layout described above will aid anyone undertaking the daunting task of reading the whole work.

CHAPTER 1 - REFERENCES

1 M Aven and H H Woodbury, Appl. Phys. Lett., 1, (1962), 53

2 G Jones and J Woods, J. Phys. D., 9, (1976), 799

3 Y Fukuda and M Fukai, J. Phys. Soc. Japan, 23, (1967), 902

4 M Aven, J. Appl. Phys., 42, (1971), 1204

5 D D Nedeoglo, Phys. Stat. Solidi (b), 80, (1977), 369

6 B R Sethi, P C Mathur and J Woods, J. Appl. Phys., 49, (1978), 3618

7 J L Heaton, E H Hammond and R B Goldner, Appl. Phys. Lett., 20, (1972), 333

8 P W Yu and Y S Park, Appl. Phys. Lett., 22, (1973), 345

9 M Aven, J. Electrochem. Soc., 11, (1962), 46

10 J H Haanstra and J Dieleman, J. Electrochem. Soc., 14, (1965), 2

11 G B Stringfellow and R H Bube, Phys. Rev., 171, (3), (1968), 903

12 A R Reinberg, W C Holton, M De Wit and R K Watts, Phys. Rev. B., 3, (1971), 410

13 Y S Park, P M Hemenger and C H Chung, Appl. Phys. Lett., 18, (1971), 45

14 R N Bhargava, S P Herko and B J Fitzpatrick, Bull. Am. Phys. Soc., 24, (1979), 402

15 G F Neumark, Bull. Am. Phys. Soc., 24, (1979), 402

16 G F Neumark, B J Fitzpatrick, P M Harnack, S P Herko, K Kosai and R N Bhargava, J. Electrochem. Soc., 127, (1980), 983

17 G F Neumark, J. Appl. Phys., 51, (1980), 3383

18 F G Wakim, J. Appl. Phys., 41, (1970), 835

19 H G Grimmeiss, C Ovren and J W Allen, J. Appl. Phys., 47, (3), (1976), 1103

20 S Satoh and K Igaki, Jpn. J. Appl. Phys., 19, (1980), 485

21 Y Shirakawa and H Kukimoto, Sol. State commun., 34, (1980), 359

22 Y Shirakawa and H Kukimoto, J. Appl. Phys., 51, (1980), 5859

23 K Kosai, J. Appl. Phys., 53, (2), (1982), 1018

24 P Besomi and B W Wessels, Electron. Lett., 16, (1980), 794

25 D Verity, F J Bryant, J J Davies, J E Nicholls, C G Scott and D Shaw, J. Phys. D: Solid State Phys., 15, (1982), 5497

26 P Besomi and B W Wessels, J. Appl. Phys., 53, (4), (1982), 3076

27 K A Christianson and B W Wessels, J. Appl. Phys., 54, (7), (1983), 4205

28 W B Leigh and B W Wessels, J. Appl. Phys., 55, (6), (1984), 1614

29 B J Fitzpatrick, C J Werkhoven, T F McGee III, P M Harnack, S P Herko, R N Bhargava and P J Dean, IEEE Trans. Electron. Dev., ED-28, (1981), 440

30 W Stutius, Appl. Phys. Lett., 40, (1982), 246

31 P J Dean, W Stutius, G F Neumark, B J Fitzpatrick and R N Bhargava, Phys. Rev. B., 27, (1983), 2419

32 A A Qidwai and J Woods, J. Phys. C., (GB), 16, (35), (1983), 6789

33 T Ido and M Okada, J. Cryst. Growth, 72, (1985), 170

34 K Yoneda, Y Hishida and H Ishii, Appl. Phys. Lett., 47, (7), (1985), 702

35 W Shockley and W T Read, Phys. Rev., 87, (1952), 835

36 R N Hall, Phys. Rev., 86, (1952), 600

37 K L Lewis, D J Cook and P B Roscoe, J. Cryst. Growth, 56, (1982), 614

38 B V Dutt, O K Kim and W G Spitzer, J. Appl. Phys., 48, (5), (1977), 2110

39 M P Kulakov and V I Grinev, Inorg. Mat., 16, (1980), 139 (from Izv. Akad. Nauk SSSR, Neorg. Mat., 16, (1980), 223)

30 K L Lewis and G S Arthur, Boulder Damage Symposium, NBS Special Publication 669, (1982), 86

CONTENTS

2 BACKGROUND THEORY

2.1 ELECTRON-HOLE STATISTICS

2.2 TRAPS, RECOMBINATION CENTRES AND DEEP DEFECTS

2.3 METAL-SEMICONDUCTOR CONTACTS

2.31 The potential barrier
2.32 The effect of surface states

2 BACKGROUND THEORY

This chapter provides a brief introduction to some of the basic theory behind the work described in this thesis. Additional theory directly related to the measurements made in the course of this work can be found in Chapters 4-6. The following sections cover electron-hole statistics, defect states in semiconductors and the elementary theory of the metal-semiconductor contact. For a more complete treatment of these subjects the reader is referred to any of the many excellent books [1-8].

2.1 ELECTRON-HOLE STATISTICS

In semiconductors only the upper energy levels of the valence band, the lower levels of the conduction band and the intermediate levels within the forbidden gap are of any importance. At a temperature of absolute zero electrons normally occupy the valence band and the lower energy states of some impurity levels. The problem is to find the distribution of these electrons over the allowed energy states, and at temperatures above absolute zero.

The probability F(E) that a certain level will be occupied is given by:

$$F(E) = \frac{1}{1 + \exp\left[(E-E_F)/kT\right]} \qquad 2.1\text{-}1$$

This function is the Fermi-Dirac occupancy function which is valid for particles obeying the Pauli exclusion principle, such as electrons. E_F is the Fermi energy, and k is Boltzman's constant.

If the datum level for zero energy is taken to be the bottom of the conduction band, and $N_C(E)dE$ is the density of allowed levels of energies between E and E+dE in the conduction band, then the number of electrons n(E)dE having the same range of energies is given by:

$$n(E)dE = 2\, N_C(E)\, F(E)\, dE \qquad 2.1\text{-}2$$

The fact that two electrons of opposite spin may occupy each level is included as the factor of two in this equation. The total number of electrons per unit volume, n, in the conduction band is then

$$n = \int_0^{E_T} N_C(E)\, F(E)\, dE \qquad 2.1\text{-}3$$

where E_T is the energy at the top of the conduction band.

The density of levels $N_C(E)dE$ is initially calculated for a semiconductor with a symmetrical band structure, and this is then extended to include other symmetries to give the effective density of states in the conduction band. Since there is only a very small probability that an electron will occupy any level in the conduction band, only the levels closest to the zero energy level will be filled. This assumption allows the upper limit in equation 2.1-3 to be extended to infinity which simplifies the evaluation of the intregral considerably.

The expression then becomes

$$n = 4\pi\left[\frac{4m_e^{*2}}{h}\right]^3 \int_0^{\infty} \frac{(E)^{1/2}dE}{1 + \exp[E-E_F)/kT]} \qquad 2.1\text{-}4$$

where: m_e^* = electron effective mass near the bottom of the conduction band

h = Planck's constant

Since it is assumed that $E-E_F >> kT$ then

$$n = 2(2m_e^*kT/h^2)^{3/2} \exp(-E_F/kT) \qquad 2.1\text{-}5$$

or

$$n = N_C\exp(2m_e^*kT/h^2)^{3/2} \qquad 2.1\text{-}6$$

where N_C is the effective density of states in the conduction band.

A similar approach may also be adopted for holes near the top of the valence band. When this is done an equation for the Fermi level for an intrinsic semiconductor is obtained as

$$E_F = -1/2E_g + 1/2kT \ln(N_v/N_c) \qquad 2.1\text{-}7$$

where E_g is the band gap and N_v is the effective density of states in the valence band.

Consider a semiconductor where there are impurity levels in the form of N_d donors and N_a acceptors per unit volume. The material is thus said to be compensated since the acceptors cancel the effect of some of the donors by trapping free electrons. The extent to which this occurs depends on the absolute concentrations. If $N_d > N_a$, the accceptor levels will be completely filled with electrons from donor levels. The number of carriers available for extrinsic conduction in an n-type material is then given by $N_d - N_a$. the density of occupied donor levels, n_d at temperature T is found by multiplying the density of donors N_d with the occupancy function to give

$$n_d = \frac{N_d}{1 + \frac{1}{g}\exp[(E_d - E_f)/kT]} \qquad 2.1\text{-}8$$

where g is the degeneracy factor of the particular donor concerned, and E_d is the position of the donor below the conduction band. At T=0°K there will be $N_d - N_a$ electrons in the donor level, and at a higher T when there are n electrons per unit volume in the conduction band we have

$$N_d - N_a = n + \frac{N_d}{1 + \frac{1}{g}\exp[(E_d - E_f)/kT]} \qquad 2.1\text{-}9$$

which can be manipulated to give

$$\frac{N_a + n}{N_d - N_a - n} = \frac{1}{g} \frac{\exp(E_F/kT)}{\exp(E_d/kT)}$$

Substituting this expression into equations 2.1-5 and 2.1-6 we have

$$\frac{Na + n}{N_d - N_a - n} = \frac{N_c}{g\ n\ \exp(E_d/kT)}$$

and finally we can write

$$\frac{n(N_a+n)}{N_d-N_a-n} = 1/gN_c \exp(-E_d/kT) \qquad 2.1\text{-}10$$

where E_d is also known as the ionisation energy of the particular donor impurity. If there is heavy compensation such that $n<<N_a<N_d$, then equation 2.1-10 reduces to

$$n = \frac{N_c(N_d-N_a)}{N_c+gN_a\exp(E_d/kT)} \qquad 2.1\text{-}11$$

The position of the Fermi level is given by

$$E_F = -kT \ln(N_c/n) \qquad 2.1\text{-}12$$

which approximates to

$$E_F = -E_d+kT \ln[(N_d-N_a)/gN_a] \qquad 2.1\text{-}13$$

when T is small, and hence $n<<N_a<N_d$. When T is large and we can assume that $n \approx N_d-N_a$, the Fermi level position is then

$$E_F = -kT \ln[N_c/(N_d-N_a)] \qquad 2.1\text{-}14$$

This regime is called the exhaustion range where the density of electrons in the conduction band is largely independent of temperature.

2.2 TRAPS, RECOMBINATION CENTRES AND DEEP DEFECTS

The nomenclature used to describe deep defects in semiconductors can often be confusing. These states are variously referred to as traps, recombination centres, deep levels, deep impurities etc. The situation is complicated by the fact that a defect state might be both a trap and a recombination centre, depending on other parameters such as doping and temperature.

If the situation in a neutral semiconductor is considered, an electron trap is defined to be a defect for which the electron capture rate c_n is much larger than the hole capture rate c_p. The distinction between this and a recombination centre is largely subjective, but in general it can be

defined as a defect for which both electron and hole capture rates are large. It is clear that the name given to a particular state in order to categorise it is largely a matter of convenience. It is more useful to regard it as a deep defect state with specific capture cross sections σ_n and σ_p for capturing electrons and holes respectively. The capture rates are then given by

$$c_n = \sigma_n \langle v_n \rangle \; n \qquad 2.2\text{-}1$$

$$c_p = \sigma_p \langle v_n \rangle \; p \qquad 2.2\text{-}2$$

where n and p are the concentration of electrons and holes, and $\langle v_n \rangle$ is the average thermal velocity of electrons given by

$$\langle v_n \rangle \approx \sqrt{\langle v_n^2 \rangle} = \sqrt{\frac{3kT}{m_e^*}} \qquad 2.2\text{-}3$$

where m_e^* is the electron effective mass, k is Boltzmann's constant, and T is absolute temperature. An equivalent expression holds for holes.

It is clear from equations 2.2-1 and 2.2-2 that a defect with given capture cross sections for holes and electrons might be either a trap or a recombination centre, depending on the carrier concentrations. In particular, consider a defect located inside the depletion layer of a Schottky barrier where n and p are essentially zero. All defects can therefore be regarded as traps in a depleted layer, since recombination cannot occur.

In a depletion layer it is more useful to define defects in terms of their thermal emission rates. The electron trap can be defined as a defect for which the emission rate for electrons, e_n, is much larger than the emission rate for holes e_p, and the hole trap is defined as being a defect for which $e_p >> e_n$. A carrier generation centre can also be defined in these terms. This is a defect for which $e_n \approx e_p$ so that it thermally emits both holes and electrons to generate a steady depletion layer current.

The thermal emission rate for electrons is given by

$$e_n = A_n \exp(-E/kT) \qquad 2.2\text{-}4$$

where A_n is a property of the defect, and E is the thermal ionisation energy. The quantity A_n can be evaluated by using the principle of detailed balance, which states that, in equilibrium, the carrier capture and emission for each electron state must be equal, hence we can write

$$e_n F = c_n(1-F) \qquad 2.2\text{-}5$$

where F is the probability that a state is occupied (equation 2.1-1). The electron concentration is given by

$$n = N_C \exp\left[-(E_C-E_F)/kT\right] \qquad 2.2\text{-}6$$

where N_C is the effective density of states in the conduction band given by equations 2.1-5 and 2.1-6.

The emission rate can then be found from equations 2.2-1, 2.2-4, 2.2-5, and 2.2-6, and is given by

$$e_n = \frac{\sigma_n \langle v_n \rangle N_C}{g} \exp(-E/kT) \qquad 2.2\text{-}7$$

where g is the degeneracy factor associated with the level.

2.3 METAL-SEMICONDUCTOR CONTACTS

2.31 The potential barrier

The rectifying property of a metal-semiconductor contact arises because of the presence of an electrostatic barrier between the metal and the semiconductor. The way this is formed is depicted in Figure 2.3/1. The work function of the metal is larger than that of the semiconductor in this example. If a true junction is to be formed between the two materials, a state of thermal equilibrium must be created. To achieve this, the Fermi levels in each material must be brought to the same energy. This is accomplished by an initial flow of electrons from

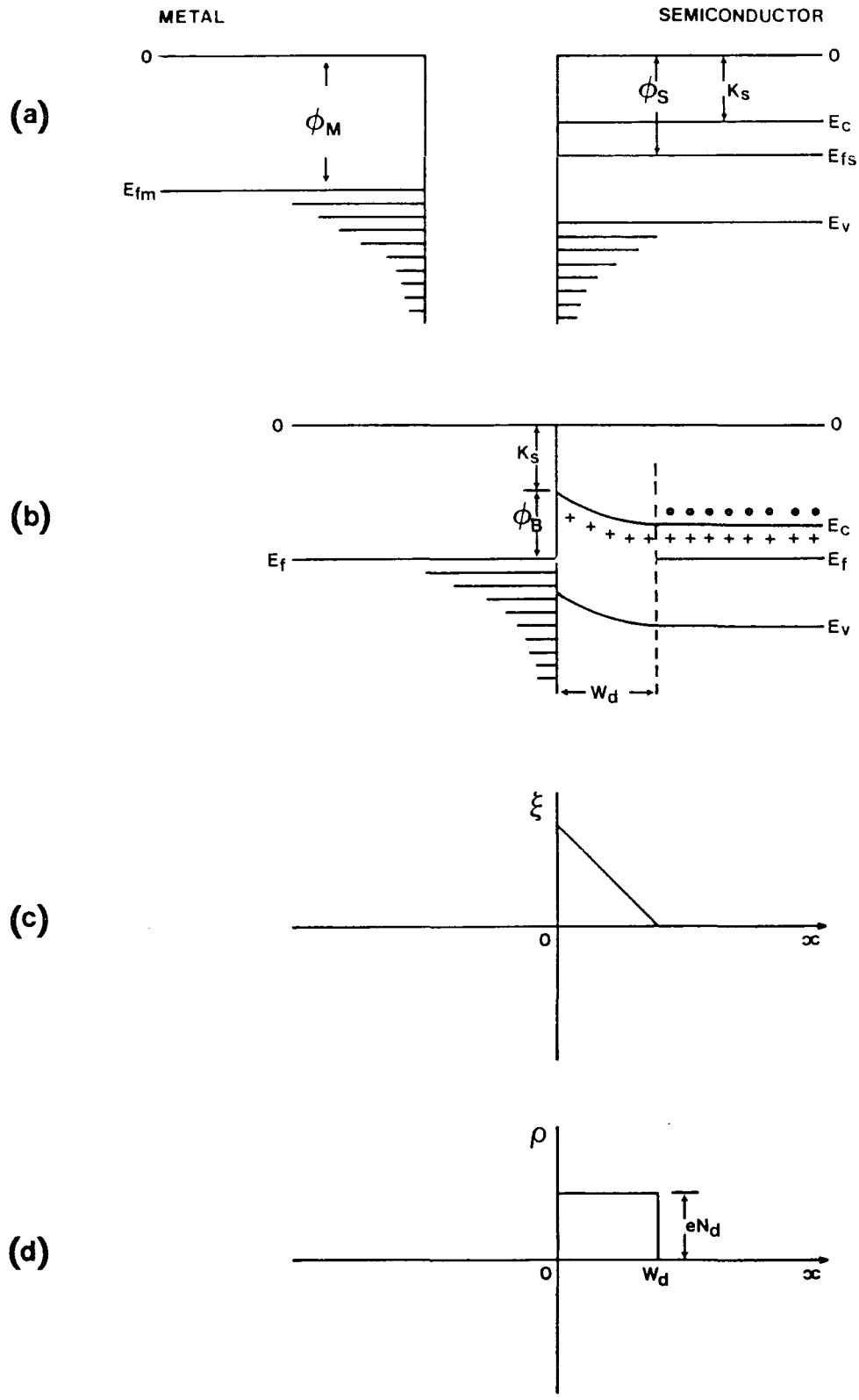

Formation of an ideal Schottky barrier junction. (a) Two separate systems, metal and semiconductor, (b) Fermi levels equalised, depletion region formed, (c) electric field strength at the junction, (d) space charge density profile.

FIGURE 2.3/1

semiconductor to metal, leaving behind a region depleted of negative charge, and creating a diffusion potential which counteracts the flow of electrons until eventually a condition of equilibrium is reached. The equilibrium state for an n-type semiconductor is shown in Figure 2.3/1(b). In the simple model of the junction, the area of band-bending is assumed to be completely devoid of conduction electrons creating a space charge region entirely due to uncompensated donors. This assumption is called 'the depletion approximation'. If the donors are assumed to be uniformly distributed throughout the depletion region, the electric field-strength will increase linearly with distance from the depletion region edge as shown in Figure 2.3/1(c).

The linear dependence of the field on distance means that the bands depicted in Figure 2.3/1(b) will be parabolic in shape. The bands are bent upwards by an amount necessary to equalise the Fermi levels ($\phi_M - \phi_S$). From inspection of the diagrams in Figure 2.3/1 it can be seen that the barrier height is given by

$$\phi_b = (\phi_M - \phi_S) + (E_C - E_F) \qquad 2.3\text{-}1$$

By applying a bias voltage to the system, the energy bands can be made to change as shown in Figure 2.3/2. Assuming that the charge distribution is such at $\rho = eN_d$ for $0 < X < W_d$ (where W_d is the depletion region width), and that $\rho = 0$ for $X > W_d$ (the abrupt junction approximation), it can be shown that the depletion region width is given by

$$W_d = \left[\frac{2E_S}{eN_d} (V_B - V - kT/e)\right]^{1/2} \qquad 2.3\text{-}2$$

the electric field strength is given by

$$|\varepsilon(x)| = \frac{eN_d}{E_S} (W_d - X) \qquad 2.3\text{-}3$$

and the potential is given by

$$V(x) = \frac{eN_d}{E_S} (W_d X - 0.5\, X^2) \qquad 2.3\text{-}4$$

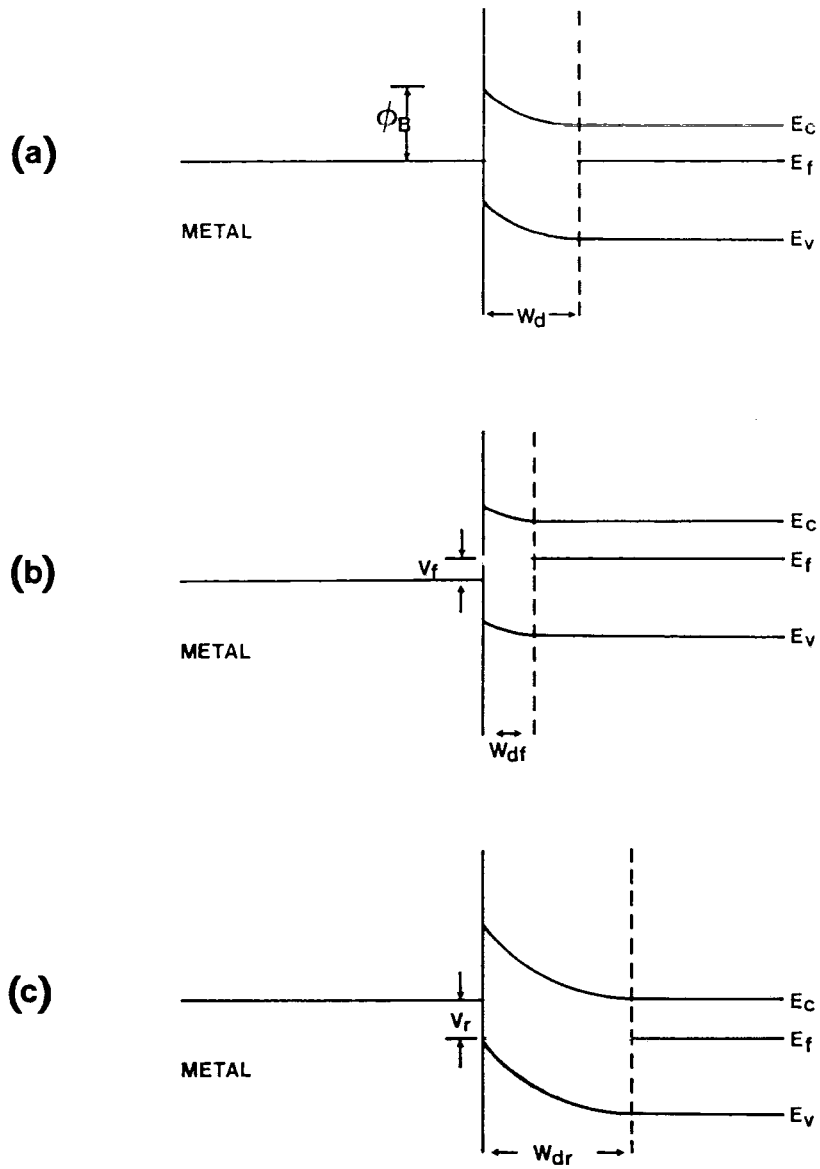

Biassing a Schottky barrier device (n-type). (a) No bias, (b) application of forward bias, V_f, (c) application of reverse bias, V_r.

FIGURE 2.3/2

where W_d = depletion region width
E_S = permittivity of semiconductor
V_B = barrier height in volts
N_d = donor concentration (cm^{-3})
V = bias voltage

Using equation 2.3-2, an expression for the space charge per unit area, Q_{SC}, can be written as

$$Q_{SC} = eN_dW_d$$

and hence

$$Q_{SC} = (2eE_SN_d(V_B-V-kT/e))^{1/2} \qquad 2.3\text{-}5$$

This equation can be used to derive the expression for the capacitance of the depletion region from

$$C_d = dQ_{SC}/dV$$

therefore

$$C_d = \left[\frac{eE_SN_d}{2(V_B-V-kT/e)}\right]^{1/2} = E_S/W_d \qquad 2.3\text{-}6$$

which can be rewritten as

$$\frac{1}{C_d^2} = \frac{2(V_B-V-kT/e)}{eE_SN_d}$$

If this expression is now differentiated with respect to V, we obtain

$$-d/dV\ (1/C_d^2) = 2/(eE_SN_d)$$

A final rearrangement of this equation then gives

$$N_d = (2/eE_S)\ (-dV/d(C_d^{-2})) \qquad 2.3\text{-}7$$

A plot of $1/C_d^2$ versus V (the bias voltage) will therefore yield a straight line with a gradient proportional to the donor concentration N_d, assuming that N_d is constant for $0<X<W_d$.

2.32 The effect of surface states

If it is assumed that the surface of the semiconductor possesses a large density of surface states associated with the discontinuity in the periodicity of the lattice (dangling bonds), then the formation of the Schottky barrier can be described by the diagrams in Figure 2.3/3. In 2.3/3(a) where the metal and semiconductor are not in contact, there is equilibrium between the surface states and the bulk of the semiconductor, but equilibrium between the metal and the semiconductor has not been established. The surface states are occupied to a level E_{FS}. When the contact is made the Fermi level of the semiconductor must drop by an amount equal to the contact potential (relative to the metal). If the density of surface states is large enough to neutralise any additional surface charges arising without appreciably affecting the occupation level E_F, the space charge in the semiconductor will remain unaffected. In this event the barrier height is determined by the semiconductor surface. The Fermi level within the semiconductor is said to be pinned to the energy E_{FS} by the surface states. In general the barrier height is determined by both the metal work function and the surface states. A straight-forward analysis gives the expression for the barrier height in the two limiting conditions as follows

$$e\phi_B = (E_g - e\phi_0) \qquad 2.3\text{-}8$$

Fermi level pinning, $D_S \to \infty$

and

$$e\phi_B = e(\phi_M - K_S) \qquad 2.3\text{-}9$$

When $D_S \to 0$ for an ideal barrier

where: ϕ_0 = energy at the semiconductor surface due to surface states
E_g = band-gap of the semiconductor
ϕ_M = metal work function
K_S = semiconductor electron affinity
ϕ_B = barrier height
D_S = density of surface states

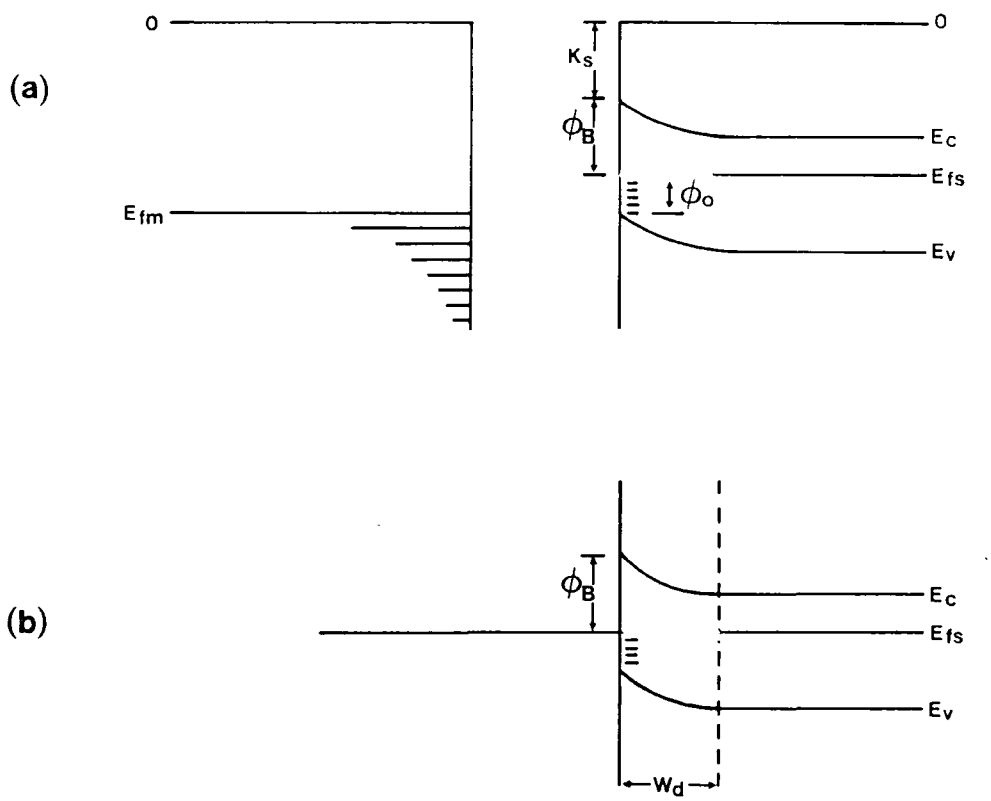

Formation of a Schottky barrier junction with the semiconductor Fermi level pinned by surface states.

FIGURE 2.3/3

CHAPTER 2 - REFERENCES

1 J S Blakemore, Solid State Physics, Saunders (1969)

2 C Kittel, Introduction to Solid State Physics, Wiley, 2nd Edition, (1963)

3 W C Dunlap, An Introduction to Semiconductors, Wiley, (1957)

4 R A Smith, Semiconductors, Cambridge University Press, (1959)

5 L V Azaroff and J J Brophy, Electronic Processes in Materials, McGraw-Hill, (1963)

6 W Shockley, Electrons and Holes in Semiconductors, Van Nostrand, (1950)

7 S M Sze, Physics of Semiconductor Devices, Wiley, (1969)

8 A G Milnes and D L Feucht, Heterojunctions and Metal Semiconductor Junctions, Academic Press, (1972)

CONTENTS

3 CRYSTAL GROWTH AND SAMPLE PREPARATION

3.1 INTRODUCTION

3.2 CRYSTAL STRUCTURE

3.3 CRYSTAL GROWTH

3.31 CVD zinc selenide
3.32 Durham material

3.322 Vapour phase growth
3.323 Introduction and extraction of impurities

3.4 SAMPLE PREPARATION

3.41 Surface treatment
3.42 Ohmic contacts
3.43 Schottky barrier formation

3 CRYSTAL GROWTH AND SAMPLE PREPARATION

3.1 INTRODUCTION

The zinc selenide crystals grown and studied during the course of this work fall into the category known as II-VI compounds, since it is a material made up of elements belonging to groups two and six of the periodic table. The samples studied were produced by two different growth techniques, both of which are described in the following sections.

3.2 Crystal structure

The combination of elements from groups two and six of the periodic table gives rise to compounds with four valence electrons per atom. In a lattice formed of covalently bonded atoms this would generate a tetrahedral structure wherein each atom is surrounded symetrically by four nearest neighbours at the vertices of a tetrahedron.

Elemental semiconductors such as Si and Ge show strong covalent bonding, as do some of the III-V compounds. The opposite extreme is exemplified in compounds such as NaCl and KCl in which electrons are largely transferred to give strong ionicity. Since the degree of ionicity of a binary compound decreases as the electronegativity difference between the two elements decreases, it can be assumed that II-VI compounds show bonding which is neither totally ionic nor totally covalent. Pauling [1] studied nearest neighbour separations calculated from the covalent and ionic radii of the appropriate atoms, and compared these results with values obtained experimentally from the lattice parameter. This work showed that most II-VI compounds can be viewed as being covalent, a result which is supported by the observed tetrahedral bonding. The ionic influence is reflected however, in the large bandgaps, high melting points and the relatively low mobilities of the charge carriers.

Tetrahedral bonding gives rise to two crystal structures in III-V and

II-VI compounds. These are wurtzite, which belongs to the hexagonal crystal class and zinc blende which lies in the cubic class. ZnSe has been grown in both the wurtzite and zinc blende modifications, however it normally exists in the latter form.

The zinc blende structure is derived from the diamond structure and is formed from two interpenetrating cubic close-packed lattices. The lattice parameter of the zinc blende phase of ZnSe is 5.67 Å and the nearest neighbour distance is 2.45 Å.

3.3 Crystal growth

There are two methods by which crystals of II-VI compounds can be grown. These are growth from the melt and growth from the vapour phase. Generally vapour growth is preferred over melt growth owing to the large vapour pressures which exist at the melting point of ZnSe (~1100°C) [2,3,4].

Burr and Woods [5] adapted the technique employed by Clarke and Woods [6] to grow cadmium sulphide crystals, and produced ZnSe from the vapour. This method is described in greater detail in section 3.32. The crystals of ZnSe studied in this work originated from two sources. CVD material was grown at AWRE, Aldermaston where it was also cut and polished. In addition material grown by the vapour phase method mentioned above was produced by the crystal growth laboratory in the Department of Applied Physics and Electronics, University of Durham.

3.31 CVD zinc selenide

Material grown by the chemical vapour deposition (CVD) technique is produced by reacting a mixture of zinc and hydrogen selenide [7]. Zinc vapour was generated by evaporation from a molten charge (Koch-Light 5N purity) contained within a carbon crucible. The vapour was entrained in a stream of argon and ducted to a reaction zone where it was mixed with

hydrogen selenide (BOC 5N purity). The reaction zone was formed by the four walls of a rectangular graphite substrate on which deposition ensued. The material used in this work was grown at temperatures between 600 and 850°C. Deposition occurred at reduced pressures.

The relevant chemical equilibria are given in equations 3.3-1 and 3.3-2, below:

$$H_2Se \longrightarrow H_2 + \tfrac{1}{2}Se_2 \qquad 3.3\text{-}1$$

$$Zn + \tfrac{1}{2}Se_2 \longrightarrow ZnSe \qquad 3.3\text{-}2$$

3.32 Durham material

Two boules of Durham-grown ZnSe, of approximately 8 mm dia. x 3 cm length were grown for part of this work. These were produced with a delay of approximately seven months between them. Boule 388, which had been grown in December 1977 was the first, while boule 400 was grown in June 1978. Between these two growth runs, research work in the crystal growth laboratory disclosed the fact that owing to changes in the silica and the furnace tubes, heavy metal impurities (such as Cu) were being incorporated [8]. Changing to higher temperature-rated Mullite furnace tubes which were less porous alleviated the problems sufficiently to enable the growth of higher purity crystals to be resumed. Apart from this difference both boules were produced by an identical growth procedure.

3.321 Preparation of starting material

The ZnSe starting material was produced by synthesis from the elements using a technique similar to the one employed by W C Holton et al [9].

The synthesis tube is shown in diagram 3.3/1. The method consisted, briefly, of placing the elements in two separate boats and passing independent streams of argon gas over them. The resultant vapour mixture, having passed into the deposition zone, then became supersaturated, and ZnSe dust precipitated out onto the silica liner.

The material produced in this way was then purified by sublimation in a flow of argon in a separate furnace shown in diagram 3.3/2. The argon gas was passed through a molecular sieve to extract moisture before being introduced to the flow run tube at a rate of 350 ml/minute. Usually about 80 grams of ZnSe sublimate was transported in the form of yellow-green platelets over a period of 5-6 days. The condensate was then used as the source material for the final growth run.

3.322 Vapour phase growth

The vertical growth system described by Clark and Woods [8] and used by them to grow CdS was adapted for the growth of ZnSe by Burr and Woods [5] and was later modified by Cutter and Woods [10] to produce the present configuration shown in diagram 3.3/3.

Flow run platelets obtained from the process described in the preceeding section were crushed and made up into a charge of approximately 20 grams. The growth tube was put through a procedure involving evacuation, bake-out and flushing with argon to purge it of adsorbed impurities, before being opened to allow the loading of the ZnSe charge. A growth tip was then placed in the expanded section of the tube, together with a piece of soft iron encapsulated in silica which was subsequently used, in conjunction with a magnet, to position the tip close to the charge as shown in diagram 3.3/4. Having again been flushed with argon gas, the growth tube was evacuated overnight and then sealed off at a pressure of 2×10^{-6} Torr. The tube was then loaded into the furnace with the growth tip positioned in the hottest zone and the power and pulling mechanism were switched on.

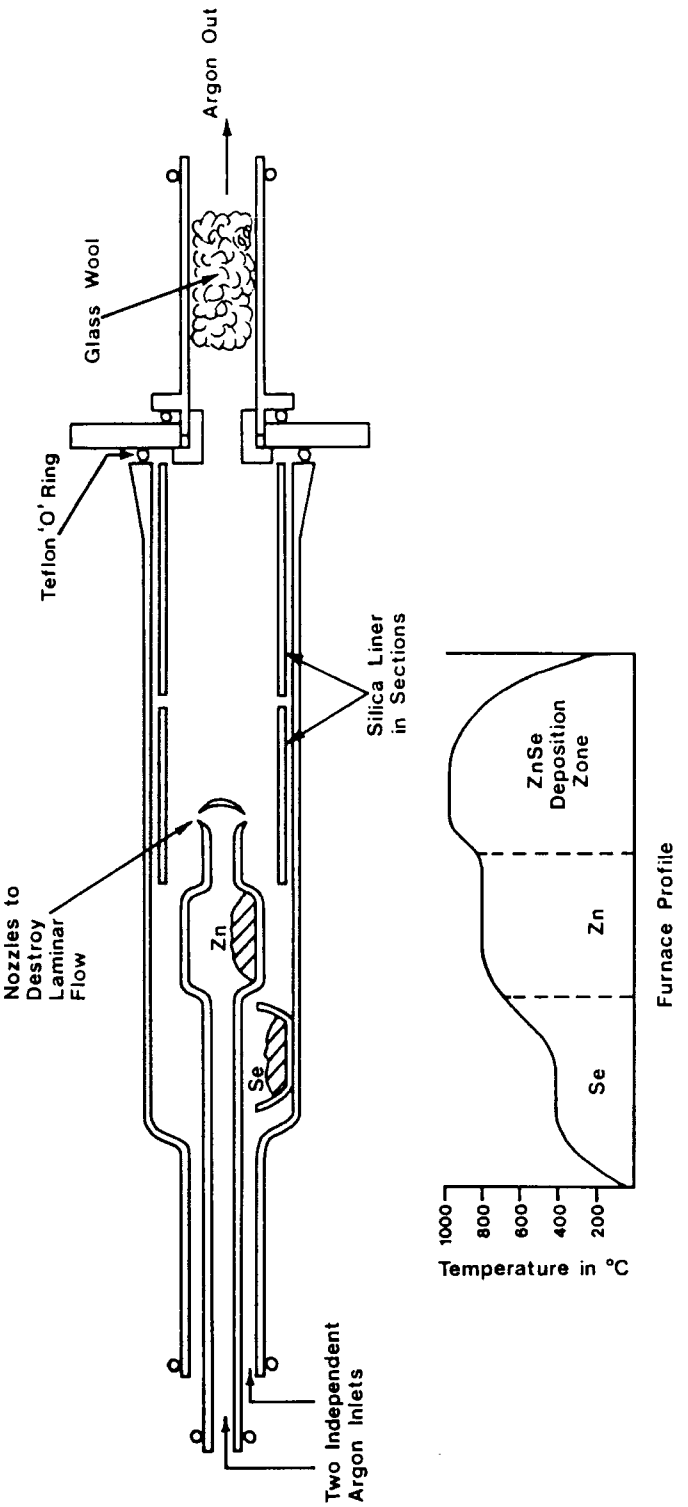

Silica reaction tube for the synthesis of ZnSe

FIGURE 3.3/1

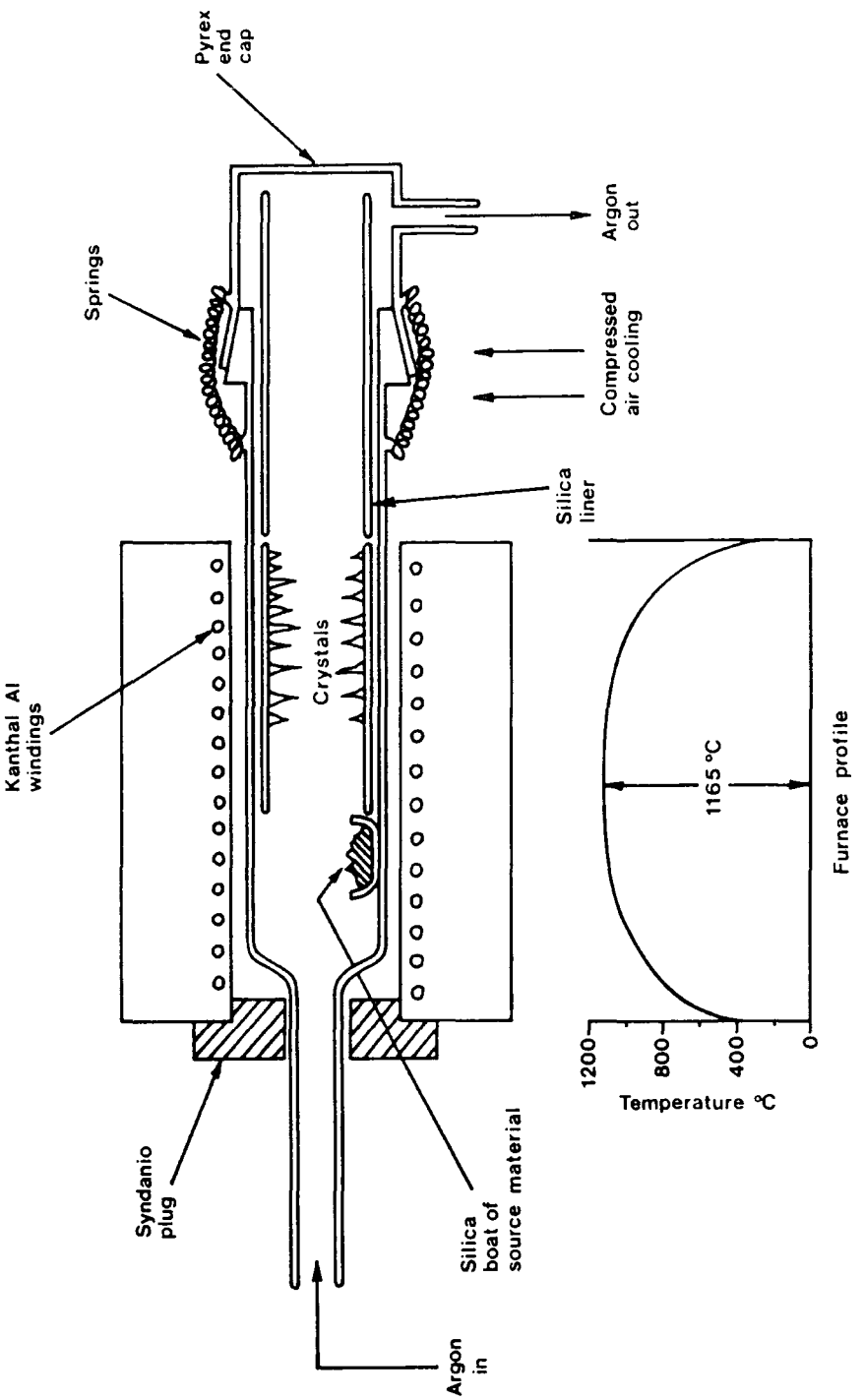

Flow run tube

FIGURE 3.3/2

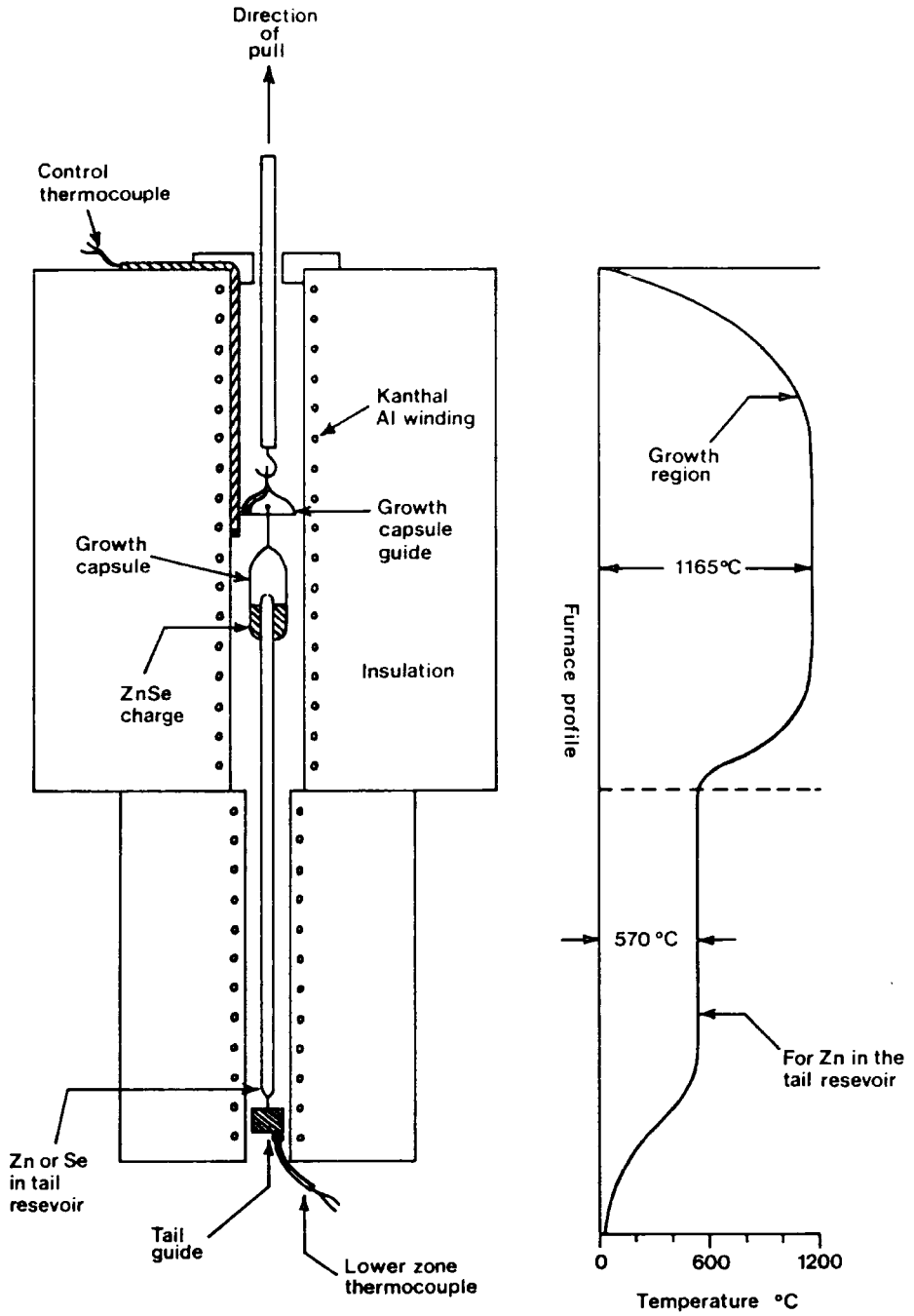

Vertical growth furnace used to produce single crystal boules of ZnSe. The system is shown with the tail furnace adjusted for Zn.

FIGURE 3.3/3

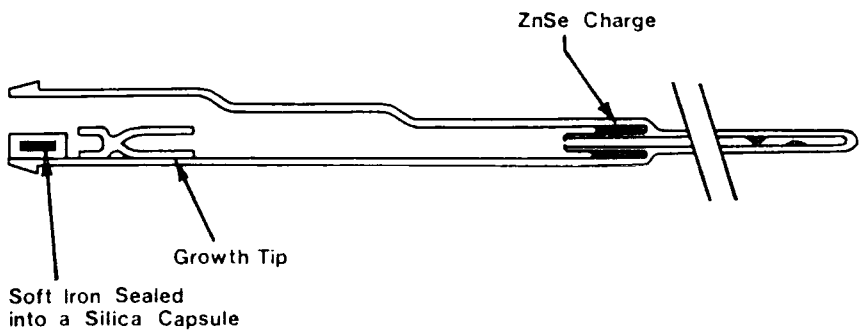

a) The charge and growth tip are loaded and the tube is flushed three times with Argon. The soft Iron is placed inside the tube.

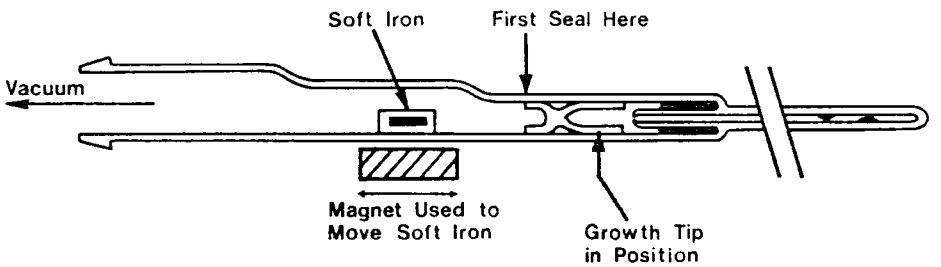

b) The growth tip is positioned using the magnet and the soft iron capsule and the tube is sealed off at 2×10^{-6} T.

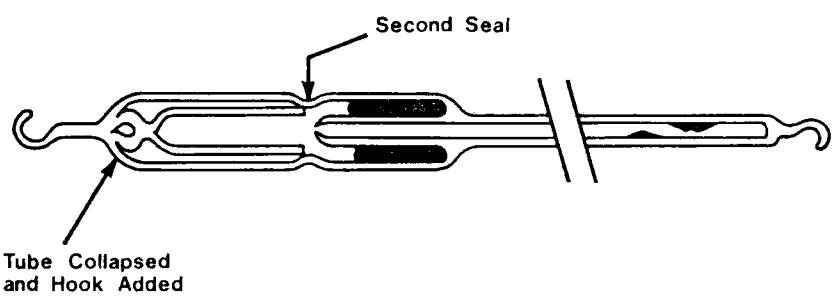

c) The finished growth tube is sealed at the bottom of the growth tip and is provided with a hook at either end.

Loading and sealing a crystal growth tube

FIGURE 3.3/4

Initially transport was from the growth tip towards the growth capsule base leading to charge compaction and removal of most ZnSe dust particles from the growth tip area. As pulling proceeded however, the temperature gradient was reversed as the charge became hotter than the growth tip, and ZnSe was transported to form a boule approximately 3 cms long by 1 cm diameter. The growing crystal interface was usually at 1120°C with the charge at 1165°C. The tail of the vertical growth system contained either Se or Zn, and was held at a temperature calculated to give the minimum total pressure inside the growth capsule for stoichiometric vapour composition. These temperatures were 310 and 570°C respectively for Se and Zn. With a pull rate of 0.1 or 0.2 mm/hr, it took the ZnSe charge fifteen days to sublime from the bottom to the top of the growth capsule. This was followed by a cooling period of 80 hours until the boule had reached room temperature.

3.323 Introduction and extraction of impurities

The resistivity of as-grown material produced by the vertical growth system was usually measured as being in the region of 10^{12} Ω-cm. In order to make devices such as Schottky barrier diodes, the resistivity was reduced to a value in the range of 1 to 100 Ω-cm by annealing the material in molten zinc. Early work involving the use of radioactive tracers [11] indicated that an out-diffusion of compensating impurities and/or native defects occurs during such a treatment. More recent studies of the process using the techniques of Hall mobility measurements [12,13] and photoluminescence [14] have tended to support this view. Typically the procedure consisted of holding several previously etched dice of dimensions 1 x 1 x 2 mm^3 in molten Zn at 850°C for 24 hours. The silica tube used to contain the dice was put through a cleansing procedure in which it was soaked in aqua regia, rinsed in methanol and dried , thus ensuring a minimum of accidental doping due to adsorbed impurities. The tube was made with ledges so that at the end of the treatment it could be inverted, allowing the still molten zinc to drain off the dice.

Resistivity was also lowered by doping the material with suitable donor impurities such as Ga or In. In this case values of between 10^6 and 10^8 ohm-cm were typical. The impurities were added in elemental form to the charge in the vertical growth system where they transported during growth to produce the doped boule. Boules have been prepared in this manner with doping levels of between 5 ppm and 1000 ppm as measured by atomic absorption spectroscopy.

Doping by this method and the technique of heat-treating the samples in molten zinc are not however, mutually exclusive. In order to investigate doped material more fully, Schottky barrier diodes have been fabricated from heat-treated gallium and indium doped dice, in which resistivities have been reduced by a further six orders of magnitude.

3.4 Sample preparation

The preparation procedures used in the course of this work are grouped under the three sub-section headings set out below. Surface treatment was found to vary in importance according to the experimental technique being used. The laser absorption measurements for instance were extremely sensitive to variations in surface quality, in contrast to those on thermoluminescence which were comparatively unaffected. Preparation of ohmic contacts and the fabrication of Schottky barriers were both straightforward procedures and yielded good results provided the surfaces had been etched and cleansed thoroughly.

3.41 Surface treatment

The surface treatment consisted of mechanical polishing and chemical etching. The polishing requirements were generally simple as in the main, the procedure was only carried out on bars or discs cut from a newly grown boule in order to provide moderately flat surfaces. Hand polishing with powders of particle sizes varying from 12 to 1 micron was undertaken to remove both diffused and evaporated contacts, although this too was a crude process.

For the laser absorption measurements made on thin discs where the ratio of bulk to surface absorption was not favourable, the polishing procedure became more important. The two faces of each disc had to be polished so that they were minutely aparallel in order to avoid internal reflection problems which would have given rise to erroneous absorption data. This skilled work was carried out at the GEC Hirst Research Centre where the expertise was available.

Except for those destined for laser absorption measurements, samples were always etched after mechanical polishing in order to remove the resultant work-damaged layer of amorphous material. An etch was also given before applying ohmic contacts of indium, and prior to evaporating a gold dot in the fabrication of a Schottky barrier diode. The procedure adopted for ZnSe was as follows. A solution of one percent bromine in methanol was made up by pipetting 0.25 ml bromine into a beaker containing 25 ml methanol. This etchant solution was then poured into five small phials and increasing amounts of methanol added to four of these to give a range of etching solution strengths from strong to weak. The sample was washed in methanol and then transferred from the stronger to the next weaker etch, remaining for twenty seconds in each of the five phials. It was then washed in methanol, dried, and transferred to a phial containing carbon disulphide where it remained for ten minutes. Finally the sample was removed, dried, and stored in a phial containing fresh methanol.

3.42 Ohmic contacts

Ohmic contacts to samples of ZnSe were provided by indium, cleaned in concentrated nitric acid. This was either evaporated or pressed onto the crystal, which was then heated to 250°C for ten minutes. The contact formation has been described in terms of a diffusion process by Blount et al [15]. However Kaufman and Dowbar [16] take the view that it is a liquid phase epitaxial mechanism. This latter explanation is supported by work showing that at the temperatures employed, diffusion is unlikely to be an important factor [17].

The apparatus used to form the contacts consisted of an argon chamber, a molybdenum hearth and an iron-constantan thermocouple. The sample was placed on the hearth and the bell jar replaced. The argon was then allowed to flow through the apparatus for three minutes before the power was switched on. Using a Regavolt transformer, the temperature was raised over a period of five minutes to 250°C where it was held for ten minutes. After this time had elapsed the sample was gradually cooled down for a further ten minutes, and then carefully removed from the hearth. The consistency of the ohmic contacts on ZnSe was quite good. Contact formation was improved by painting the etched contact areas with an amalgam of mercury and indium before pressing the indium slugs into position. This had the effect of wetting the contact surfaces to a greater extent, giving a larger contact area.

I-V plots were performed on all bar samples to verify that the contacts were ohmic. With Schottky barriers two ohmic contacts were made and an I-V plot recorded before one contact was polished off prior to the evaporation of the gold dot. In addition to the I-V technique, testing the mechanical strength was found to be a useful, but occasionally a destructive guide to the degree of success.

3.43 Schottky barrier formation

The Schottky barriers studied in this work were all formed on ZnSe by the vacuum deposition of pure gold onto a freshly etched surface.

After one of the pair of ohmic test-contacts had been removed by mechanical polishing (section 3.41), a protective layer of 'lacomit' varnish was applied to the remaining one in order to protect it from any adverse effects of the etching solution. Etching as described in section 3.41 was then carried out. Before evaporating, the mask and gold wire were cleaned in chromic acid to remove any oxides and adsorbed impurities. Evaporation took place at a pressure of approximately 5×10^{-6} Torr and produced a circular gold film of either 1 or 1.5 mm^2 in area. Characterisation of the barrier was then carried out, by performing I-V and C-V measurements [18].

CHAPTER THREE - REFERENCES

1 L Pauling, The Nature of the chemical bond, Cornel U P, (1961), NY, 3rd Edit.

2 A G Fischer, Z Nature forsh, 13a, (1958), 2549

3 A G Fishcer, J Electrochem Soc., 106, (9), (1959), 838

4 Y Tsujimoto, Y Onodera and M Fukai, Jap J Appl Phys., 5, (1966), 636

5 K F Burr and J Woods, J Cryst Growth, 9, (1971), 183

6 L Clarke and J Woods, J Cryst Growth, 3, (4), (1968), 127

7 K L Lewis, D J Cook and P B Roscoe, J Cryst Growth

8 G J Russel and J Woods, J Cryst Growth, 46, (1979), 323

9 W C Holton, R K Watts and R D Stinedurf, J Cryst Growth, 6, (1969), 97

10 J R Cutter and J Woods, J Cryst Growth, 47, (3), (1979), 405

11 M Aven and H H Woodbury, Appl Phys Lett, 1, (1962), 53

12 B R Sethi, P L Talwar, O P Sharma and P C Mathur, Phys Stat Solidi A, 42, (2), (1977), 791

13 B R Sethi, P L Talwar, O P Sharma and P C Mathur, Phys Stat Solidi A, 47, 2), (1978), 699

14 A C Popadopoulo, A M Jean-Louis and J Charil, J Cryst Growth, 44, (5), (1979), 587

15 G H Blount, M W Fisher, R G Morrison and R H Bube, J Electrochem Soc, 113, (1966), 690

16 R G Kaufman and P Dowbar, J Appl Phys, 45, (10), (1974), 4487

17 H Bjerkland and I Holwech, Phys Norv, 6, (3-4), (1972), 139

18 D D Bedeolgo, Dang Huy Lam and A V Simashkevich, Phys Stat Solidi A, 44, (1), (1978), 83

CONTENTS

4 THERMALLY STIMULATED LUMINESCENCE AND CONDUCTIVITY

4.1 INTRODUCTION

4.2 THEORY

4.21 A mathematical model to describe TSC and TSL

4.211 Simplifications to the kinetic equations

4.23 Determination of trapping parameters

4.221 A study of methods used to obtain trap depths

4.23 Reliability of values obtained for trap depth

4.24 Limitations of the conventional model

4.241 Excited states
4.242 Trap distributions
4.243 Donor-acceptor pair recombination
4.244 Temperature-dependent capture cross-sections
4.245 Additional considerations

4.3 EXPERIMENTAL APPARATUS AND PROCEDURE

4.4 RESULTS

4.41 Introduction
4.42 Methods of analysis
4.43 Durham-grown material

4.431 As-grown material
4.432 Analysis of a Schottky barrier diode

4.44 CVD material
4.45 Computer modelling of results

4.5 DISCUSSION

4 THERMALLY STIMULATED LUMINESCENCE AND CONDUCTIVITY

4.1 INTRODUCTION

The techniques of thermally stimulated luminescence (TSL) and thermally stimulated conductivity (TSC) are methods whereby the thermal ionisation energies associated with deep defect levels in semiconductors may be evaluated. Both methods require only a simple experimental arrangement and can provide a very rapid assessment of a material.

The TSC technique involves the cooling of a sample of the material to a base temperature (usually chosen to be 77°K) and then stimulating it with an injection pulse which floods both the valence band and the conduction band with carriers. Often this is accomplished by illuminating the sample with monochromatic light of an energy greater than the bandgap of the material. This is done for a time long enough to completely fill all majority and minority carrier traps. A number of traps are then occupied by electrons or holes which cannot escape due to there being insufficient thermal energy available to them at the base temperature. When a temperature ramp is applied to the sample the trapped carriers are freed. If a bias voltage has been applied, the rate at which this occurs can be monitored by measuring the conductivity as a function of temperature.

TSL is a similar technique, except that the luminescence due to the recombination of the freed carriers is monitored during the temperature ramp. The intensity of the emitted light is governed by the amount of recombination traffic at the luminescent centres, and hence it can be used as a measure of the rate at which trapped charge is being released.

The method of thermoluminescence curves (glow curves) was first proposed by Urbach [1] and then developed by Herman et al [2]. The first theoretical treatment was provided by Randall and Wilkins [3], whose work was concerned with luminescence in phosphors. Since then the model used to explain the phenomenon has been developed by other workers [4-13], and numerous publications have been produced on the methods of analysis of both TSC and TSL curves, to determine trapping parameters [14-57].

Despite the apparent potential of TSC and TSL to provide an efficient and accurate means of evaluating trapping parameters, there is still very little evidence in the literature that consistent quantitative data can be obtained. This may be due, in part, to the fact that quite often analysis methods developed for TSC data have been used on TSL curves and vice-versa, without first establishing that the procedure is valid [25,37,38]. Some authors [19,39,40,41] have used a large number of analysis methods on the same sample data in order to compare the results given by each. They found that very often the methods gave answers for the thermal ionisation energy which varied considerably. As a result other workers [42] have concluded that a prior knowledge of the defect structure is necessary before deciding on the most appropriate analysis method. More recently a review of the most popular methods was undertaken by Hagebeuk and Kivits [33,34]. The method they adopted was to solve the kinetic equations describing the simple insulator model by numerical analysis on a computer. This enabled TSC and TSL curves to be generated for which the trapping parameters were already known. The analysis methods were then applied to the computer-generated curves to check for reliability under a variety of different conditions. The results of this study are discussed in Section 4.23.

4.2 THEORY

4.21 A mathematical model to describe TSC and TSL

The simple model which is most often used [10,11,33,34] to describe the transitions giving rise to the phenomena of TSC and TSL is shown in Figure 4.2/1. Electrons are thermally excited into the conduction band of the material (transition 1) where they contribute to the conductivity, providing the enhancement seen in TSC measurements. They are then either retrapped (transition 2) or else they recombine with holes which are trapped at recombination centres (transition 3), giving out energy in the form of light to provide a TSL signal. The kinetic equations governing these processes are given by

$$\frac{dn_1}{dt} = -\gamma n_1 + \beta (N_1 - n_1) \qquad 4.2\text{-}1$$

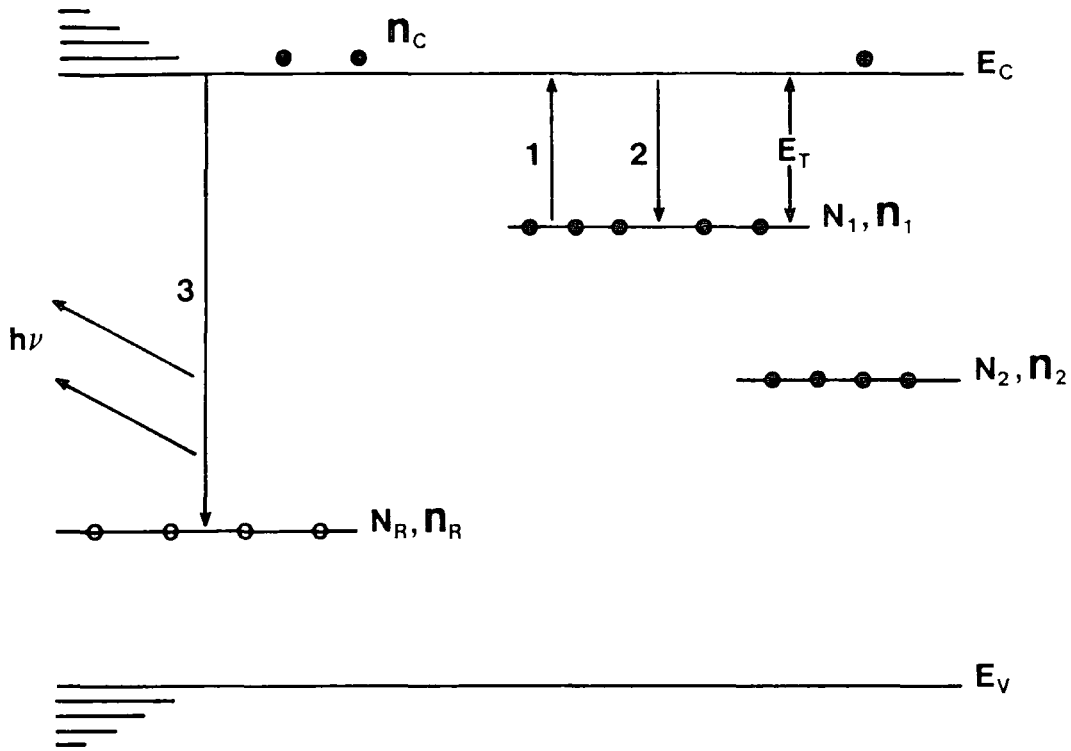

Transition 1: escape of trapped carriers to the conduction band
Transition 2: retrapping of escaped carriers
Transition 3: recombination path
n_c = conc. of free electrons in the conduction band (cm^{-3})
N_1 = conc. of shallow levels (cm^{-3})
n_1 = conc. of electrons trapped at levels N_1 (cm^{-3})
N_2 = conc. of deeper levels (cm^{-3})
n_2 = conc. of electrons trapped at levels N_2 (cm^{-3})
N_R = conc. of recombination centres (cm^{-3})
n_R = conc. of carriers at levels N_R (holes) (cm^{-3})
E_T = thermal activation energy of levels N_1 (eV)

Simple model used to describe the phenomena of TSC and TSL in semiconductors [34]

FIGURE 4.2/1

$$\frac{dn_c}{dt} = -\frac{dn_1}{dt} - \alpha n_c n_R \qquad 4.2\text{-}2$$

where β = capture rate for traps N_1 ($cm^3 s^{-1}$)

α = capture rate for recombination centres N_R ($cm^3 s^{-1}$)

γ = emission rate for traps N_1 (s^{-1})

t = time (s)

and other symbols are defined in Figure 4.2/1.

It is assumed that the traps N_1 and N_2 are 'thermally disconnected', which means that the occupancy of traps N_2 remains unchanged during the emptying of traps N_1. In practice this is rarely the case, and a complex TSC or TSL spectrum is usually produced by traps emptying simultaneously.

The principle of detailed balance provides the expression

$$n_R(t) = n_c(t) + n_1(t) + n_2(t) \qquad 4.2\text{-}3$$

assuming that there are no free holes in the valence band.

From 4.2-2 and 4.2-3 it follows that

$$\frac{dn_R}{dt} = -\alpha n_c n_R \qquad 4.2\text{-}4$$

which is proportional to the luminescence intensity.

The emission rate for traps N_1, which are at an energy E_T(eV) below the conduction band edge is given by

$$\gamma = S\exp(-E_T/kT) \qquad 4.2\text{-}5$$

where: S = pre-exponential factor or frequency factor given by

$$S = \frac{\beta N_c}{g} \qquad 4.2\text{-}6$$

where g = degeneracy of the levels N_1 (taken to be unity) and

N_c = effective density of conduction band states (cm^{-3}).

The two capture rates α and β can be related to the relevant capture cross-sections as follows:

$$\alpha = \sigma_R \langle v \rangle \qquad 4.2\text{-}7$$

and

$$\beta = \sigma_1 \langle v \rangle \qquad 4.2\text{-}8$$

where $\langle v \rangle$ = thermal RMS velocity of electrons (cms^{-1})

σ_1 = capture cross-section for electrons, of traps N_1 (cm^{-2})

σ_R = capture cross-section for electrons, of the recombination centres N_R (cm^{-2})

In addition, the thermal velocity

$$\langle v \rangle = \sqrt{\frac{3kT}{me^*}} \qquad 4.2\text{-}9$$

where me^* = effective mass of the electron.

Assuming a dependence on temperature of T^{-n} for the capture cross-sections σ_1 and σ_R, where $0 \leq n \leq 4$ [43], the temperature dependences for α, β and S are expressed as:

$$\alpha = k_\alpha T^p \quad \left(-\frac{7}{2} \leq p \leq \frac{1}{2}\right) \qquad 4.2\text{-}10$$

$$\beta = k_\beta T^p \qquad 4.2\text{-}11$$

$$S = k_S T^q \quad (-2 \leq q \leq 2) \qquad 4.2\text{-}12$$

where k_α, k_β and k_S are all temperature invariant parameters.

When $E_T >> kT$ (true for all zinc selenide samples studied) the terms α, β and S vary only slowly with temperature compared to the trap emission rate, γ, in 4.2-5. For this reason it is often assumed that these parameters remain effectively constant over the temperature range employed in the TSC and TSL experiment.

The TSC signal is proportional to the number of free carriers present in the material. For the sake of simplicity, it will be assumed that the samples are all n-type. The conductivity is then given by:

$$\sigma_n = n_c \, e \, \mu_n \qquad 4.2\text{-}13$$

where μ_n = electron mobility ($cm^2v^{-1}s^{-1}$).

Over the temperature range used for TSC and TSL in this study (77-400°K), the mobility is assumed to be constant in zinc selenide [44].

The heating rate is given by

$$\Omega = dT/dt \qquad 4.2\text{-}14$$

If the heating rate is constant, the temperature is then expressed as:

$$T = T_0 + \Omega t \qquad 4.2\text{-}15$$

Ideally, analytical solutions for dn_R/dt (TSL) and $n_c(t)$ (TSC) should be found from Equations 4.2-1,2,3,5 and 15, however, this task has proved too difficult up to now. Instead, approximation expressions have been derived by making simplifications in the model. Throughout the following section, the boundary conditions at the base temperature, T_0 are assumed to be:

1 $n_1 = N_1$ (N_1 traps full)
2 $n_2 = N_2$ (N_2 traps full)
3 $n_R = n_1 + n_2$
4 $n_c = 0$ (conduction band empty)

4.211 Simplifications to the kinetic equations

An assumption which is often made in order to simplify the expressions for the TSC and TSL curves is:

$$\left| \frac{dn_c}{dt} \right| \ll \left| \frac{dn_1}{dt} \right| \qquad 4.2\text{-}16$$

From 4.2-2 and 4.2-4 it is clear that this assumption means that the luminescence intensity only depends on the change in occupancy of the levels N_1. This only holds when the recombination lifetime is sufficiently small, such that the recombination centres capture all escaped electrons shortly after they are released to the conduction band. The lifetime is given by

$$\tau = \frac{1}{\alpha n_R} \qquad 4.2\text{-}17$$

As electrons are captured by recombination centres N_R, the number of trapped holes, n_R, decreases, increasing τ. Therefore τ increases with temperature, causing the expression in 4.2-16 to become less reliable. A further assumption that $n_1 << n_2$, and hence that $n_R(To) \approx n_2(To) = N_2$, allows this difficulty to be circumvented, since τ will then remain constant while traps N_1 are emptying. Equation 4.2-2 is then considerably simplified.

Another simplification is given by the assumption

$$n_c << n_1 \qquad 4.2\text{-}18$$

Referring to equation 4.2-1, it can be seen that, in this event

$$\frac{n_c}{n_1} = \frac{\frac{dn_1}{dt} + \gamma n_1}{\beta n_1 (N_1 - n_1)} < \frac{\gamma}{\beta (N_1 - n_1)}$$

Since $dn_1/dt < 0$.

For higher temperatures $(N_1 - n_1)$ will be approximately constant while γ still increases exponentially. Therefore, since $n_1 << N_1$, it can be seen that

$$\frac{n_c}{n_1} < \frac{\gamma}{\beta N_1} = \frac{N_c}{N_1} \exp(-E_T/kT) \qquad 4.2\text{-}19$$

from 4.2-5 and 4.2-6.

The model given by the kinetic equations 4.2-1 and 4.2-2 is essentially a second order process, although it can be approximated in some cases to be first order by assuming that the retrapping of freed carriers is negligible, such that $\beta << \alpha$. Another way of simplifying these expressions is to set $\beta = \alpha$, making the assumption that the probability of a free electron being captured by the recombination centres is equal to the probability of it being recaptured by levels N_1. In the former case, the simplifying assumption of $\beta << \alpha$ often goes under the name of 'mono-molecular kinetics'. Similarly, when β/α (the retrapping ratio) is unspecified, the term 'bimolecular kinetics' is used. Both names are derived from chemical kinetics and are used to denote first and second order recombination processes respectively. The implications of the three assumptions $\beta/\alpha << 1$, $\beta/\alpha = 1$ and $\beta/\alpha \leq 1$ have been discussed previously [19,21].

Following Hagebeuk and Kivits [34] by using the simplifications discussed above, it is possible to write down expressions for the TSL intensity and the TSC signal. First of all, it is convenient at this point to define two additional parameters.

$\delta = \beta/\alpha$ the retrapping ratio

and $\varepsilon = N_2/N_1$ the ratio of deep trap population to shallow, thermally disconnected trap population.

The set of non-linear, first order differential equations 4.2-1, 4.2-2, and 4.2-4 can be combined in a second order expression of the sort in 4.2-20 given below (see Appendix-1). This equation was derived assuming that there are no traps N_2, in the bandgap, which means that the simplification of $N_2 >> N_1$ is not made in this case.

$$\frac{dn_R}{dt} = \frac{\gamma (n_R)^2 + n_R^{-1}(d^2 n_R/dt^2)}{n_R(1-\delta)+N_1\delta + \alpha^{-1}[\gamma - (1+\delta)(n_R)^{-1}(dn_R/dt)]} \qquad 4.2\text{-}20$$

from 4.2-2 and 4.2-3 it is trivial to show that

$$n_c = -(1/n_R\alpha)\ \frac{dn_R}{dt} \qquad 4.2\text{-}21$$

From 4.2-20 and 21 above, it is possible to calculate values for the TSC and TSL intensities as a function of E_T, S, Ω, δ, N_1 and α [33]. Using the simplifications 4.2-16 and 4.2-18 the two expressions above can be re-written as (Appendix-1)

$$\frac{dn_R}{dt} = \frac{-\gamma (n_R)^2}{n_R(1-\delta)+N_1\delta} \qquad 4.2\text{-}22$$

$$n_c = \frac{\gamma n_R}{\alpha(n_R(1-\delta)+N_1\delta} \qquad 4.2\text{-}23$$

The variation of TSC and TSL curve shape and position has been calculated for a range of values for E_T, S, Ω, N_1 and α by the use of a computer procedure [33]. Part of this work is reproduced in Figure 4.2/2. The peak temperatures for the TSC and TSL curves depend mainly on the values

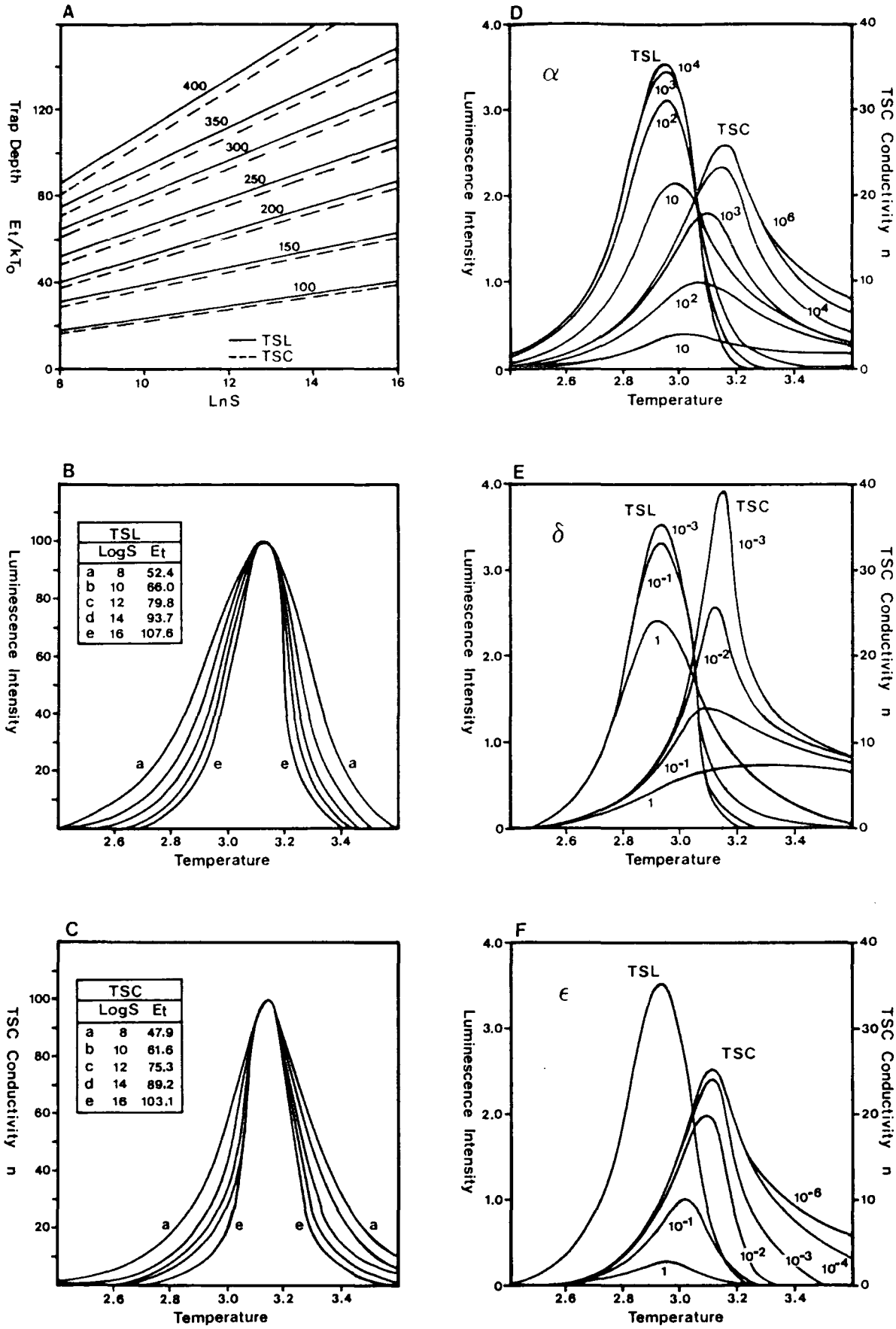

A Lines of constant peak temperature for TSC and TSL. $\alpha = 10^8$, $\delta = 10^{-2}$, $\epsilon = 10^{-3}$.

B Varying width of TSL along a line of constant peak temperature. α, δ, ϵ as in A.

C Varying width of TSC as in B.

D Influence of α. Et = 75, $S = 10^{12}$, $\delta = 0.01$, $\epsilon = 10^{-6}$.

E Influence of δ. $\alpha = 10^8$. Et, S and ϵ as in D.

F Influence of ϵ. Et, S, α and δ as in D and E.

FIGURE 4.2/2

of E_T and S (Figure 4.2/2(a)), however the parameters δ, α and ε have some effect on peak position and curve FWHM. The lines of constant peak temperature in 4.2/2(a) correspond to TSC and TSL peaks with a typical set of parameters α, δ and ε. The FWHM value varies along a given line as shown in 4.2/2(b) and 4.2/2(c). Figure 4.2/2(d) shows that variation of α has very little effect on the TSL curve, however the TSC curve depends very strongly on α for $\alpha < 10^4$ cm^2S^{-1}. Varying the retrapping ratio, δ, has no effect on the TSL curve for $\delta < 10^{-2}$ whereas the TSC curve is always very strongly dependent on it (Figure 4.2/2(e)). Finally the variation with the distribution of trapped charge in the bandgap is shown in Figure 4.2/2(f). For values of $\varepsilon < 10^{-3}$, the TSC curve peak maximum hardly changes with ε. For values of ε which are very small (implying small N_2 values usually), the lifetime of free carriers can increase with temperature (equation 4.2-17), causing the sort of assymmetry seen for $\varepsilon = 0$ in 4.2/2(f). This sort of shape is very rarely seen in TSC measurements and usually only occurs when highly pure crystals are being studied. This highlights the importance of assuming a second trap population and hence that $N_2 \neq 0$. Generally the observed TSC curve shape corresponds approximately to the case for which $\varepsilon = 10^{-3}$. The TSL curve does not vary significantly with ε if $\delta < 0.01$.

4.2.2 Determination of trapping parameters

There are numerous methods in the literature which purport to evaluate TSC and TSL data to produce parameters associated with the deep levels involved. All of these methods give the thermal ionisation energy, and some also give a measure of other parameters, such as the carrier capture cross-section. By way of a summary, some of the most widely used methods will be briefly described in this section. The methods can be separated into three different sorts. The first type, which will be called CLASS 1 methods from now on, are derived by assuming that $\delta << 1$, which is to say that the degree of retrapping is negligible. From the discussions in Section 4.211, it will be remembered that this case corresponds to mono-molecular kinetics. CLASS 2 methods are derived by assuming that $\delta = 1$, in order to facilitate mathematical manipulation of the kinetic equations, and CLASS 3 (also called GENERAL CLASS) methods are derived making no

assumptions as to the value of δ. Additionally, the methods can be subdivided into three different groups according to the technique used to implement them. In this instance they can be listed under the headings:

(A) Methods making use of the variation of peak temperature with heating rate

(B) Geometrical approximation methods

(C) Other techniques

In this selection of methods which follows, certain parameters and notations are used. These are explained in full below. Figure 4.2/3 shows how some of these are related to the characteristics of TSC or TSL curves.

T_m = Temperature at which TSC or TSL maximises

L_m = Maximum TSL luminescence (occurs at T_m)

n_m = Maximum TSC conductivity (occurs at T_m)

T1 = Temperature at half maximum (rising edge)

T2 = Temperature at half maximum (falling edge)

ω = T2-T1 FWHM (full width at half maximum)

σ = $T2-T_m$

λ = T_m-T1

χ = σ/λ

μ_g = σ/ω

Some additional parameters used are

Δ = E_T/kT_m

and Ω = Heating rate ($^\circ Ks^{-1}$)

Whenever the subscript 'i' is used, this denotes the value or parameter which was obtained in the ith experiment. Numerical subscripts should be taken to denote particular experiments.

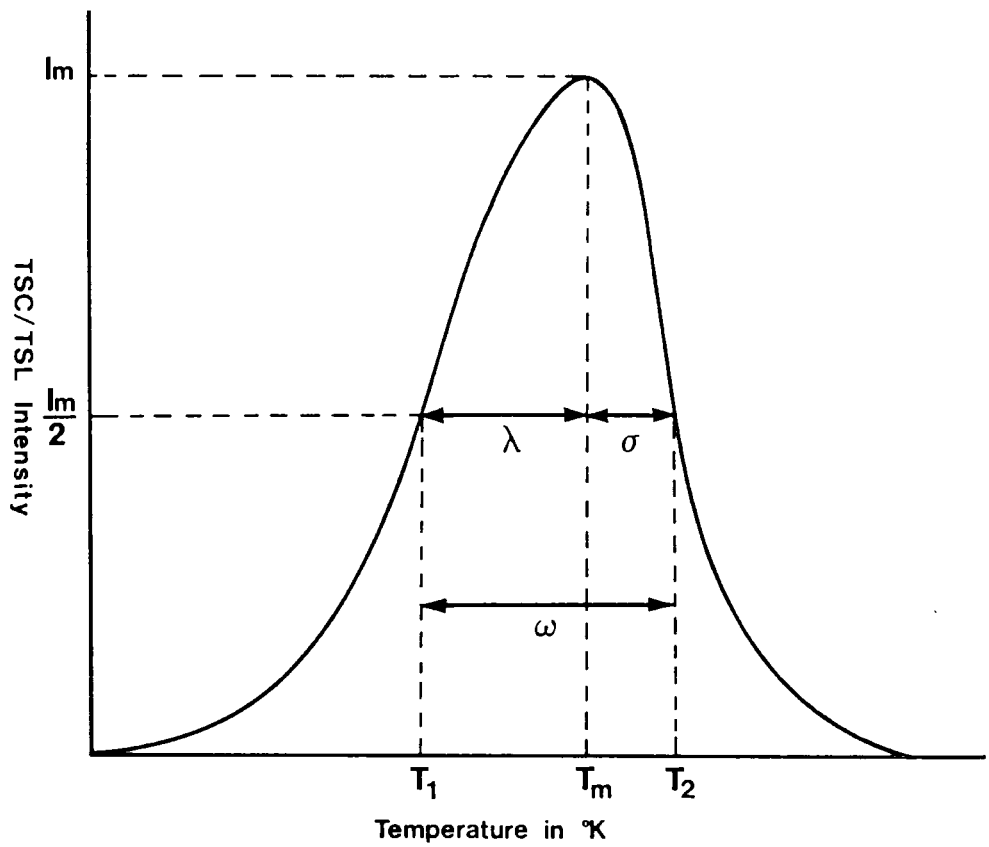

Typical TSC/TSL peak labelled with parameters used to characterise the curves

FIGURE 4.2/3

4.221 A survey of methods used for obtaining trap depths

(A) Methods making use of heating-rate variations in Tm, nm and Lm

(i) CLASS 1 METHODS

1 Booth, Bohun and Parfianovitch [15,45,46]
Derived for TSL analysis
By using two different heating rates, Ω_1 and Ω_2 $^{\circ}Ks^{-1}$, one obtains

$$E_T = \{kT_{m1}.T_{m2}/(T_{m1}-T_{m2})\} \ln(\Omega_1 T_{m2}^2/\Omega_2 T_{m2}^2) \qquad 4.2\text{-}24$$

2 Böer, Oberländer and Voight [47]
Derived for TSL analysis
Plotting $\ln\{\Omega_i\}$ versus $1/T_{mi}$ yields a straight line of slope $-\rho E_T/k$, where $0.7 < \rho < 0.9$

(ii) CLASS 2 METHODS

3 Chen and Winer [27]
Derived for TSL analysis
Plotting $\ln(L_{mi}T_{mi}^4/\Omega_i^4)$ versus $1/T_{mi}$ yields a straight line of of slope E_T/k

(iii) GENERAL CLASS METHODS

4 Hoogenstraaten [48]
Derived for TSL analysis
Plotting $\ln(T_{mi}^2/\Omega_i)$ versus $1/T_{mi}$ should yield a straight line with a gradient given by E_T/k. This method is a generalised version of method 1, and can be extended to include data using more than two heating rates to improve accuracy.

5 Bube, Haering and Adams [49,16]

Derived for TSC analysis

Plotting $\ln(n_{mi})$ versus $1/T_{mi}$ yields a straight line with a slope of $-E_T/k$. This method is valid when $E_T >> kT_{mi}$. When δ is large ($\delta >> 1$), another condition is that $N_1/N_C >> \exp(-E_T/kT_{mi})$.

6 Unger [50]

Derived for TSC analysis

Plotting $\ln(n_{mi})$ versus $1/Tl_i$ yields a straight line with a slope of $-E_T/k$.

7 Schön [51]

Derived for TSC analysis

$$E_T = \{kT_{m1}.T_{m2}/(T_{m1}-T_{m2})\}\ln(\Omega_1.T_{m2}^{3.5}/\Omega_2.T_{m1}^{3.5}) \qquad 4.2\text{-}25$$

8 Boiko, Rashba and Trofimenko-1 [52]

Derived for TSC analysis

Plotting $\ln(n_{mi}/T_{mi}^{1.5})$ versus $1/T_{mi}$ gives a straight line with slope $-E_T/k$.

9 Boiko, Rashba and Trofimenko-2 [52]

Derived for TSC analysis

Plotting $\ln(\Omega_i/T_{mi}^{3.5})$ versus $1/T_{mi}$ gives a straight line of slope $-E_T/k$.

This method is actually an extension of method 7, due to Schön.

(B) Methods making use of geometrical approximations

(i) CLASS 1 METHODS

10 Luschik [7]

Derived for TSC analysis

$$E_T = kT_m^2/\sigma \qquad 4.2\text{-}26$$

11 Halperin and Braner-1 [9]

Derived for TSL analysis

$$E_T = (1.72\ kT_m^2/\lambda)\ (1-5.16/\Delta) \qquad 4.2\text{-}27$$

with the condition that $\mu_g \leqslant e^{-1}(1+2/\Delta)$

12 Halperin and Braner-2 [9]

Derived for TSL analysis

$$E_T = kT_m^2/\sigma \qquad 4.2\text{-}28$$

with the condition that $\mu_g \approx e^{-1}$

13 Chen-1 [53]

Derived for TSL analysis

$$E_T = 2kT_m\ (1.25\ T_m/\omega-1) \qquad 4.2\text{-}29$$

with the condition that $\Delta >> 1$

14 Chen-2 [53]

Derived for TSL analysis

$$E_T = 2.29\ kT_m^2/\omega \qquad 4.2\text{-}30$$

which is a simplified version of method 13

15 Chen-3 [53]

Derived for TSL analysis

$$E_T = (1.548\ kT_m^2/\lambda)\ (1-3.16/\Delta) \qquad 4.2\text{-}31$$

16 Chen-4 [53]

Derived for TSL analysis

$$E_T = 1.52\ kT_m^2/\lambda - 3.16\ kT_m \qquad 4.2\text{-}32$$

17 Chen-5 [53]

Derived for TSL analysis

$$E_T = AkT_m^2/\sigma \qquad 4.2\text{-}33$$

where $A = 0.976 \pm 0.004$, established from a computer fit.

This is a refined version of method 10, due to Luschik.

18 Chen-6a,6b [54,55]

Derived for TSC analysis

$E_T = 3\sigma\ kT_m^2/\omega\lambda$ (a) 4.2-34

$E_T = 2.8\sigma\ kT_m^2/\omega\lambda$ (b) 4.2-35

(ii) CLASS 2 METHODS

19 Halperin and Braner-3 [9]

Derived for TSL analysis

$E_T = (2kT_m^2/\lambda)\ (1-6/\Delta)$ 4.2-36

with the condition that $\mu_g \geq e^{-1}\ (1+2/\Delta)$

20 Halperin and Braner-4 [9]

Derived for TSL analysis

$E_T = 2kT_m^2/\sigma$ 4.2-37

with the condition that $\mu_g \approx 0.5$.

21 Halperin and Braner-5 [9]

Derived for TSL analysis

$E_T = (1+\omega/\lambda)kT_m^2/\sigma$ 4.2-38

with the condition that $\mu_g \approx 0.5$. This method was derived for the case where $\delta = 1$.

22 Chen-7 [53]

Derived for TSL analysis

$E_T = 2kT_m\ (1.77\ T_m/\omega - 1)$ 4.2-39

23 Chen-8 [53]

Derived for TSL analysis

$E_T = 1.813\ kT_m^2/\lambda - 4kT_m$ 4.2-40

24 Chen-9 [53]

Derived for TSL analysis

$$E_T = B.2kT_m^2/\sigma \qquad 4.2\text{-}41$$

where B = 0.853 ± 0.0012 derived from a computer fit. This is in fact method 20, refined by computer analysis to include the constant B.

(C) Other methods of analysis

(i) CLASS 1 METHODS

25 Randall and Wilkins [3]

Derived for TSL analysis

$$E_T = 25\ kT_m \qquad 4.2\text{-}42$$

It is assumed that $\gamma = 1$ when $T=T_m$, and $0.5<\Omega<2.5°Ks^{-1}$, and $S = 2.9 \times 10^9\ s^{-1}$.

26 Grossweiner [14]

Derived for TSL analysis

$$E_T = 1.51kT_mT_1/\lambda \qquad 4.2\text{-}43$$

The expression for E_T is derived here assuming that the TSC curve can be approximated by a triangle. This holds when $\Delta > 20$ and $S/\Omega > 10^7\ k^{-1}$.

27 Franks and Keating [17,18]

Derived for TSL analysis

$$1/\Delta = (\omega/T_m)(1.2\chi-0.54)+5.5 \times 10^{-3} - \tfrac{1}{4}(\chi W-0.75)^2 \qquad 4.2\text{-}44$$

with the condition that $10<\Delta<35$ and $0.75<\chi<0.9$

28 Dussel and Bube [10]

Derived for TSC analysis

$$E_T = CkT_mT_1/\lambda \qquad 4.2\text{-}45$$

when Δ = 17,22 or 26 a value for C must be taken of 1.402, 1.415 or 1.421 respectively. This method is a refined version of method 26.

(ii) GENERAL GLASS METHODS

29 Garlick and Gibson [6]

Derived for TSL analysis

This is often called the 'initial rise method'. A plot of ln(L) versus 1/T is taken over the initial rising part of the TSL curve. The gradient of this should yield $-E_T/k$. Haake [56] concludes that this method becomes more accurate for larger values of S, and lower values of E_T.

30 Sandomirskii and Zhdan [57]

Derived for TSL analysis

$$E_T = 1.455\ kT_mT1/\lambda\ -0.79\ kT1 \qquad 4.2\text{-}46$$

when $1.02 < (T_m/T1) < 2.0$

This expression is the same as 4.2-43 (due to Grossweiner), but it is corrected by computer analysis.

31 Voigt [57]

Derived for TSC analysis

$$18\ kT_m < E_T < 25\ kT_m \qquad 4.2\text{-}47$$

4.23 Reliability of values obtained for trap depth

In their paper on the evaluation of the model for TSC and TSL [34], Kivits and Hagebeuk used the results of previous work [33] to generate theoretical TSC and TSL curves, using a numerical analysis technique on a computer. Most of the methods listed in section 4.22 were then applied to these curves, for which all the parameters were known. This enabled the methods to be tested for reliability under various conditions of retrapping ratio δ, trap depth E_T, attempt-to-escape frequency S, and heating rate Ω. The actual values they chose, in order to cover a broad range, were

E_T = 0.273, 0.341, 0.511 and 0.682 eV

δ = 0.01, 1.0 and 3.0 for TSL

δ = 0.01, and 0.1 for TSC

s = 1.25×10^6, 1.25×10^9 and 1.25×10^{12} s^{-1}

Ω = 0.01, 0.1 and 1.0°Ks^{-1}

For each curve with a specific set of values δ, S, Ω and E_T, a relative error in the method was calulated using

$$\varepsilon_R = (E_m - E_T)/E_T \qquad 4.2\text{-}48$$

where ε_R is the relative error, E_T the 'true' trap depth and E_m the value for the trap depth obtained by using the method under test. The results of this exercise are given in full in [34], however it is sufficient here to simply summarise them.

All these methods which make use of T2 were found to be sensitive to the value $\varepsilon(N_2/N_1)$ when used to analyse TSL data. This follows from discussions of TSL curve shape in 4.211 and from the TSL curves shown in Figure 4.2/2(f). For both the TSL and TSC the methods of Chen and Winer (method 3), Hoogenstraaten (method 4), Bube et al (method 5) and Unger (method 6) were found to produce the best value for trap depth. All of these methods gave values for E_M which differed by 1% or less from the 'correct' value, E_T, for all values of δ, E_T and S. Table 4.2/4 shows a simplified summary of the performance of the methods.

Apart from the four methods mentioned above, which stand apart from the rest because of their consistent accuracy, there are only four other methods which are applicable to the analysis of TSC curves. Three of these, methods 11, 14 and 15, are only correct when there is very little retrapping of freed carriers, and method 14 is sensitive to the parameter ε. The method due to Sandomirskii and Zhdan (method 30) does rather better since it gives correct values over an order of magnitude variation in δ.

The fact that so few methods can be applied to TSC data highlights the care that must be taken in the analysis stage. Indiscriminate application of methods to TSL and TSC curves alike can create a confusing set of results which make little sense. Methods 25 (Randall and Wilkins) and 31 (Voigt) turn out to be inaccurate since they are very dependent upon the heating rate and frequency factor. The method of Grossweiner (method 26) is found to be very dependent upon the value of δ, and from the results obtained in [34], it is estimated that it may be correct for a value of $\delta \approx 0.1$, for TSL curves.

METHOD		TSL				TSC		
METHOD AUTHORS	METHOD NUMBER	δ			VARIATION WITH ε	δ		VARIATION WITH ε
		0.01	0.1	3		0.01	0.1	
Chen and Winer	3	*	*	*	No	*	*	No
Hoogenstraaten	4	*	*	*	No	*	*	No
Bube et al	5	*	*	*	No	*	*	No
Unger	6	*	*	*	No	*	*	No
Luschik	10	*	-	-	Yes	-	-	Yes
Halperin and B.-1	11	*	-	-	No	*	-	No
Chen-1	13	*	-	-	Yes	-	-	Yes
Chen-2	14	*	-	-	Yes	*	-	Yes
Chen-3	15	*	-	-	No	*	-	No
Chen-4	16	*	-	-	No	-	-	No
Chen-5	17	*	-	-	Yes	-	-	Yes
Chen-6a	18	*	*	-	Yes	-	-	Yes
Chen-7	22	-	*	-	Yes	-	-	Yes
Chen-8	23	-	*	-	No	-	-	No
Chen-9	24	-	*	-	Yes	-	-	Yes
Dussel and Bube	28	*	-	-	No	-	-	No
Garlick and Gibson	29	*	-	-	No	-	-	No
Sand. and Zhdan	30	*	-	-	No	*	*	No

* Method gave values for E_m which differed by 5% or less from the correct value, E_T.

- Method inaccurate

SUMMARY OF THE WORK OF KIVITS AND HAGEBEUK [34] IN THE EVALUATION OF THE RELIABILITY OF TSC AND TSL ANALYSIS METHODS

FIGURE 4.2/4

4.24 Limitations of the conventional model

The simple model used to describe the processes of TSC and TSL (Figure 4.2/1) has been extended by Kivits [13] to take into account recombination by excited states, the presence of a trap distribution, donor-acceptor pair recombination, the presence of additional centres, temperature-dependent rate parameters, the thermal quenching of luminescence and scattering due to ionised defect centres.

4.241 Excited states

Impurity centres may be expected to have excited states [58] which can contribute to the free electron capture process [59] (Figure 4.2/5). If recombination via excited states is important in a given material, then the transition probability, W, (Figure 4.2/5) will be large. Under these circumstances the TSL intensity is given by [13]

$$\frac{dn_R}{dt} = -\chi n_R \qquad 4.2\text{-}49$$

which indicates first order (mono-molecular) kinetics.

Since the expression for TSL intensity derived for the simple model (equation 4.2-22) reduces to a similar expression for $\delta \ll 1$ (mono-molecular kinetics), the TSL experiment does not in itself reveal when recombination via excited states is taking place. However a TSC measurement, undertaken simultaneously with TSL, should provide a guide, since no conduction will be observed when the model described in Figure 4.2/5 is operative.

4.242 Trap distributions

In the simple model, the ionisation energy of a particular defect is assumed to depend solely upon the local distortion its presence induces in the host lattice. However, this can be modified significantly if the defect is surrounded by other charged centres at short distances, due to the coulombic interaction. A population of defects present in the host

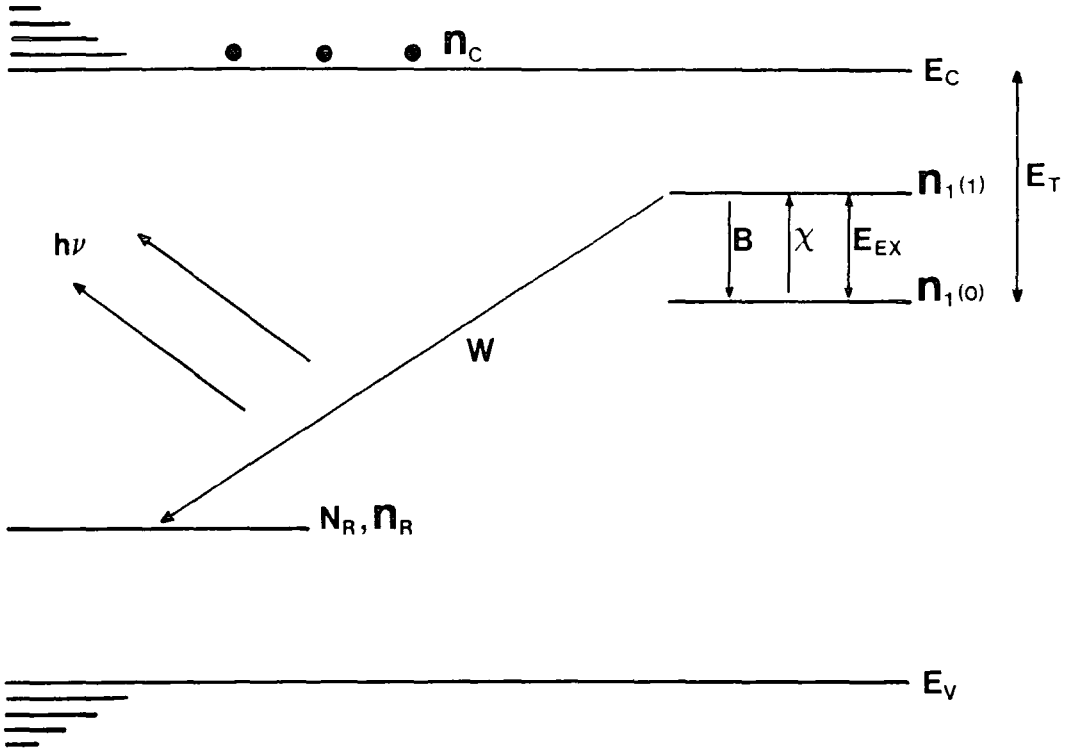

B = Transition probability to ground state (s^{-1})

χ = S_{EX} exp $(-E_{EX} / kT)$
Transition probability to excited state (s^{-1})

E_{EX} = Energy difference between ground and excited states

W = Transition probability of recombination between excited state and recombination centres, N_R (s^{-1})

Scheme describing recombination via excited state of levels N_1 to recombination centres, N_R.

FIGURE 4.2/5

material may therefore be described in terms of a distribution of ionisation energies within the bandgap.

Kivits [13] has investigated the effect, on the TSL curve, of assuming a Poisson distribution of ionisation energies for a trap population. It is found that the methods of Hoogenstraaten (method 4) and Bube (method 5) give an accurate value for E_{max}, the ionisation energy associated with the distribution maximum, for a large-range of trap concentrations. Both methods were, in addition, found to be insensitive to the distribution function chosen. All other methods tried yielded a lower value for the ionisation energy.

In order to check for the presence of a trap distribution the method of 'decayed glow curves' [48], or 'thermal cleaning' [19] may be used. This technique involves warming the previously photoexcited crystal to a temperature less than the typical TSC or TSL peak temperature, and then cooling it again. If a trap distribution is present, most of the shallower traps will have been emptied by this procedure, and when the crystal is heated at a fixed rate to produce the complete TSC or TSL curve, the analysis for the trap depth will produce an increased value for E_T. Conversely if the value for E_T, the trap depth, remains constant the TSC or TSL curve is most likely to be due to a discrete level within the bandgap.

4.243 Donor-acceptor pair recombination

The probability of donor-acceptor pair recombination occurring in a material is determined by the degree to which the donor and acceptor wavefunctions overlap [60]. Immediately after excitation of the crystal at low temperatures, a slow decay of luminescence is sometimes observed, which is unaccompanied by any equivalent decay of conductivity. Hoogenstraaten [48] and later Riehl [61] suggested that this was due to the decay of D-A pairs. It is evident that the longer the crystal is kept at the base temperature, the more electrons are lost from traps via the mechanism of D-A pair recombination, giving a smaller value for the integrated light intensity in a subsequent TSL run. To check whether

traps are leaking by this route, the light sum in TSL experiments for various excitation levels or waiting times after excitation has been terminated can be measured [48].

In general the various analysis methods used to evaluate the trap depth will be unaffected by D-A pair recombination. Techniques which make use of the integrated luminescence intensity in order to give a value for the trap concentration may be in error however, since the assumption that all traps are full at the base temperature, T_0, will not be true.

4.244 Temperature dependent capture cross-sections

In Section 4.21 it was mentioned that the slow temperature variation of the capture parameters associated with recombination centres and traps, compared with the exponential dependence of the emission rate, γ, (equation 4.2-5) meant that these quantities were usually taken to be temperature invariant. Exponential dependence of capture cross-section with temperature has been observed, however [62], and the effect of this will be briefly discussed.

Assuming that the capture cross-sections associated with traps and recombination centres depend exponentially on temperature, the expressions for these parameters can be written as

$$\sigma_1 = \sigma_{1,0} \exp(-E_\beta/kT) \qquad 4.2\text{-}50$$

$$\sigma_R = \sigma_{R,0} \exp(-E_\alpha/kT) \qquad 4.2\text{-}51$$

where $\sigma_{1,0}$ and $\sigma_{R,0}$ are both constants

E_α = activation energy of the capture process for recombination centres

E_β = activation energy of the capture process for traps

and σ_1 and σ_R are the same parameters as those used in equations 4.2-7 and 4.2-8.

From equation 4.2-5 it follows that the emission rate for traps can be written as

$$\gamma = S_{1,0} \exp(-(E_\beta + E_T)/kT) \qquad 4.2\text{-}52$$

where $S_{1,0} = N_C \langle \nu \rangle \sigma_{1,0}$

Similarly, from equations 4.2-7 and 4.2-8, the expressions for the capture rates are now given by

$$\beta = \langle \nu \rangle \sigma_{1,0} \exp(-E_\beta/kT) \qquad 4.2\text{-}53$$

$$\alpha = \langle \nu \rangle \sigma_{R,0} \exp(-E_\alpha/kT) \qquad 4.2\text{-}54$$

Since $\delta = \beta/\alpha$, the expression for the retrapping ratio, δ, can be written as

$$\delta = \delta_0 \exp(-(E_\beta - E_\alpha)/kT) \qquad 4.2\text{-}55$$

where $\delta_0 = \sigma_{1,0}/\sigma_{R,0}$

Using these modified parameters, a new expression for dn_R/dt can be derived by following exactly the same reasoning as that outlined in Appendix-1, to yield a result similar to equation 4.2-20. The differences between the two expressions are as follows

(a) There is an extra term $\Omega E_\alpha/kT^2$ incorporated in the denominator of 4.2-20. This can be neglected [13] because of the large value of α [33] in most cases.

(b) The temperature dependence of α. As long as α is greater than approximately 10^4 S^{-1} (Figure 4.2/2(d)), then the TSC and TSL curve shapes are not affected by variation of this parameter. Generally, this holds for all ZnSe samples studied. Equation 4.2-21 indicates that TSC is affected more than TSL by variations in α.

(c) The temperature dependence of δ. This affects both TSL and TSC curves. As discussed in 4.211 however, TSL curves show very little change when $\delta < 10^{-2}$ (Figure 4.2/2(e)).

(d) The dependence of γ on temperature. This has a strong effect on both TSC and TSL curves. From equation 4.2-52 it is clear that all of the analysis techniques discussed so far will yield the value $E_\beta + E_T$. In this case, further experimentation is needed to separate E_β from the thermal ionisation energy E_T.

Using the same technique as that explained in [34], Kivits [13] tested various methods of analysis on TSC curves generated for different values of E_α, E_β and E_T. It was concluded that the method of Hoogenstraaten (method 4) was the only one to yield a consistent value for E_T+E_β. All other methods gave low answers, which differed from E_T+E_β by approximately E_α.

4.245 Additional considerations

In all of the cases discussed so far it has usually been assumed that there is a very large concentration of recombination centres, N_R, in the material. It is assumed that the density of trapped holes, n_R, does not change significantly in the temperature range considered (77-400°K). Such might not be the case if the recombination centres are sufficiently near to the valence band for the trapped holes to be freed at some temperature within the range of interest. If this happens, a change in the free electron lifetime, τ (equation 4.2-17) will occur. In order to ascertain whether this is occurring in a sample, the photoluminescence may be monitored as a function of temperature. If the luminescence due to the radiative transition 3, in Figure 4.2/1, falls as the sample is heated, then thermal quenching is indeed taking place. A quantitative investigation of thermal quenching may then allow the model to be corrected accordingly, so that the TSC and TSL curves can be analysed.

Another important factor influencing the model is the temperature variation of mobility. This depends on the particular scattering

mechanism which dominates at a given temperature. Usually, the results in a $T^{-1.5}$ dependence for acoustic-mode lattice scattering, or a $T^{+1.5}$ dependence when carriers are mainly scattered by charged impurities within the material. It is evident that such a slow variation with temperature can be neglected when compared to the large rate of change of occupancy of traps when they are in the process of emptying. A complication might arise however, if ionised impurity scattering is the dominant process, since the mobility also depends upon the density of these centres in the material. The change in the charge state of any emptying traps might therefore be found to alter the mobility under some circumstances. Kivits has considered this possibility [13] and he found that the initial rise section of the TSC curve, and the value of T1 were both appreciably affected, while the peak maximum temperature remained the same as before. The initial rise was flatter, and the value of T1 shifted to lower temperature, rendering all methods which use these characteristics inaccurate.

4.3 EXPERIMENTAL APPARATUS AND PROCEDURE

For TSC and TSL experiments, the samples were mounted in the liquid nitrogen cryostat shown in Figure 4.3/1. This featured an O-ring seal at the neck which reduced heat conduction at low temperatures, and allowed the sample fixed on the cold-finger to be rotated to face either the U/V source or the photomultiplier without breaking the vacuum seal. This feature was helpful when the TSL intensity was low, since the sample orientation could then be altered to optimise the signal. All windows were made of quartz, and were butted against O-ring seals to provide a vacuum-tight joint. To cool the cryostat to liquid nitrogen temperatures, it was first necessary to evacuate it to prevent icing. Liquid nitrogen was then poured into the neck which led down to the copper cold-finger. Typically, the sample temperature reached 80°K. To warm the apparatus, a simple heater was made using kanthal wire, a silica former and a silica tube, sealed at one end. This arrangement was placed in the cryostat neck and powered from the laboratory 24V supply. The heating rate could be adjusted in the range 0.09 to 0.70°Ks^{-1} by using a series-connected rheostat. During a TSC or TSL run, the temperature of the sample was continuously monitored using a Control and Readout temperature meter type CRL 206. This instrument featured automatic cold-junction compensation,

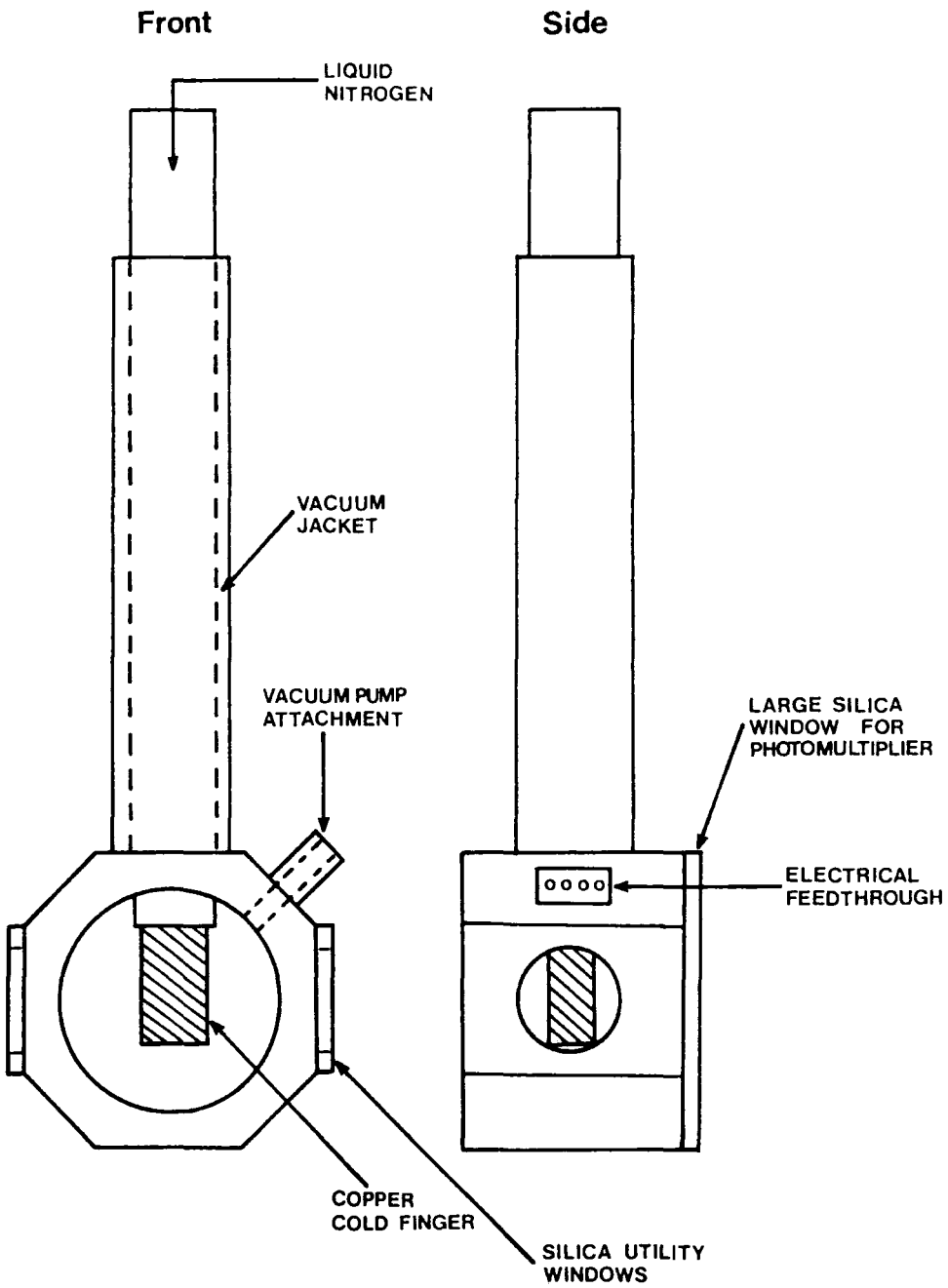

Liquid Nitrogen Cryostat used for TSC,TSL and DLTS

FIGURE 4.3/1

and the conversion to a meter reading was achieved by using a look-up table contained in an EPROM, which gave a 256 breakpoint approximation to the copper-constantan thermocouple characteristic. The accuracy over the -200 to +200°C range was ±2%.

TSL measurements were made using an EMI 9558AM photomultiplier. The unit was powered by a 0-2KV Brandenberg supply. Signal currents produced by the final amplification stage were passed through a decade resistance box, which enabled the sensitivity to be altered to suit the chart recorder f.s.d.

TSC measurements were made using the circuit shown in Figure 4.3/2. The sample was biassed at about 30V DC using a floating stabilised power supply. A Keithley Instruments model 602 electrometer was used to detect the TSC currents flowing in the circuit. To minimise noise pickup from interference, the whole of the circuit was shielded by an earthed screen, which was also connected to the brass cryostat body. Low capacitance coaxial microphone cable was used to carry the signals. All leads were kept to the minimum length consistent with the experimental arrangement, to minimise the circuit capacitance, which has been shown to increase the noise spectrum [63]. The currents measured in zinc selenide samples studied in this project were never lower than 10^{-13}A, which meant that the noise currents present in the Keithley Electrometer ($\sim 10^{-15}$A) were negligible in all the experiments conducted. Similarly the rise-time of the device was such that no shaping of the TSC curves occurred. For heating rates greater than $1°Ks^{-1}$ however, this factor might become important when the Electrometer is used on the NORMAL setting. A FAST setting was provided, for measuring quickly changing signals, and in this mode the rise-time is typically decreased by a factor of ten. Usually the instrument was operated in the NORMAL mode, in order to damp out some of the residual high frequency noise in the signal, which was caused by the laboratory environment.

The excitation was provided by a compact 250W high pressure mercury arc-lamp powered by a stabilised power supply operating at mains voltage. A large silica lens was used to focus the beam onto the sample through two

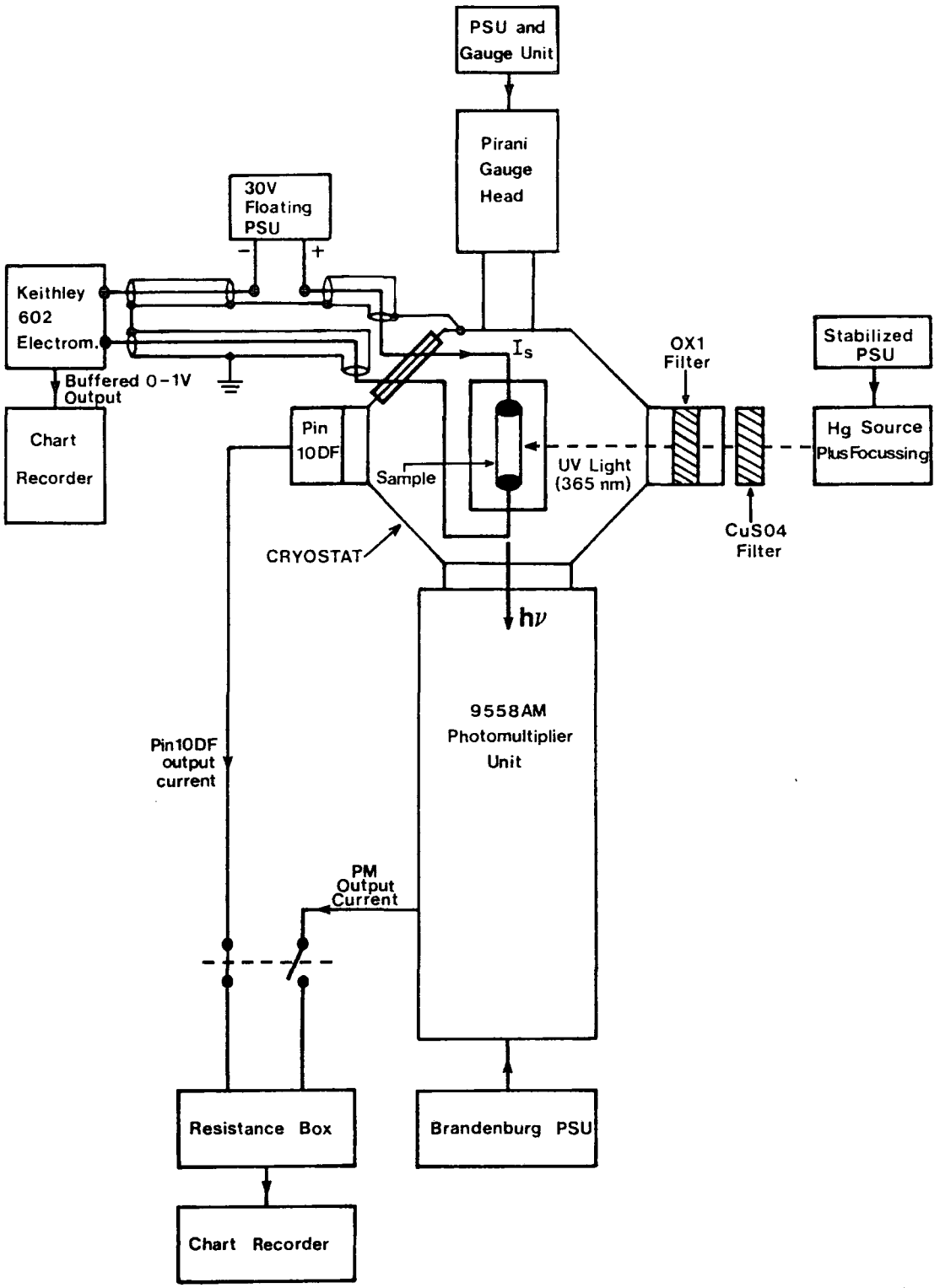

Arrangement for TSC and TSL experiments, using the liquid nitrogen cryostat shown in FIGURE 4.3/1

FIGURE 4.3/2

optical bandpass filters. The filter fixed to the cryostat input window was an OX1 Chance Glass component, designed to allow a very restricted band of frequencies through, centred on the 360 nm line. Unfortunately, this type of filter also transmits in the near infrared. Since IR wavelengths can quench the luminescent processes occurring in materials, it is desirable to filter these out completely. To do this a silica cell 1 cm thick, filled with 10% $CuSO_4$ solution was used to block light of wavelength greater than 550 nm.

4.4 RESULTS

4.41 INTRODUCTION

Measurements were performed on Durham-grown ZnSe and AWRE-grown CVD ZnSe in order to compare the native defects and impurity levels occurring in each using the established techniques of thermally stimulated luminescence and thermally stimulated conductivity as described in section 4.3.

The Durham-grown material was taken from three boules: 345, 388 and 400. Boule 388 was subject to high levels of copper contamination during growth due to the type of furnace tube used, whereas boule 400 was thought to be relatively free of Cu impurity. The material provided by AWRE was grown by the CVD technique and proved to be difficult to analyse by the TSC and TSL methods owing to the nature of the grain structure (Chapter 6). These samples required a very long settling time after the photo-excitation source had been removed in order to allow the background photo-current and photo-luminescence to subside to a level such that the TSC and TSL spectra could be observed. In some of the samples this settling time was as long as four hours.

TSC spectra obtained from samples of each type of material studied are shown in Figure 4.4/1. From these curves it can be seen that common peaks exist at approximately 110, 150-160, and 210°K. In the curve obtained from a sample of boule 388, an additional peak is observed at about 260°K, however this peak was swamped by the rising dark current and was difficult to analyse. The curves in Figure 4.4/1 show the problems involved in the

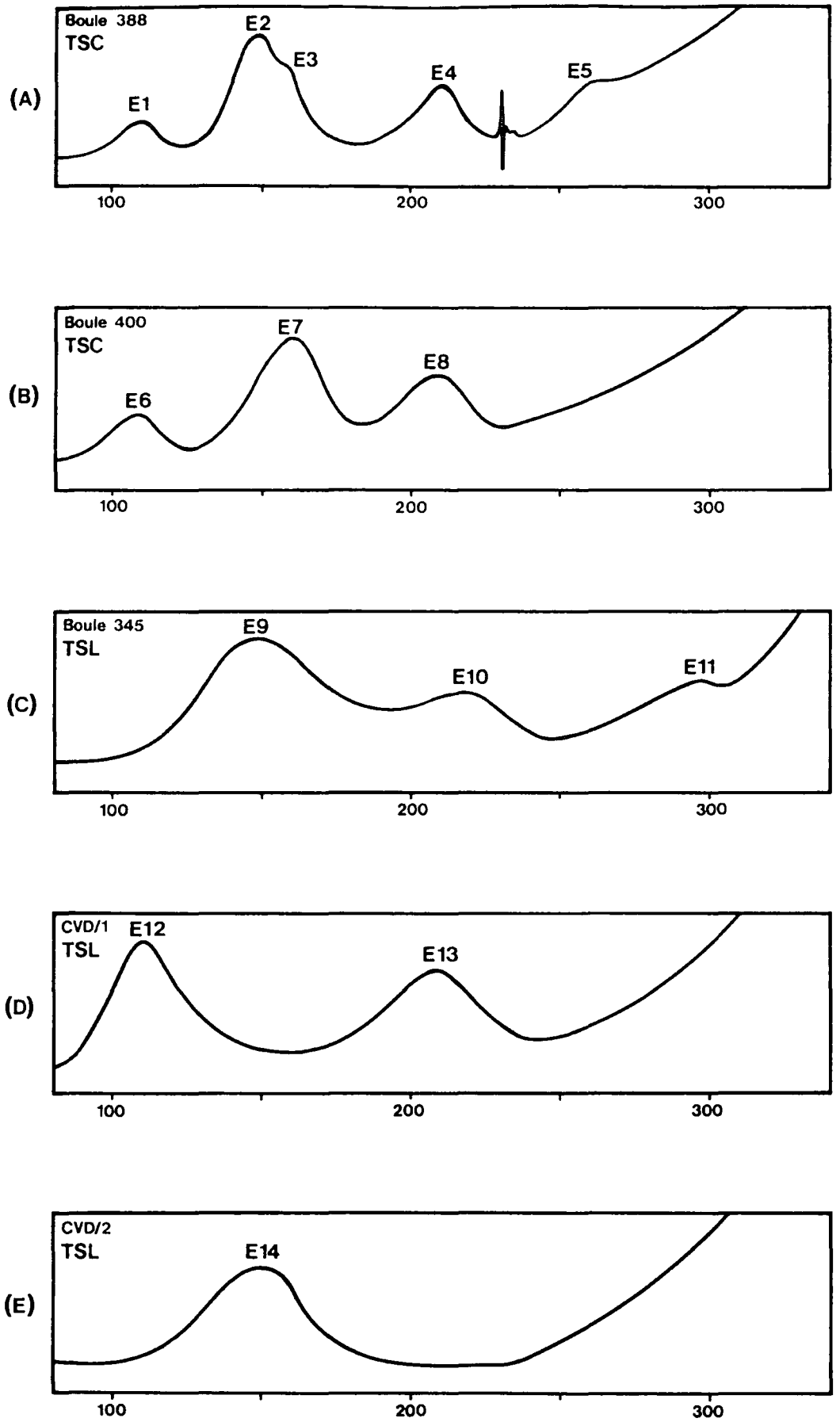

TSC and TSL spectra obtained from Durham-grown and CVD grown ZnSe showing the positions of the principal peaks

FIGURE 4.4/1

analysis of some peaks, which are overlapping. In this case the method of thermal cleaning discussed in Section 4.242 was used to empty the trap population on the low temperature side of the peak of interest, and hence make it possible to apply analysis methods relying on peak temperature as a function of heating rate to obtain the thermal ionisation energy (e.g. methods 4, 5 and 6, Section 4.221).

4.42 Methods of analysis

Prior to the application of the TSC and TSL methods to analyse each sample a current-voltage plot in the dark was first performed in order to verify that the contacts were ohmic. The subsequent analysis of TSC and TSL spectra was accomplished with reference to the methods used by Kivits et al [34] who made an extensive evaluation of the reliability of most of the techniques which have been put forward in the literature over the years. A discussion and summary of this work is presented in Section 4.23 from which it is clear that methods 3, 4, 5 and 6 stand out from all the rest in the respect that they were found to be accurate for a wide range of material parameters. In addition method 4, due to Hoogenstraaten, stands out from the rest in this group because of its accuracy in a situation where trap distributions or temperature-dependent capture cross-sections are an important factor. Another very important point is that the method due to Hoogenstraaten only involves the use of the peak maximum temperature, and the heating rate at peak maximum. The other three methods involve the use of the peak height (either TSL intensity or TSC current density) which can depend strongly on the excitation intensity/period or the temperature at which the traps are initially filled. In the course of the present work it was found that even if a very regimented initial trap filling procedure was adopted these three methods usually gave anomalous results over several different heating rates, whereas method 4 (Hoogenstraaten) was always extremely consistent. The method due to Unger (method 6) also uses the temperature at half maximum, T1, on the rising side of the TSC/TSL curve. This adds another problem when a complex spectrum is observed, since interfering peaks can cause T1 to be in error. Thermal cleaning cannot be used in this instance, since the method also relies on the peak height as mentioned previously.

In order to avoid the problems discussed above the results obtained from the method due to Hoogenstraaten were assumed to be correct, and the results of all of the other methods were compared with this value in the light of the work done by Kivits et al [34]. Each peak in a given sample was analysed by measuring either TSC or TSL (sometimes both) at several different heating rates (at least four) and by tabulating heating rate, T1, TM, T2, and peak height in each case. These data were then used by a computer procedure to produce trap depth values calculated by the 18 methods listed in the table in Figure 4.2/4. Finally, computer modelling of a number of samples of Durham-grown and CVD ZnSe was performed (Section 4.45) in order to check the consistency of the mathematical model, and to try to obtain some verification of the values assumed for retrapping ratio and trap depth.

4.43 Durham-grown ZnSe

4.431 As-grown material

The complete TSC spectrum obtained from a sample of boule 388 is shown in Figure 4.4/1. A very rapid series of current fluctuations was observed at a temperature of about 230°K, which were found to be repeatable. At some points these fluctuations caused a reversal of the current flow. Observation of the current using an oscilloscope revealed nothing of interest and the investigation of this phenomenon was quickly dropped, since it was observed to be either completely different, or even totally absent when samples obtained from neighbouring areas of the same boule were tested.

Trap E2 was examined first, and the results are shown in Figure 4.4/2 plotted according to the method of Hoogenstraaten. The trap depth assigned to this level was 0.23 eV. The thermal cleaning technique (Section 4.242) was employed in order to test this level for a possible trap distribution. The results of six successive thermal cleaning runs are shown in Figure 4.4/3. The characteristic peak temperature of the TSC was 150°K, and this peak was cleaned to six temperatures between 133.2 and 158.2°K.

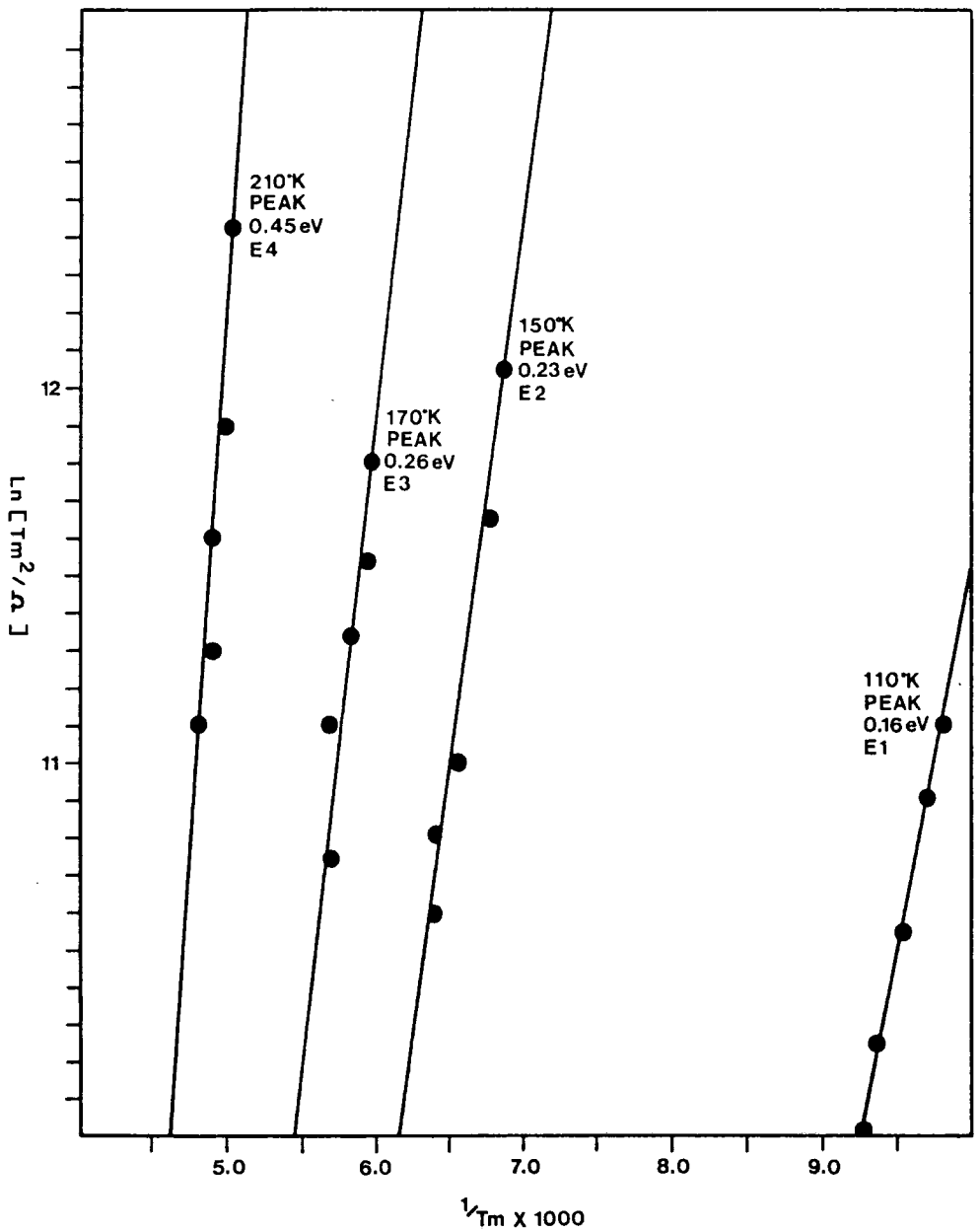

Analysis of the main peaks in boule 388 using the method due to Hoogenstraaten (method 4)

FIGURE 4.4/2

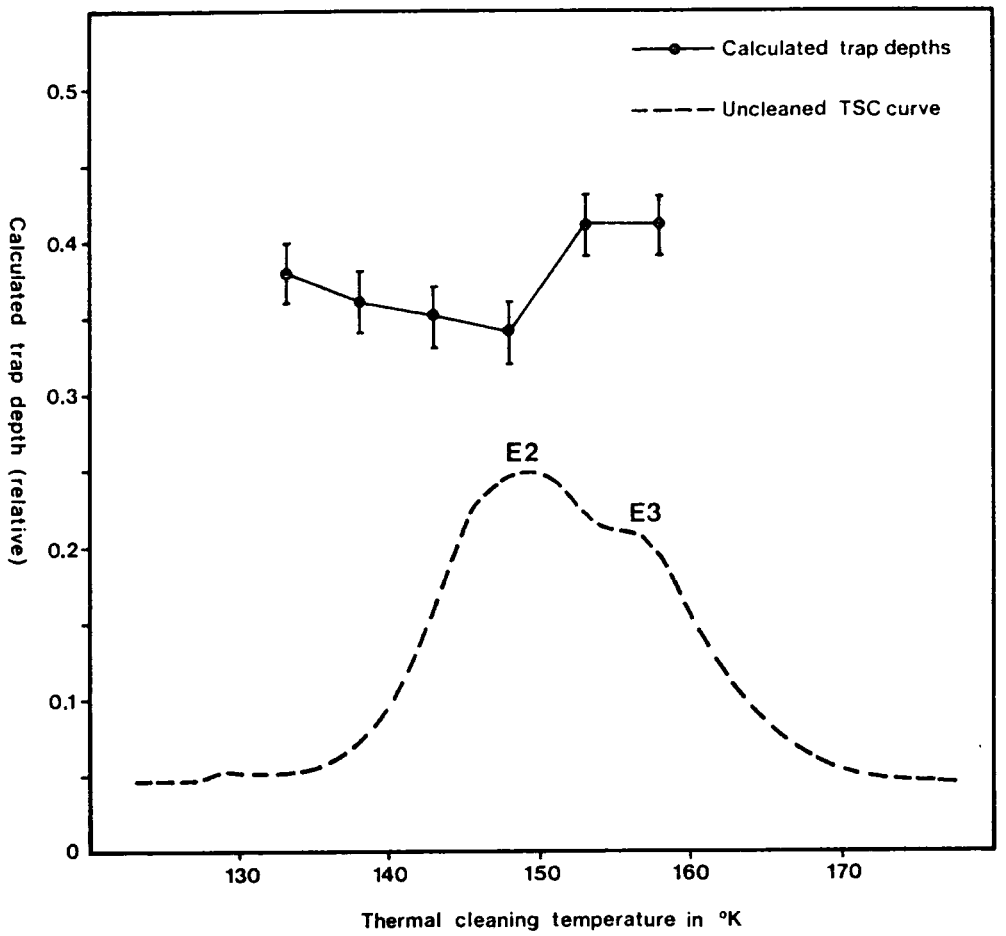

Calculated trap depth (relative) as a function of thermal cleaning temperature for a sample of boule 388.

FIGURE 4.4/3

The results show the variation (relative) in the thermal ionisation energy calculated in each case by the method of Garlick and Gibson (method 29). Superimposed on this is the TSC curve which was observed when no thermal cleaning procedure was undertaken. The results show that there is no trap distribution up to a temperature of 148.2°K, since the ionisation energy is essentially invariant up to this point within the errors of measurement. At 153.2°K there is a sudden increase in the measured trap depth, after which it remains constant once again. This is thought to be due to two discrete levels close together in the bandgap, and not a trap distribution which would be expected to give a smoother increase in the trap depth values over the temperature range of thermal cleaning. The sample was subsequently thermally cleaned to a temperature of 153.2°K repeatedly, to enable this deeper trap, E3, to be analysed. Using the method of Hoogenstraaten (method 4), Bube et al (method 5), and Unger (method 6), a value for the thermal ionisation energy of 0.26 eV was calculated. It is also interesting to note that the method of Chen-6 (method 18), which Kivits [34] showed to be correct when the retrapping ratio was 0.01, gave a value of 0.25 eV. This is supported by the computer modelling results, which are discussed fully in Section 4.45.

The remaining trapping levels, denoted E1, E4 and E5 were analysed using the same heating rate methods (methods 4,5 and 6) to produce the trap depth values given in Figure 4.4/4. The results for all of the traps discussed so far are shown in Figure 4.4/2, plotted according to the method of Hoogenstraaten. Unfortunately trap E5 was on the rising part of the dark current and was most difficult to analyse since it was almost swamped by the background. Subtraction of the dark current alone, obtained by doing a non-photoexcited TSC run, allowed an approximate value of 0.6 eV to be assigned to it, with an estimated error of 0.1 eV. Trap E1 occurring at 110°K was calculated to have an ionisation energy of 0.16 eV, and trap E4 at 210°K was found to be 0.45 eV. The latter result had a large error of 0.05 eV associated with it due to the presence of several small peaks nearby in the TSC spectrum on the high temperature side of the peak.

Samples cut from boule 400 were examined in exactly the same way as described above. Figure 4.4/1 shows a full TSC spectrum which is typical

TRAPPING LEVEL	TYPICAL PEAK TEMPERATURE (°K)	TRAP DEPTH (eV)	ERROR (eV)
E1	110	0.16	0.003
E2	150	0.23	0.012
E3	170	0.26	0.02
E4	210	0.45	0.05
E5	260	~0.60	0.1

TABLE OF TRAP DEPTHS OBTAINED FROM SAMPLES OF MATERIAL FROM BOULE 388 DURHAM-GROWN ZnSe

FIGURE 4.4/4

of all samples studied. Three peaks E6, E7 and E8 were observed. These peaks occurred at characteristic temperatures of 110, 160 and 210°K, which coincide with equivalent peaks in boule 388. The only obvious differences between the TSC curves obtained from each boule is the absence of the 150, and 260°K peaks from samples of boule 400. A detailed analysis of the peaks observed in boule 400 is given in Figure 4.4/5 where the results are plotted according to the method of Hoogenstraaten. A summary table containing trap depths and errors is given in Figure 4.4/6. The value calculated for trap E6 at 110°K is 0.17 eV, which is very close to the value of 0.16 eV obtained for the equivalent trap, E1, in boule 388. Similarly trap E7 at 160°K, was calculated to have a thermal ionisation energy of 0.27 eV which is close to the 0.26 eV of trap E3 in boule 388, and finally trap E8 at 210°K, is equivalent to trap E4 in boule 388 with a calculated trap depth of 0.43 eV.

4.432 Analysis of a ZnSe Schottky barrier diode

A ZnSe sample in the form of a Schottky barrier diode was obtained for analysis. The material was cut from boule 345 which was grown at Durham. The technique used was TSL, and the spectrum obtained from it is shown in Figure 4.4/1. The first peak at about 150°K was very broad, spanning about 50°K, therefore the thermal cleaning technique was employed to investigate the possibility of a trap distribution. Figure 4.4/7 shows the TSL curves obtained after decaying (or 'cleaning') the peak to various temperatures. The curves are plotted on a Log-1/T scale so the central straight section of each one is proportional to the thermal ionisation energy of the trap. It can be seen that the thermal ionisation energy (trap depth) increases dramatically between curves D and F. The table in Figure 4.4/8 gives the calculated values for the trap depths taken from these curves. On the basis of these results it was decided to analyse the 150°K peak using the method due to Hoogenstraaten (a) with no thermal cleaning, and (b) with thermal cleaning to 148.2°K. In (a) the value obtained was 0.11 eV whereas case (b) gave 0.3 eV, a considerable difference. Although it is probably correct to say that the 0.3 eV result is an accurate value which can be assigned to the deeper of two discrete levels, the value for the shallower trap is not as easy to assess, since the shift of the TSL peak maximum as a function of heating rate would be affected by the detrapping processes of both levels if no thermal cleaning procedure was adopted.

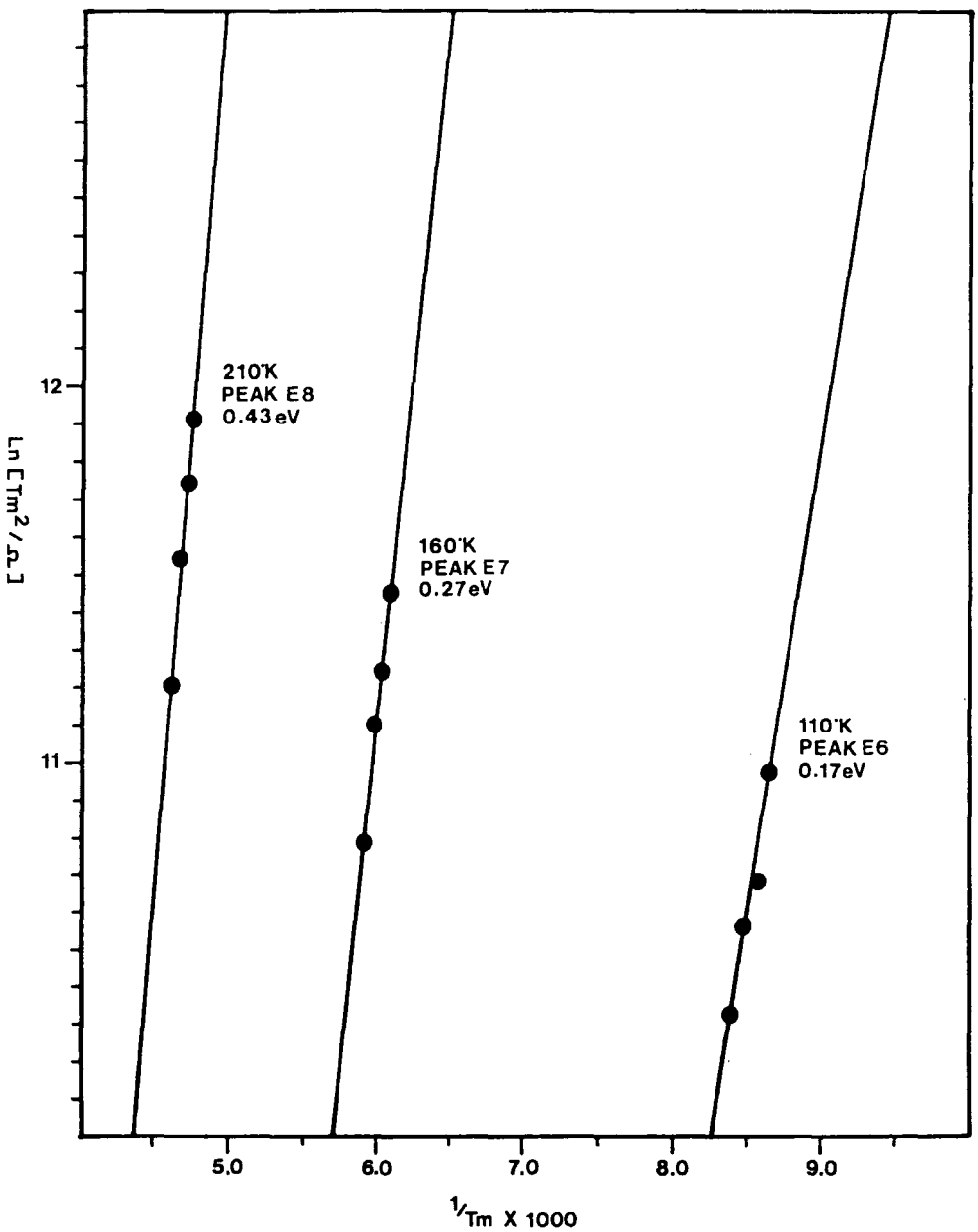

Analysis of the main peaks in boule 400 using the method due to Hoogenstraaten (method 4)

FIGURE 4.4/5

TRAPPING LEVEL	TYPICAL PEAK TEMPERATURE (°K)	TRAP DEPTH (eV)	ERROR (eV)
E6	110	0.17	0.02
E7	160	0.27	0.01
E8	210	0.43	0.02

TABLE OF TRAP DEPTHS OBTAINED FROM SAMPLES CUT FROM BOULE 400

FIGURE 4.4/6

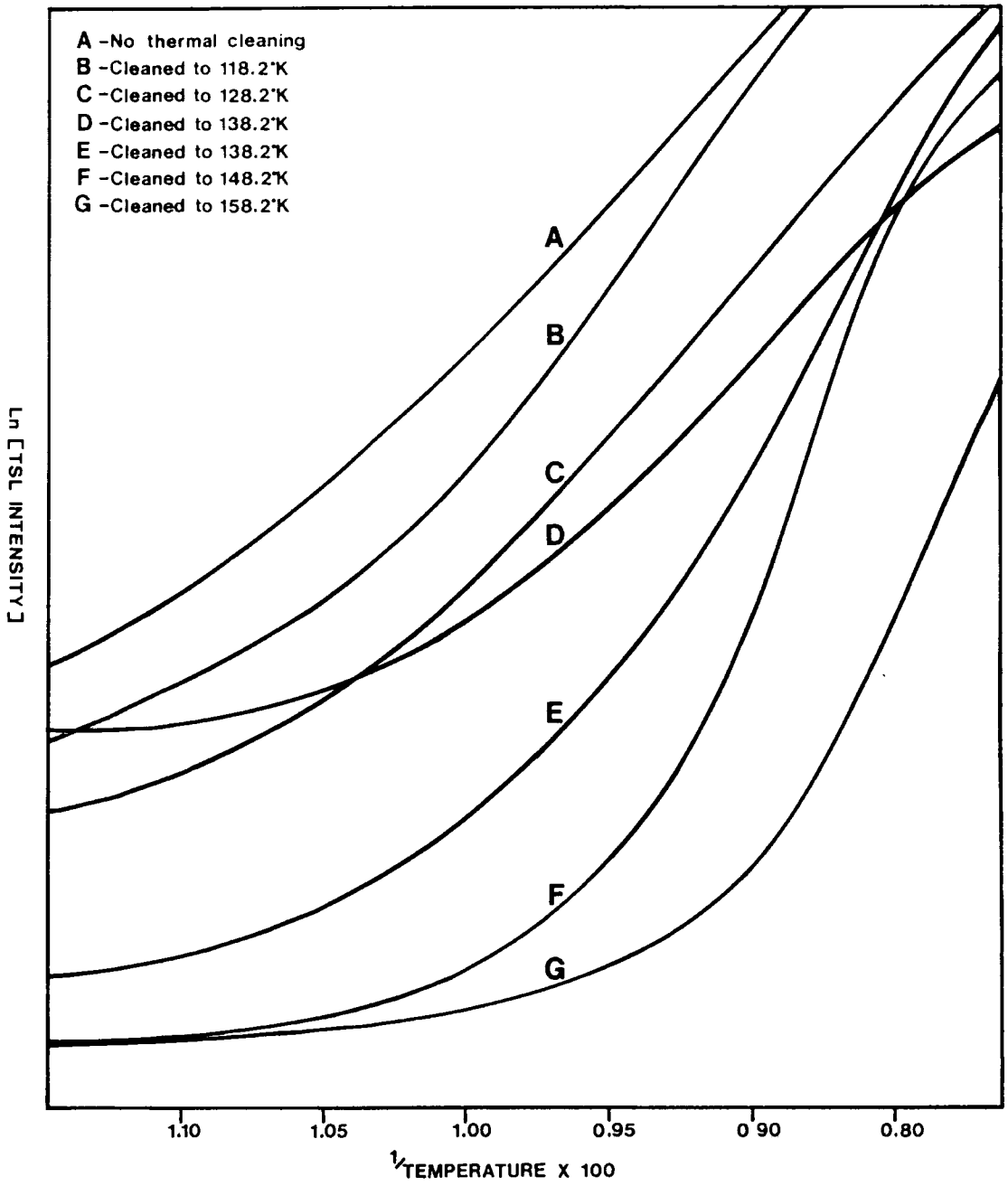

The initial rise section of the 150°K peak in a Schottky barrier sample cut from boule 345. Each curve shows the effect of thermal cleaning to various temperatures.

FIGURE 4.4/7

TSL CURVE	THERMALLY CLEANED (°K)	TRAP DEPTH (eV)
A	NONE	0.11
B	118.2	0.12
C	128.2	0.14
D	138.2	0.26
E	138.2	0.24
F	148.2	0.28
G	158.2	0.26

TRAP DEPTHS CALCULATED BY THE INITIAL RISE METHOD OF GARLICK AND GIBSON (METHOD 29) FOR DIFFERENT THERMAL CLEANING TEMPERATURES ON A SCHOTTKY BARRIER SAMPLE FROM BOULE 345

FIGURE 4.4/8

The analysis of all three peaks observed in this sample is shown in Figure 4.4/9, plotted according to the method of Hoogenstraaten. A summary of the trap depths obtained is given in a table in Figure 4.4/10. Peak E9 when thermally cleaned to 148.2°K as described above, maximised at a characteristic temperature of 165°K, and the trap depth was calculated to be 0.3 eV. Peak E10, at 220°K was calculated to be 0.6 eV, and peak E11, at 300°K was found to have a trap depth of 0.7 eV. It is interesting to note that the value obtained for TSL peak E10 supports the estimate of 0.6 eV given for trap E5 occurring in samples from boule 388 although E5 was seen at temperatures of about 250-26°K. This is probably due to the two different techniques used. E5 was detected using the TSC technique, which (in ZnSe) usually peaks after TSL by 10-20°K. Trap E11, found to correspond to a trap depth of 0.7 eV has not been seen in any other samples and is the deepest trap so far observed.

4.44 CVD material

The work done with the CVD-grown material was focussed on two samples denoted CVD/1 and CVD/2. When current-voltage plots were attempted with these samples in order to characterise the contacts, a problem was encountered. After a voltage step was applied to either of the samples the current would decay over a very long period before finally settling to a constant value, rendering the characterisation very difficult. An example of this behaviour is shown in Figure 4.4/11, where the current through CVD/2 after a 30V step is observed to be still falling after 1.5 hours. This phenomenon was later found to be due to the grain boundary structure of the CVD material, which is discussed at length in Chapter 6. Initial attempts to perform TSC and TSL measurements also met with little success, due to a very slow decay of photo-current and photo-luminescence after the trap-filling irradiation had been switched off. Consistent results from both methods were obtained by following a strict excitation/settling-time schedule to ensure repeatability.

The main peaks observed in both samples are shown in Figure 4.4/1. In CVD/1 there were two peaks at 110°K and 220°K, denoted E12 and E13. In CVD/2 there was only one peak observed at approximately 150°K, denoted E14. The peaks in both samples were analysed using the heating rate method due to Hoogenstraaten to give the results shown in Figure 4.4/12.

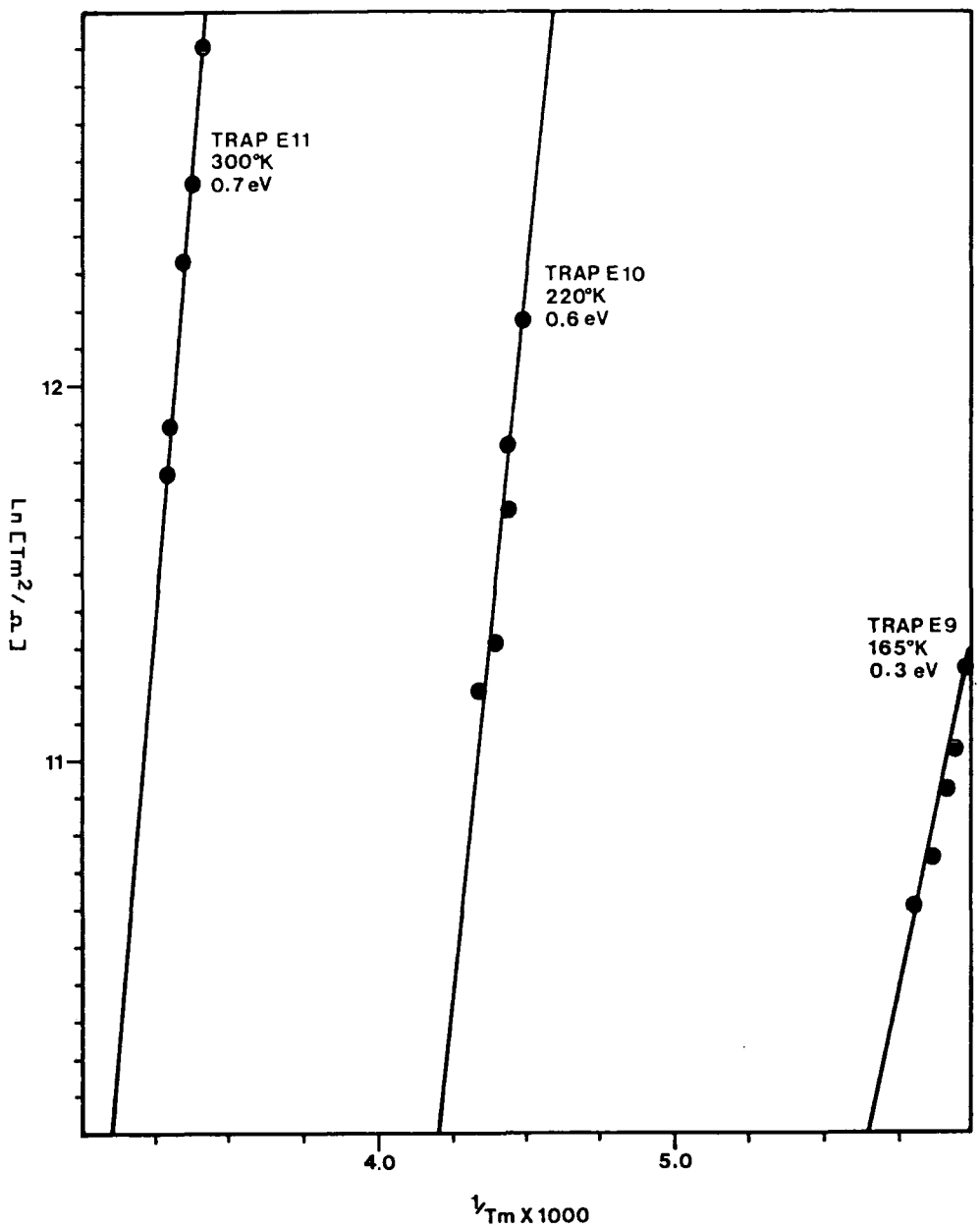

Analysis of TSL peaks observed in a Schottky barrier diode sample from boule 345 (ZNSE Durham-Grown)

FIGURE 4.4/9

TRAPPING LEVEL	TYPICAL PEAK TEMPERATURE (°K)	TRAP DEPTH (eV)	ERROR (eV)
E9	165	0.30	0.04
E10	220	0.60	0.05
E11	300	0.70	0.01

SUMMARY OF THERMAL IONISATION ENERGIES CALCULATED FOR THE TSL PEAKS OBSERVED IN THE SCHOTTKY BARRIER DIODE SAMPLE FROM BOULE 345

FIGURE 4.4/10

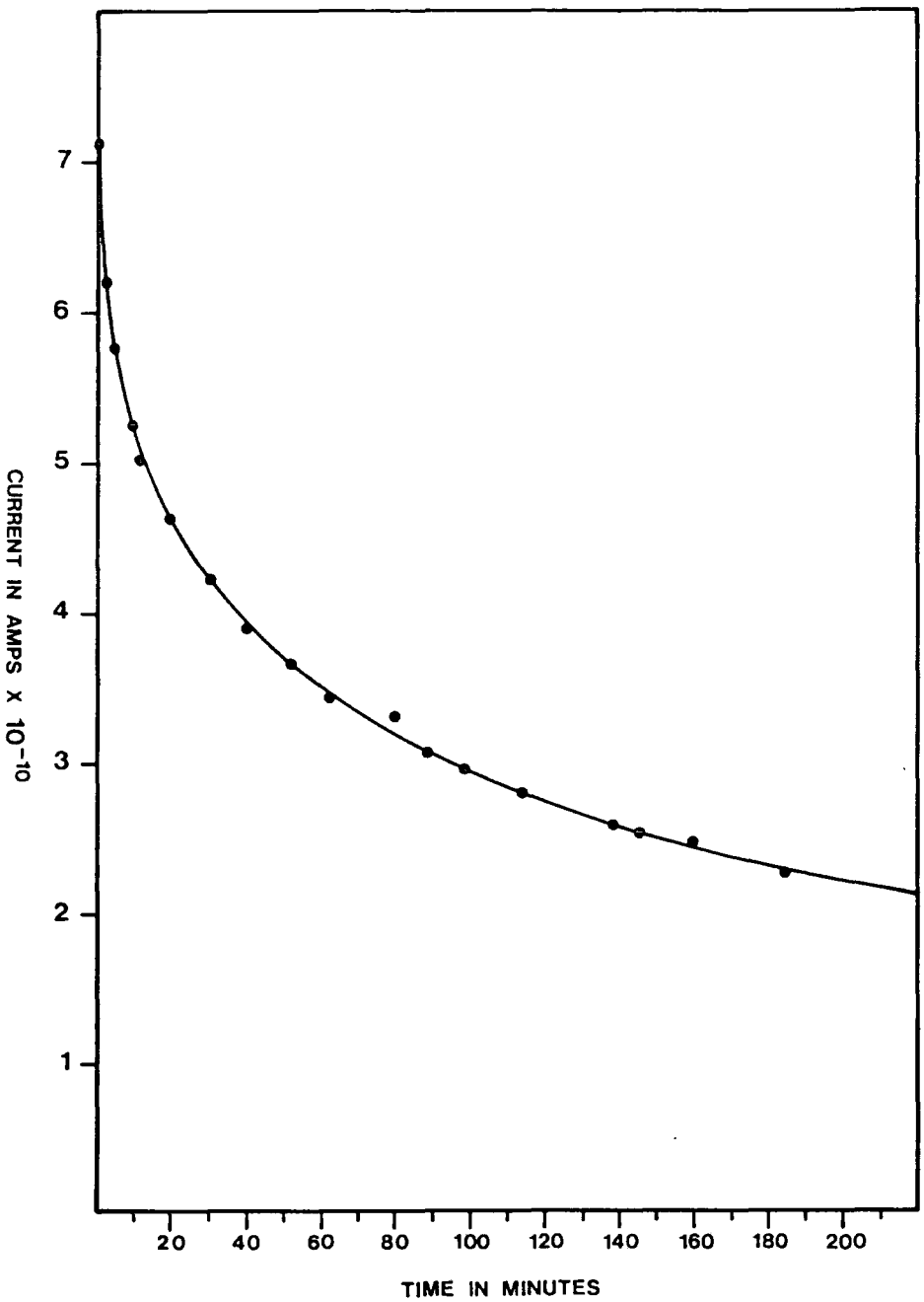

Decay of DC current in sample CVD/2 after a positive voltage step from 0v to 30v, at time t = 0

FIGURE 4.4/11

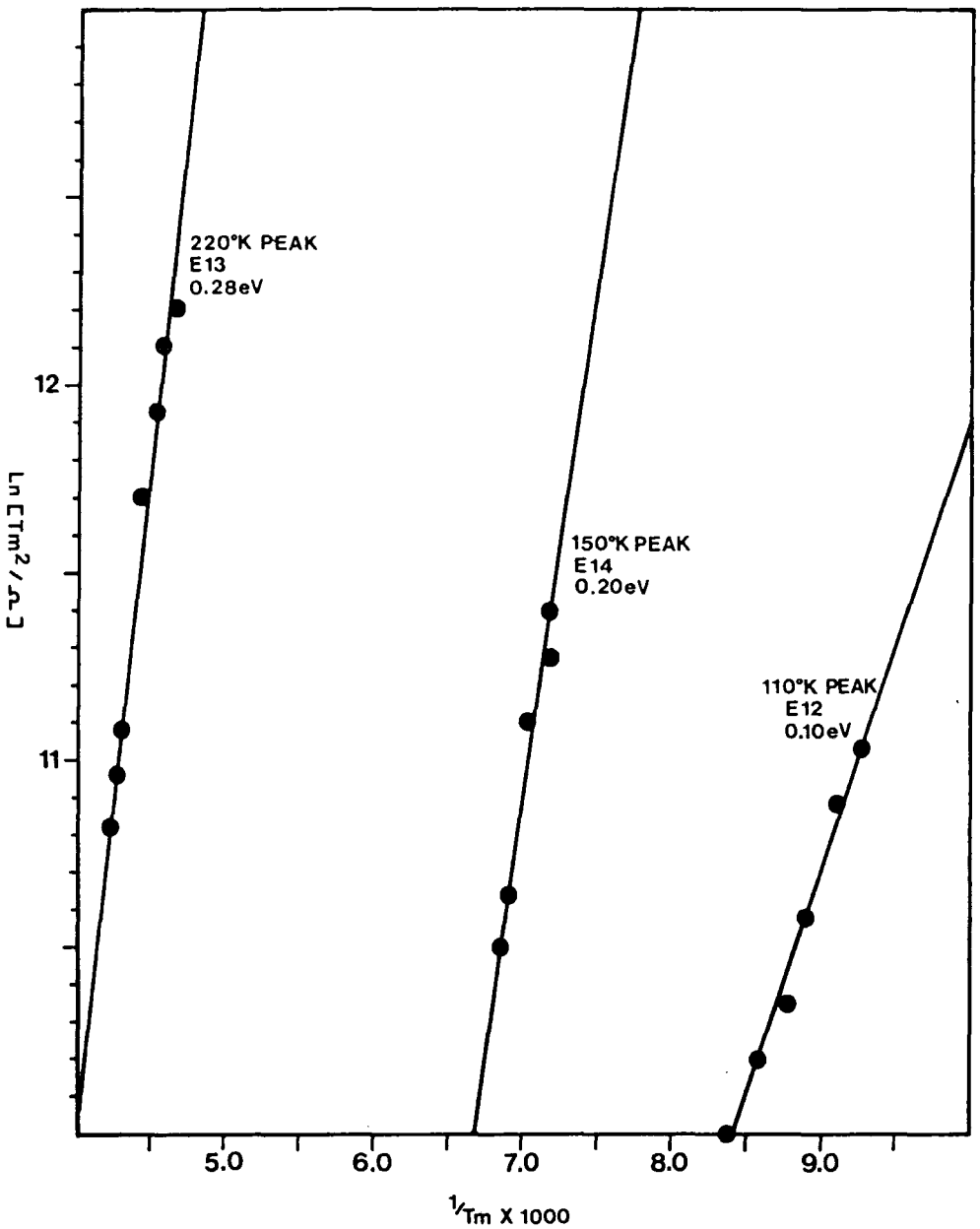

Analysis of the peaks observed in samples CVD/1 and CVD/2 using the method due to Hoogenstraaten (method 4)

FIGURE 4.4/12

For reasons which will be explained further on, all the analyses were performed using the TSL technique. Trap E12 was found to have a trap depth of 0.1 eV, and the level at 220°K, E13 was found to be 0.28 eV. Trap E14 in CVD/2 was found to have a trap depth of 0.2 eV, showing it to be very different from CVD/1. A summary of these values is given in the table in Figure 4.4/13, together with the errors of measurement.

In order to help to check the validity of the mathematical model in this material, the apparatus was modified to perform simultaneous TSC and TSL measurements. The results of a typical run obtained with sample CVD/1 are shown in Figure 4.4/14. There are two surprising points to note: (a) the first TSC peak occurs approximately 12°K before the corresponding TSL peak, and (b) the second TSC peak is very small considering the size of the corresponding TSL peak. Point (a) is very unusual since from equation 4.2-21, relating the electron population in the conduction band (TSC) to the rate of change of the population of holes in the recombination centres (TSL), the TSC peak maximum should occur either after the TSL peak, or (possibly) at the same time. Point (b) is also surprising, and it suggests that either the mobility or the free-electron lifetime was decreasing with temperature. Since quenching of photo-conductivity has been reported before [5.14, 64, 65], the dependence of the steady-state photo-conductivity as a function of temperature was investigated. The results of this are shown in Figure 4.4/15, where it can be seen that the photo-current produced by the high-pressure UV lamp used to excite the sample prior to TSC and TSL measurements, dropped by approximately 40-50x between 100 and 240°K. The activation energy of this quenching process was calculated to be 0.11 eV. Usually thermal quenching of photo-conductivity does not take place before 240-250°K in ZnSe [5.14]. The results shown in Figure 4.4/15 could also offer an explanation for the TSC peak at 110°K occurring prior to the TSL peak. The sudden quenching of photo-conductivity at about 100°K indicates a decrease in the free-electron lifetime. Since the TSC peak occurs just after this temperature the high temperature side of the peak will be cut off causing the TSC to peak early as seen in Figure 4.4/14. Because the TSC peak was thought to be modified in this way the heating rate analysis to determine the trap depths was performed using the method of TSL, which was unaffected.

TRAPPING LEVEL	TYPICAL PEAK TEMPERATURE (°K)	TRAP DEPTH (eV)	ERROR (eV)
E12	110	0.10	0.005
E13	220	0.28	0.018
E14	150	0.20	0.02

SUMMARY OF TRAP DEPTHS CALCULATED FOR TSC AND TSL PEAKS OBSERVED IN SAMPLES CVD/1 AND CVD/2

FIGURE 4.4/13

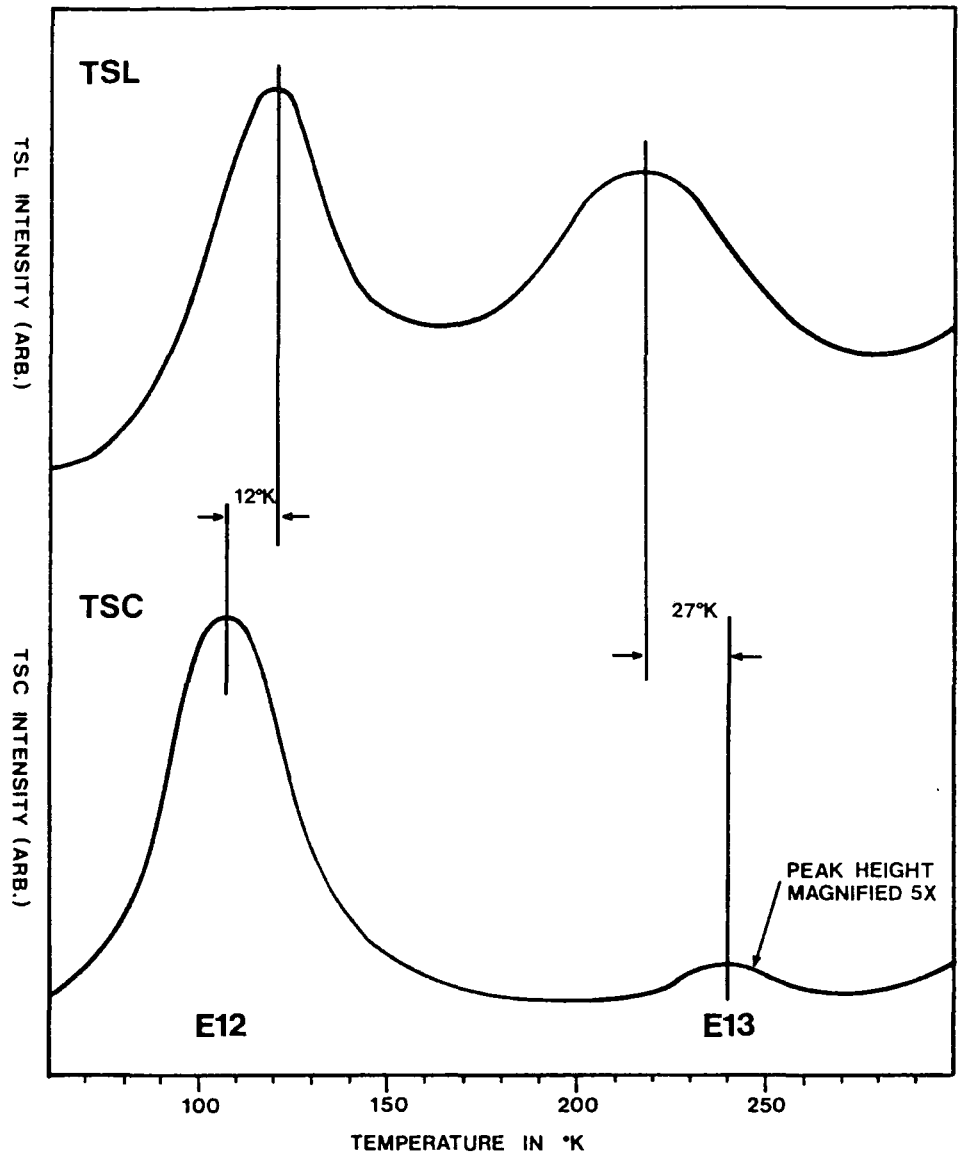

Simultaneous TSC and TSL curves taken from sample CVD/1 showing (a) TSC occuring before the corresponding TSL peak and (b) an unexpectedly small TSC peak for trap E13

FIGURE 4.4/14

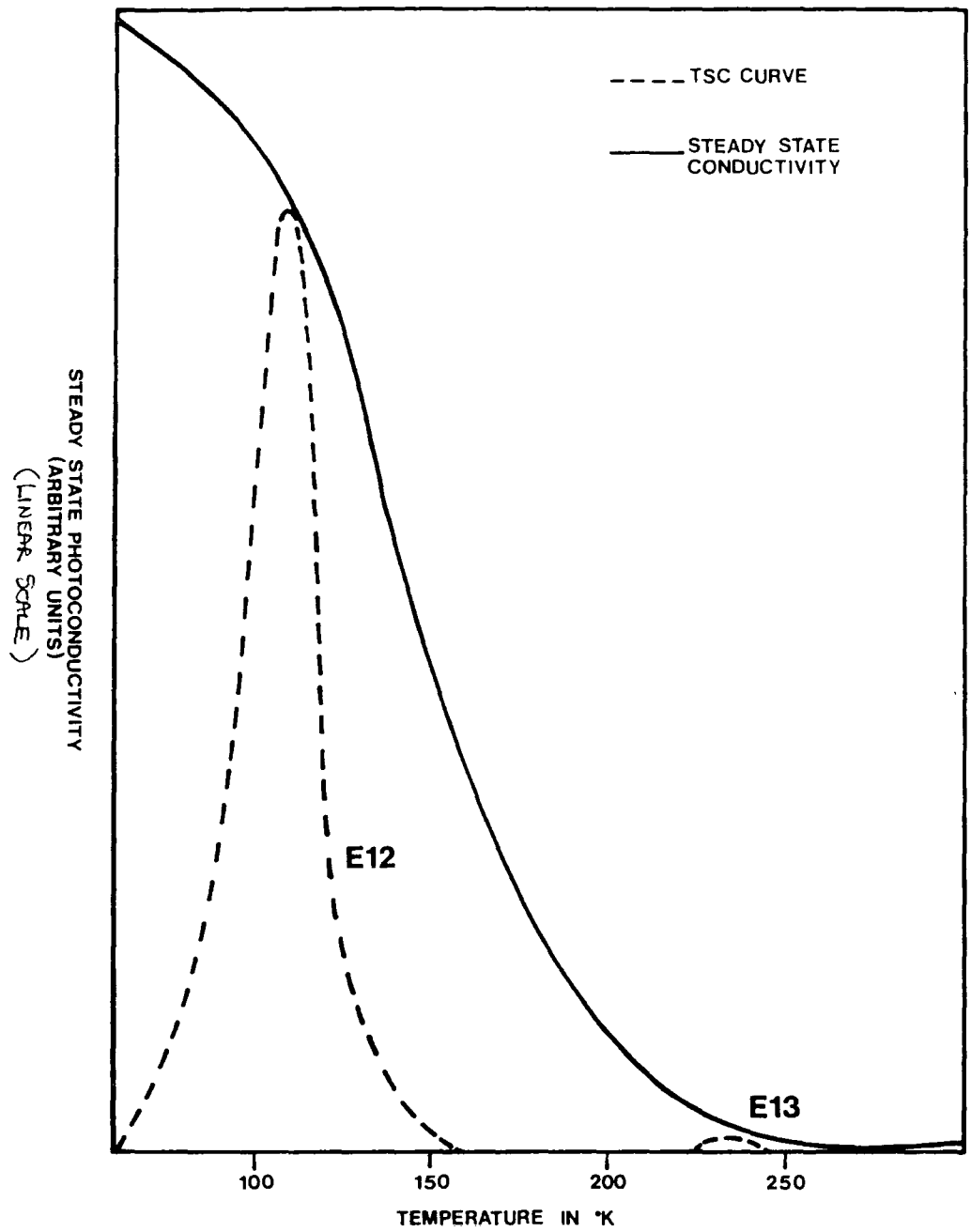

Steady state photoconductive response as a function of temperature for sample CVD/1

FIGURE 4.4/15

Thermal cleaning studies of the peak at 220°K in sample CVD/1 showed it to be due to a discrete level. Similar measurements could not easily be made on the peak at 110°K since it occurred so near to the base temperature. In theory the base temperature was 77°K, but in practice this was usually elevated to around 90°K by problems with the thermal contact between the sample and the cryostat cold-finger. Instead, a different procedure was adopted. Before each simultaneous TSC and TSL run a fixed settling time, t_S was observed in order to allow the decay of the photo-current and photo-luminescence produced by the excitation source. An additional waiting period, t_W, was added to t_S and this was then varied systematically from 0-50 minutes. The effect on the TSC and TSL was recorded for each value of t_W. Since the TSC and TSL peak for the trap in question began emptying immediately on warming the sample, the detrapping of carriers was obviously happening at the base temperature causing 'leakage'. This is shown in Figure 4.4/16 where the peak height decreases as t_W is increased. The interesting feature of these results is the shift in the peak temperatures with increasing t_W. This is thought to imply that there is a trap distribution, since the shallower traps would then empty first, causing the effect observed. The peak shift is not thought to be due to the influence of the second peak because it is also seen in the TSC curves where the second peak has an insignificant effect on the first. The postulation of a trap distribution throws doubt on the value of 0.10 eV for the thermal ionisation energy of the shallow traps, although it has been shown [13] that the method due to Hoogenstraaten is able to accurately reflect the energy of the distribution maximum.

The filling of the trap population during excitation was studied by the method of built-up TSC and TSL. In this procedure, the primary excitation source is reduced to a level such that the traps are only partially filled. This was done by irradiating the sample for a fixed time (30 sec) through different neutral density filters prior to performing simultaneous TSC and TSL runs. The results are shown in Figure 4.4/17. the interesting feature of these results is the anomalous behaviour of the TSC. The saturation of both TSL curves is as expected, but the TSC curve exhibits a strange shape as the trap is gradually filled. This is thought to be due to the effect of the thermal quenching of photo-conductivity described above, which would modify the peak height quite considerably and

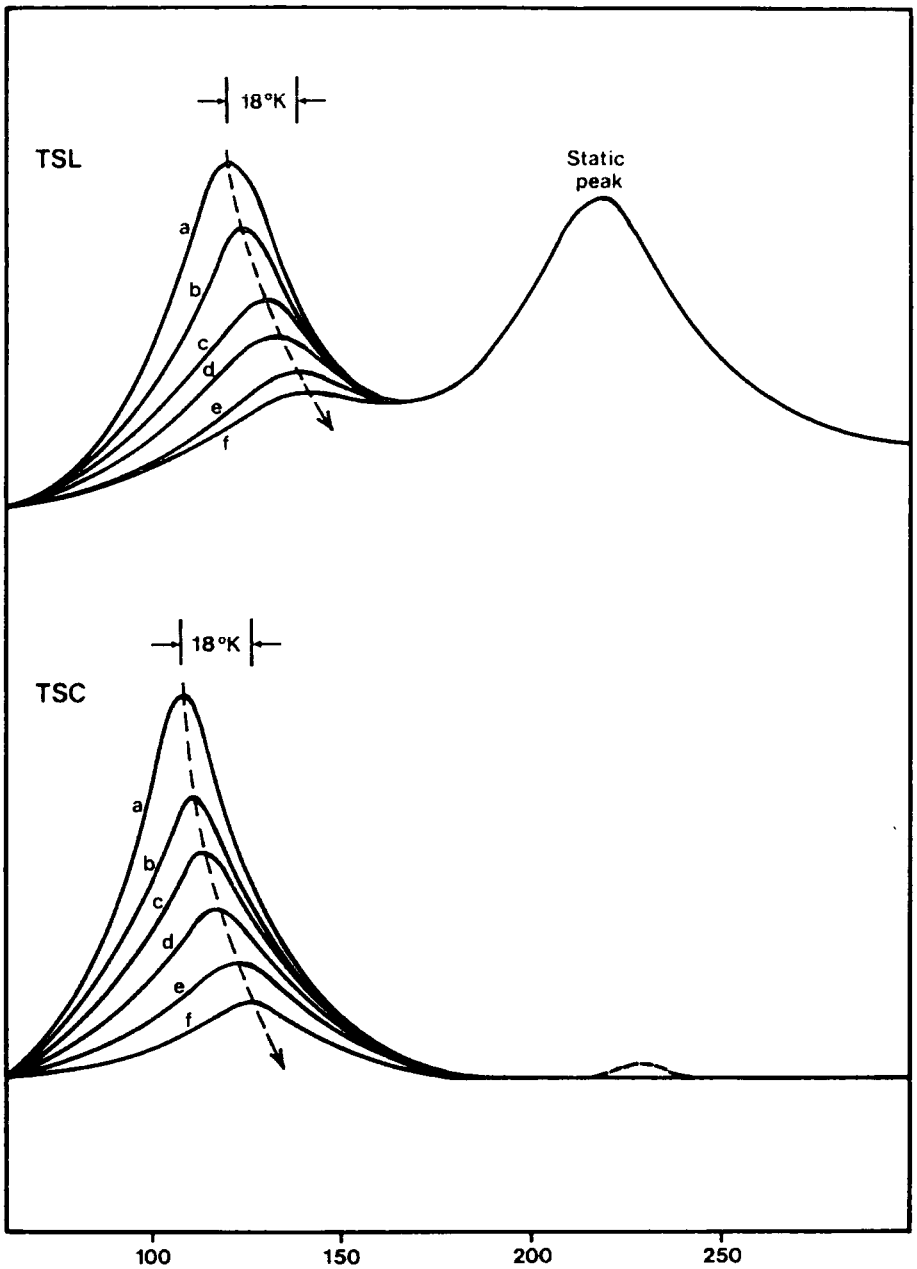

Decay of TSC and TSL peaks with waiting time t_w.

a $t_w = 0$ **b** $t_w = 10$min **c** $t_w = 20$min **d** $t_w = 30$min
e $t_w = 40$min **f** $t_w = 50$min.

FIGURE 4.4/16

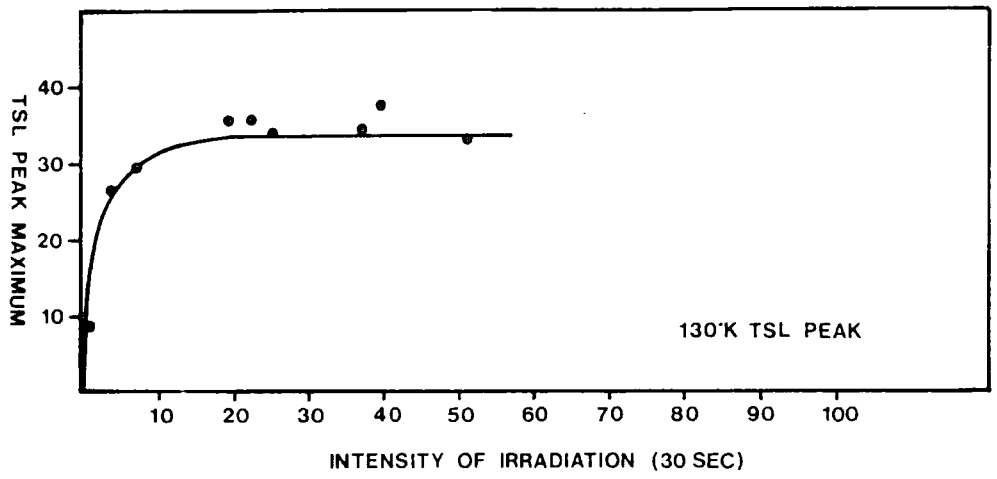

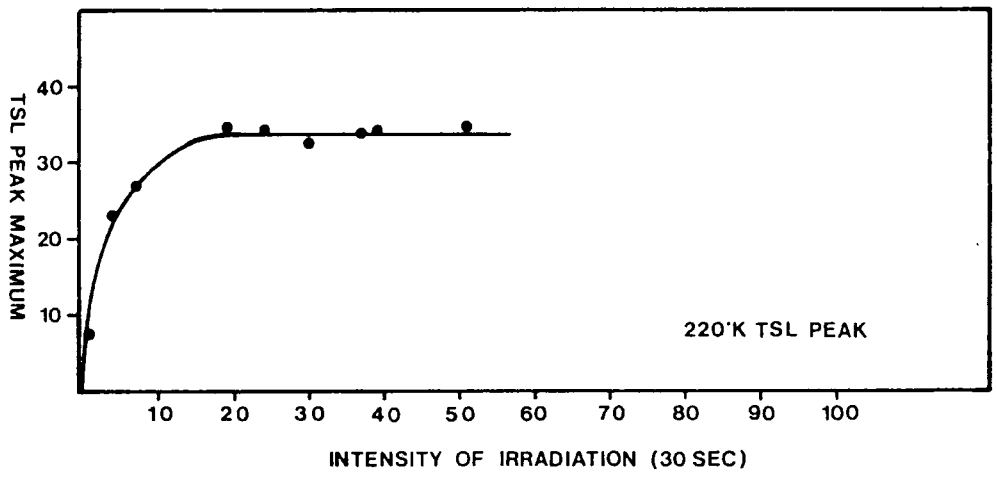

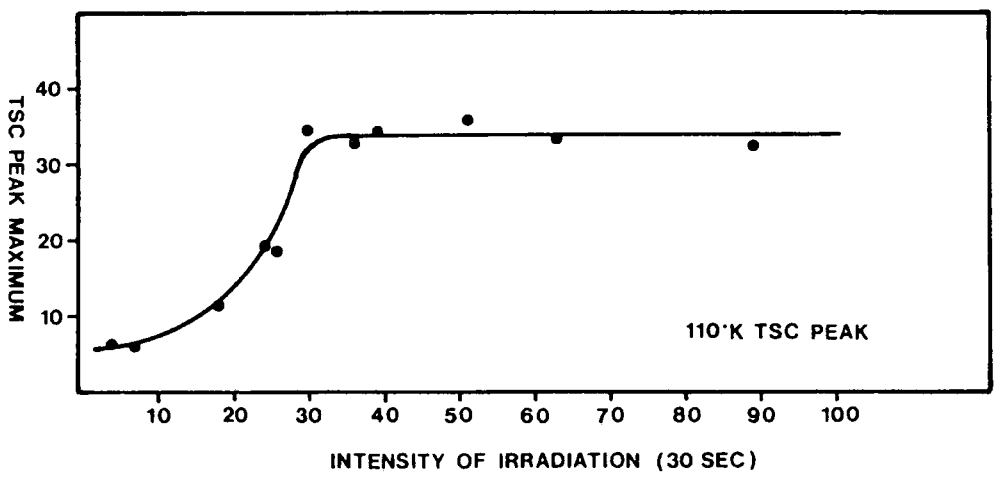

Built-up TSC and TSL as a function of irradiation intensity for 30 seconds when filling traps at the base temperature

FIGURE 4.4/17

cause a slower build-up than that observed for the equivalent TSL curve.

4.45 Computer modelling of results

A computer modelling procedure based on the work of Kivits [33] was developed for a BBC-B micro-computer in order to verify that the mathematical model described in Section 4.21 could be applied to the samples studied in this work. The program accepts all the relevant variables: trap depth, retrapping ratio, trap concentrations, frequency factor, heating rate, mobility dependence etc., and then calculates the theoretical TSC and TSL curves within a specified temperature range. Experimentation with the values of the parameters has led to a better understanding of the way they affect the shape of the curve, and hence to an appreciation of the mechanisms involved in the detrapping processes occurring within the material.

Most of the TSC and TSL heating rate analyses described in the previous sections have been modelled in an attempt to generate sets of curves with peak temperatures which match those obtained from the experimental data. The modelling procedure was as follows: the correct trap depth was taken to be the value calculated by the method of Hoogenstraaten, the retrapping ratio was initially taken to be 0.001, the ratio of deep traps to shallow traps was taken as 0.001, and the mobility was assumed to be constant. A single curve was then generated at one of the heating rates used in the real experiment and the peak maximum temperature was compared with the measured value. The frequency factor was then altered and the procedure repeated until the peak temperatures were identical. The complete set of curves was then generated and all peak maximum temperatures were compared. Some of the other parameters were then altered, if necessary, and the curves regenerated. This iterative procedure was continued until a good fit to the experimental data was obtained.

Several traps in both the Durham-grown and the CVD-grown material were modelled. Figure 4.4/18 is a table summarising the results obtained when the 110°K trap E1 in boule 388 was theoretically modelled. The values of

HEATING RATE ($°KS^{-1}$)	MEASURED T_m ($°K$)	MODELLED T_m ($°K$)
0.16	102.0	102.0
0.19	103.2	103.0
0.40	106.6	106.5
0.52	107.8	108.0
0.57	108.3	108.5

Modelling Parameters:

Trap depth	(E_T)	= 0.18 eV
Retrapping ratio	(δ)	= 0.001
Deep/shallow trap conc.	(ε)	= 10^{-3}
Frequency factor	(s)	= 1.3×10^{8} s^{-1}
Recombination rate	(α)	= 10^{-8} $cm^3 s^{-1}$
Trapping rate	(β)	= 10^{-11} $cm^3 s^{-1}$

SUMMARY TABLE: MODELLING OF BOULE 388 110°K TRAP, E1

FIGURE 4.4/18

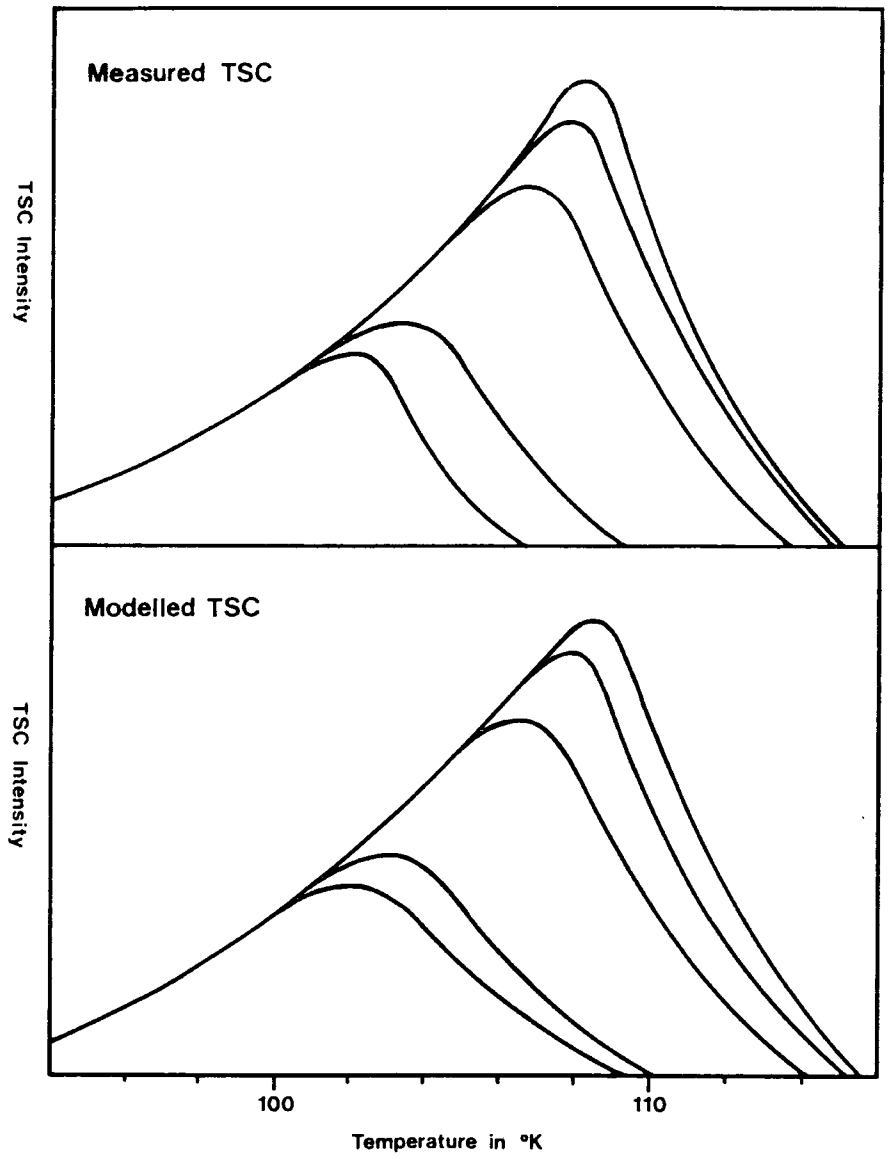

Comparison between measured TSC curves and those produced by the computer modelling.

FIGURE 4.4/19

HEATING RATE ($°KS^{-1}$)	MEASURED T_m ($°K$)	MODELLED T_m ($°K$)
0.12	145.5	145.0
0.19	147.7	148.0
0.39	153.2	153.5
0.49	155.9	155.5
0.61	157.2	157.5

Modelling Parameters:

Trap depth	(E_T)	= 0.23 eV
Retrapping ratio	(δ)	= 0.001
Deep/shallow trap conc.	(ε)	= 10^{-3}
Frequency factor	(s)	= 8.5×10^6 s^{-1}
Recombination rate	(α)	= 10^{-9} $cm^3 s^{-1}$
Trapping rate	(β)	= 10^{-12} $cm^3 s^{-1}$

SUMMARY TABLE: MODELLING OF BOULE 388 150°K TRAP, E2

FIGURE 4.4/20

HEATING RATE ($°KS^{-1}$)	MEASURED T_m ($°K$)	MODELLED T_m ($°K$)
0.21	167.1	167.5
0.28	169.6	170.0
0.35	171.6	172.0
0.47	175.5	174.5
0.66	176.2	177.5

Modelling Parameters:

Trap depth	(E_T)	= 0.26 eV
Retrapping ratio	(δ)	= 0.01
Deep/shallow trap conc.	(ε)	= 10^{-3}
Frequency factor	(s)	= $6.8 \times 10^{6}\ s^{-1}$
Recombination rate	(α)	= $10^{-8}\ cm^3 s^{-1}$
Trapping rate	(β)	= $10^{-10}\ cm^3 s^{-1}$

SUMMARY TABLE: MODELLING OF BOULE 388 170°K TRAP,E3

FIGURE 4.4/21

HEATING RATE ($°KS^{-1}$)	MEASURED T_m ($°K$)	MODELLED T_m ($°K$)
0.19	107.8	108.0
0.22	109.5	109.5
0.32	112.3	112.5
0.41	114.0	114.5
0.51	116.6	116.5
0.70	119.9	119.5

Modelling Parameters:

Trap depth	(E_T)	= 0.10 eV
Retrapping ratio	(δ)	= 0.001
Deep/shallow trap conc.	(ϵ)	= 10^{-5}
Frequency factor	(s)	= 1.8×10^4 s^{-1}
Recombination rate	(α)	= 10^{-7} $cm^3 s^{-1}$
Trapping rate	(β)	= 10^{-10} $cm^3 s^{-1}$

SUMMARY TABLE: MODELLING OF CVD/1 110°K TRAP, E12

FIGURE 4.4/22

HEATING RATE ($°KS^{-1}$)	MEASURED T_m ($°K$)	MODELLED T_m ($°K$)
0.23	214.0	215.5
0.26	217.8	217.5
0.32	220.8	220.0
0.42	224.9	223.5
0.83	232.4	233.0
0.95	234.2	235.0
1.13	237.7	238.0

Modelling Parameters:

Trap depth	(E_T)	= 0.28 eV
Retrapping ratio	(δ)	= 0.001
Deep/shallow trap conc.	(ε)	= 10^{-6}
Frequency factor	(s)	= 5.6×10^{4} s^{-1}
Recombination rate	(α)	= 10^{-9} $cm^3 s^{-1}$
Trapping rate	(β)	= 10^{-12} $cm^3 s^{-1}$

SUMMARY TABLE: MODELLING OF CVD/1 220°K TRAP, E13

FIGURE 4.4/23

the peak temperatures for each heating rate are given, together with the parameter values used. The peak temperatures are all within 0.2°K of each other. The measured curves and the computer-generated equivalents are shown in Figure 4.4/19, where it can be seen that there are some minor differences in the curve shapes. These are very hard to model, since the shapes of measured TSC curves are almost always affected by the presence of other traps nearby in the forbidden gap. Summary tables for the modelling of traps E2 and E3 in the Durham-grown material, and traps E12 and E13 in the CVD-grown material are given in Figures 4.4/20 to 4.4/23. The main difference between the two types of material, high-lighted by the modelling procedure, is that the attempt-to-escape frequency factors obtained for the CVD material were all about two orders of magnitude lower than those found to fit the Durham-grown samples. The low values chosen for the retrapping ratio (0.01 or less) were found to fit the measured data in all cases, indicating that the capture cross-sections of the traps examined were all at least two orders of magnitude lower than the capture cross-section of the recombination centres.

4.5 DISCUSSION

Samples from three Durham-grown ZnSe boules and two samples of CVD-grown ZnSe were examined using the techniques of thermally stimulated luminescence (TSL) and thermally stimulated conductivity (TSC). Using the method of 'thermal cleaning' [19], certain TSC and TSL peaks were isolated for analysis. This method was also used to check that the peak was due to a discrete trapping level as opposed to a population of traps with a distribution of thermal ionisation energies. The technique of simultaneously measured TSC and TSL was developed and used in the examination of the CVD material. As a direct result it was noticed that the TSC peak at 240°K in CVD/1, corresponding to a large TSL peak at 220°K was 40-50 times smaller than expected. A brief study of the steady-state photo-conductive response as a function of temperature showed that this was due to a quenching of the free-electron lifetime with an activation energy of 0.11 eV, and beginning at a temperature of about 100°K. This is approximately 150°K earlier than that previously reported in ZnSe [5.14, 64, 65]. The quenching effect was also used to explain the fact that the TSC peak at 110°K in the same sample, reached its maximum 12°K earlier than the corresponding TSL peak contrary to the findings of the mathematical model discussed in Section 4.21 (see equation 4.2-21).

A summary of all the trap depths measured in the materials studied is given in a table in Figure 4.5/1. It is apparent from these results that there are several trapping levels which occur in more than one of the materials. Trap E1 in boule 388 at 0.16 eV also occurs in boule 400 (0.17 eV), as trap E6. These results agree well with an electron trap reported at 0.17 eV in LPE-grown ZnSe by Kosai [5.15], and Ido et al [66] recently found a level at 0.15 eV in ZnSe:Ga grown by the same method.

Trap E2 in boule 388 at 0.23 eV might be the same as trap E14 in CVD/2 at 0.20 eV. A hole trap 0.21 eV above the valence band was reported by Christianson and Wessels [56], however it was only present in samples which had been annealed in liquid zinc to reduce the resistivity. Since E14 in CVD/2 was found to be an electron trap, and E2 was observed in as-grown ZnSe no firm comparisons can be made.

There is also a distribution of traps between 0.26-0.30 eV in all of the materials studied. In the literature Verity et al [5.17] found a trap at 0.34 eV and Besomi and Wessels [5.18] found levels between 0.30-0.35 eV which they ascribed to Cl, Al or In impurities. More recently electron traps have been reported at 0.33 eV [67], 0.30 eV and 0.35 eV [68], and 0.29 eV [66]. The authors [67] suggested that the first of these was due to Se divacancies, since their concentration was found to increase as the square of the vapour phase Zn/Se ratio.

There are very few references to be found in the literature to levels corresponding to the values of 0.45 eV and 0.43 eV calculated for traps E4 and E8 in boules 388 and 400 respectively. Qidwai and Woods [69] reported an acceptor level at 0.40 eV which appeared with increasing concentrations of Ga. A similar level at 0.41 eV was found to appear with increasing concentration of In by Qidwai [70].

The values of ~0.6 eV for trap E5 in boule 388 and 0.60 eV for trap E10 in boule 345 agree reasonably well with the value of 0.64 eV found by Kosai [5.15] in LPE-grown ZnSe. Acceptors at 0.59 eV have also been reported by Qidwai [70] and by Nyaga et al [71] who linked this level with $(V_{Zn}$-impurity)'.

TRAPPING LEVEL	ORIGIN	TYPICAL PEAK TEMPERATURE (°K)	TRAP DEPTH (eV)
E1	BOULE 388	110	0.16
E2	"	150	0.23
E3	"	170	0.26
E4	"	210	0.45
E5	"	260	~0.60
E6	BOULE 400	110	0.17
E7	"	160	0.27
E8	"	210	0.43
E9	BOULE 345	165	0.30
E10	"	220	0.60
E11	"	300	0.70
E12	CVD/1	110	0.10
E13	CVD/1	220	0.28
E14	CVD/2	150	0.20

SUMMARY TABLE OF MEASURED THERMAL IONISATION ENERGIES ASSOCIATED WITH EACH TRAP

FIGURE 4.5/1

The value of 0.10 eV for electron trap E12 in CVD/1 may be suspect since it was found that there was a trap distribution present, however, it has been shown [13] that the method of analysis due to Hoogenstraaten produces an accurate value for the thermal ionisation energy of the traps at the maximum of the distribution. The 0.10 eV level does not correspond to any traps discovered in the Durham-grown ZnSe, and it does not appear in sample CVD/2.

There are only three traps observed in the two samples of CVD-grown material studied. The reason for this is that traps in this type of material with thermal ionisation energies above about 0.30 eV empty at temperatures too high to be detected by the methods of TSC and TSL. This property was demonstrated by the computer modelling, where the values for the frequency factor were all found to be at least two orders of magnitude lower than those for traps in Durham-grown ZnSe. An example of this is given by a comparison of trap E7 in Durham-grown boule 400 (0.27 eV), with trap E13 in CVD/1 (0.28 eV). Although the trap depths are very nearly equal, the latter empties at about 220°K, whereas the former reaches peak maximum at approximately 160°K.

From equations 4.2-6 and 4.2-8, the expression for the frequency factor can be written as

$$S = \sigma_1 N_C \langle v \rangle \qquad 4.5\text{-}1$$

where S = frequency factor (s^{-1})
σ_1 = capture cross-section of traps (cm^{-2})
N_C = effective density of states (cm^{-3})
$\langle v \rangle$ = thermal velocity of electrons (RMS) (cms^{-1})

From equation 4.5-1 it is straightforward to see that the low values for the frequency factor observed in CVD ZnSe are most probably due to low values for the capture cross-sections of traps in this material compared to similar trapping levels occurring in Durham-grown ZnSe.

CHAPTER 4 - REFERENCES

1 F Urbach (1930), 'Zur Lumineszenz der Alkalihalogenide', Sitzber. Akad. Wiss. Wien, Math. Naturw. K, Abt., II(a), 139, 363

2 R C Herman and R Hofstadter, Phys. Rev., 57, (1940), 936

3 J T Randall and M H F Wilkins, Proc. Roy. Soc., A184, (1945), 366

4 H E Klasens and M E Wise, Nature, 158, (1946), 483

5 V V Antonov-Romanovski, Izvest. Akad. Nauk. SSSR. Ser. Fiz., 10, (1946), 477

6 G F J Garlick and A F Gibson, Proc. Roy. Soc., 60, (1948), 574

7 Ch. B Lushchik, Doklady Akad. Nauk. SSSR, 101, (1955), 641

8 J J Hill and P Schwed, J. Chem. Phys., 23, (1955), 652

9 A Halperin and A A Braner, Phys. Rev., 117, (1960), (2), 408

10 G A Dussel and R H Bube, Phys. Rev., 155, (3), (1967), 764

11 I J Saunders, J. Phys. C (Sol. State Phys.), 2, (1969), 2181

12 P Kelly and P Braunlich, Phys. Rev. B., 1, (4), (1970), 1587

13 P Kivits, J. Luminescence, 16, (1978), 119

14 L J Grossweiner, J. Appl. Phys., 24, (1953), 1306

15 A H Booth, Canad. J. Chem., 32, (1954), 214

16 R R Haering and E N Adams, Phys. Rev., 117, (2), (1960), 451

17 P N Keating, Proc. Phys. Soc., 78, (1961), 1408

18 J Franks and P N Keating, J. Phys. Chem. Sol., 22, (1961), 25

19 K H Nicholas and J Woods, Brit. J. Appl. Phys., 15, (1964), 783

20 R H Bube, G A Dussel, Ching-Tao Ho and L D Miller, J. Appl. Phys., 37, (1), (1966), 21

21 T A T Cowell and J Woods, Brit. J. Appl. Phys., 18, (1967), 1045

22 P J Kelly and M J Laubitz, Canad. J. Appl. Phys., 45, (1967), 311

23 M E Haine and R E Carley-Read, Brit. J. Appl. Phys., 1, (1968), 1257

24 P L Land, J. Phys. Chem. Sol., 29, (1968), 1681

25 R Chen, Chem. Phys. L., 11, (1971), 371

26 D Shenker and R Chen, J. Phys. D: Appl. Phys., 4, (1971), 287

27 R Chen and S A A Winer, J. Appl. Phys., 41, (13), (1970), 5227

28 J G Simmons and G W Taylor, Phys. Rev. B., 5, (4), (1971), 1619

29 C S Shalgaonkar and A V Narlikar, J. Mater. Sci., 7, (1972), 1465

30 R Chen, J. Mater. Sci., 9, (1974), Letters, 345

31 J G Simmons, G W Taylor and M C Tam, Phys. Rev. B., 7, (8), (1973), 3714

32 A Bosacchi, S Franchi and B Bosacchi, Phys. Rev. B., 10, (12), (1974), 5235

33 H J L Hagebeuk and P Kivits, Physica, 83B, (1976), 289

34 P Kivits and H J L Hagebeuk, J. Luminescence, 15, (1977), 1

35 A Samoc, M Samoc and J Sworakowski, Phys. Stat. Sol. (a), 36, (1976), 735

36 R P Khare and R Nath, Phys. Stat. Sol. (a), 44, (1977), 627

37 I J Saunders, Brit. J. Appl. Phys., 18, Letters, (1967), 1219

38 P Braunlich and P Kelly, Phys. Rev. B., 1, (4), (1970), 1596

39 H Dittfield and J Voigt, Phys. Stat. Sol., 3, (1963), 1941

40 B S Barkhalov and E Lutsenko, Phys. Stat. Sol. (a), 11, (1972), 433

41 P S Walsh and E C Lightowlers, J. Luminescence, 4, (4), (1971), 393

42 P J Kelly and M J Laubitz, Phys. Rev. B., 4, (1971), 1960

43 R Chen and R J Flemming, J. Appl. Phys., 44, (1973), 1393

44 G Jones and J Woods, J. Phys. D: Appl. Phys., 9, (1976), 799

45 A Bohun, Czech. J. Phys., 4, (1954), 91

46 I A Parfianovich, J. Exp. Theor. Phys. SSSR., 26, (1954), 696

47 K W Boer, S Oberlander and J Voigt, Ann. Phys. Lpz., 2, (1958), 130

48 W Hoogenstraaten, Phillips Res. Reports, 13, (1958), 515

49 R H Bube, J. Chem. Phys., 23, (1955), 18

50 K Unger, Phys. Stat. Sol., 2, (1962), 1279

51 M Schon, Tech. Wiss. Abh. Osram Ges., 7, (1958), 175

52 I I Boiko, E I Rashba and A P Trofimenko, Sov. Phys. S.S., 2, (1960), 99

53 R Chen, J. Appl. Phys., 40, (1969), 570

54 R Chen, Chem. Phys. L., 11, (1971), 371

55 R Chen, Chem. Phys. L., 6, (1970), 125

56 C Haake, J. Opt. Soc. Am., 47, (1957), 649

57 J Voigt, Diplomabeit, Berlin (1958)

58 J S Blakemore, Semiconductor Statistics, Pergamon Press, N.Y., (1962), 283

59 M Lax, Phys. Rev., 119, (1960), 1502

60 P J Dean, Prog. Sol. State Chem., 8, Pergamon Press, Oxford and New York, (1973), 1

61 N Riehl, J. Luminescence, 1-2, (1970), 1

62 C H Henry and D V Lang, Proc. 12th Int. Conf. on Physics of Semiconductors, Stuttgart, (1974), 411

63 P G Cath and A M Peabody, Anal. Chem., 43, (11), (1971), 91A

64 G B Stringfellow and R H Bube, Phys. Rev. B., 14, (1968), 903

65 G Jones and J Woods, J. Luminescence, 9, (1974), 389

66 T Ido and M Okada, J. Cryst. Growth, 72, (1985), 170

67 K A Christianson and B W Wessels, J. Appl. Phys., 54, (7), (1983), 4205

68 W B Leigh and B W Wessels, J. Appl. Phys., 55, (6), (1984), 1614

69 A A Qidwai and J Woods, J. Phys. C (GB), 16, (35), (1983), 6789

70 A A Qidwai, PhD Thesis, Durham, England, (1982)

71 A I Nyaga, V A Korotkov, G P Peka and A V Simashkevich, Fiz. & Tekh. Poluprovodn. (USSR), 16, (6), (1982), 1005

CONTENTS

5 DEEP LEVEL TRANSIENT SPECTROSCOPY

5.1 INTRODUCTION

5.2 THEORY

5.21 The space-charge layer

5.211 Detection of trapping levels in space-charge layers
5.212 Bias voltage pulses
5.213 Variations of signal sensitivity in time and space
5.214 Transient magnitudes of uniformly distributed trap concentrations

5.22 Single-shot measurement techniques
5.23 Deep level transient spectroscopy (DLTS)

5.231 Determination of activation energies
5.232 Determination of other parameters

5.3 EXPERIMENTAL APPARATUS AND PROCEDURE

5.31 DLTS apparatus
5.32 Experimental procedure

5.4 EXPERIMENTAL RESULTS

5.41 Durham-grown material

5.411 Schottky barrier characterisation
5.412 Determination of trapping parameters
5.413 Capacitance transient measurements as a function of bias

5.42 CVD zinc selenide

5.5 DISCUSSION

5 DEEP LEVEL TRANSIENT SPECTROSCOPY

5.1 INTRODUCTION

In order to supplement the TSC and TSL work which was undertaken to investigate the trapping parameters of defects lying deep (>0.05 eV) from band edges) within the forbidden gap of the ZnSe samples studied, an equipment to perform the technique of Deep Level Transient Spectroscopy (DLTS) was designed and built. The technique in its present form was provided by Lang [1] and is a high-frequency junction capacitance transient, thermal-scanning method which is able to display the spectrum of defect levels near a p-n junction or Schottky barrier as positive or negative peaks on a flat baseline as a function of temperature. It has the advantage over TSC and TSL that measurements are made rapidly and are, for the most part, easy to analyse. The position of the peaks generated during a temperature scan is uniquely determined by the thermal emission parameters of the trap concerned. The sign of the peak shows whether majority or minority carriers are involved, while the peak height is proportional to the trap concentration. The thermal activation energy can be found from a simple Arrhenius plot, and by adopting a straightforward biassing procedure, the concentration profile of each level near the p-n junction or Schottky barrier can be determined.

5.2 THEORY

5.21 The space-charge layer

The space-charge layer present at the metallurgical junction in p-n and Schottky barrier diodes is necessary for the maintenance of thermal equilibrium between the two materials forming the device. It can be viewed as an insulating region of variable width. The quiescent width is determined by the electronic properties of the two materials, such as work functions, Fermi-levels and permittivity, but can be modified by the application of a bias voltage. Typically the layer varies in thickness from 0.1 to 10 μm. For reverse bias voltages of 1-100V, the maximum field strength in the depletion region, ε_{max} is about 10^4-10^6 V_m^{-1}. The space-charge layer is assumed to be completely devoid of free carriers, the space-charge being entirely due to uncompensated donors or acceptors

which are uniformly distributed. This assumption is called the depletion approximation. Unlike the bulk insulator, the space-charge layer possesses a spatially varying electric field even at zero bias, causing carriers which are excited out of trapping levels within it to be swept out of the layer in around 10^{-10} to 10^{-12} seconds. Retrapping effects are therefore negligible, leading to considerable simplifications in the analysis of thermal emission transients.

5.211 Detection of trapping levels in space-charge layers

The detection of trapping levels within space-charge layers may be accomplished by measuring their effect on either the capacitance or the junction current. Detection of junction current effects is exactly analogous to the detection of the thermally-stimulated detrapping currents in a thin bulk semiconductor or insulator in which there is negligible retrapping. There is, however, no such analogy in the case of the detection of junction capacitance effects, which is unique to space-charge layers.

It follows from Poisson's equation that any change in the shallow charge density $-eN_D$, will induce a change in the capacitance C_D of the space-charge region. Similarly, if any change in the concentration of eletrons or holes trapped at deep levels occurs, either by thermal or optical capture or emission, this variation in trapped charge can be readily monitored by measuring the corresponding change in the constant-bias junction capacitance signal. All forms of capacitance spectroscopy are based on this fact. The advantage that this form of measurement has over the traditional methods, such as thermally stimulated conductivity or photoconductivity, is that it gives a direct measure of trapped carrier concentration [2].

When the trap concentrations are small, thus inducing small capacitance changes compared with the overall junction capacitance, the thermal emission capacitance transients are simple exponential decays which are directly proportional to the trap occupancy, n cm^{-3}. For large

concentrations, however, the situation is more complex and the emission transients are usually non-exponential.

5.212 Bias voltage pulses

The ability to vary the width of the space-charge layer as a function of the applied bias voltage makes it possible to separate measurements of capture and emission processes at deep levels almost totally. This technique is illustrated in Figure 5.2/1, for a majority-carrier pulse in a Schottky barrier device. In Figure 5.2/1(a) the device is under quiescent reverse bias Vqr. The occupancy of the trap levels under examination is static, and the depletion width is Wdqr. If the bias is reduced to a value Vrr > Vqr, the depletion width also decreases to a value Wdrr, leaving some of the deep trap levels formerly within it, outside in neutral material. This is depicted in Figure 5.2/1(b). During the time that the bias is at this level the deep traps can capture majority-carriers and tend to become filled. After the pulse, when the bias has returned to its quiescent value Vqr (Figure 5.2/1(c)), the junction capacitance will have changed due to the captured carriers. As these captured carriers are thermally emitted again, a capacitance transient is observed.

Thus the majority-carrier pulse is a means whereby the majority carrier concentration can be switched on and off in a small volume of the sample. Majority-carrier capture dominates when the pulse is switched on, whereas majority-carrier emission dominates when it is turned off.

A minority-carrier (injection) pulse corresponds to the diode being forward-biassed during a pulse so that both majority and minority carriers are introduced. This makes minority-carrier capture possible so that minority-carrier traps may be studied. In Schottky barrier devices this technique is not applicable, however the same effect can be produced by using a means other than alteration of the bias voltage to generate injection conditions. This might be accomplished by using an optical pulse, or a pulse of high-energy electrons in an electron microscope.

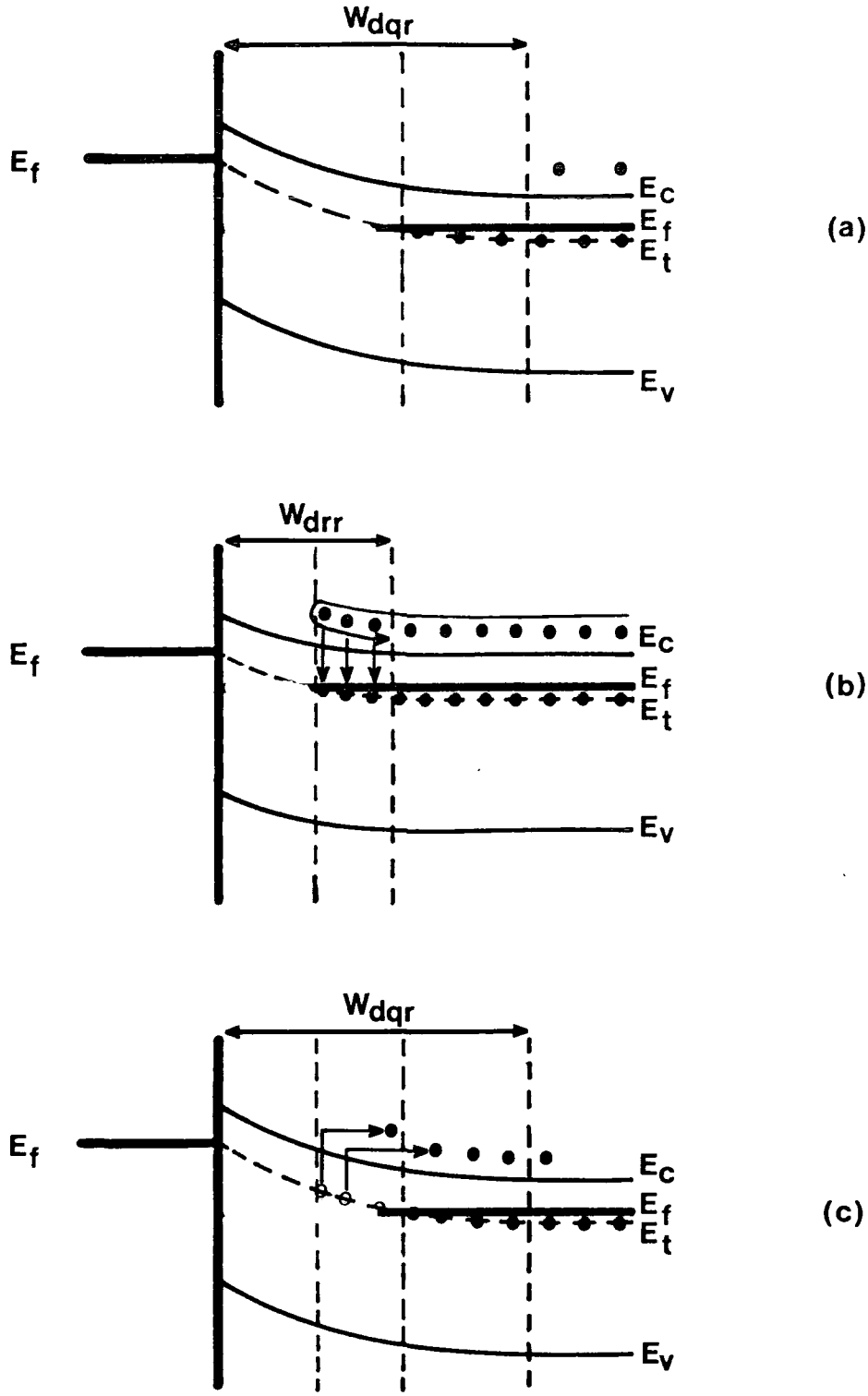

(a) Quiescent reverse bias.

(b) Reduced reverse bias traps filling.

(c) Traps emptying back at quiescent reverse bias.

FIGURE 5.2/1

An additional feature of bias-voltage variations is that they allow the possibility of obtaining a spatial profile of trap concentration. This can be done by either varying the steady-state bias voltage, or by varying the amplitude of the majority-carrier pulse. In either case the spatial region in which deep levels are observed is varied and the spatial profile may be obtained.

5.213 Variations of signal sensitivity in time and space

The magnitude of a capacitance or current transient corresponding to the thermal emission of carriers from a trap depends on the location of the trap within the depletion region. The relative change in capacitance $[\Delta C/C]_x$ produced by n(x) trapped electrons in the interval between position x and $x+\Delta x$, where $0 \leq x \leq W_d$, in the space-charge layer of an n-type Schottky barrier can readily be calculated. From Poisson's equation it can be shown that the voltage change induced by trapping n(x) electrons at x is

$$\Delta V = \frac{e}{\varepsilon} [N_D W_d . \Delta W_d - n(x).x.\Delta x] \qquad 5.2\text{-}1$$

where N_D is the positive space charge at W_d, due to ionised donors

Since it is the capacitance change at constant applied bias which is required, $\Delta V=0$.

$$\left[\frac{\Delta C}{C}\right]_x = - \frac{n(x)}{N_D W_d^2} . x\Delta x \qquad 5.2\text{-}2$$

It is important to note that the sensitivity increases linearly from zero at the junction to a maximum at the edge of the depletion region. This means that the detection of capacitance changes associated with a change in occupancy of traps located close to the junction is not easily achieved. Difficulty may therefore be experienced in detecting capacitance changes produced by an inhomogeneous trap distribution wherein most of the traps lie near to the junction.

The capacitance transients in the limit $\Delta C \ll C$ are proportional to the trapped electron concentration n(t) for electron emission, or trapped hole concentration 1-n(t) for hole emission. The time dependence of n is given by [2]

$$\frac{n(t)}{N_T} = \left[\frac{1}{\frac{e_p}{(e_n+e_p)}} \left(1 + \frac{e_n}{e_p} \exp(-[e_n+e_p]t)\right) \right]_{t>0}^{t\leq 0} \qquad 5.2\text{-}3$$

(where e_n, and e_p are the electron and hole emission rates, respectively.)

in the example where a majority carrier pulse completely fills the traps (n-type material); and

$$\frac{n(t)}{N_T} = \left[\frac{0}{\frac{e_p}{(e_n+e_p)}} \left(1 - \exp(-[e_n+e_p]t)\right) \right]_{t>0}^{t\leq 0} \qquad 5.2\text{-}4$$

when an injection pulse at t=0 completely fills the traps, of concentration N_T, with holes (empties it of electrons).

Using this notation, a trap for which $e_n \ll e_p$ is called a minority carrier trap in n-type material, and a majority carrier trap in p-type material. The opposite is true for a trap for which $e_p \ll e_n$. For capacitance measurements these notations are useful, since a negative transient is always generated by a majority carrier emission and a positive transient always derives from minority-carrier emission.

For $\Delta C \ll C$, the capacitance signal is a direct measure of n(t) and hence may be described by either 5.2-3 or 5.2-4. By comparison, current transients are dependent upon the transient time-constant, and hence upon the thermal emission rate of the trap. This is due to the fact that the current is given by the rate of change of charge density, which means that current measurements are most sensitive to fast transients. The

capacitance signal, being independent of transient rate, is most useful when transients of long time constant are being studied.

5.214 Transient magnitudes of uniformly distributed trap concentrations

In order to evaluate the magnitude of the total signal in a particular sample we must integrate 5.2-2, with respect to x, over the region of the space-charge layer where emission is actually taking place (Figure 5.2/2).

Two important regions of the device must be considered. At the outer edge of the layer there is a transition between the conducting bulk and the central part of the space-charge layer which is essentially depleted of free carriers. For a specific deep level this gives rise to the so-called edge region of thickness λ, defined by the point at which the trap level E_T crosses the Fermi level E_F. From Poisson's equation it can readily be shown that

$$\lambda = \left[\frac{2\varepsilon (E_F - E_T)}{e^2 N_D}\right]^{\frac{1}{2}} \qquad 5.2\text{-}5$$

- assuming N_D is uniform.

Within this region, the traps are below the Fermi level and therefore filled with electrons, i.e. the capture rate is much larger than the thermal emission rate. There is another region, close to the junction, which is dependent upon the bias voltage. This region is denoted $\lambda(V_r)$ in Figure 5.2/2, and within it the deep traps are always empty due to the capture rate for holes, C_h, being much greater than the emission rate α_h. Between these two edge regions lies the inner carrier depletion layer in which the capacitance and current transients are generated. Note that the free-carrier concentration present in the edge region, λ, is such that it has a negligible effect on the shape of the junction band-bending. For this reason it does not play a part in the calculation of W_d. There are, however, sufficient carriers in the edge region to affect the deep-level occupation. Thus, the total capacitance signal produced by a majority carrier pulse which brings the bias to zero volts for a time long enough to completely fill a trap of concentration N_T, is obtained by integrating

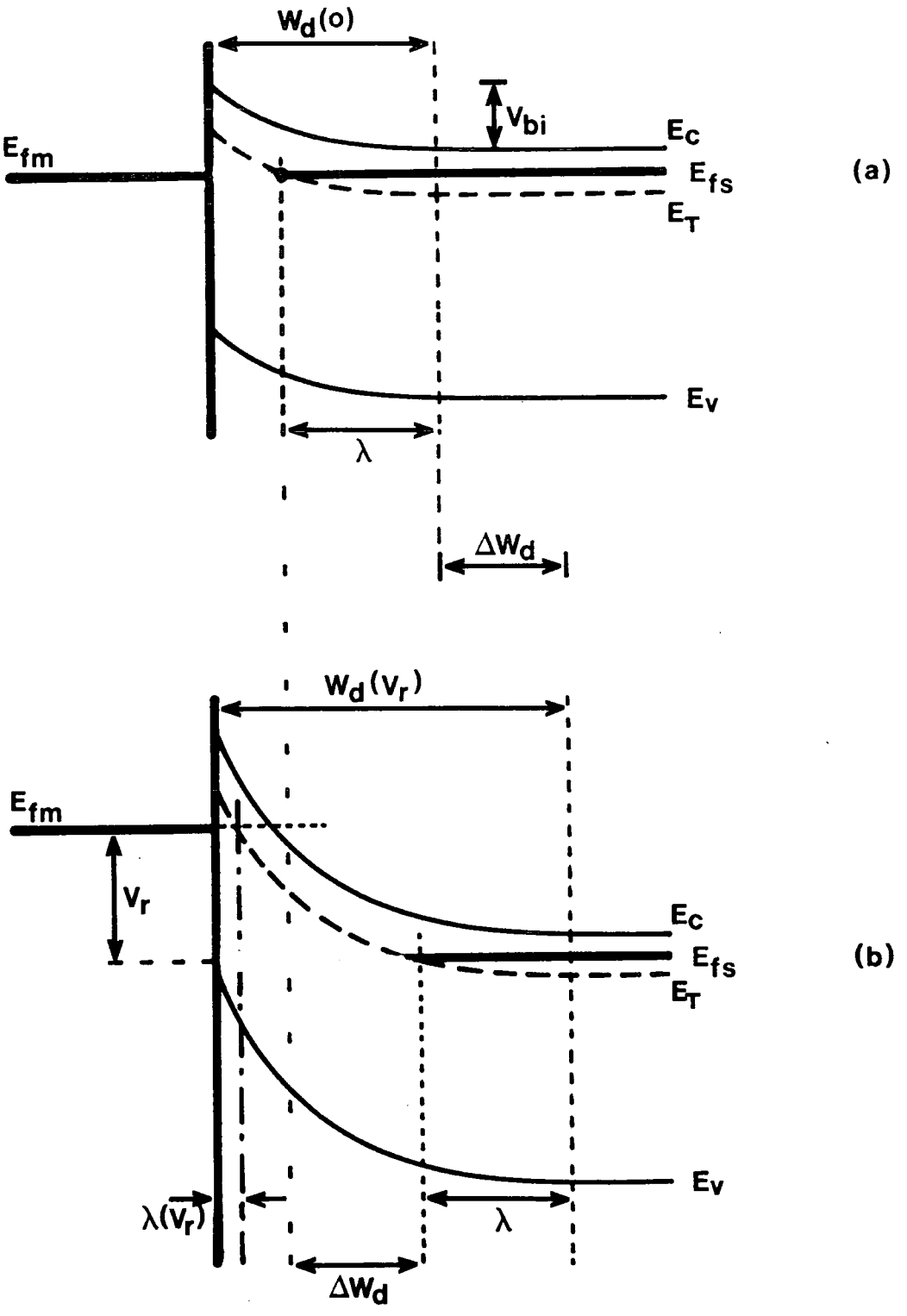

Energy diagram of a Schottky barrier under zero bias (a) and under reverse bias (b), Vr.

$$\Delta W_d = W_d(V_r) - W_d(o)$$

FIGURE 5.2/2

5.2-2 with respect to position, x, over the region bounded by $x = W_d(0)-\lambda$ and $x = W_d(V_r)-\lambda$. The result is expressed as fractional capacitance change in 5.2-6 below.

$$\frac{\Delta C}{C} = -\frac{N_T}{2N_D}\left[1 - 2\,\frac{\lambda}{W_d(V_r)}\left(1 - \frac{C_D(V_r)}{C_D(0)}\right) - \left(\frac{C_D(V_r)}{C_D(0)}\right)^2\right] \qquad 5.2\text{-}6$$

If the edge region was ignored, the large bracketed term in 5.2-6 would reduce to unity, and with a typical bias pulse of a few volts, an error of approximately a factor of two would occur in the calculation of trap concentration, N_T [2]. This error arises because the pulse used to fill the deep levels does not cover the whole of the depletion region.

5.22 Single-shot measurement techniques

All techniques involving the use of thermally stimulated space-charge spectroscopy to determine trapping parameters are based on the measurement of the thermal emission transient at some fixed temperature. Isothermal capacitance transients were first proposed as a technique to study traps in semiconductors by Williams [3], and by Furukawa and Ishibashi [4,5]. The capacitance transient associated with majority-carrier emission is always negative. Figure 5.2/3 shows such a transient with the various conditions of the space-charge region depicted at each stage of the emission. Similarly Figure 5.2/4 shows a positive transient due to minority-carrier emission following an injection pulse. Note that for Schottky barriers, this is not applicable due to the nature of the metal-semiconductor contact. In this case another method must be found to inject minority carriers, such as optical stimulation. The example used in Figure 5.2/4 is that of a p^+n junction, forward-biassed to provide minority carriers in the injection pulse.

The ionisation energy $E_e=E_C-E_T$ or $E_h=E_T-E_V$ for electron and hole traps respectively, can be found from the slope of an Arrhenius plot; i.e. a plot of the natural logarithm of the transient decay rate as a function of reciprocal absolute temperature. This follows from the relationships in 5.2-7 for electrons, and 5.2-8 for holes.

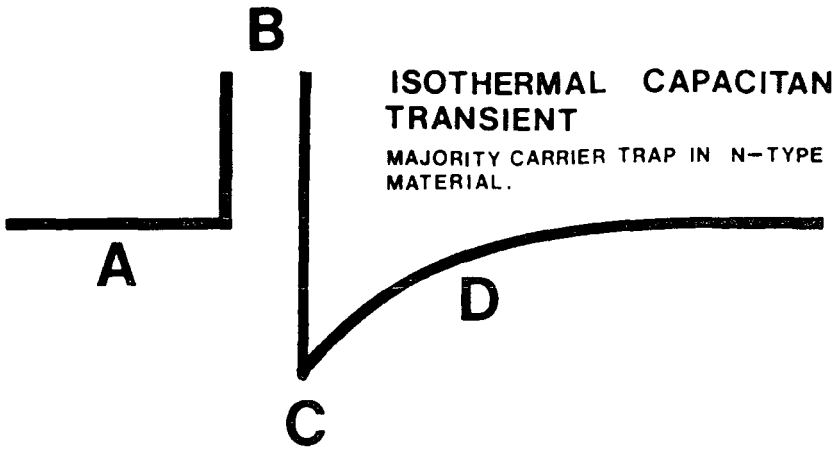

ISOTHERMAL CAPACITANCE TRANSIENT

MAJORITY CARRIER TRAP IN N-TYPE MATERIAL.

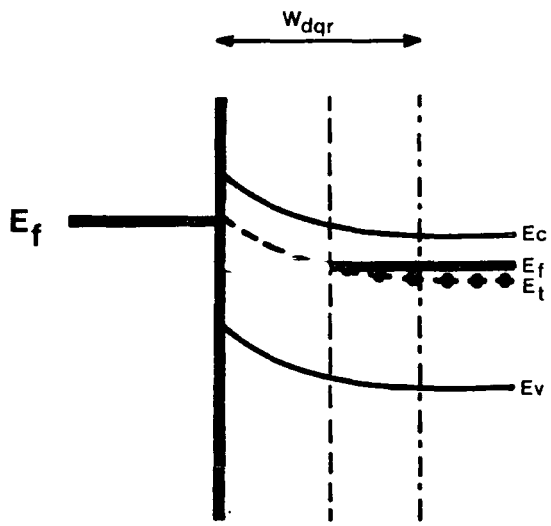

A QUIESCENT CONDITIONS.

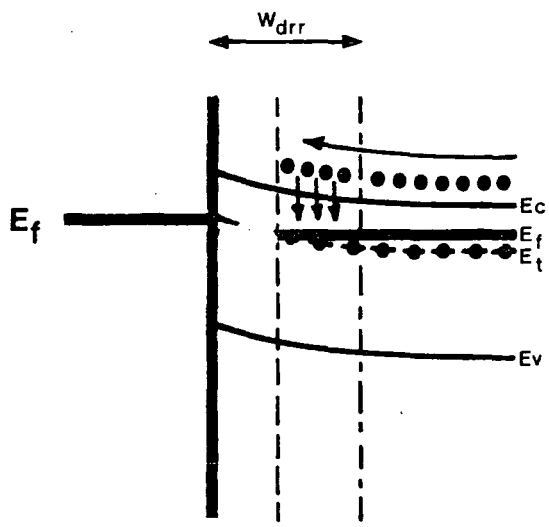

B MAJORITY PULSE. BIAS IS REDUCED ALLOWING CARRIERS TO BE TRAPPED.

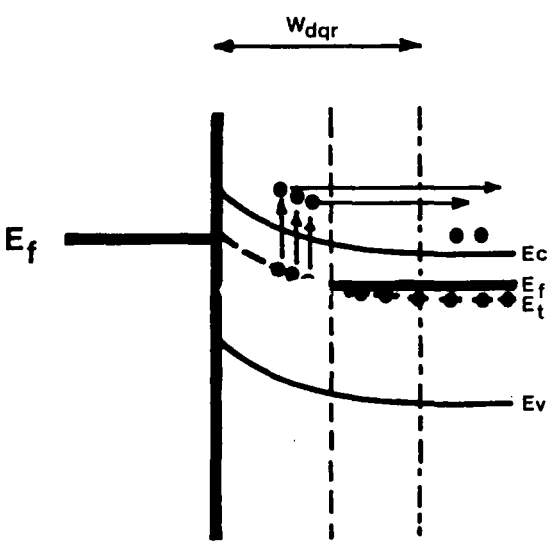

C BEGINNING OF TRANSIENT. CAPACITANCE ALTERED DUE TO TRAPPED CHARGE.

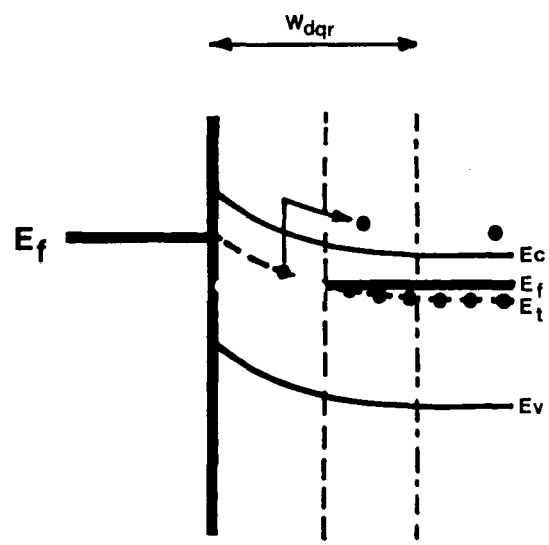

D DECAY OF CAPACITANCE TRANSIENT AS ALL CARRIERS TRAPPED DURING THE MAJORITY PULSE ESCAPE.

FIGURE 5.2/3

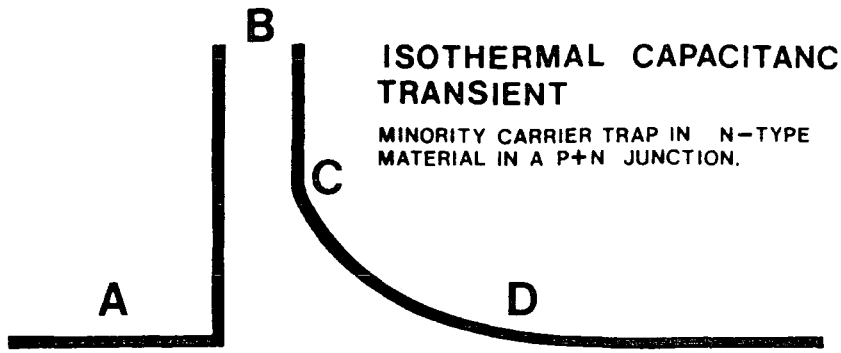

ISOTHERMAL CAPACITANCE TRANSIENT

MINORITY CARRIER TRAP IN N–TYPE MATERIAL IN A P+N JUNCTION.

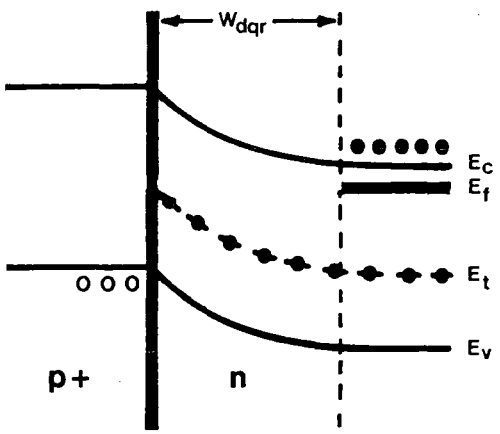

A QUIESCENT CONDITIONS.

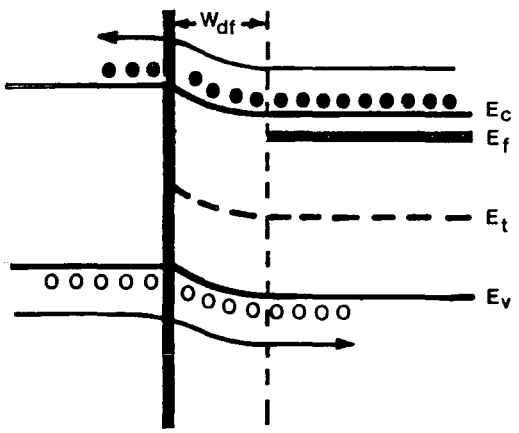

B FORWARD BIAS. ACCEPTOR LEVELS E_t ARE ALL EMPTIED AND ANY MAJORITY TRAPS PRESENT ARE FILLED.

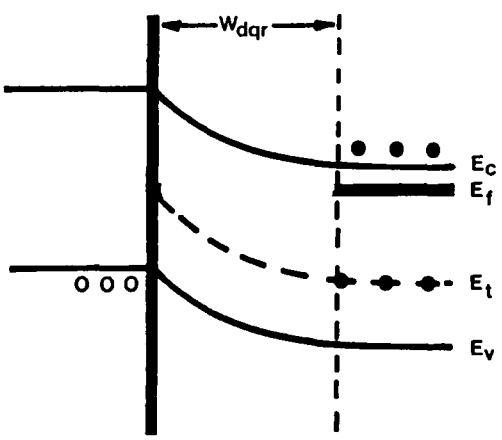

C BEGINNING OF THE CAPACITANCE TRANSIENT.

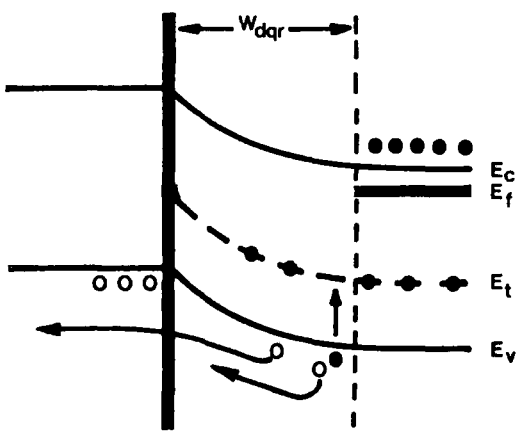

D THERMAL EMISSION OF TRAPPED HOLES PRODUCING TRANSIENT DECAY.

FIGURE 5.2/4

$$\alpha_e = \nu_e \exp(-E_e/kT) \qquad 5.2\text{-}7$$

$$\alpha_h = \nu_h \exp(-E_h/kT) \qquad 5.2\text{-}8$$

(ν_h, ν_e are the attempt to escape frequencies for holes and electrons in each trap).

Another class of techniques, involving the use of irreversible thermal scans, can be applied to the study of traps inside the space-charge region. These techniques bear a strong resemblance to many of the thermally stimulated phenomena observed in bulk materials. A full discussion of these methods can be found in Chapter four.

Single shot techniques have the advantage of relative simplicity, and can be very useful as survey or comparison methods where a large number of devices need to be examined. For greater sensitivity however, the DLTS technique is preferred.

5.23 Deep level transient spectroscopy (DLTS)

The basic idea of DLTS lies in the concept of the so-called 'rate window' detection method. This is depicted in Figure 5.2/5. Consider a Schottky barrier undergoing repetitive majority-carrier pulses of the type shown in Figure 5.2/3. A series of capacitance transients will be produced at a repetition rate determined by the bias pulse repetition rate. Usually, the frequency of pulse repetition is set such that there is enough time for the longest decay to reach the quiescent capacitance again. As the temperature is varied, the time constant of the capacitance transient will vary exponentially with reciprocal temperature as discussed in 5.213. This is shown in Figure 5.2/5. The DLTS equipment contains a device which only gives a signal when the transient decay lies within a certain range of time-constants, or decay rates. Within this range, or 'window', the signal output is a measure of how near the decay-rate is, as it varies with temperature, to a specific value chosen previously by the operator. The signal output is thus a series of peaks as the temperature is scanned (Figure 5.2/5). Such a plot is called a DLTS spectrum.

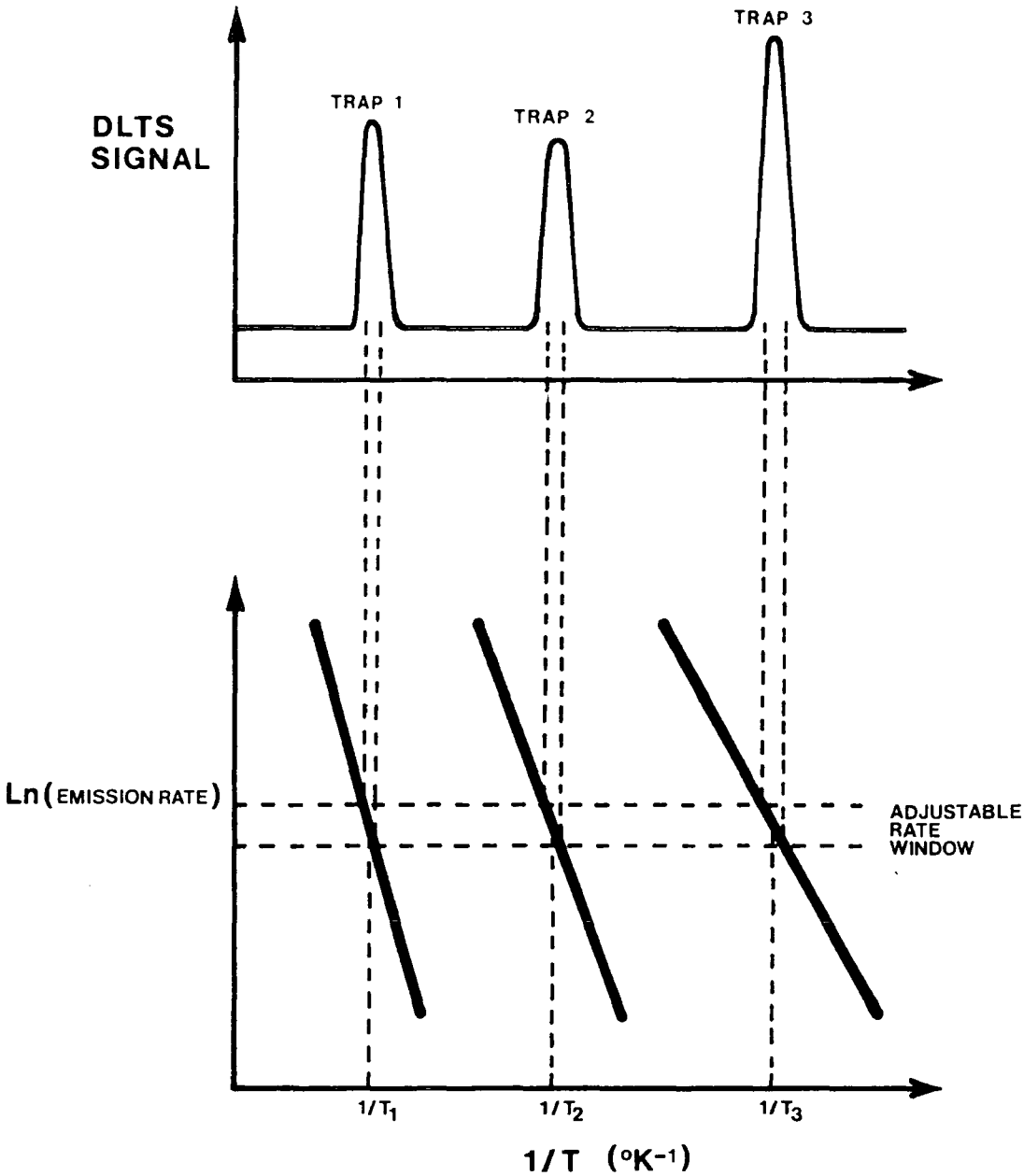

THE RATE WINDOW CONCEPT, WHICH IS FUNDAMENTAL TO THE DLTS METHOD. A SIGNAL IS PRODUCED ONLY WHEN EACH OF THE THREE TRAPS EMPTIES AT A RATE WHICH IS WITHIN THE RATE WINDOW.

FIGURE 5.2/5

Although the spectrum looks like the signals produced by single shot techniques, it has several important differences. Firstly it is reversible; the operator can scan up or down in temperature any number of times, or even stop at a particular temperature to study capture properties or spatial profiles. Secondly the baseline is, inherently, always flat due to the good common-mode rejection of the steady-state capacitance variations. This gives a good sensitivity.

There are a number of ways in which the DLTS rate-window may be realised in practice. The first method proposed in the original DLTS experiments involved the use of a dual-gated integrator (double-boxcar) [1]. In this method, the transient amplitude is sampled at two times t_1 and t_2 after the bias pulse, as shown in Figure 5.2/6. The DLTS signal is defined as being the difference between these transient amplitude samples. At very slow or very fast emission rates, the signal is zero (Figure 5.2/6), however, when the emission rate is such that the time-constant is approximately equal to the gate separation, a difference signal is generated and passes through a maximum as a function of temperature. The position of this maximum is given by

$$\tau_{max} = \frac{t_1 - t_2}{\ln(t_1/t_2)} \qquad 5.2\text{-}9$$

This expresses the time constant of emission which will produce a maximum DLTS signal for gate times t_1 and t_2 on the double-boxcar.

Alternative methods of achieving a rate window for the DLTS measurment are the lock-in amplifier technique and the exponential correlator [2]. The most sensitive and discriminating method of picking out an exponential transient of particular time-constant is provided by the correlation method. A way of realising this technique would be to use computerised data acquisition to analyse each and every transient as the temperature of the sample was varied.

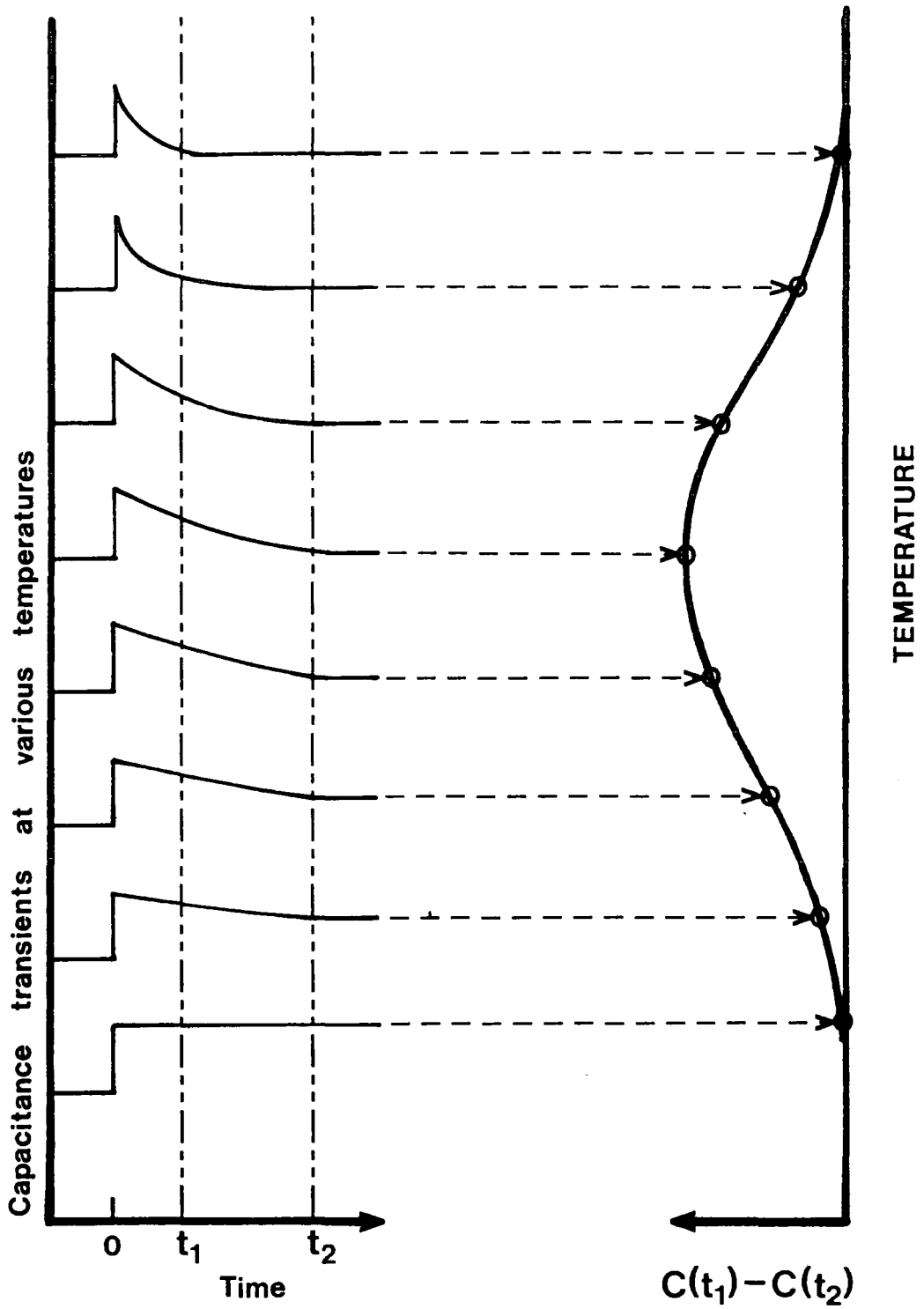

Implementation of a DLTS rate window by means of a double-boxcar integrator with gates set at times t_1 and t_2.

FIGURE 5.2/6

5.231 Determination of activation energies

The best way to determine the activation energy of a deep level is to construct an Arrhenius plot by plotting the natural logarithm of the rate window time-constant, Equation 5.2-9, versus the reciprocal temperature of the DLTS peak, which results from that rate window setting. The plot is built up by repeating DLTS scans for different rate window settings, simultaneously, for all peaks relating to different traps.

Usually the Arrhenius plot is constructed by plotting $\ln(\tau T^2)$ versus $1/T_{max}$. This follows from the expression

$$1/\tau = \sigma\langle\bar{\nu}\rangle Nc \exp(-E/kT) \qquad 5.2\text{-}10$$

where σ = pre-exponential constant

$\langle\nu\rangle$ = thermal velocity of electrons ($\langle\nu\rangle \propto T^{1/2}$)

Nc = effective density of states in the conduction band ($Nc \propto T^{3/2}$)

Equation 5.2-10 can be written as:

$$1/\tau = AT^2 \exp(-E/kT)$$

Therefore $T^2\tau = 1/A \exp(E/kT)$ where A = lumped constant

and hence $\ln(T^2\tau) = \ln(1/A) + E/kT$

Therefore the gradient of the graph of $\ln(\tau T^2)$ versus $1/T$ is of value E/k.

5.232 Determination of other parameters

Using the DLTS technique, the majority and minority carrier trap concentration profiles may be measured by the systematic variation of the biassing parameters between temperature scans. The capture cross-sections may also be found, by a similar method.

Before attempting to measure the concentration profile of a population of deep defect states, it is first necessary to know the concentration

profile of the shallow levels. Many ways of accomplishing this from the C-V characteristic of the junction have been outlined [6-9].

One of the most convenient ways of measuring the spatial distribution of deep levels, which is especially useful at low concentration levels, is to record the magnitudes of a series of capacitance transients produced by majority carrier pulses of increasing amplitude. The deep level concentration, as reflected by the capacitance signal, is then probed inward from Wd(-Vq), the quiescent depletion width, as the amplitude is increased from zero. Equation 5.2-6 is then used to calculate N_T, the trap concentration, as a function of position within the depletion region. Another way of accomplishing the same measurement is to keep the majority-carrier pulse at zero volts, and alter the quiescent reverse bias level from zero volts to $-V_r$ in regular intervals. This time the deep level concentration is probed outwards from Wd(0), the depletion width at zero bias.

Measurement of capture and emission rates for deep levels follows from the expressions given in 5.2-11 and 12.

$$N(t) = N_T\,(1-\exp[-c_n n t]) \qquad 5.2\text{-}11$$

$$N(t) = N_T \exp[-e_n t] \qquad 5.2\text{-}12$$

where: $N(t)$ = trap occupancy at time t (cm^{-3})
N_T = trap concentration (cm^{-3})
c_n = electron capture rate (cm^3S^{-1})
e_n = electron emission rate (S^{-1})
n = free carrier density in conduction band (cm^{-3})

In order to measure the capture rate, the trap concentration N(t), which is derived from the magnitude of the capacitance transient, is recorded as a function of t_D, the duration of the filling pulse, for several values of t_D. The gradient of $\ln\{1-N(t_D)/N_T\}$ versus t_D then gives the capture rate in units of cm^3S^{-1}.

5.3 EXPERIMENTAL APPARATUS AND PROCEDURE

5.31 DLTS apparatus

A block diagram of the apparatus arrangement is shown in Figure 5.3/1. The various circuits built for the experiment are shown in Figure 5.3/2. The Boonton 72B capacitance meter, used to monitor junction capacitance in the Schottky barrier devices fabricated in this project, is a differential input device with a sinisoidal drive of 1 MHz at 10 mV r.m.s. Its capacitance range is 1-3000 pF. In order to obviate problems of saturation, caused by the voltage bias pulses which are applied to the diode sample, a circuit was designed which enabled the capacitance meter input to be disabled during such times. This was accomplished by using the trigger generator in Figure 5.3/2(c) to drive a pulse-shaper circuit, which could provide a gating signal of variable delay and duration, to the Boonton capacitance meter. Samples were placed in the cryostat (Section 4.12) which was used to vary the temperature from 77 to 400°K by means of a wirewound heater-element. Temperature was monitored using a Control and Readout digital meter which converted the millivolt signals from a copper-constantan thermocouple junction into a reading in degrees celsius. Cold-junction compensation was internal to the instrument. Accuracy was ±0.1°C.

The rate window was realised by using the double-boxcar technique (Section 5.23). A single boxcar integrator can be formed by using a Brookdeal Scan delay generator (type 9425) to drive a Linear Gate (Brookdeal, type 9415). When a trigger pulse was delivered to it, the scan delay generator produced a gating pulse of a chosen width after a chosen delay time, t_D. In the DLTS equipment, the trigger pulse rising edge coincided with the falling edge of the diode bias pulse returning to its quiescent value. The user could, in addition, specify a linear increase in t_D with time. This was the 'scan' option, which was used to plot out transients which were too fast to capture on a chart recorder in single-shot mode.

The output pulse from the scan delay generator was fed into the trigger input of the linear gate. This device was also connected to the transient signal to be sampled, and featured an averaging circuit, which had a

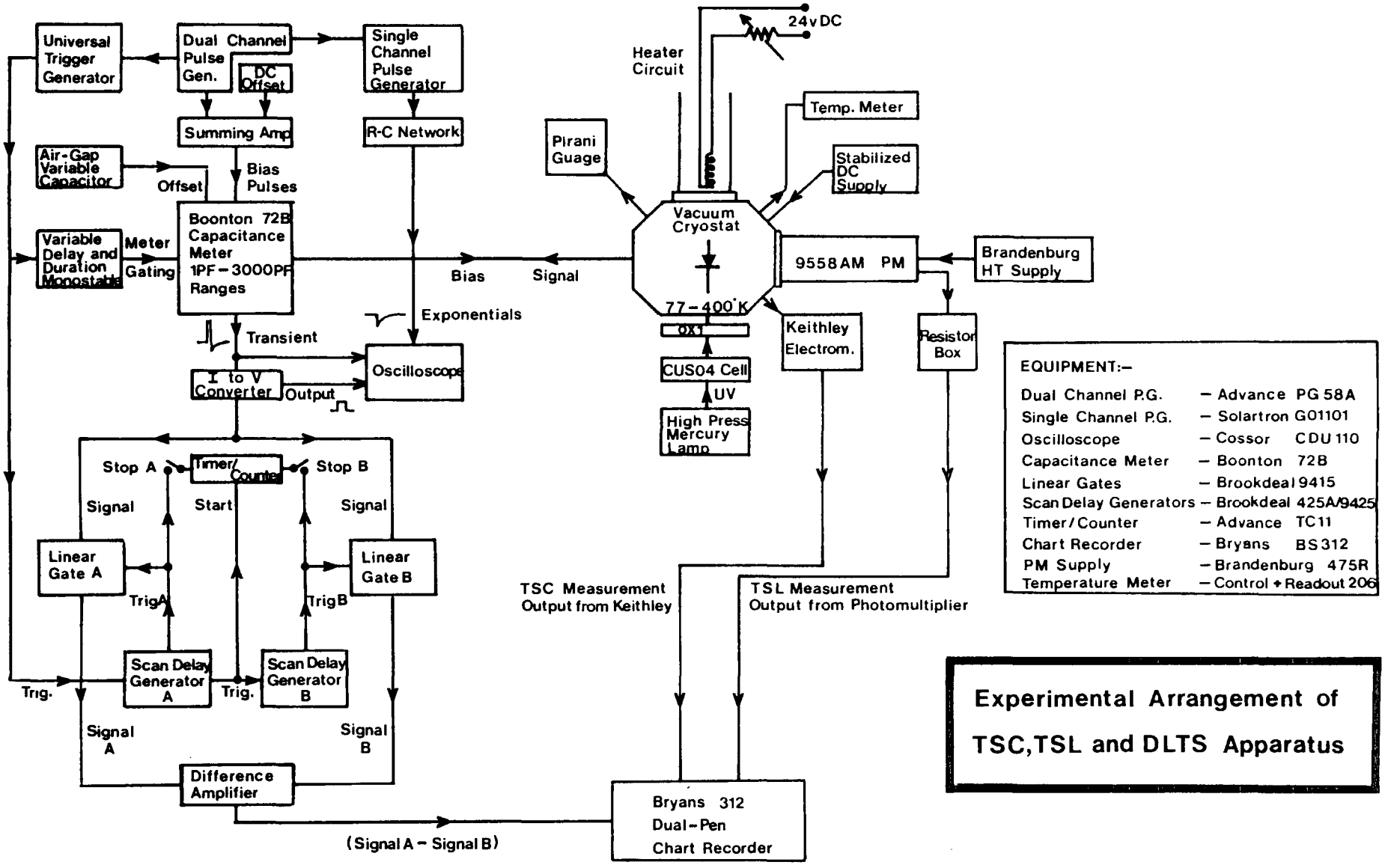

FIGURE 5.3/1

Experimental Arrangement of TSC, TSL and DLTS Apparatus

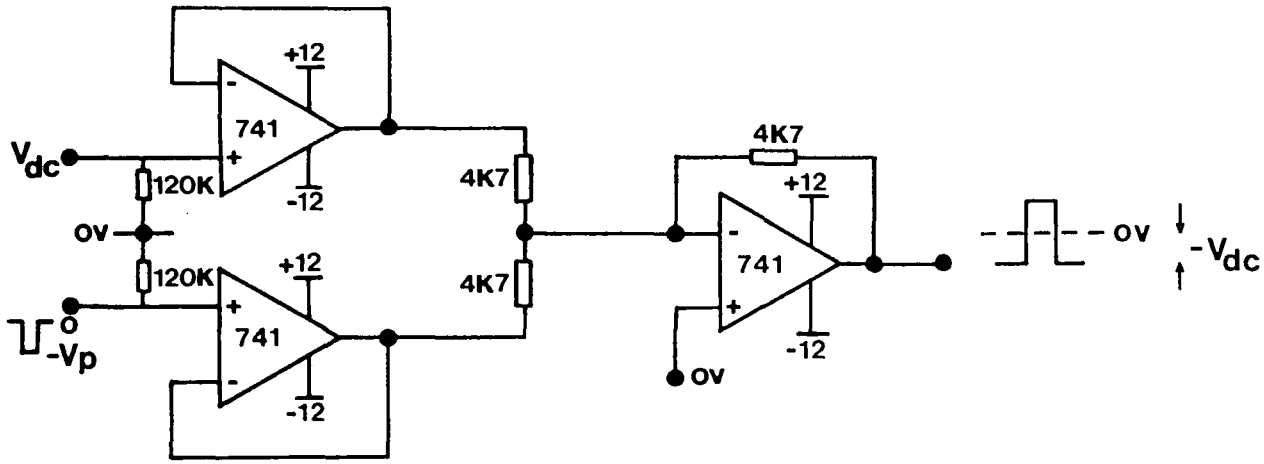

(a) Summing Amplifier

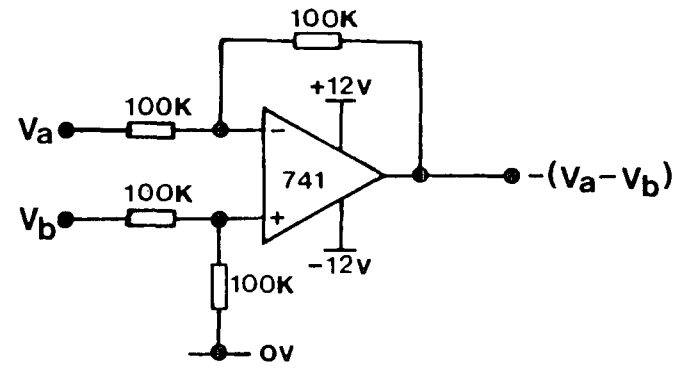

(b) Difference Amplifier

FIGURE 5.3/2

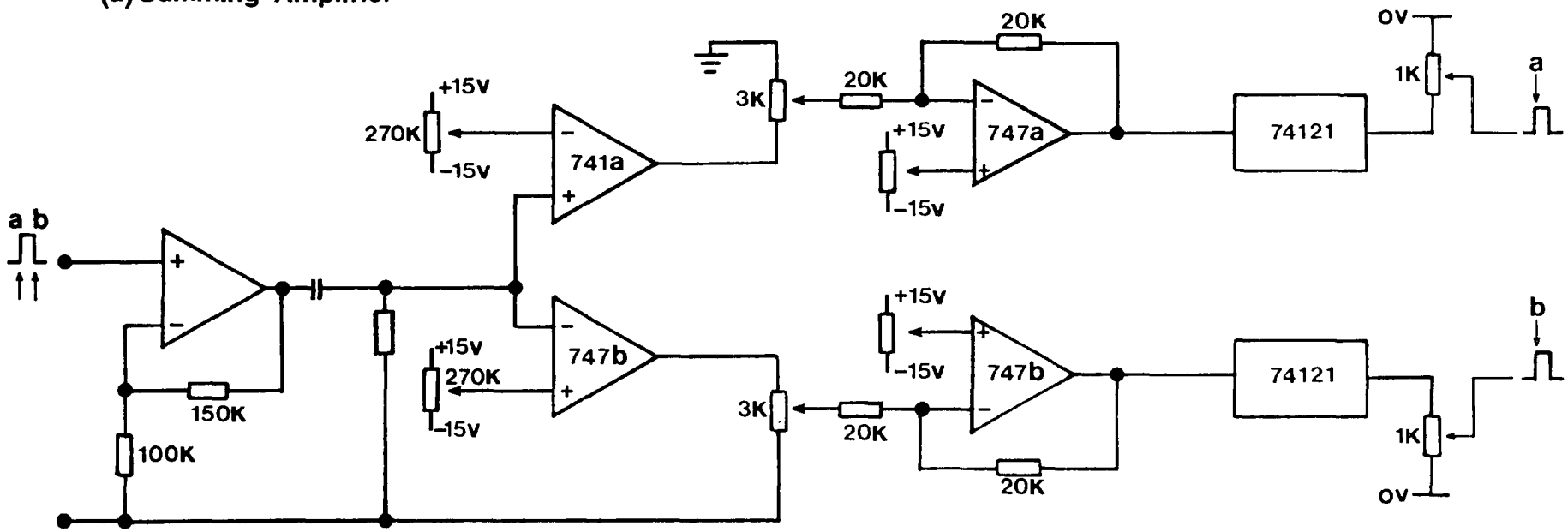

(c) Trigger Generator (Edge Detector)

user-selectable time-constant. The trigger pulse from the scan-delay generator was used by the linear gate as a gating pulse. For the duration of this pulse, the gate measured the value of the input signal and averaged it with the previous signals. The output was finally delivered either to a difference amplifier for DLTS measurements, or to a Bryans chart recorder, (type BS312) when transients were to be plotted out.

Using two sets of such instruments, a double-boxcar averager was available for the realisation of the DLTS rate window. The scan delay generators were used in delay-mode; the scan delay generator attached to the linear gate measuring the transient first, at t_1, was adjusted to give a delay equal to t_1. The scan-delay generator attached to the second channel was set to give a trigger pulse at t_2. In this way, averaged values of the capacitance of the transient at times t_1 and t_2 after the bias pulse were produced. These values are denoted $C(t_1)$ and $C(t_2)$ in Figure 5.2/6. The two signals were then delivered to a difference amplifier which gave an output proportional to $C(t_1)-C(t_2)$. This was displayed on the chart recorder as the DLTS signal.

In order to set the delay times t_1 and t_2, a timer/counter was connected such that the start signal was provided by the falling edge of the diode bias pulse, and the stop signal was given by the scan delay generator trigger output.

An oscilloscope was used to monitor capacitance transients, and to facilitate the matching of 'artificial' R-C exponentials to the signals generated in the various experiments.

Signals were carried to the Boonton 72B capacitance meter from the cryostat using low-capacitance coaxial cable. Cable and sample-mount capacitance were offset using an air-gap variable capacitor which was enclosed in a container filled with silica-gel.

5.32 Experimental procedure

Samples of zinc selenide to be used in DLTS measurements were first fabricated into Schottky barrier diodes in the manner described in Section 3.323. These devices were then soldered onto a thin brass backplate using indium. Usually an array of several devices were affixed to the same backplate to minimise the experimental time spent in changing samples over. With the gold dot uppermost, an electrical contact could be quickly made using a piece of Spring-steel wire (Figure 5.3/3).

With a new Schottky barrier installed in the cryostat, a quick characterisation of the device was done. Current-voltage and capacitance-voltage responses were recorded to provide basic information such as diode ideality, barrier height, and donor concentration. Occasionally one of the two boxcar averagers was used to plot out an interesting transient in order to evaluate the time-constant. This was achieved by using the 'scan' option on the scan-delay generator. Unfortunately, only transients occurring at 77°K (liquid nitrogen temperature) and room temperature were investigated due to the lack of a temperature controller system at the time.

The DLTS experiment was begun by filling the vacuum-cryostat with liquid nitrogen to cool the cold-finger and sample-platform to 77°K. Whilst the apparatus was cooling, the delay times t_1 and t_2 were chosen and the two scan-delay generators adjusted accordingly. This was done by choosing a rate-window time constant, τ, and consulting a table of t_1 and t_2 values generated by computer using Equation 5.2-9. The choice of t_1 and t_2 was not uniquely defined by τ. Usually the decision was governed by which two values would give the best sensitivity. This meant that t_1 was mostly chosen to be as small as possible since transient variations at times greater than 50 mS after the bias pulse were generally very small indeed. As the sample was warmed, the capacitance difference $C(t_1)$-$C(t_2)$ was recorded on the chart recorder. Temperature was recorded as a series of 'blips' at 5°C intervals, read from the temperature meter, using the second pen as a baseline marker. DLTS peaks were observed if the traps in the space-charge region affected by the biassing emptied at the

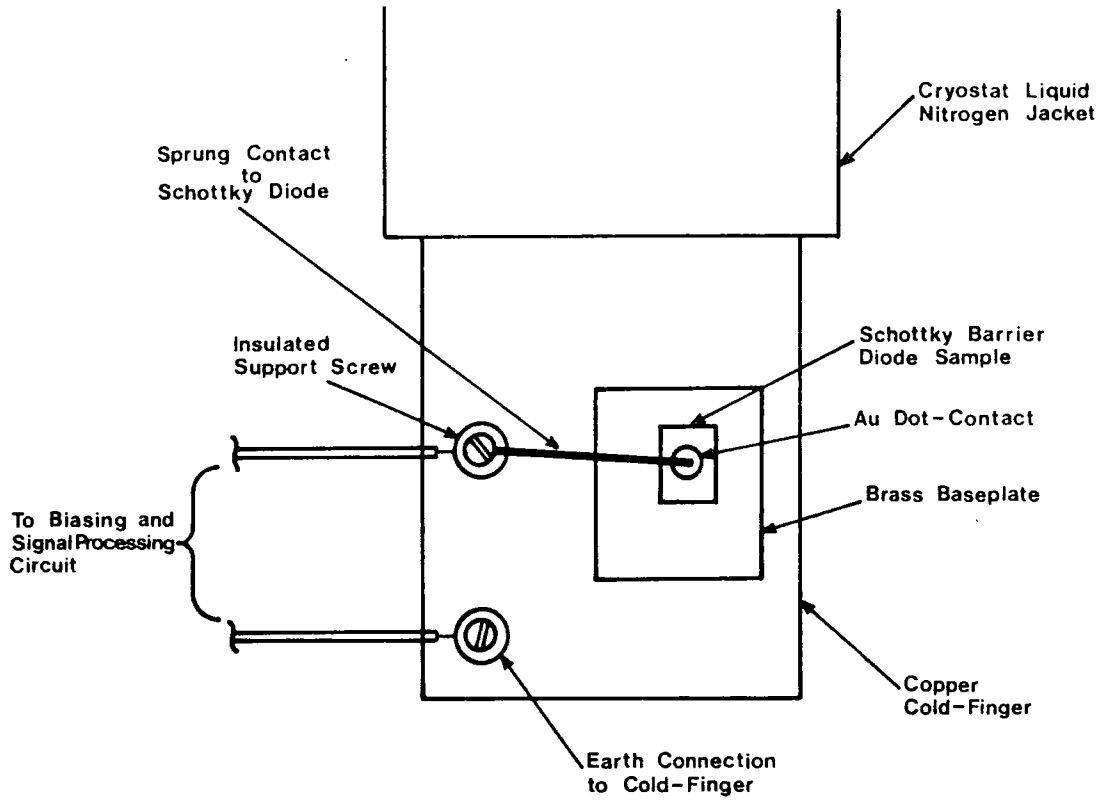

Arrangement of Schottky Barrier Devices on the Cryostat Cold-Finger

FIGURE 5.3/3

rate-window time-constant anywhere in the temperature scan. If peaks were observed, the procedure was repeated for 8 or 10 different rate-window settings. When peaks were not observed, the biassing was adjusted until a more satisfactory result was obtained.

From the DLTS spectra, the 8 or 10 peak temperatures were noted down together with the corresponding rate-window settings. The Arrhenius plot discussed in Section 5.231 was then made to obtain the values for ionisation energy (thermal) of the appropriate trap. The same graph can also be used to yield a parameter called the capture-cross-section at 'infinite temperature', by using the intercept where $1/T = 0$.

Other trapping parameters such as the concentration profile and the capture cross-section could be found by adopting the procedures decribed in Section 5.232.

5.4 EXPERIMENTAL RESULTS

A number of Schottky barrier samples were prepared from both Durham-grown ZnSe and CVD material obtained from AWRE, Aldermaston, by using the method described in Section 3.43.

Of the samples fabricated from Durham-grown material, the results obtained from four typical diodes are reported. Due to the nature of the grain boundaries present in the CVD ZnSe however, only one Schottky barrier was successfully made on this material. The difficulty was discovered to be due to the electrically active nature of the grain-boundaries (Chapter 6) which limit current flow. Despite repeated annealing in fresh molten zinc (Section 3.323) the DC resistivity values of CVD samples rarely fell below 1 kilohm. The problem was minimised to a degree by making an array of barriers and ohmic contacts on the sample. The best barrier/ohmic contact combination was then chosen. Unfortunately, the complexity of the grain-boundary structure meant that this procedure was largely unrewarding.

5.41 Durham-grown material

5.411 Schottky barrier characterisation

In order to characterise the Schottky barrier, several C^{-2} versus V plots were made. Results were obtained at 77°K and 295°K for diode DG388SB. The C^{-2} versus V curves for this sample are shown in Figure 5.4/1. Calculated parameters, including the barrier height and shallow donor concentration are given in Table 5.4/2 for all samples. At room temperature the value for the barrier height, of 2.1 eV agrees reasonably well with values obtained previously on devices fabricated from similar material [10]. The C^{-2} versus V plots shown in Figure 5.4/1 both exhibit a kink where the gradient fluctuates across a small bias range. The kink occurred at a bias of -5.5 volts at room temperature, and at -0.8 volts when the same experiment was done at 77°K. Both C^{-2} versus V characteristics were repeatable whether the plot was recorded with increasing or decreasing bias. The kink positions remained the same to within ±0.1V. The results gave a carrier concentration of 6×10^{15} cm^{-3} at room temperature.

A graph of lnJ versus V_f (current density versus forward bias) is presented in Figure 5.4/3. This result was obtained from sample DG388SB, and is typical of all samples studied. The ideality factor was calculated to be 1.20. The relatively high saturation current (~4.4 μA) measured is probably due to the contribution of leakage paths caused by the conducting layers left on the sample surfaces by etching [11].

5.412 Determination of trapping parameters

Monitoring the high-frequency capacitance of the depletion layer as the bias voltage was pulsed from a quiescent reverse bias to a reduced reverse bias, yielded transients of the sort depicted in Figure 5.4/4. The magnitudes of these transients were found to be sensitive to the duration of the filling pulse, and the values set for quiescent and

(a) C^{-2} vs V at room temperature

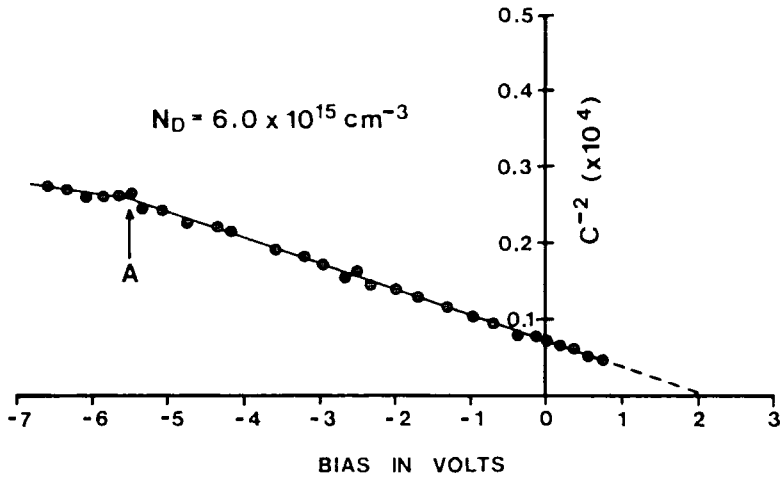

(b) C^{-2} vs V at 77°K

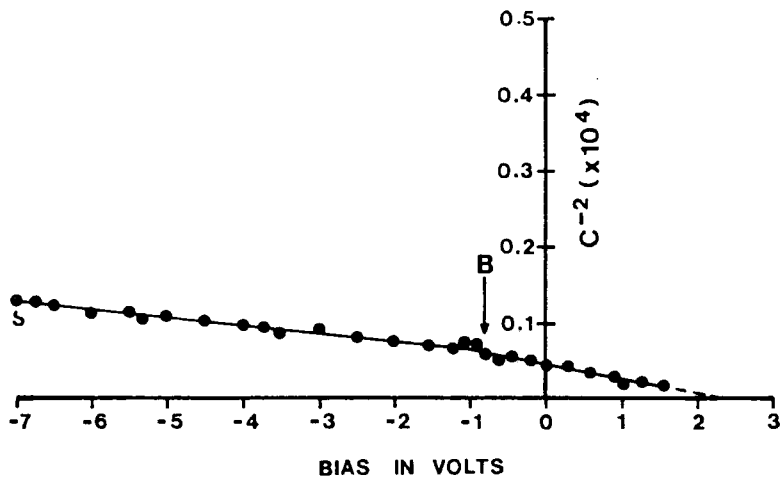

C^{-2} versus V plots for sample DG388SB (a) room temperature and (b) at 77°K. There are two gradient changes A at −5.5v & B at −0.8v.

FIGURE 5.4/1

SAMPLE	BARRIER HEIGHT (V)		DONOR DENSITY (cm^{-3})	J_{SAT} (Am^{-2})	IDEALITY FACTOR
	77°K	295°K			
DG388SB	2.28	2.10	6.0×10^{15}	4.4×10^{-6}	1.20
DG400SB/1	2.30	2.25	8.8×10^{14}	6.1×10^{-8}	1.60
DG400SB/2	2.01	1.98	9.0×10^{15}	3.1×10^{-5}	1.31
IN407SB	2.46	2.21	5.6×10^{15}	1.2×10^{-9}	1.46

CHARACTERISATION RESULTS FOR DURHAM-GROWN SAMPLES

FIGURE 5.4/2

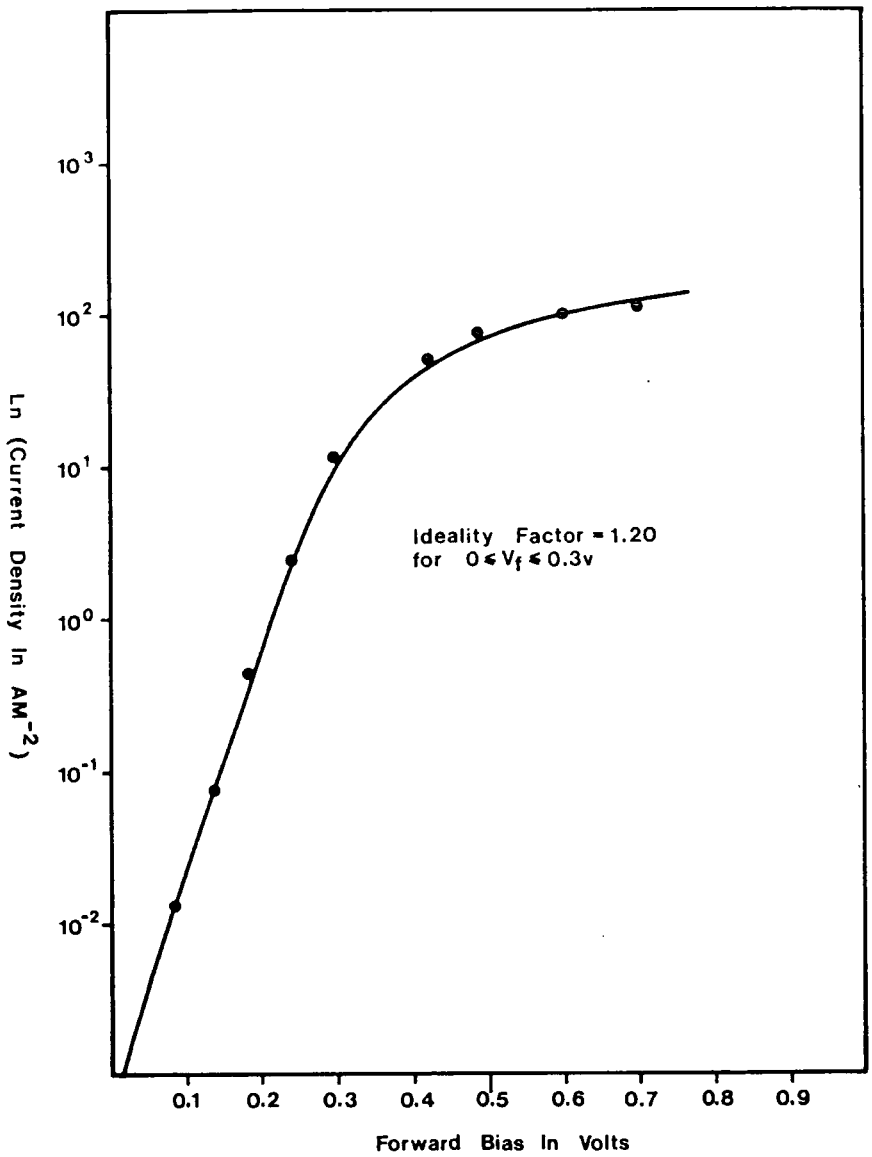

Ln (J) vs V_f for diode DG388SB

FIGURE 5.4/3

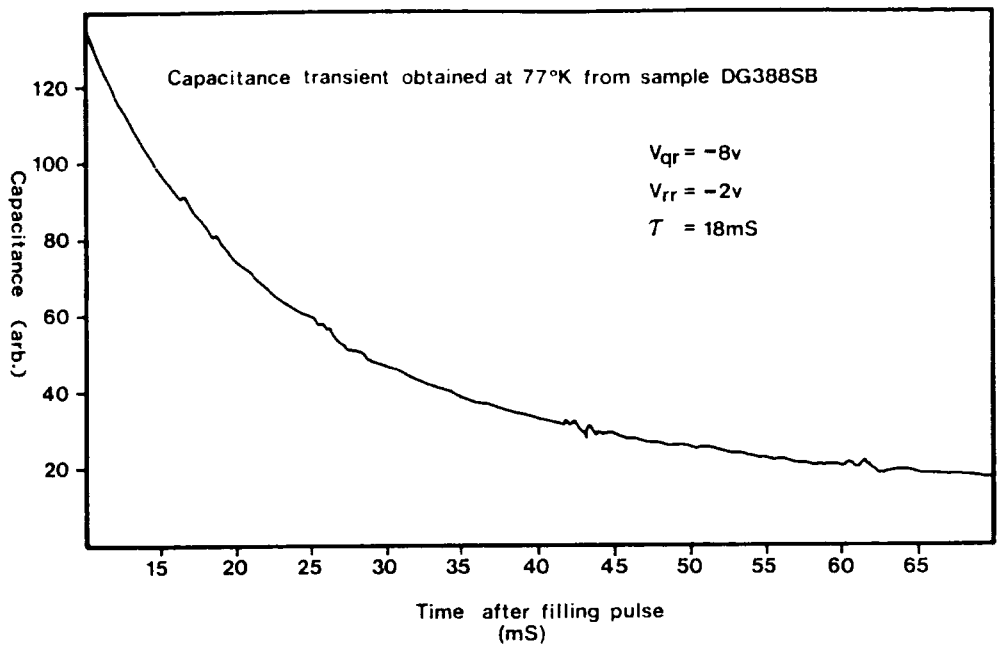

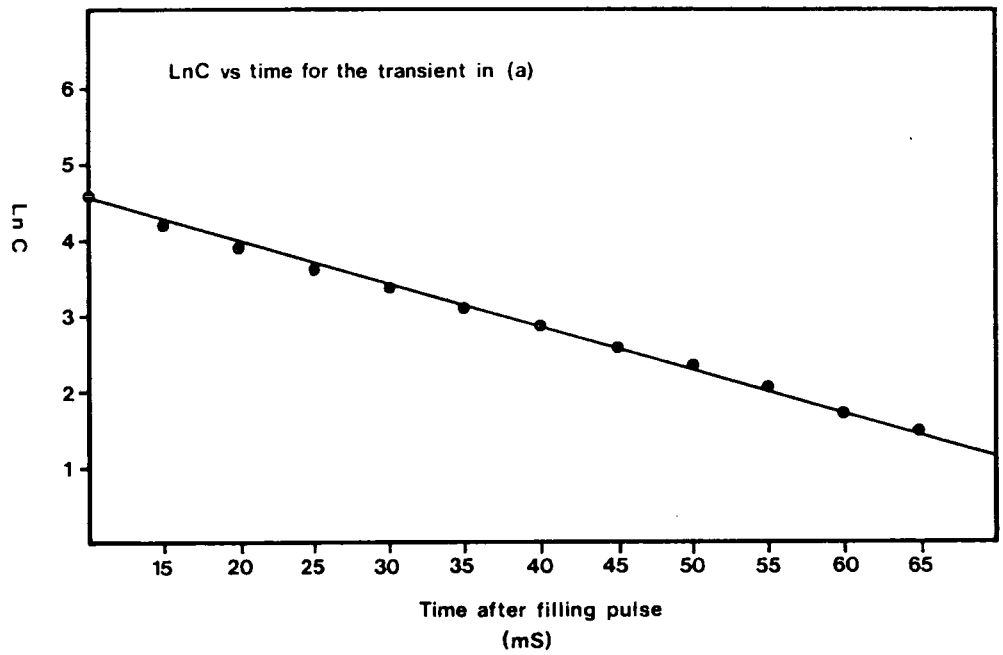

Capacitance transient obtained from sample DG388SB

FIGURE 5.4/4

reduced-reverse bias voltages. The results obtained from sample DG388SB were typical of all devices studied. Varying the quiescent reverse bias of this sample systematically while keeping the reduced reverse-bias level constant at zero volts yielded the DLTS curves shown in Figure 5.4/5. A simple calculation enabled the total capacitance change at the maximum of each DLTS peak to be found, and hence the concentration of defect levels giving rise to the signal could be calculated from Equation 5.2-6. The resulting concentration profile for each trap is shown in Figure 5.4/6 for a small region of the depletion layer.

Systematic variation of the filling pulse duration, keeping the biassing levels constant gave the series of DLTS curves shown in Figure 5.4/7. For durations less than 0.02 mS, the traps were not all filled. This caused the capacitance signal to follow the simple exponential law given in Equation 5.2-11. A plot of occupancy factor $(1-N(t_D)/N_T)$ versus filling pulse duration is shown for all three traps in Figure 5.4/8. From these results the capture cross-sections and capture rates were calculated. All three values for the capture cross-section lie within an order of magnitude of each other at about 10^{-17} cm^{-2}. These results differ from those obtained from the intercept of the Arrhenius plot (Table 5.4/9), however, it is known that capture-cross sections calculated by the latter method may be seriously in error [12].

Using the DLTS method described in Section 5.3, four samples of Durham-grown ZnSe were examined. Typical DLTS spectra obtained from each sample are shown on a common temperature axis for comparison, in Figure 5.4/10. All the peaks correspond to electron traps, since the capacitance transients which yielded them were negative. A straightforward analysis of peak position versus rate-window gave the trap depths shown in Figure 5.4/11. Also given are the infinite-temperature capture cross-sections, derived from the intercept on the Arrhenius plot for each trapping level, together with the measured values for capture cross-section obtained for sample DG388SB.

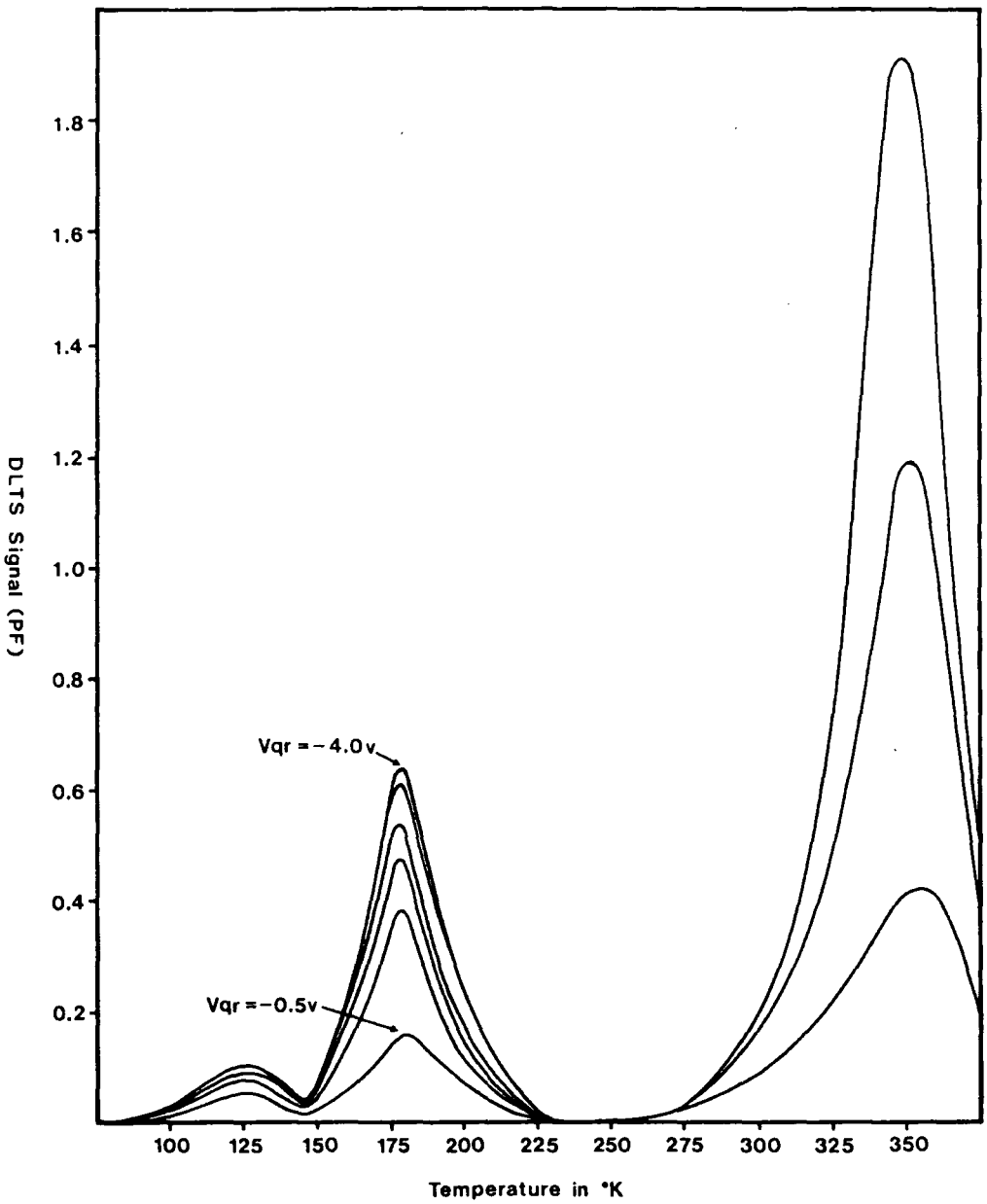

DLTS spectra produced by varying the quiescent reverse bias between -4.0v and -0.5v whilst keeping the reduced reverse bias level constant at 0v. Pulse width was 50μs and the rate window was 7.2mS.

FIGURE 5.4/5

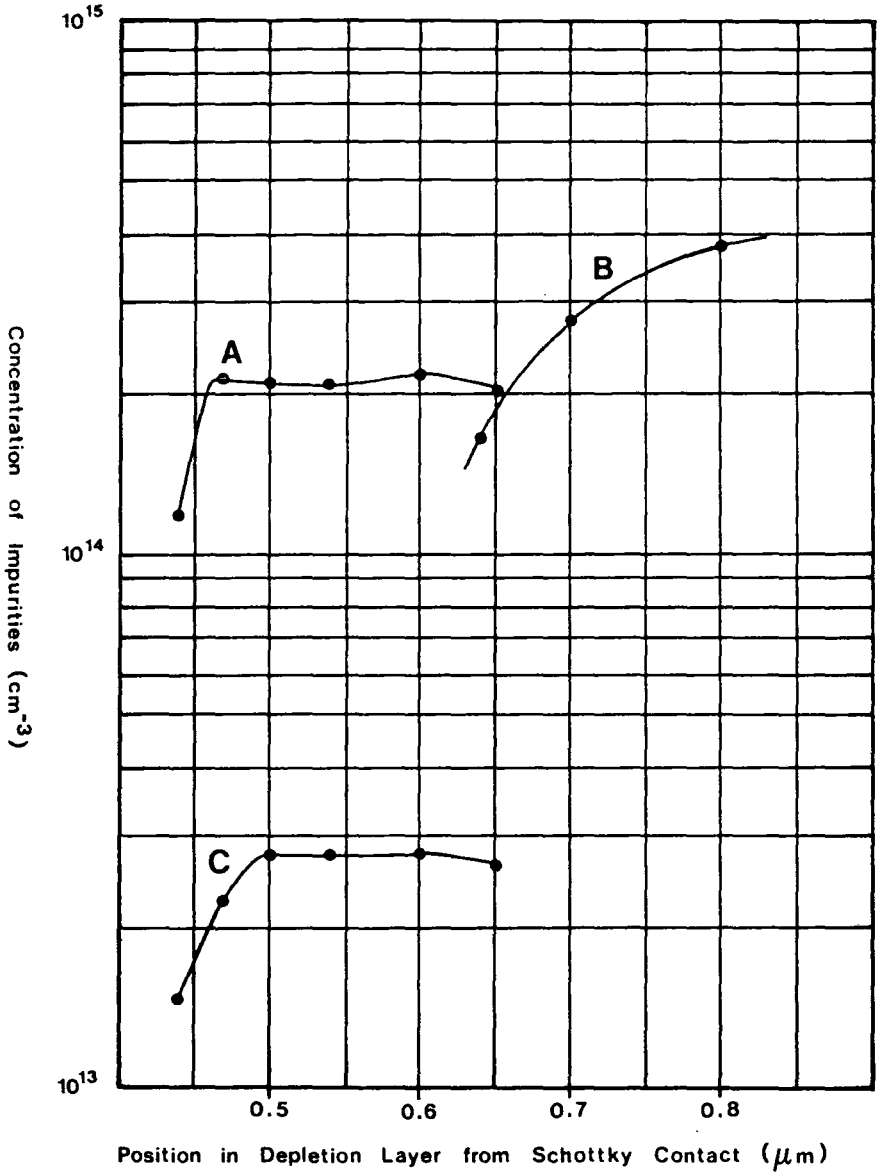

Concentration profiles of the three electron traps observed in sample DG388SB. A−0.23 eV traps, B−0.62 eV traps, C−0.14 eV traps.

FIGURE 5.4/6

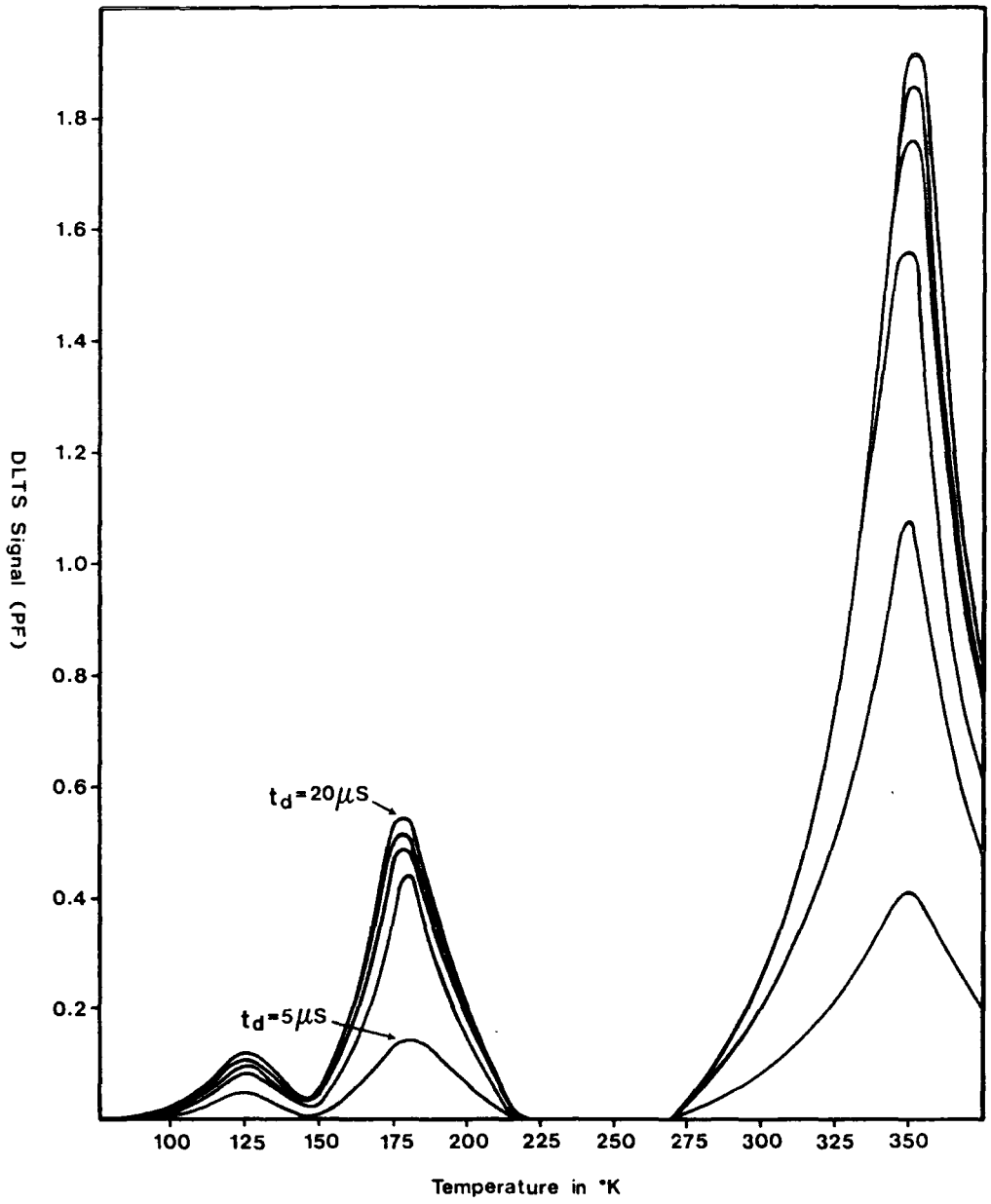

DLTS spectra obtained from sample DG388SB when the filling pulse duration was varied between 5μS and 20μS with all other biassing conditions constant. Vrr = 0v, Vqr = −2v, rate window = 7.2 mS.

FIGURE 5.4/7

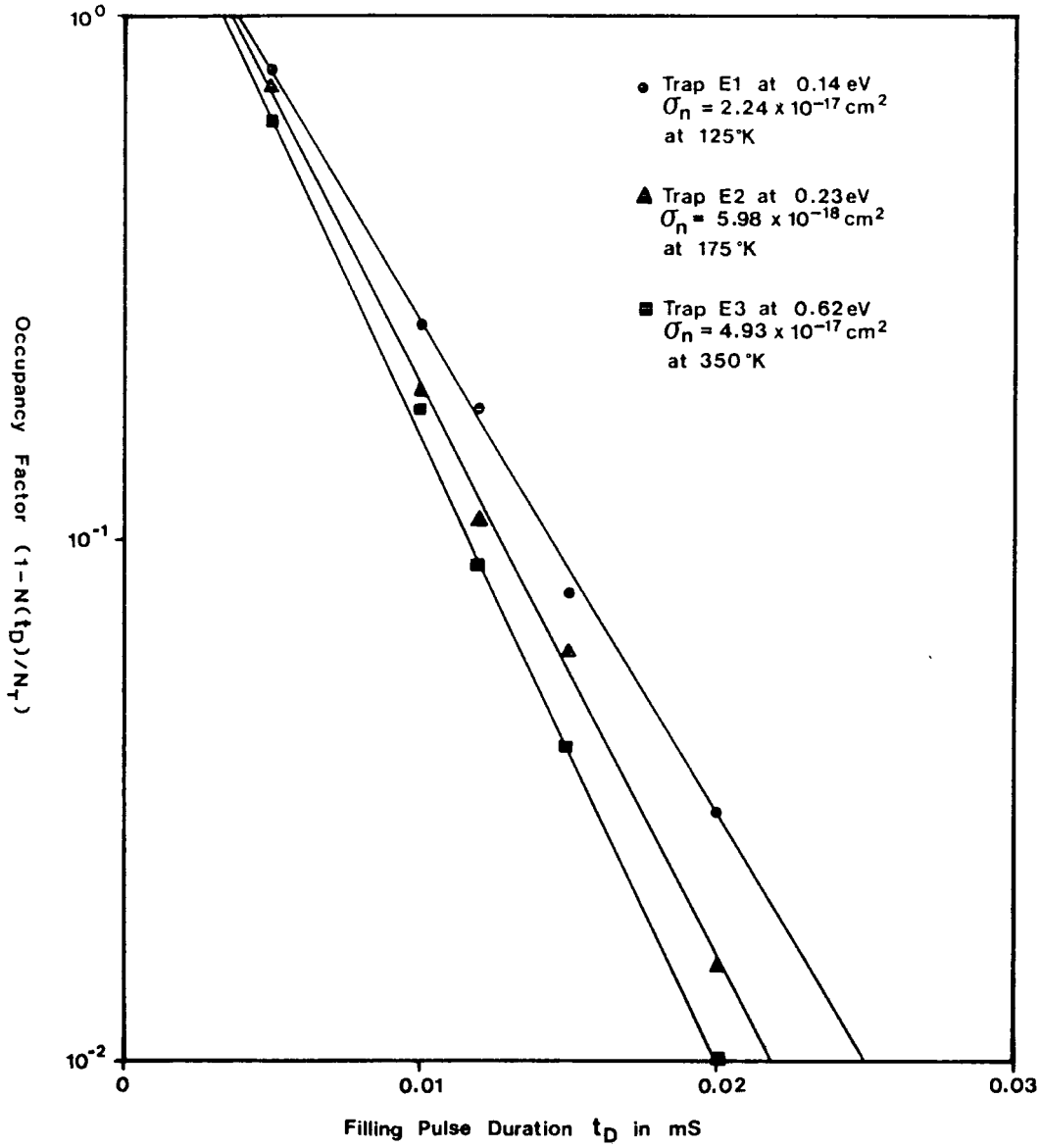

Occupancy factor $(1-N(t_D)/N_T)$ as a function of filling pulse duration, t_D. Below 10^{-2} there are >99% of traps filled, which is ~100% due to the sensitivity of the apparatus. Occupancy of 10^0 implies that all traps N_T, are empty.

FIGURE 5.4/8

TRAP IDENTITY	E1	E2	E3
Characteristic temperature T_C (°K)	125	175	350
Capture rate at T_C $C_n(T_C)$ (cm^3s^{-1})	4.24×10^{-12}	1.33×10^{-12}	1.55×10^{-11}
Capture cross-section at T_C, $\sigma_n(T_C)$ (cm^2)	2.24×10^{-17}	5.98×10^{-18}	4.93×10^{-17}
Capture cross-section at $T=\infty$, σ_∞ (cm^2)	7.48×10^{-18}	3.65×10^{-17}	2.65×10^{-13}
Trap concentration N_T, (cm^{-3})	2.74×10^{13}	2.14×10^{14}	3.8×10^{14}
Thermal activation energy, E_T (eV)	0.14	0.23	0.62

SUMMARY TABLE SHOWING ALL TRAP PARAMETERS MEASURED FOR THE THREE TRAPS FOUND IN SAMPLE DG388SB

FIGURE 5.4/9

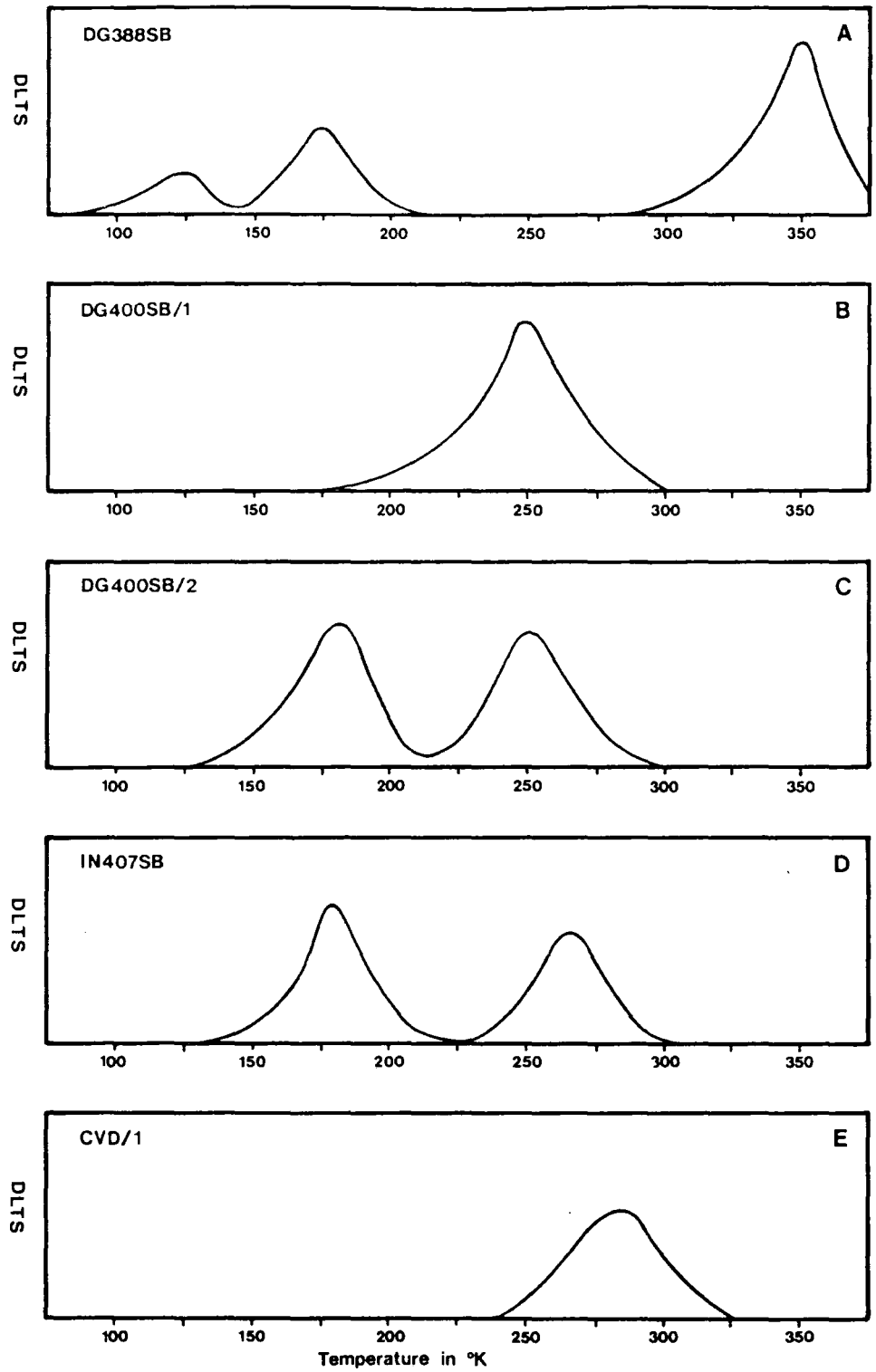

DLTS spectra obtained from all samples studied, showing the typical peak temperatures and the number of traps

FIGURE 5.4/10

SAMPLE	TRAP DEPTH (eV)	σ_∞ (cm^2)	σ_m (cm^2)	COMMENTS
DG388SB	0.14	7.48×10^{-18}	2.24×10^{-17}	TRAP E1
	0.23	3.65×10^{-17}	5.98×10^{-18}	TRAP E2
	0.62	2.65×10^{-13}	4.93×10^{-17}	TRAP E3
DG400SB/1	0.44	8.3×10^{-17}		
DG400SB/2	0.30	6.2×10^{-16}		
	0.41	8.6×10^{-14}		
IN407SB	0.24	2.4×10^{-16}		INDIUM-DOPED
	0.43	6.7×10^{-17}		
CVD/1	0.27	6.6×10^{-20}		CVD MATERIAL

SUMMARY OF TRAP DEPTHS AND CAPTURE CROSS-SECTIONS OBTAINED FOR ALL SAMPLES STUDIED

FIGURE 5.4/11

5.413 Capacitance transient measurements as a function of bias

Interesting results were obtained from the examination of sample DG388SB when the value for the peak voltage of the reduced reverse bias pulse was varied systematically while the quiescent reverse bias level was kept constant at a setting of -9.6 volts. The results obtained at 77°K are shown in Figure 5.4/12. As the reduced reverse bias was increased from -6V to -3V, the transient observed was positive. In this régime it seems that the transient was caused by traps filling with electrons as the bias returned to its quiescent value of -9.6 volts. As the reduced reverse bias pulse was increased past -2.5 volts however, the capacitance transient became negative indicating that traps were emptying of electrons as the bias was returned to the quiescent condition. The negative transient became larger in magnitude as the bias pulse was increased, reaching a maximum at a reduced bias-level of -1.6 volts. As the reduced bias was increased further, the transient became very distorted and decreased in magnitude. The positive capacitance transient was not observed for quiescent reverse bias settings greater (more positive) than -9.2 volts at 77°K, indicating that the effect was subject to a threshold.

When the same experiment was performed with a quiescent reverse bias of -9.0 volts a positive transient was not observed. The time constants seen at each point of the curve in Figure 5.4/12 are shown plotted against reduced reverse bias voltage in Figure 5.4/13. A marked change is observed from a short time constant of about 500 μS, associated with the positive transient, to a long time constant of approximately 20 mS, associated with the negative transient. Clearly the process which gave rise to the positive signal is much faster than that which caused the negative one. The explanation of these results is not altogether obvious. Judging by the time constant of the positive transient, it is caused by an electron capture process, which would be expected to occur very quickly [13]. This is to be contrasted with the 20 mS decay observed for the negative transient, which must be caused by electron emission. There is strong evidence to suggest that samples prepared by the methods described (Section 3.232) are MIS structures with associate surface states [10]. The band structure would hence be similar to that shown in Figure 5.4/14.

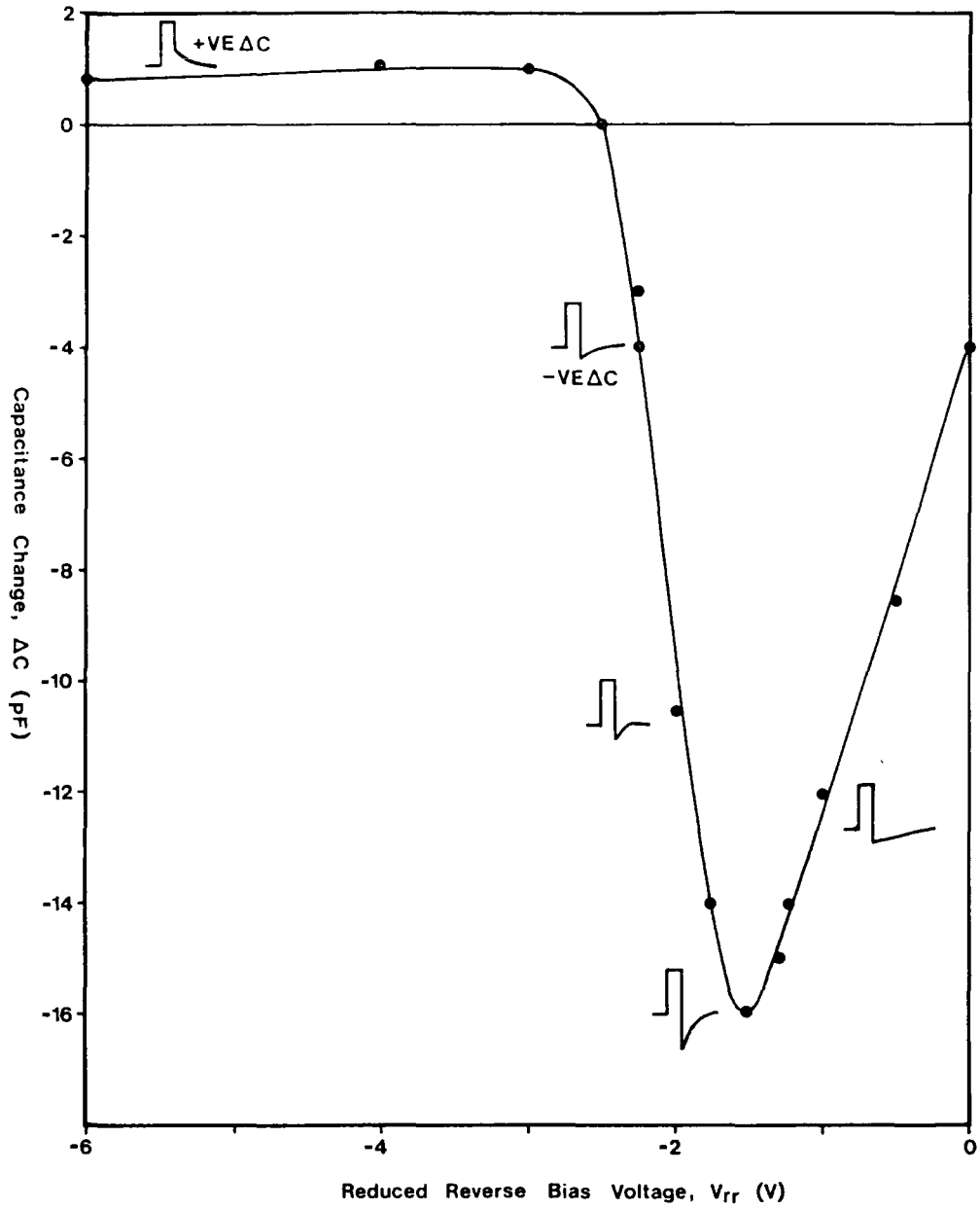

Variation of capacitance change, ΔC, as a function of bias voltage, V_{rr}, for Schottky diode sample DG388SB at 77°K.

FIGURE 5.4/12

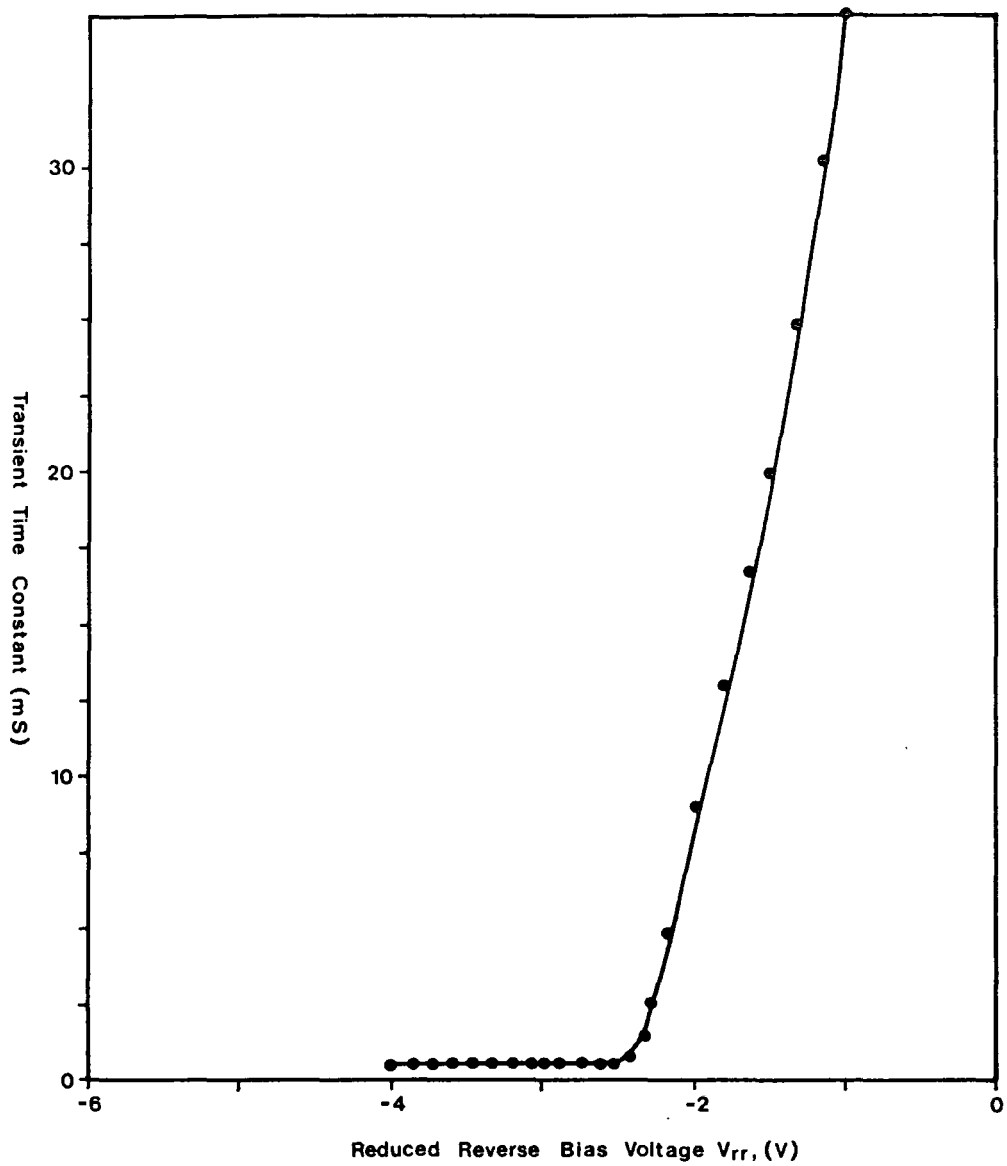

Variation of the transient time constant with reduced reverse bias for DG388SB at 77°K

FIGURE 5.4/13

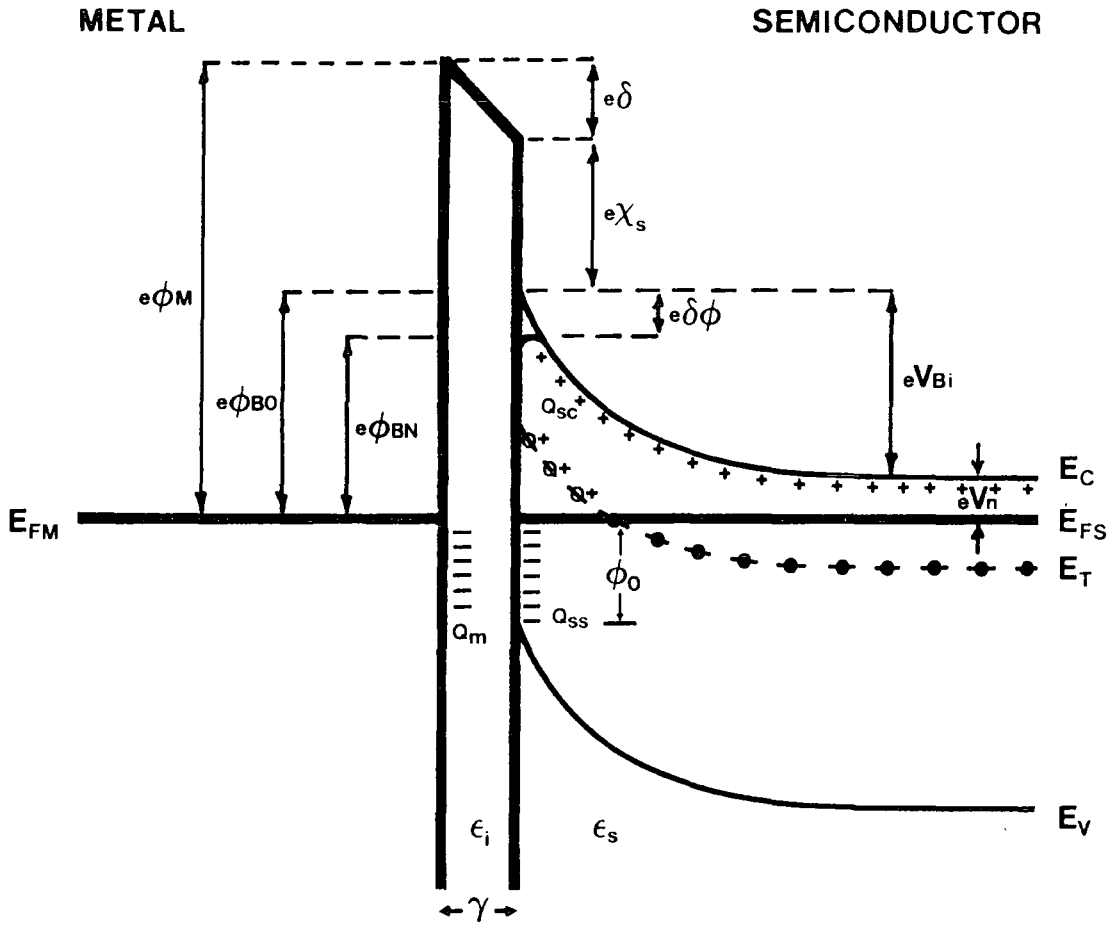

ϕ_M = Metal work function
ϕ_{BN} = Barrier height including Schottky lowering term
ϕ_{B0} = Uncorrected barrier height
ϕ_0 = Surface energy
$\delta\phi$ = Image force lowering
δ = Interfacial layer potential drop
χ_S = Semiconductor electron affinity
V_{Bi} = Diffusion potential
γ = Interfacial layer thickness
Q_{sc} = Semiconductor space charge density
Q_{ss} = Surface-state charge density
Q_m = Surface charge induced on the metal
ϵ_i = Permittivity of insulating interfacial layer
ϵ_s = Permittivity of semiconductor
E_T = Deep levels in the bulk material

FIGURE 5.4 / 14

If it is assumed that the sample under discussion was an MIS device, the results above might be explained in terms of the behaviour of surface state occupancies at the metal-semiconductor interface. The positive transient could be produced by surface states which were persuaded to empty as the reverse bias voltage was pulsed to between -6 and -3 volts. These levels would then fill with electrons again as the bias returned to its quiescent value. This implies that the surface states were acting like hole traps, and that holes were being captured during the bias pulse. Usually this phenomenon is only observed when the capacitance of a p-n junction is monitored just after an injection pulse (Section 5.22) where both holes and electrons are injected into the valence and conduction bands of the material at the junction. In the MIS structure a similar effect might be produced at the surface if the device was biassed into inversion, causing a build-up of holes at the metal-semiconductor interface. As the bias was then reduced, some of these holes might be captured by surface states and the positive transient would then be observed as the bias was returned to its quiescent value. The threshold effect whereby no positive transient was seen for quiescent reverse bias voltages greater than -9.2 volts may indicate that heavy inversion at the surface of the device began at that value. When a p-n junction is studied under injection pulse conditions, the capacitance transients observed are produced by a combination of both the majority and the minority carrier release mechanims. In the results shown in Figure 5.4/12, the change from a positive to a negative transient at the reduced reverse bias voltage of -2.5 volts indicates that levels which behaved as electron traps began to dominate the transient at this point.

5.42 CVD zinc selenide

The C^{-2}-V characteristic recorded for diode CVD/1 was found to be reasonably linear (Figure 5.4/15), giving a donor concentration of 1.6×10^{15} cm^{-3} and a calculated barrier height of 1.92 volts. The ideality factor was found to be very large, at 2.56, which is thought to be due to the proliferation of electrically active grain boundaries within the material (Section 6.34).

In order to supplement the data obtained on the deep levels in this

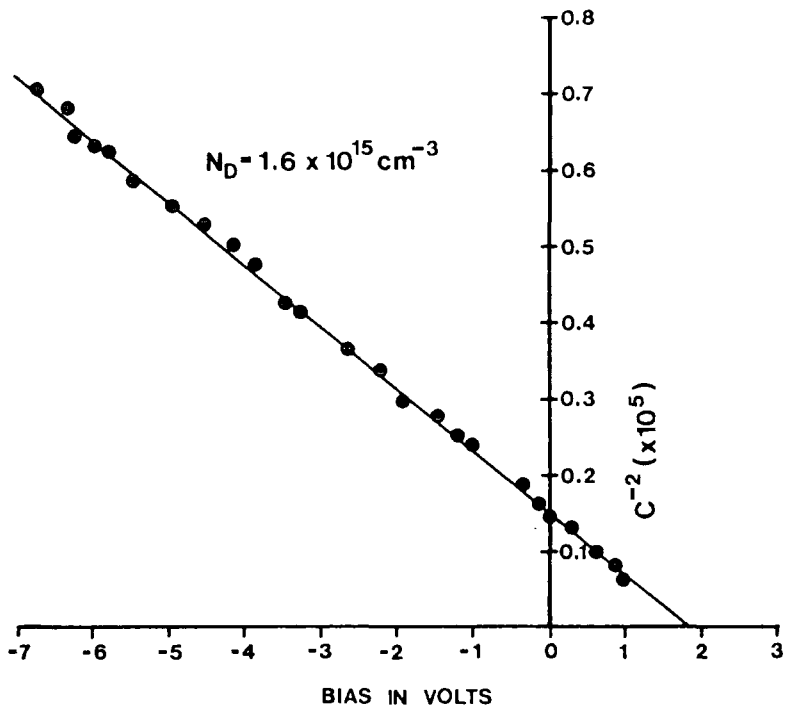

C^{-2} vs V plot for diode CVD/1 at room temperature

FIGURE 5.4/15

material, several DLTS scans were performed (Figure 5.4/16) and analysed. Only one peak was observed, at a temperature of 284°K (60.8 S^{-1} rate window). The sign of the capacitance transients indicated that the defect was an electron trap. The Arrhenius plot resulting from the data gathered from performing scans with the rate window varying from 22.1 S^{-1} to 60.8 S^{-1} gave a trap depth of 0.27 eV below the conduction band edge (Figure 5.4/17).

Using the same method as before, the concentration profile of the electron traps at 0.27 eV was plotted out as a function of the calculated position within the depletion region. These results are shown in Figure 5.4/18.

5.5 DISCUSSION

Schottky barrier diode samples of ZnSe were examined by studying the capacitance transients produced when the biassing of the junction was repeatedly pulsed. Using the technique of DLTS [1], the thermal ionisation energies of the deep levels observed in each sample were accurately determined. By the application of back-extrapolation to the Arrhenius plot associated with each trap, the capture cross-sections at infinite temperature were also calculated.

The results obtained from three samples of Durham-grown ZnSe were presented. These devices were fabricated from material produced in three different growth runs. Boule 388 was suspected to be heavily contaminated with copper. Material from growth run 400 however, was thought to be relatively copper-free due to the success of the research and development work conducted by the crystal growth laboratory to isolate the cause of the contamination. The third boule, number 407, was intentionally doped with indium to a level of about 13 ppm [14]. Only one sample of CVD ZnSe was examined using DLTS due to the difficulties described earlier (Section 5.4).

The DLTS technique was adopted as a means of supplementing the large amount of work undertaken to determine the thermal ionisation energies of

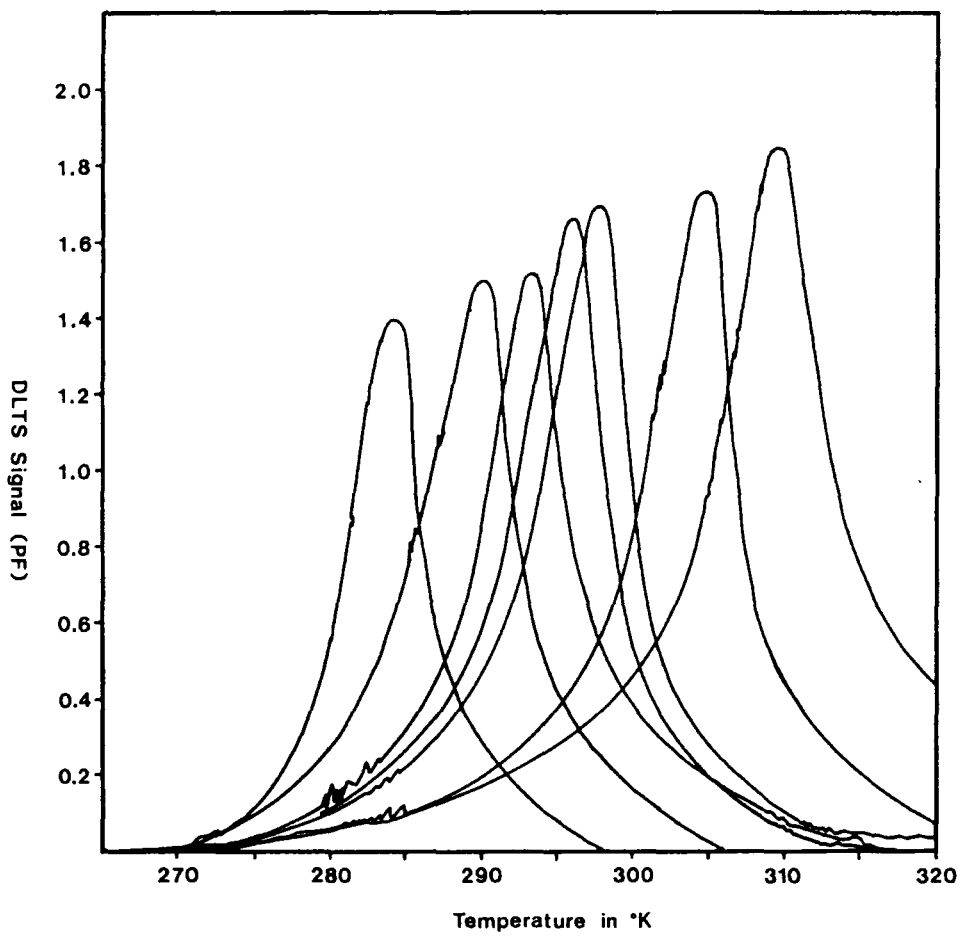

DLTS spectra obtained from sample CVD/1 using rate windows between 22.1 - 60.8mS.

FIGURE 5.4/16

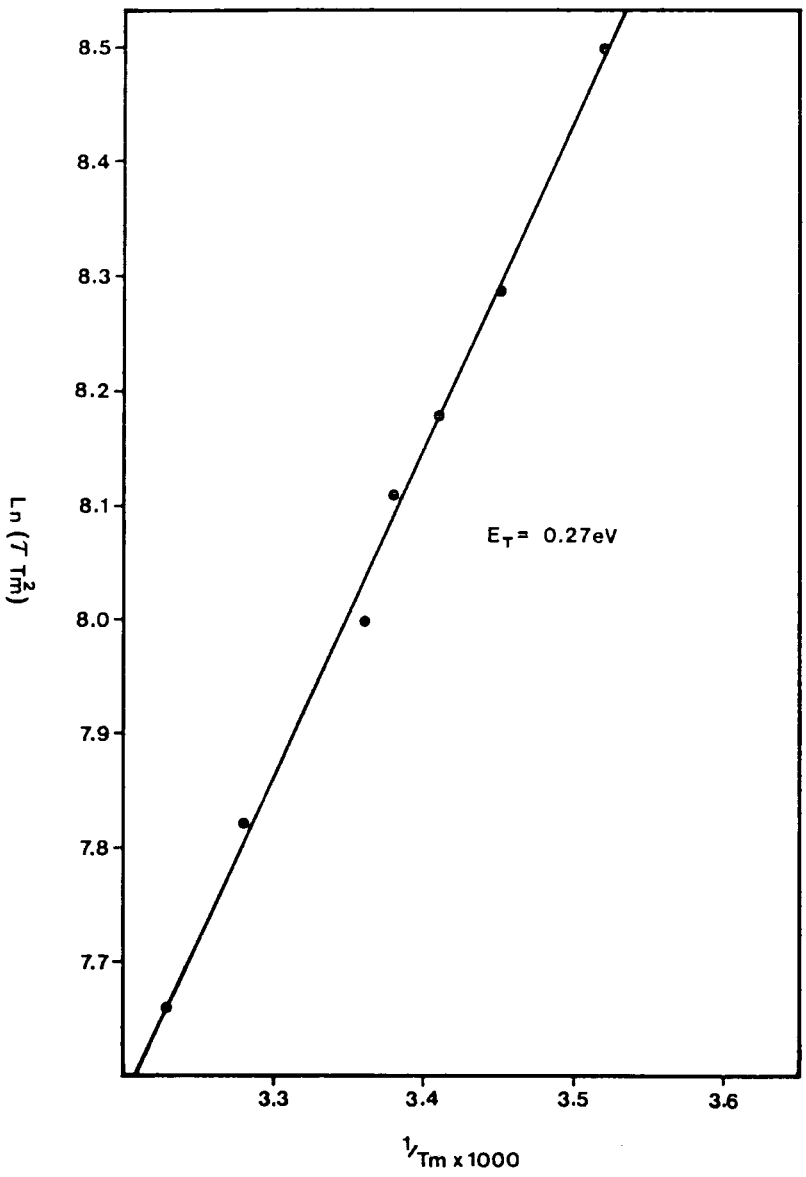

Arrhenius plot of $Ln(\tau T_m^2)$ vs $^1/_{Tm}$ for sample CVD/1. Trap depth $E_T = 0.27eV$

FIGURE 5.4/17

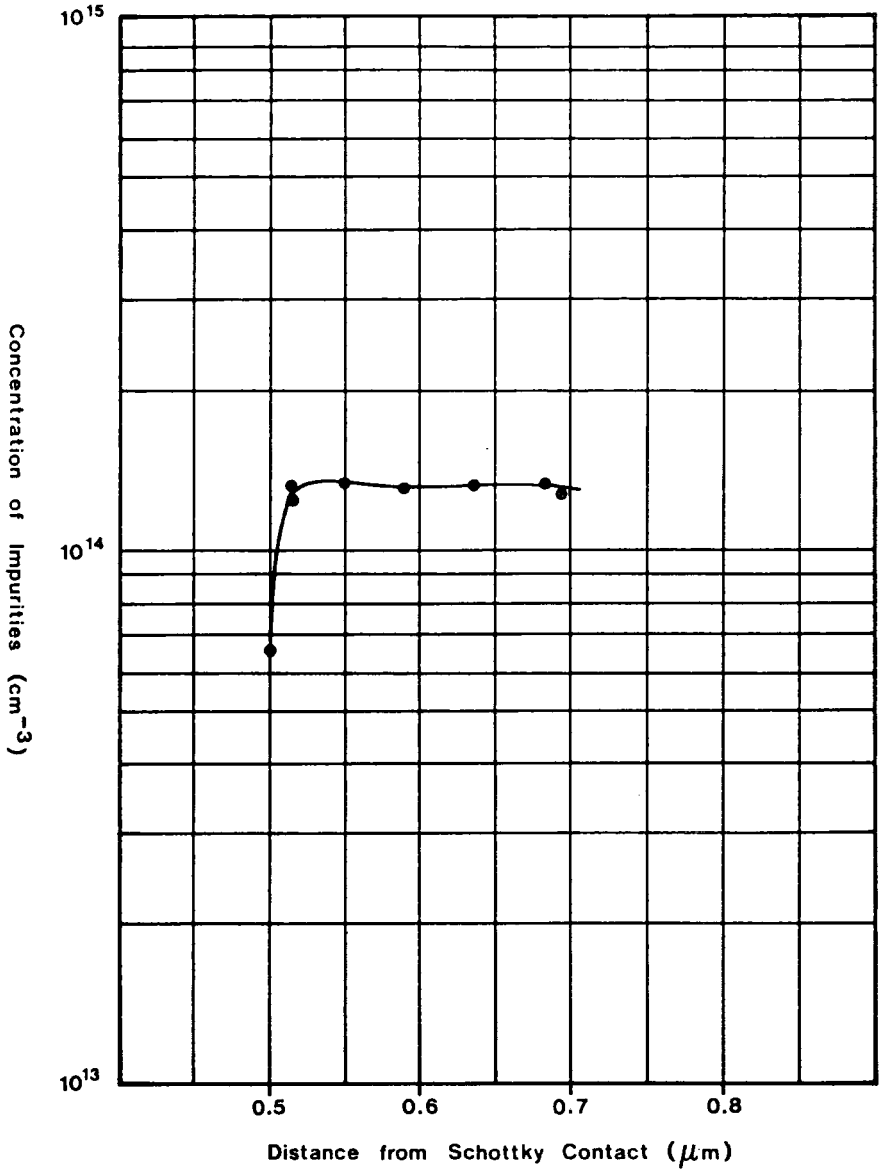

Concentration profile of the single electron trap at 0.27eV observed in sample CVD/1.

FIGURE 5.4/18

trapping levels in ZnSe by using TSC and TSL (Chapter 4). At this point it is therefore appropriate to consider the results obtained independently by these methods. The comparison is drawn up as a table in Figure 5.5/1. TSC and TSL measurements made to the Durham-grown 388 samples (suspected to be Cu-doped) showed the presence of five trapping levels which were analysed to give thermal ionisation energies of 0.16 eV, 0.23 eV, 0.26 eV, 0.45 eV and ≈0.60 eV. TSC and TSL work, undertaken concurrently to the measurements described here, revealed a well-defined trap with an ionisation energy of 0.13 eV in ZnSe:Ga and ZnSe:In [14]. This agrees well with the value of 0.14 eV for the electron trap discovered by DLTS in the Durham-grown material, indicating that the level may be due to a native defect or to an impurity incorporated unintentionally in all the growth runs. In the literature Kosai [15] reported an electron trap at 0.17 eV and Ido et al [4.66] found donors at 0.14 eV and 0.15 eV in LPE-grown ZnSe layers. No suggestions as to the identity of the impurity or defect concerned were put forward in either case. It is interesting to note that TSC and TSL detected a level at about 0.16 eV in both the 388 and the 400 samples, whereas DLTS only shows a trap of 0.14 eV in boule 388. This may indicate that the 0.17 eV level found by TSC/TSL in boule 400 was an acceptor, and hence a completely different impurity/defect from the 0.16 eV levels observed in boule 388. Hole traps at 0.16 eV above the valence band have been reported by Leigh and Wessels [4.68] in VPE-grown ZnSe layers recently. The DLTS analysis of the 0.14 eV trap in boule 388 showed that the impurity/defect was present in the concentration of about 3×10^{13} cm^{-3}.

Excellent agreement between the different methods was obtained on 388 samples for traps at 0.23 eV. Recently Besomi and Wessels [16] reported a level at 0.24 eV, although they associated this with the presence of the dopant In. No other references to an electron trap of this ionisation energy in undoped ZnSe have been found.

The DLTS analysis of samples DG400SB/1 and DG400SB/2 showed that each contained electron traps between 0.41 and 0.44 eV below the conduction band edge. A similar level, at 0.43 eV, was detected in diode IN407SB, agreeing well with a value of 0.42 eV obtained independently [14]. TSC/TSL measurements revealed a trap at 0.43-0.45 eV in samples cut from

METHOD	MATERIAL	SAMPLE	TRAP DEPTHS (in eV)						NO. OF PEAKS
			1	2	3	4	5	6	
DLTS	CVD	CVD/1			0.27				1
	DURHAM	DG388SB	0.14	0.23			0.62		3
		DG400SB/1				0.44			1
		DG400SB/2			0.31	0.41			2
		IN407SB		0.24		0.43			2
TSCL	CVD	CVD/1	0.11		0.28	?			3
		CVD/2		0.20		?	?		3
		DG388	0.16	0.23	0.26	0.45	0.60		5
		DG400	0.17		0.27	0.43	?		4
		DG407[13]				0.42			-
		DG345SB			0.30		0.60	0.70	3

(? Denotes that a trap was observed, but could not be analysed to give a trap depth value)

SUMMARY OF THERMAL IONISATION ENERGIES MEASURED BY THE METHODS OF DLTS AND TSC/TSL ON CVD AND DURHAM-GROWN ZnSe

FIGURE 5.5/1

boules 388 and 400. This confirms the results obtained by DLTS on the 400 material, but the failure of this technique to detect the same levels in the 388 material is confusing, since the magnitude of the TSC/TSL signal seemed to indicate that the impurity or defect concerned was present in quite a large concentration. The only reference to a comparable level is provided by Besomi and Wessels [16] who reported an electron trap at 0.42 eV in a concentration of 5×10^{12} cm^{-2}.

An electron trap at an energy of 0.31 eV below the edge of the conduction band was detected in sample DG400SB/2 using DLTS. TSC/TSL analysis carried out on the same material yielded a possible match at 0.27 eV. Shirakawa and Kukimoto [19] associated a trap at 0.33 eV with the selenium vacancy V_{Se}. More recently Verity et al [17] reported electron traps at 0.34 eV in ZnSe annealed in liquid zinc, which they suggested may be due to complex centres involving a native defect, such as V_{Se} or Zn_i (zinc interstitial), and a residual impurity. They observed only a very slight drop in the measured concentration of 0.34 eV levels as the liquid zinc annealing procedure was prolonged. The number of V_{Se} and Zn_i defects is expected to increase in ZnSe with prolonged annealing in liquid zinc, whereas the concentration of residual impurities should decrease. Besomi and Wessels [18] ascribed levels at 0.30-0.35 eV below the conduction band edge to Cl, Al or In impurities. More recently Leigh and Wessels [4.68] found two electron traps in VPE-grown ZnSe layers at 0.30 eV and 0.35 eV, and Christianson and Wessels [4.67] reported a level 0.33 eV below the conduction band edge which they attributed to Se divacancies, since the concentration of the levels was found to increase as the square of the vapour phase Zn/Se ratio.

DLTS measurements done on sample DG388SB revealed the presence of an electron trap at 0.62 eV. The profiling study (Figure 5.4/6) showed that the bulk concentration of this trap population was 3.8×10^{14} cm^{-3}. TSC/TSL studies on material from the same boule suggest that a trap population was present with an ionisation energy of about 0.60 eV. The analysis of these results was difficult because the emptying of the traps occurred against the background of a steeply rising dark current. Kosai [15] used a variety of methods to characterise LPE-grown ZnSe, and found an electron trap at 0.64 eV. Qidwai [4.70] reported an acceptor at

0.59 eV, and Nyaga et al [4.71] have linked an identical level with (V_{Zn}-impurity)'.

In addition to the extensive analysis of all of the samples by DLTS to attempt to clarify the values of the ionisation energies of the deep levels found in ZnSe, a detailed study of sample DG388SB revealed that the device could probably be described as an MIS structure (Figure 5.4/14). Interface states were thought to be present due to the presence of kinks in the C^{-2} versus V plots, which shifted with temperature in the manner described by Simmons and Wei [20]. The local changes in the slope of these plots is thought to be caused by the transition from the non-steady-state change of interface state occupancy during a bias ramp, to the steady state as the Fermi level passes the point in the energy-gap which corresponds to the edge of the trap distribution. These kinks would be expected to shfit to more positive voltages (for an n-type semiconductor), as the Fermi level moves to higher energies. This is exactly what is observed with diode DG388SB in Figure 5.4/1, where the kink occurred at -5.5 volts at 295°K and -0.8 volts at 77°K. the absence of observable hysteresis is probably explained by the slow sweep rate (approximately 0.1 vs^{-1}). This would mean that the emptying and filling of the surface states was very close to being in equilibrium with the voltage ramp. It is not thought that any of the peaks observed in the DLTS analysis of the sample (Figure 5.4/7) are due to surface states. If this was so the concentration profiles would be expected to show a sharp decrease as the depletion region was widened [21]. This would be observed as a decrease in the peak magnitude as the bias pulse amplitude was increased. As can be seen from Figure 5.4/7, the opposite effect is observed for the three traps, indicating that they are probably discrete levels in the bulk material.

The fabrication of Schottky barrier diodes using CVD material is extremely difficult owing to the nature of the electrically active grain structure (Chapter 6). Using the method outlined previously (Section 5.4), a device was made and several DLTS runs were completed before the barrier degraded. The C^{-2}-V plot suggested that the concentration of shallow donors was 1.6×10^{14} cm^{-3} and the barrier height was 1.95 eV. A single DLTS peak was observed, associated with an electron trap calculated to be 0.27 eV

below the condution band edge. The measured trap concentration was 1.36×10^{14} cm^{-3}. The ionisation energy obtained by the DLTS measurements agrees well with the value of 0.28 eV provided by TSC/TSL. The latter methods also revealed a trap at 0.10 eV. The 0.27-0.28 eV trap is thought to be due to a lattice defect such as a vacancy or vacancy-impurity complex [19,22], whereas the 0.10 eV level has been linked with Na, which acts as an acceptor [19,23,24,4.66]. If this is the case DLTS measurements would not reveal the presence of the minority carrier trap for the reasons discussed earlier (5.212). The level at 0.27-0.28 eV in CVD ZnSe can be linked with the level at 0.31 eV found in sample DG400SB/2, for which a similar vacancy or vacancy-impurity complex is postulated.

The difference between the samples DG400SB/1 and DG400SB/2 is interesting, since both dice were cut from the same boule. The absence of the trap at 0.31 eV in sample DG400SB/1 could be explained by a non-uniform impurity distribution. Both samples contained electron traps at 0.41-0.44 eV in approximately equal concentrations.

CHAPTER FIVE - REFERENCES

1 D V Lang, J Appl Phys, 45, (7), (1974), 3023

2 G L Miller, D V Lang and L C Kimmerling, Ann Rev Mater Sci, 7, (1977) 377

3 R Williams, J Appl Phys, 37, (1966), 3411

4 Y Furukawa and Y Ishibashi, Jap J Appl Phys, 5, (1966), 837

5 Y Furukawa and Y Ishibashi, Jap J Appl Phys, 6, (1967), 503

6 J Hildebrand and R D Gold, RCA Rev, 21, (1960), 245

7 P J Baxandall, D J Colliver, A F Fray, J Sci Instrum, 4, (1971), 213

8 J A Copeland, IEEE Trans, ED-16, (1969), 445

9 G L Miller, IEEE Trans, ED-19, (1972), 1103

10 M E Ozsan and J Woods, Sol State Electron, 20, (1977), 343

11 M E Ozsan and J Woods, Sol State Electron, 18, (1975), 519

12 D V Lang, H J Grimmeiss, E Meijer and M Jaros, Phys Rev, B22, (1980), 3917

13 C T Sah and H S Fu, Phys State Solidi (a), 14, (1972), 59

14 B Vincent, PhD Thesis, University of Durham, (1980)

15 K Kosai, J Appl Phys, 53, (2), (1982), 1018

16 P Besomi and B W Wessels, J Appl Phys, 53, (4), (1982), 3076

17 D Verity, F J Bryant, C G Scott and D Shaw, J Cryst Growth, 59, (1982), 232

18 P Besomi and B W Wessels, Electron Letters, 16 (1980), 794

19 Y Shirakawa and H Kukimoto, J Appl Phys, 51, (1980), 5859

20 J G Simmons and L S Wei, Sol State Electron, 16, (1973), 53

21 M Housin, M Fialin, G Bastide, G Sagnes and M Rouzeyre, J Cryst Growth, 59, (1982), 246

22 D Verity, F J Bryant, J J Davies, J E Nicholls, C G Scott and D Shaw, J Phys C: Solid State Physics, 15, (1982), 5497

23 H Tews, H Venghans and P J Dean, Phys Rev B, 19, (1979), 5178

24 K A Christianson and B W Wessels, J. Luminescence, 31-32, (1984), 433

CONTENTS

6 SEM STUDIES AND LASER ABSORPTION MEASUREMENTS

6.1 INTRODUCTION

6.2 SEM INVESTIGATION

6.21 Theory
6.22 Experimental results

6.3 LASER ABSORPTION MEASUREMENTS

6.31 Theory

6.311 Optical absorption processes in IR-transmitting materials
6.312 Analysis of laser calorimetric data

6.32 Apparatus and experimental procedure

6.33 Results

6.34 Discussion

6 SEM STUDIES AND LASER ABSORPTION MEASUREMENTS

6.1 INTRODUCTION

During recent years infra-red physics technology has progressed significantly. In particular there has been considerable development of materials suitable for use in the optics of IR systems. In a field once limited by the inadequate performance of small, impure and delicate crystals, chemical vapour deposited (CVD) ZnSe and ZnS have provided answers to many of the problems encountered earlier.

The present work constituted a major investigation carried out on several typical CVD ZnSe samples. Studies were conducted to learn more about the behaviour of active impurities incorporated in the material and their influence on macroscopic properties, such as transparency [1].

It has been suggested previously [2] that grain boundaries present in crystals can act as 'sinks' for impurities. The CVD ZnSe studied in this project was examined in a scanning electron microscope (SEM) using both the Electron-Beam Induced Current (EBIC), and the Cathodoluminescence (CL) modes. The grain boundaries were discovered to be electrically active and photosensitive. In addition they were shown to suppress both the blue and the copper-red components of the cathodoluminescence emission.

Additional information was obtained in the form of infra-red absorption measurements made at the GEC Hirst Research Centre using the technique of laser absorption calorimetry.

6.2 SEM INVESTIGATION

Samples were examined in the Cambridge S600 scanning electron microscope using three different modes of operation. Surface morphology was studied using the instrument in the secondary electron emission mode. A secondary emission micrograph of a typical CVD ZnSe sample is shown in Figure 6.2/1. The SEM was set up to do cathodoluminescence measurements by replacing the scintillator with a light-pipe. The photomultiplier used in this

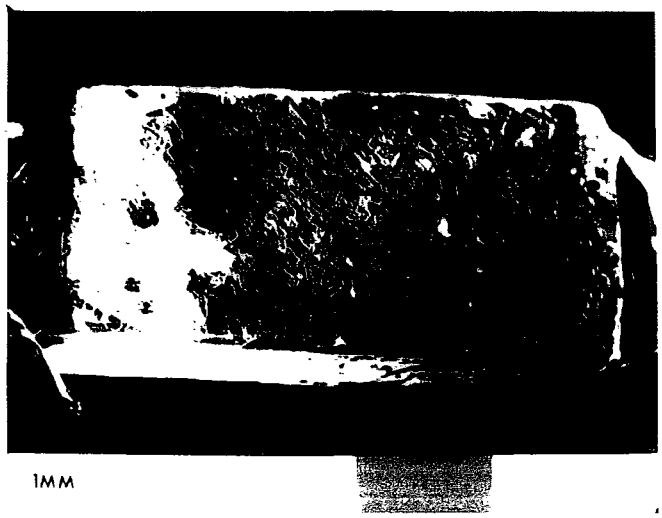

A CVD sample viewed in secondary emission mode

FIGURE 6.2/1

application was an EMI 9924B, with a rubidium-caesium photocathode, limiting the system to measurements of the blue edge-emission band at 460 nm only. Access to a similar SEM fitted with a wavelength-dispersive detector system was provided by the GEC Hirst Research Centre, however, enabling the copper-red component to be studied separately. Finally, bar samples of CVD ZnSe, prepared with two ohmic contacts as described in Section 3.42, were connected as shown in diagram 6.2/2. The biassing arrangement allowed any electrically active defects to be examined in the EBIC mode as a function of bias voltage. The contrasts observed in most samples were caused by electrically active regions within the material. Their extensive nature is shown clearly in Figure 6.2/3, which is a photograph of the same sample as in Figure 6.2/1, in EBIC mode. It has been noted previously [2] that these regions always coincide with the grain boundaries, when the sample is viewed in secondary emission mode for comparison. A qualitative explanation of how this might arise is presented in the following section.

6.21 Theory

Single crystals of ZnSe:In and ZnSe:Ga were the first subjects of study in the EBIC mode of the SEM at the Department of Applied Physics and Electronics, University of Durham. These were closely followed by the CVD ZnSe samples studied in this project. Soon after the initial observations had been made, a qualitative theory was developed [2] to explain the EBIC micrographs in terms of electrically active grain boundaries present in both the CVD samples and those grown at Durham.

The EBIC contrast at grain boundaries, such as that shown in Figure 6.2/3, occurs because of the potential barrier formed there. The model proposed to explain this effect can be understood by reference to the diagrams in Figure 6.2/4. Grain boundaries are thought to act as 'sinks' for impurities, which are trapped there as they migrate through the material. This may, for example, occur during some form of heat treatment such as the annealing in molten zinc performed as described in Section 3.323.

All samples which exhibited EBIC contrast had previously been annealed in this way, in order to decrease their resistivities. Impurities segregated to the grain boundaries in such a manner could behave as acceptor states and act to produce a sheet of negative charge there. To redress the

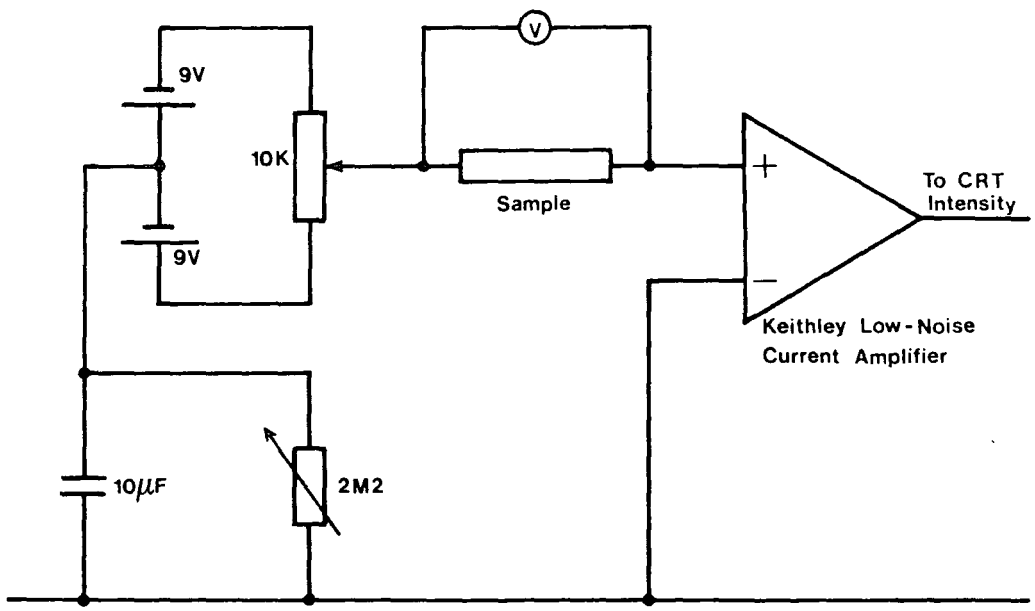

Biassing and EBIC signal detection circuit for high impedance samples.

FIGURE 6.2 / 2

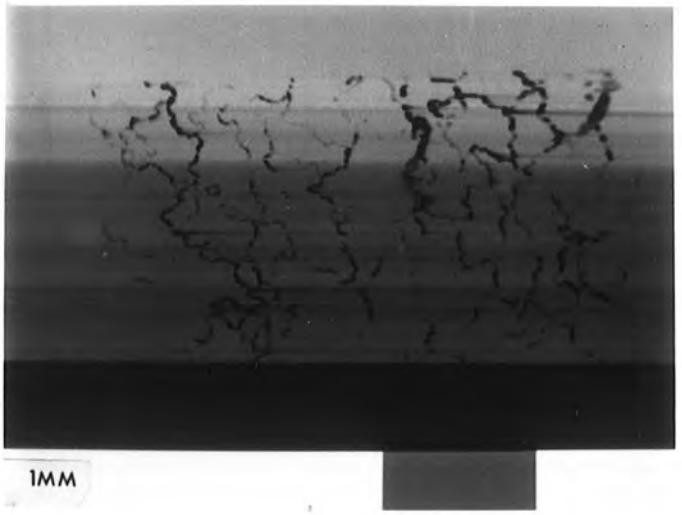

The same sample as in 6.2/1 viewed in EBIC mode

FIGURE 6.2/3

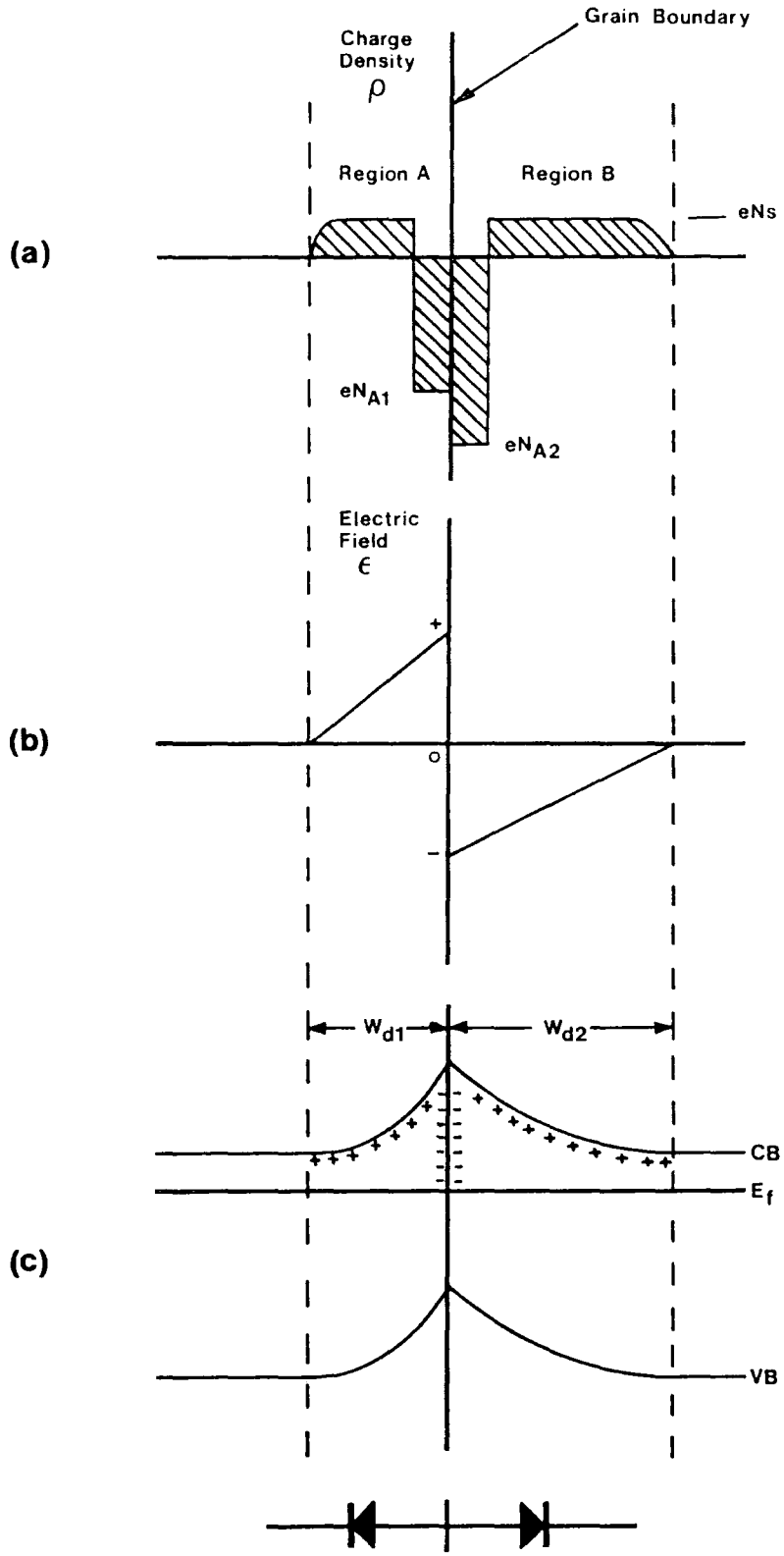

Diagramatic representation of the electrical characteristics of a grain boundary in CVD ZnSe

FIGURE 6.2/4

charge balance the surrounding area would become depleted of electrons, leaving a positive 'sea' of static charge behind. The resulting potential barrier is depicted in Figure 6.2/4(c), where the conduction band and valence band are both bent upwards in n-type ZnSe. The contrast observed on the SEM display can be understood by considering Figure 6.2/4(b) which shows the electric fields present close to the boundary. An electron beam sweeping across from left to right would first encounter depletion region A and bombardment-induced electron-hole pairs would be separated by the internal field before they could recombine. Electrons would be driven towards the contact to the left of the picture, and holes would recombine at the grain boundary. The cathodoluminescence images in Figures 6.2/17 (a) and (b) demonstrate that such recombination centres exist at the grain boundaries by showing that all emission bands in the sample are quenched there. The resulting beam-induced current would be registered on the SEM screen as either a light or dark area, depending upon which way the sample was connected in the circuit shown in Figure 6.2/2. Once the electron beam had crossed the grain boundary into region B, electron-hole pairs created by it would be separated as they were previously. However, because the internal field present there has the opposite directional sense to its counterpart in region A, electrons this time would be driven to the right-hand contact and holes would recombine at the grain boundary as before. The alteration in the beam-induced current direction would therefore induce a contrast on the SEM screen at the grain boundary.

The seven band diagrams in Figure 6.2/5 show band-bending under various bias conditions for both symmetric and asymmetric grain boundaries. Assuming that a flow of electrons to the left-hand contact would give a white area on the display, the sample under zero bias in Figure 6.2/5(a) would appear as a white/black contrasting line. An example of this is shown in the micrograph reproduced in Figure 6.2/9. Applying a negative bias on the left-hand contact results in a modification of the band-bending as shown in 6.2/5(b). In this instance the boundary would appear as a single, thick black line on the display screen. This is exactly what is seen in Figure 6.2/10. Reversing the bias would produce the complementary solid white lines, as exemplified in Figure 6.2/11.

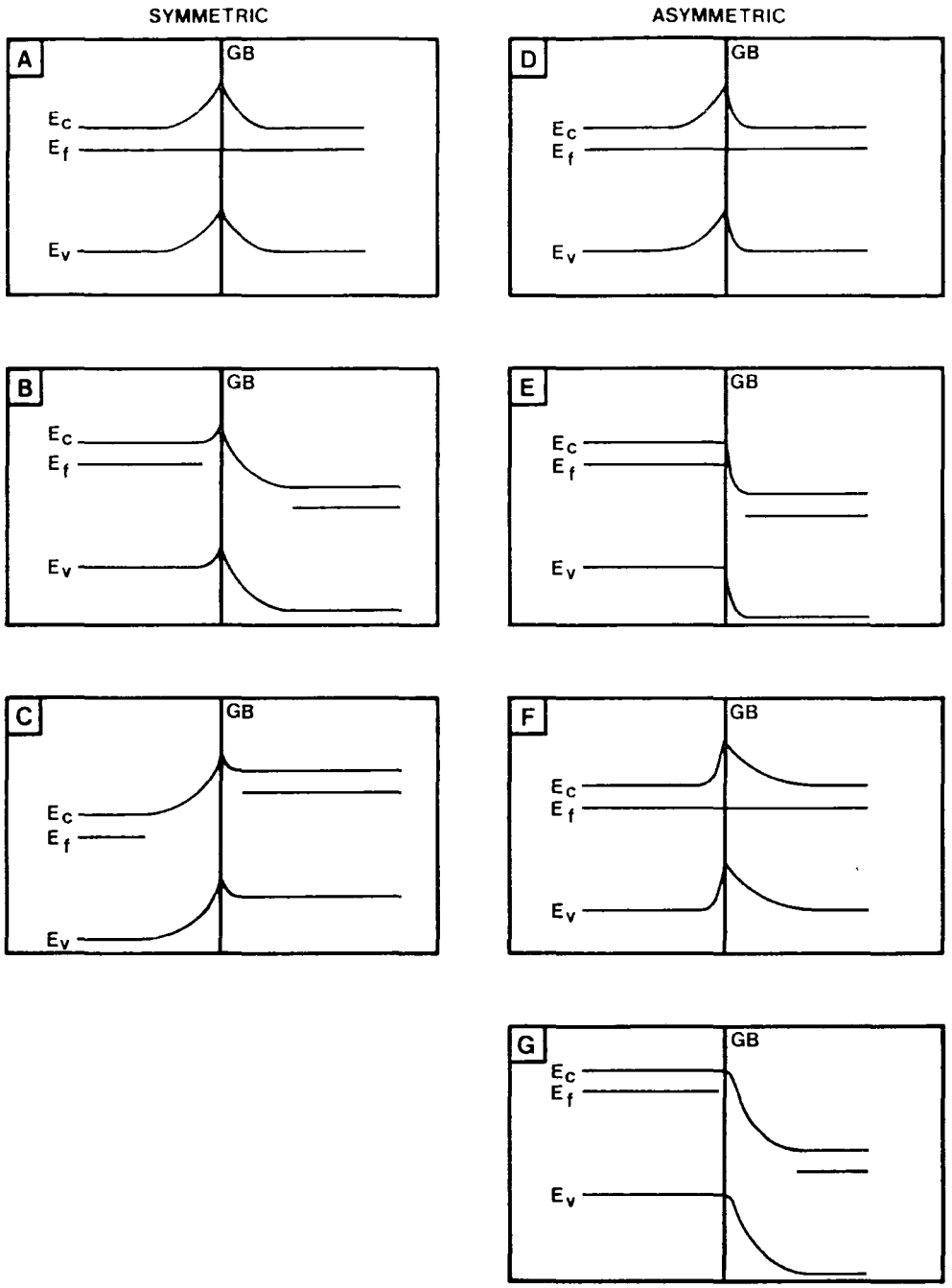

Energy band diagrams for symmetric and asymmetric grain boundaries with and without bias

A A symmetric grain boundary without bias
B The boundary in A with −ve bias on the left contact
C The boundary in A with −ve bias on the right contact
D An asymmetric grain boundary without bias
E The boundary in D with −ve bias on the left contact
F The other configuration for an asymmetric boundary without bias
G The boundary in F with −ve bias on the left contact

FIGURE 6.2/5

It is expected that the band-bending will be asymmetric since it is unlikely that exactly equivalent concentrations of segregated impurity will collect at each side of the grain boundary during the annealing process. This generalised representation is depicted in Figures 6.2/5(d) and (f).

This band model, though simple, can be used to explain all the EBIC observations made in the SEM during the course of the present work. The following section deals with some of these results, together with those obtained using other experimental techniques.

6.22 Experimental results

Before examination in the SEM a bromine-in-methanol etch was administered as described in Section 3.41, to reveal the grain structure. An example of a secondary emission micrograph is shown in Figures 6.2/1 and 6.2/6, the latter demonstrating that the material had a grain size of 20 to 200 microns.

The secondary emission image in Figure 6.2/6 was recorded with zero bias applied to the sample. When -3V was applied to the contact to the right of the field of view a change in the contrast of the SEM image was seen. This voltage contrast effect is shown in Figure 6.2/7. The central grain grew paler with respect to the grains surrounding it. Reversing this bias state by applying -3V to the opposite contact gave the image shown in Figure 6.2/8, where the same grain became very dark compared with surrounding grains. The suggestion that the central grain was surrounded by a potential barrier coincident with the grain boundary was confirmed when the EBIC image was viewed. In zero bias it appeared as shown in Figure 6.2/9. Referring to Figure 6.2/5 in the preceeding section, it can be seen that the grain boundary shown there corresponds to the asymmetric case and that both possible configurations are represented, suggesting that the distribution of segregated impurity is extremely varied.

Application of -3V to the left-hand contact gave rise to the EBIC picture in Figure 6.2/10. The all-white grain boundary corresponds to the situation in Figure 6.2/5(e) or 6.2/5(g) where the bands are bent such that current is induced to flow in one direction only. Switching the

Secondary emission image at zero bias

FIGURE 6.2/6

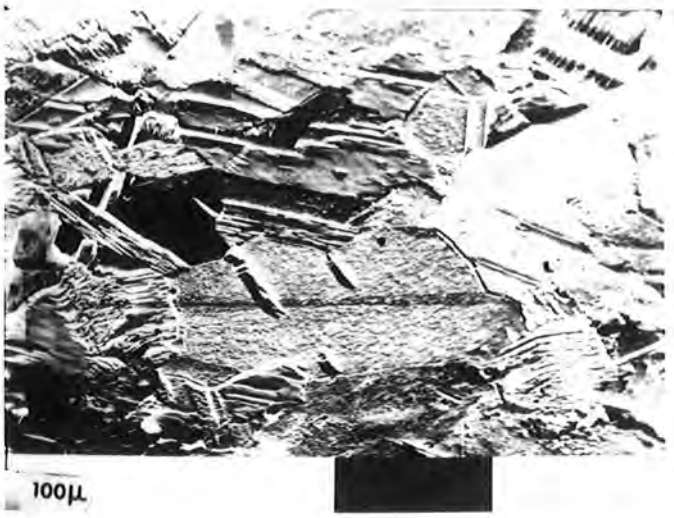

Secondary emission image with -3v applied to the contact at the right of the picture

FIGURE 6.2/7

Secondary emission image with -3v applied to the left-hand contact

FIGURE 6.2/8

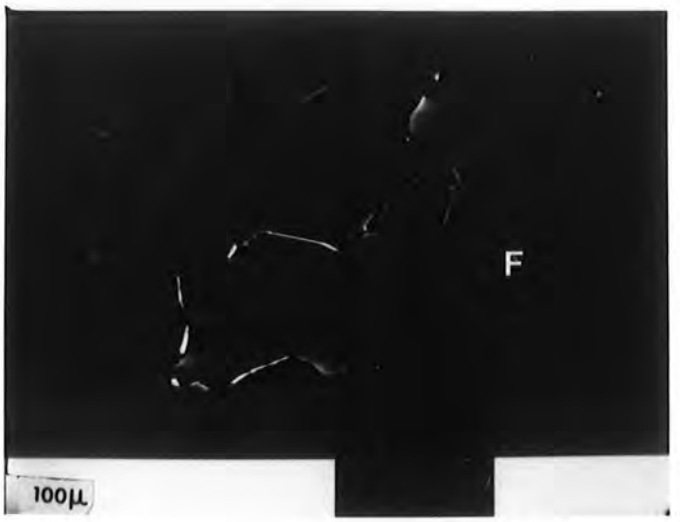

EBIC image recorded at zero bias

FIGURE 6.2/9

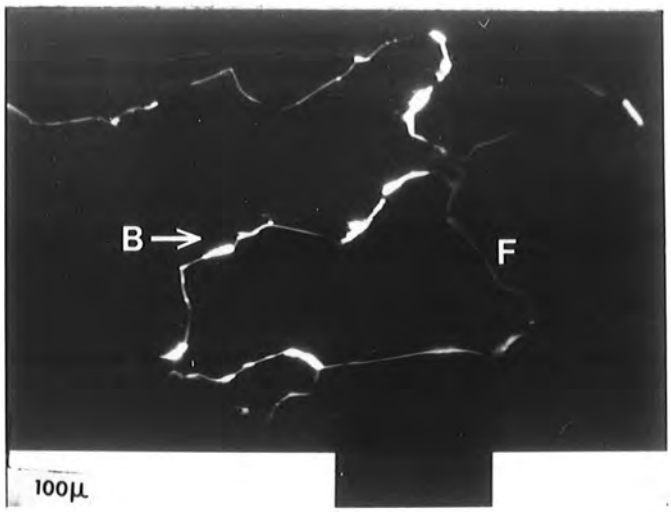

EBIC image with -3v applied to the left-hand contact

FIGURE 6.2/10

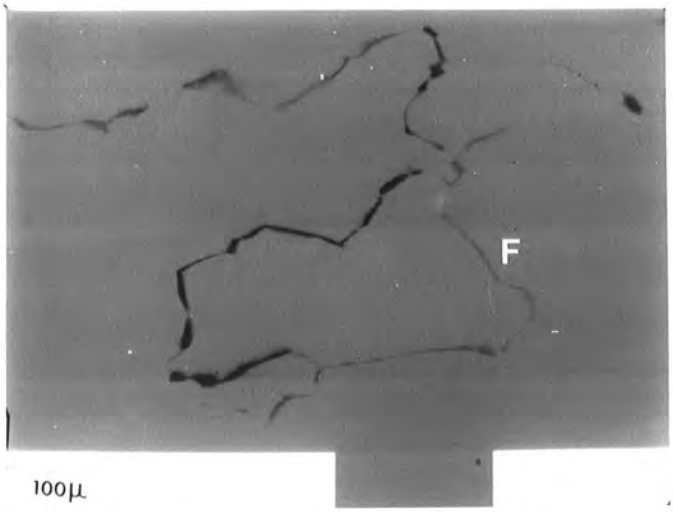

EBIC image with -3v applied to the right-hand contact

FIGURE 6.2/11

bias such that -3V was applied to the right-hand contact gave the picture shown in Figure 6.2/11. The black grain boundary shows that the energy bands had been altered to give a situation similar to that shown in Figure 6.2/5(c), causing the induced current to flow in the opposite direction. When the SEM sample stage was rotated through 180° the same EBIC contrasts were seen, showing the effect to be independent of the direction of the beam scan.

The influence of local crystallographic features on the EBIC image can be seen in Figures 6.2/12,13 and 14. The secondary emission image in 6.2/12 shows a grain boundary at the surface of an etched sample of ZnSe. The etch has revealed the crystallography clearly, and a twin-band is seen to intersect the grain boundary at the arrowed point T. Turning to the EBIC micrograph of the same region, with a negative bias applied to the contact to the right of the field of view, it is seen in Figure 6.2/13 that the image is interrupted at the point where this intersection occurs, and again at a point further on in the same direction. Reversing the biassing conditions, so that a negative voltage was applied to the left-hand contact produced the image seen in Figure 6.2/14. No such discontinuity is observed in this case. The effect can be understood if it is assumed that changes in grain orientation at the grain boundary can influence the impurity segregation process. Crystallographic features such as the twin-band shown in Figure 6.2/12 could preclude such occurrences at regions of intersection, leaving the band structure unmodified at that site on the boundary. If impurity had been allowed to accumulate on the other side, the extremely asymmetric behaviour seen in Figures 6.2/13 and 14 would be observed when the bias polarity was altered from one extreme to the other.

The Durham SEM was fitted with a linescan option, which allowed the operator to display the intensity of a single line across the sample image. When a linescan was made across the EBIC image in Figure 6.2/10 in the direction arrowed B, the lower of the two traces in Figure 6.2/15 was obtained. Illuminating the whole sample with a 12W tungsten bulb sealed in the SEM chamber, and repeating the procedure yielded the upper trace. The differences in the two traces indicates that the grain boundaries in CVD ZnSe are photosensitive.

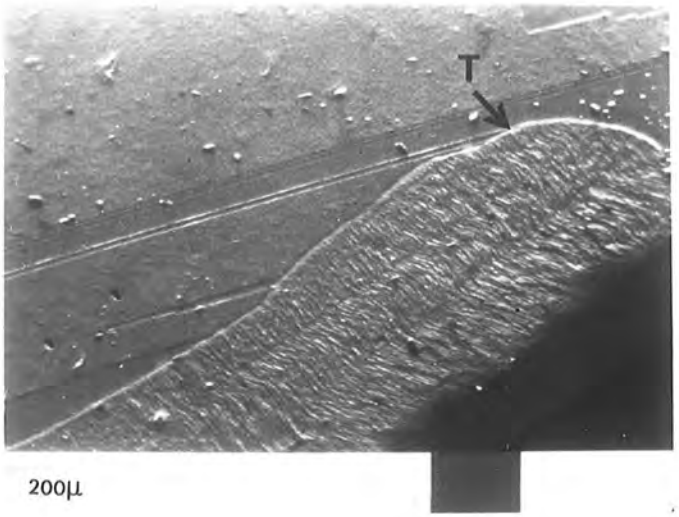

Secondary emission image of an etched sample of ZnSe. The intersection of a twin band with a grain boundary is indicated at point T.

FIGURE 6.2/12

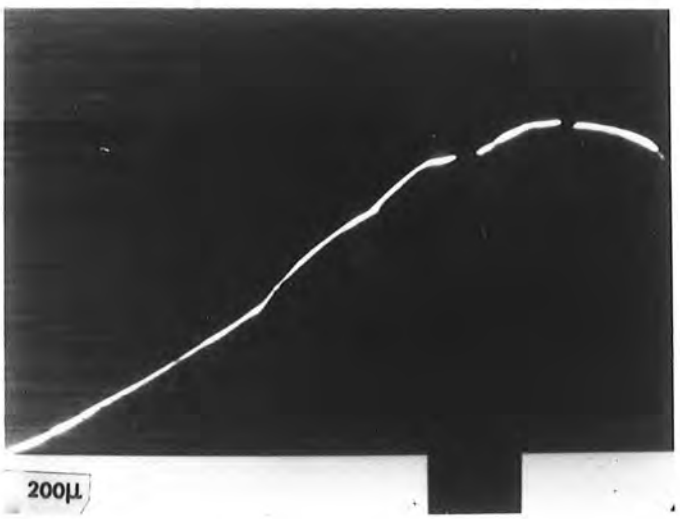

EBIC image of the area in 6.2/12 with -3v applied to the right-hand contact

FIGURE 6.2/13

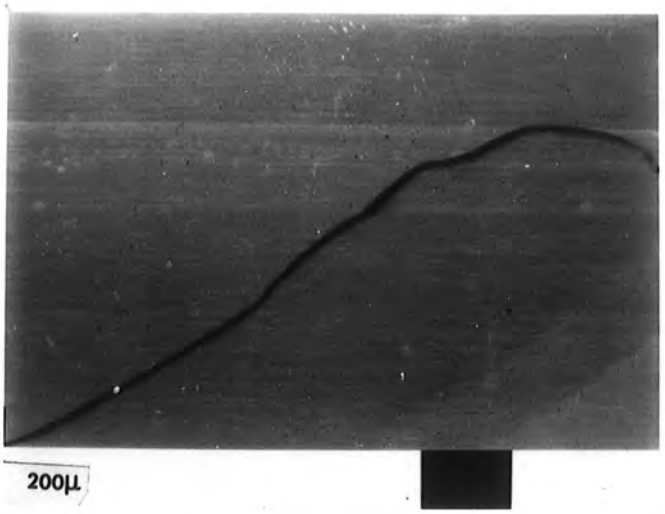

EBIC image of the area in 6.2/12 with −3v applied to the left−hand contact

FIGURE 6.2/14

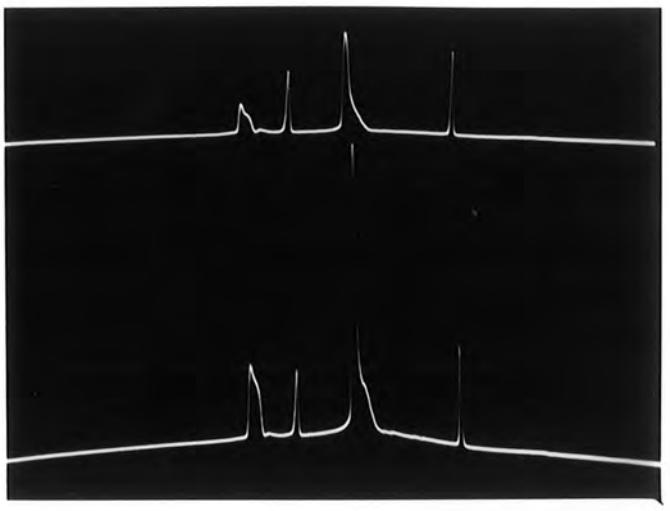

Linescan of intensity along the direction arrowed B in figure 6.2/10

FIGURE 6.2/15

The grain boundaries can be expected to limit the current flow in a sample when they form a continuous barrier across the contacts. When this happens they are clearly evident in EBIC measurements. However, some of the boundaries join up in meandering paths connecting the contacts, and as a result have only a minor effect on the total current flow. These barriers show up as very faint contrasts in the manner of the boundary labelled F in Figures 6.2/9, 10 and 11. The overall effect of the potential barriers is to limit total DC current flow. The zinc annealing treatment described in Section 3.323 lowered the resistivity of Durham-grown zinc selenide to 1-10 Ω-cm. The lowest DC resistivity obtained with the CVD samples was 1.56×10^3 Ω-cm, despite repeated annealng. When the AC conductivity of the four CVD ZnSe samples was measured from DC to 200 KHz, the curves shown in Figure 6.2/16 were obtained. The AC conductivity at 200 KHz was found to be 50 to 100 times greater than the value observed at DC.

The cathodoluminescence of CVD ZnSe at room temperature consists of two emission bands, one at 465 nm corresponding to the blue band-edge emission, and the other at 630 nm. Both components of the CL emission were found to be suppressed at the grain boundaries as can be seen in Figure 6.2/17 (a) and (b). The dark lines in both of these pictures correspond to grain boundaries where the luminescence has been quenched. Extensive work on photoluminescence suggests that the 630 nm emission is probably the well known copper-red band in ZnSe [3]. Atomic absorption spectroscopy has revealed the presence of copper in the samples studied at levels of about 0.4 ppma (Figure 6.2/18). The suppression of the red luminescence at the grain boundaries could therefore be explained by a copper deficiency at these sites, however this is thought to be unlikely since grain boundaries are expected to act as sinks for impurities.

The infrared transmission trace of a disc of ZnSe produced by the CVD process is shown in Figure 6.2/19 and it confirms an absorption band at 1620 cm^{-1} which corresponds to the frequency of the vibrational mode in the diatomic ZnH molecule [4,5]. Samples from batches common to CVD/1, CVD/2 and CVD/3 were studied in this way at AWRE, Aldermaston [6] where their respective copper-red emission intensities were also recorded. All samples exhibited the same absorption band as shown in Figure 6.2/19 implying that all the CVD ZnSe samples studied in the course of this work contained the hydride impurity. Using the IR spectra to calculate approximately the concentration of hydride in each sample, the graph shown in Figure 6.2/20 was plotted.

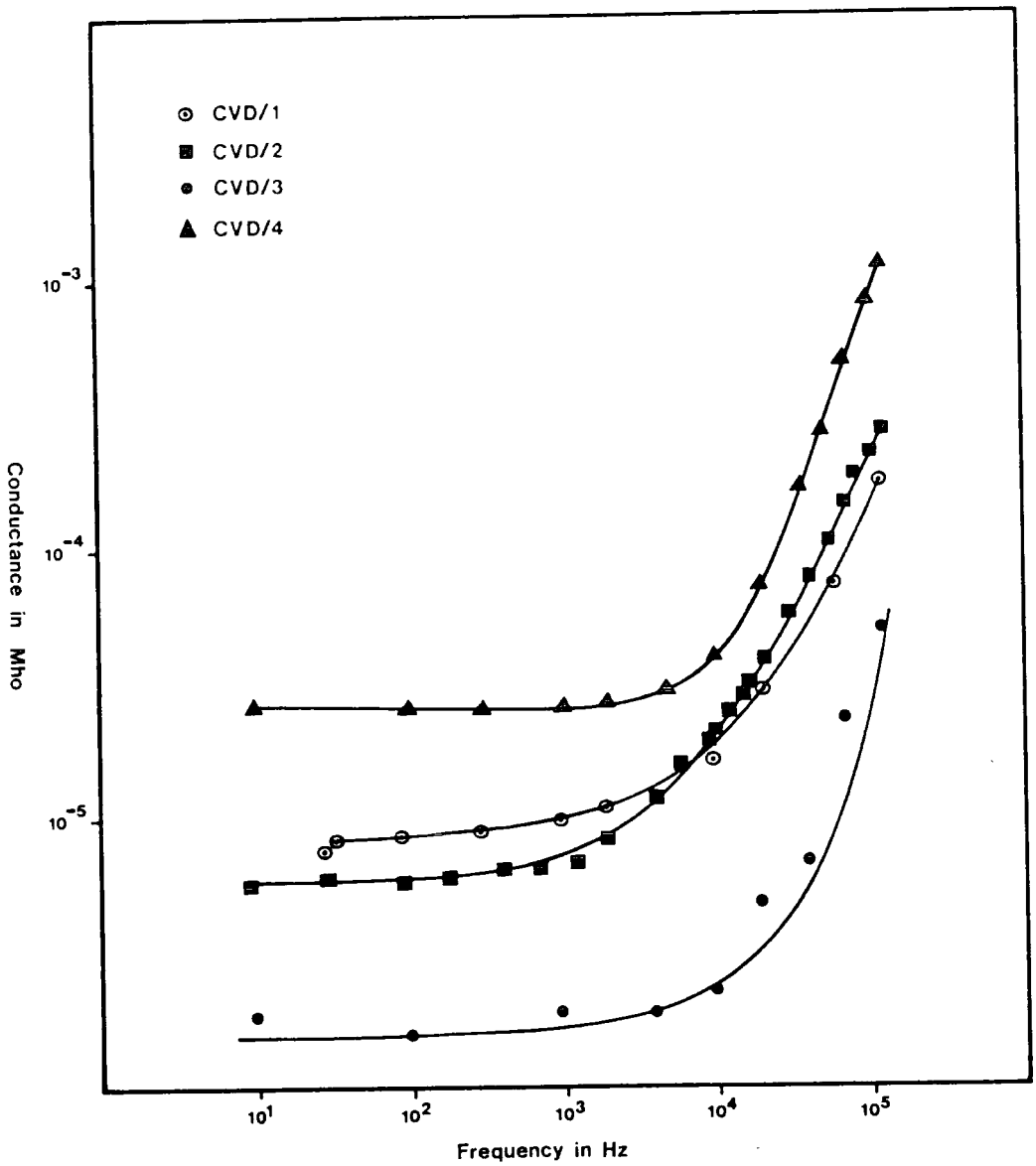

Conductance vs Frequency results obtained from the CVD ZnSe samples

FIGURE 6.2/16

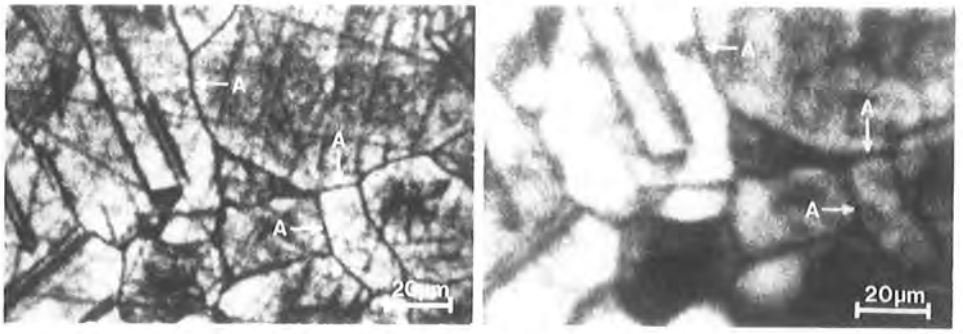

(a) (b)

Cathodoluminescence images of CVD ZnSe at room temperature (a) of the edge emission band at 465nm and (b) of the copper-red band at 630nm. Both components are suppressed at the grain boundaries at points A.

FIGURE 6.2/17

IMPURITY	CVD/1	CVD/2	CVD/3
Cu	0.45	0.45	0.34
Fe	1.20	0.50	0.90
Mg	<3.00	<3.00	<0.30
Ni	0.25	0.25	0.25
Cr	0.80	0.80	0.80
Co	<0.60	<0.60	<0.60
Al	<2.70	<2.70	<2.70
Mn	<0.05	<0.05	<0.05
Cl	0.12	0.12	0.12
Br	<0.05	<0.05	<0.05
I	<0.03	<0.03	<0.03

IMPURITY LEVELS FOUND IN CVD ZnSe (ppma)

FIGURE 6.2/18

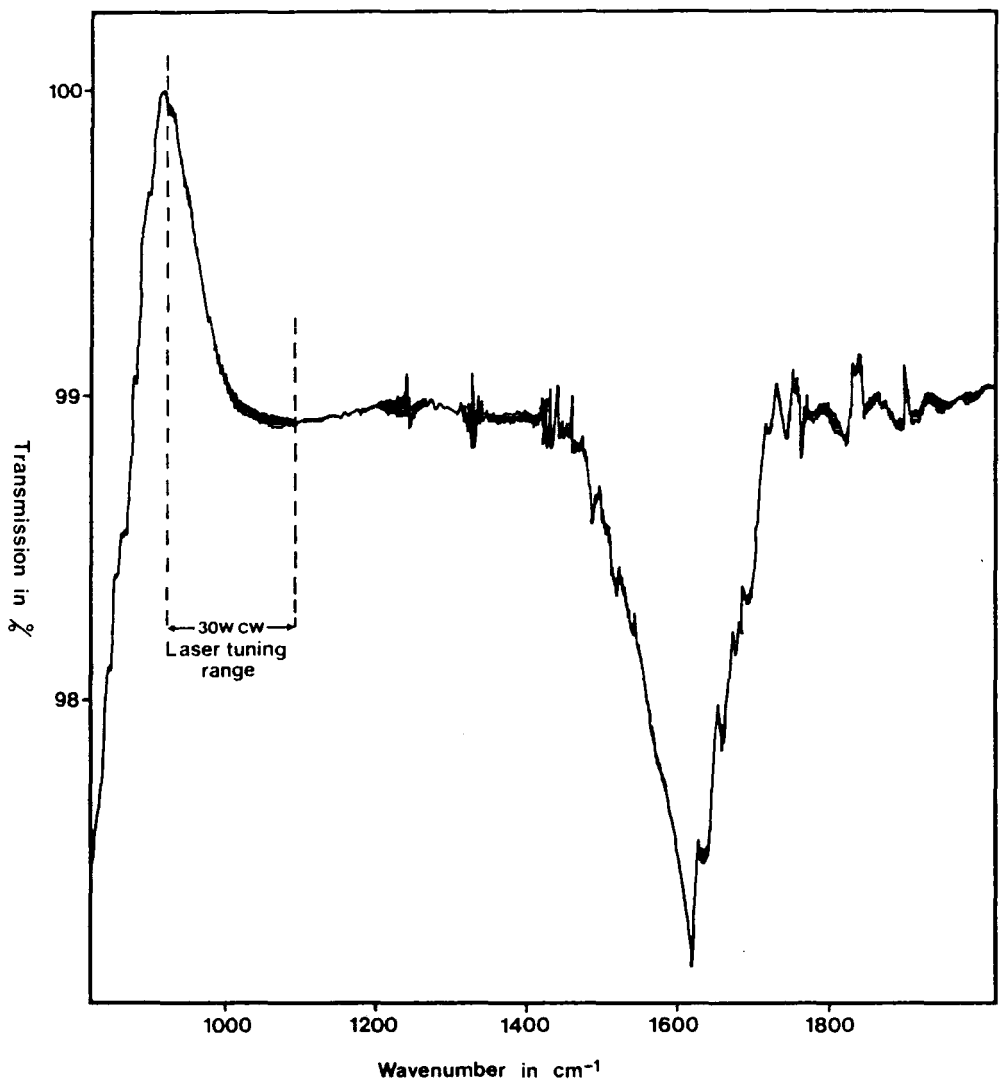

Absorption band at 1620cm^{-1} due to the hydride species incorporated during the growth of CVD ZnSe.

FIGURE 6.2/19

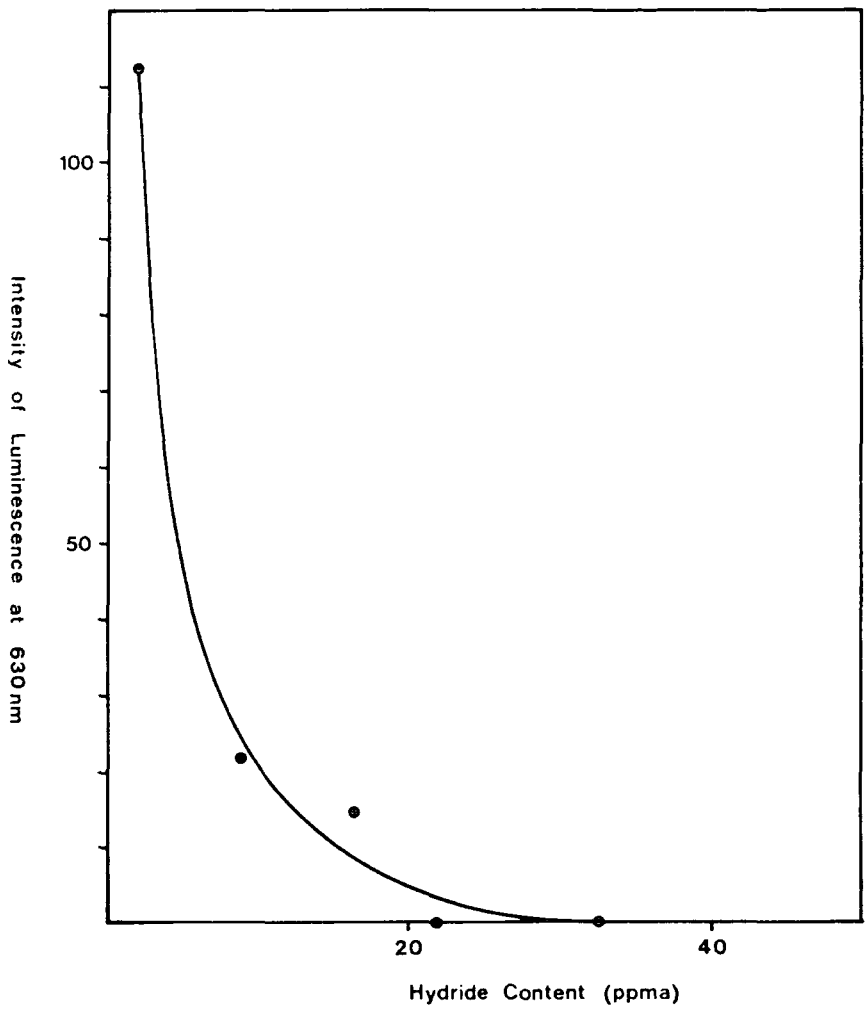

Quenching of the copper-red luminescence in ZnSe by the hydride species.

FIGURE 6.2/20

6.3 Laser absorption measurements

The links established by the SRC CASE scheme between Durham University Department of Applied Physics and Electronics and AWRE, Aldermaston, led to part of the present project being devoted to a study of the performance of ZnSe in its role as an infrared laser window. The extremely wide range of power and energy characteristics available from lasers at their present stage of development has enabled an increasing range of applications to be realised. Laser systems have gradually become both more efficient and much smaller in response to pressure exerted on manufacturers by industry. This has led, inevitably, to power and energy densities which damage the components comprising the laser resonator (mirrors, windows and beam-splitters). Measurement techniques have been developed to characterise components in terms of their power and energy handling capabilities before incorporating them into systems. Investigations have also been undertaken to understand more about the physical processes governing laser-induced damage.

In the fabrication of a laser window, the manufacturer aims to produce an optic which affects the transmitted portion of the incident beam as little as possible. The degree of success can be found by measuring the fraction of transmitted radiation which is absorbed in the bulk of the component. This loss factor is termed the absorption coefficient and is usually expressed in units of cm^{-1}. In general, absorption in a thin laser window occurs both in the bulk and at the air-window interfaces where the surface or coating may have been damaged or where organic deposits might have formed during handling. The method usually adopted to isolate the contribution of the bulk to the overall absorption coefficient involves the careful preparation of a series of samples of the same material, each having a different thickness [7]. If the surfaces of each are polished and handled identically it follows that the surface absorption will be the same in each case. By contrast the total bulk absorption will be determined by the product of the sample thickness and the absorption coefficient. This allows the two components to be separated by a simple straight-line plot of absorption versus sample thickness. The intercept yields the surface absorption, and the gradient has a value equal to the bulk absorption coefficient.

The total absorption of a window sample can be obtained in several ways. The spectral emissivity [8] of the material can be measured with reference to the emission of a black body at the same temperature, giving the absorption as a function of wavelength. A more popular method, which also yields broadband information, is dual-beam spectroscopy [9]. This technique makes use of a single light-source, which is split into two identical beams. One passes through the sample and the other bypasses it, acting as a reference. The ratio of the final intensities then provides the absorption figure. The addition of a monochromator to the front-end of such an instrument allows the absorption coefficient to be determined as a function of wavelength quickly and easily. However, state-of-the-art spectrophotometers only have sensitivites in the order of 10^{-3} cm^{-1}. Absorption coefficients as low as 10^{-5} cm^{-1} have been recorded regularly in components fabricated from the alkali halides, and ZnSe has been produced with absorptance values as low as 10^{-4} cm^{-1}. Laser calorimetry [10,11] was first used to measure the absorption coefficients of optical components in 1971 [12]. The large power densities available in the coherent beam of a laser, together with sensitive temperature-sensing devices provide a basis for measurements accurate to 10^{-6} cm^{-1}. The main drawback is the limitation of the apparatus to wavelengths at which laser power is obtained. This is not a great problem in the field of laser component assessment, because these are usually the wavelengths of paramount interest anyway. It can, however, impede research undertaken to isolate the absorption mechanisms involved.

6.31 Theory

6.311 Optical absorption processes in IR-transmitting materials

The most widely used substrate materials in IR systems are the four semiconductors germanium, zinc selenide, gallium arsenide and cadmium telluride, together with the two water-soluble alkali-halides potassium chloride and sodium chloride [13].

All of these window materials are characterised by a highly transparent wavelength region where the absorption coefficient typically falls to values below 10^{-3} cm^{-1}. This low absorption range is bounded by the restrahlen band at long wavelengths, which is due to the lattice.

The high frequency side of this band (verging on the transparent region) is due to intrinsic multiphonon absorption [14] which results from the combination of two distinct processes occurring within the crystal lattice itself. The first is the direct coupling of light incident on the material, to the electric moment M, which relates to the polarisation of the charge densities in the lattice structure. The second process is concerned with the dissipation of the incipient energy by the formation of additional phonons from repeated anharmonic coulombic interactions between the periodic charge densities. Generally this region can be described by Equation 6.31-1, although when $\omega/\omega_0 >> 1$, an enhancement of the absorption coefficient

$$\beta_L(\omega) \approx A\exp(-B\omega/\omega_0) \qquad 6.31\text{-}1$$

where:

β_L = absorption coefficient due to the lattice
ω_0 = fundamental lattice resonance frequency
A $\approx 10^4$-10^5
B $\approx$ 4-5 in most solids

is expected due to the increased number of available anharmonic interaction paths in this regime.

Moving to the short wavelength side of the transparent region, the onset of heavy absorption as the frequency is increased marks the beginning of absorption processes due to the fundamental band-gap electronic transition. The change in absorption with wavelength can be described in terms of the exponential function in 6.31-2 [15].

The absorption tail, which extends into the transparent wavelength region consists of contributions from indirect and direct transitions, coulombic interactions, exciton formation, the incorporation of dopants, and crystal defects [16].

$$d(\log_e \beta_E)/d(h\nu) = 1/kT \qquad 6.31\text{-}2$$

where:

h = Plancks constant (JS)
ν = frequency (Hz)
β_E = absorption coefficient (cm^{-1})
k = Boltzmanns constant ($J°K^{-1}$)
T = temperature (°K)

For a material such as zinc selenide, the total absorption is given by the expression in 6.31-3.

$$\beta_{TOT}(\omega,T) = \beta_L(\omega,T) + \beta_I(\omega,T) + \beta_f(\omega,T) + \beta_S(\omega,T) \qquad 6.31\text{-}3$$

where

β_L = intrinsic lattice absorption coefficient
β_I = intrinsic bandgap absorption coefficient
β_f = free carrier absorption
β_S = surface absorption

In the transparent wavelength region of ZnSe (0.5-20 μm), the intrinsic weak wing absorption associated with the lattice and the charge carriers excited across the bandgap drops to an estimated minimum of 2×10^{-4} cm^{-1} [7]. Under these circumstances, the total absorption coefficient, given by 6.31-3 above, is dominated by free carrier absorption and the extrinsic absorption processes deriving from the surface. Previous work [4] has shown that a number of distinct bands related to incorporated impurities and species adsorbed onto the sample surfaces can be found in ZnSe grown by the CVD method.

More recently [17] Attenuated Total Reflectivity measurements have shown that the surface absorption spectrum of some samples can be dominated by features due to -OH and $-CH_n$ vibrational modes, assumed to be due to adsorbed atmospheric moisture and hydrocarbon deposits caused by handling. In the same publication, it was demonstrated that these features

could be reduced by an order of magnitude by cleaning the surfaces with trichloroethane followed by acetone.

It is necessary, at this point, to consider the contribution to the overall absorption coefficient arising from free charge carriers in the material, since deep level impurities can be expected to have some effect on the free carrier density. Jensen [18] derived the expression in 6.31-4 for the value of the absorption coefficient.

$$\beta_f = n_c\sigma \qquad 6.31\text{-}4$$

where $\sigma = \sigma_0 \, (H(x,r)/(x^4(1+x)D(x,r))$ 6.31-4(a)

n_c = number of free carriers (cm^{-3})

$x = \hbar\omega/Eg.2\pi$ 6.31-4(b)

r = spin orbit splitting ($=\infty$)

$\sigma_0 = 2/3(e^2/nEg^3)\ Ni(k^2/2m_0nEg)\ (4\pi e^2/\varepsilon_s)^2\ (Eg/2m_0nc^2)$

m_0 = electron rest mass

n = refractive index (=2.4)

ε_s = static dielectric constant (=9.12)

Eg = bandgap (=2.7 eV)

Ni = density of charged impurities (cm^{-3})

and D and H are complex functions of x and r

In the limit of $r\to\infty$ the value for σ given in Equation 6.31-4(a) simplifies to:

$$\sigma = 2\sigma_0/x^{3.5}$$

for the case where the final electron state lies in the parabolic region of the conduction band.

or $\sigma = \sigma_0/x^5$

for the case where the final electron state lies in the hyperbolic region of the conduction band.

Since $\lambda = 1.24/h\nu$, it is simple to show that the absorption coefficient due to free carriers is given by:

$$\beta_f = 2n_c \left(\frac{Eg}{1.24}\right)^{3.5} \lambda^{3.5} \quad \text{for the parabolic limit} \qquad 6.31\text{-}5$$

and

$$\beta_f = n_c \left(\frac{Eg}{1.24}\right)^{5} \lambda^{5} \quad \text{for the hyperbolic limit} \qquad 6.31\text{-}6$$

The direct dependence of the absorption coefficient on the concentration of free carriers emphasises the importance of deep traps within the material, which can, under certain circumstances, be expected to modify the parameter n_c, and hence alter the optical performance of laser components.

6.312 Analysis of laser calorimetric data

Absorption calorimetry [12,12,19] involves the measurement of fractional losses in radiation transmitted through a sample by the use of extremely accurate thermometric techniques. One approach is to irradiate a thermally isolated sample with light of a known intensity and to measure the resulting temperature rise after a set time interval. A straightforward calculation involving the specific heat of the optical component being studied yields the percentage of the total energy absorbed. The determination of the intensity of the radiation incident on the sample can be difficult to accomplish. To circumvent this problem, some workers [20] have developed a method whereby the sample is electrically heated, subsequent to the laser irradiation procedure described above in order to calibrate the apparatus. Another approach [21] involves the use of a

reference sample which has a known absorptivity. The temperature rise in this absorption standard is then compared with the temperature rise in the sample under study to calibrate the apparatus and to yield an absorption coefficient. The latter method is used in the measurements undertaken in the present work (Section 6.32).

Analysis of the data is straightforward and can be understood by reference to Figure 6.31/1 which shows two temperature-rise curves taken from the apparatus used in this project (Section 6.32). Curve A derives from the reference temperature measurement circuit and curve B from the circuit connected to the sample. Using a technique of back-extrapolation [22] to correct for the cooling curves, the two temperature rises, denoted T_A and T_B in Figure 6.31/1 are found. The absorption, expressed as a fraction can then be calculated from the expression in Equation 6.31-7 below.

$$\frac{A_S}{A_R} = \frac{T_B}{T_A} \cdot \frac{G_A}{G_B} \cdot \frac{M_S.C_S + M_{SH}.C_{SH}}{M_R.C_R + M_{RH}.C_{RH}} \qquad 6.31\text{-}7$$

where:

A_S = sample absorption
A_R = reference absorption
T_B, T_A = temperature rises : sample, reference
M_S, M_R = masses : sample, reference
M_{SH}, M_{RH} = masses : sample-holder, reference-holder
C_S, C_H = specific heats : sample, reference
C_{SH}, C_{RH} = specific heats : sample-holder, reference-holder
G_A, G_B = amplifier gains : reference channel, sample channel

All of the parameters to the right of the equation are either measured directly or already known. The reference absorption A_R is found indirectly by substituting a sample for which A_S is known accurately, into the sample-holder, and repeating the experiment. The sample used to perform this calibration was a brass disc painted on one face with Nextel 3M matt-finish paint. In order to be sure of the absorption of the

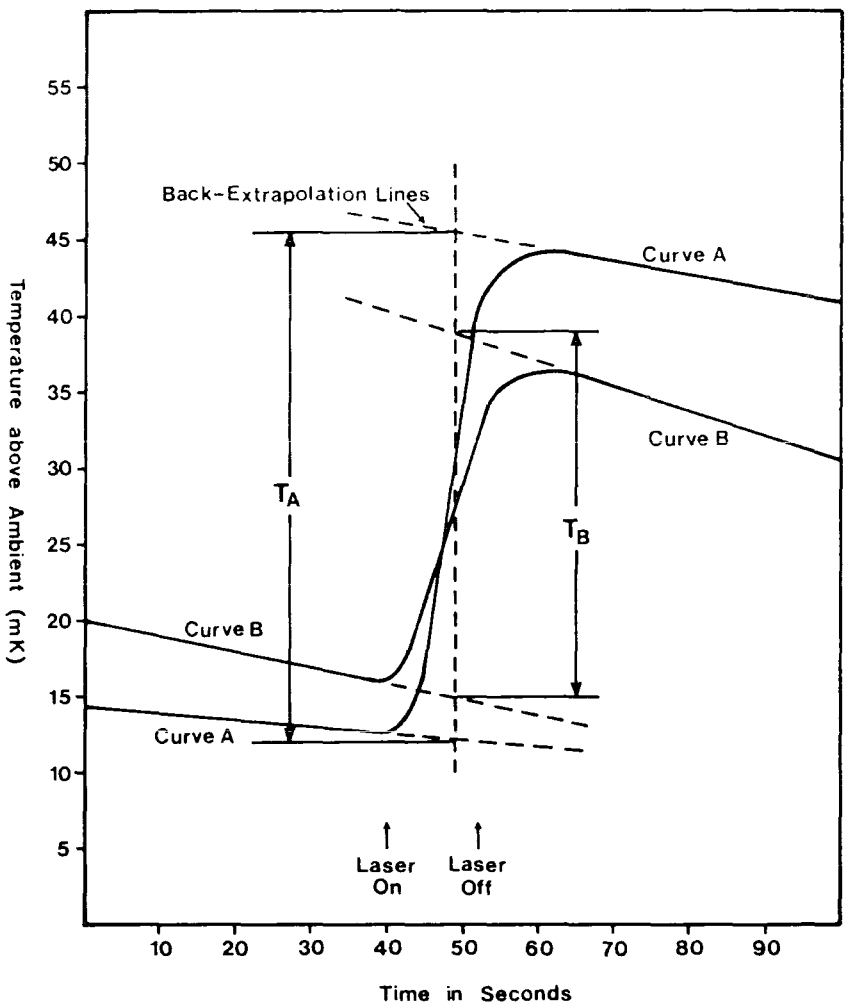

Temperature rise curves obtained from the laser calorimeter. Curve A is produced by the reference and curve B by the sample.

FIGURE 6.31/1

calibration standard, the 3M disc was sent to the National Physical Laboratory (NPL) at Teddington, where it was found to be 96.0% absorbing at 10.6 μm.

The absorption coefficient can be calculated knowing the sample thickness, d, and the total absorption A_S from equation 6.31-8.

$$\beta = A_S/d \quad \text{if} \quad A_S << \frac{1-R}{R} \qquad 6.31\text{-}8$$

where:

β = absorption coefficient in cm^{-1}
d = sample thickness in cm
A_S = sample absorption
R = reflectivity of a single surface

The condition involving the reflectivity derives from the consideration of multiple internal reflections within the sample [20].

6.32 Apparatus and experimental procedure

The apparatus used to undertake the laser absorption measurement is shown schematically in Figure 6.32/1. The source of radiation was a continuous wave CO_2 laser, type CW30TX which was step-tunable over 80 discrete lines from 9.15 μm to 10.91 μm (Figure 6.32/2). A maximum power of 28W was available on the P20 line at 10.6 μm in TEM_{00} mode. The beam was reflected off a diamond-turned copper reference mirror, and passed through a focussing lens onto the window sample under test. The sample and reference components were both mounted in precisely machined brass holders, constructed to give the tight fit necessary for good thermal contact. A pair of miniature bead thermistors were embedded in the rim of each holder diametrically opposite each other. These sensors were wired in series in order to provide a total resistance value proportional to the average temperature across the diameter of the component.

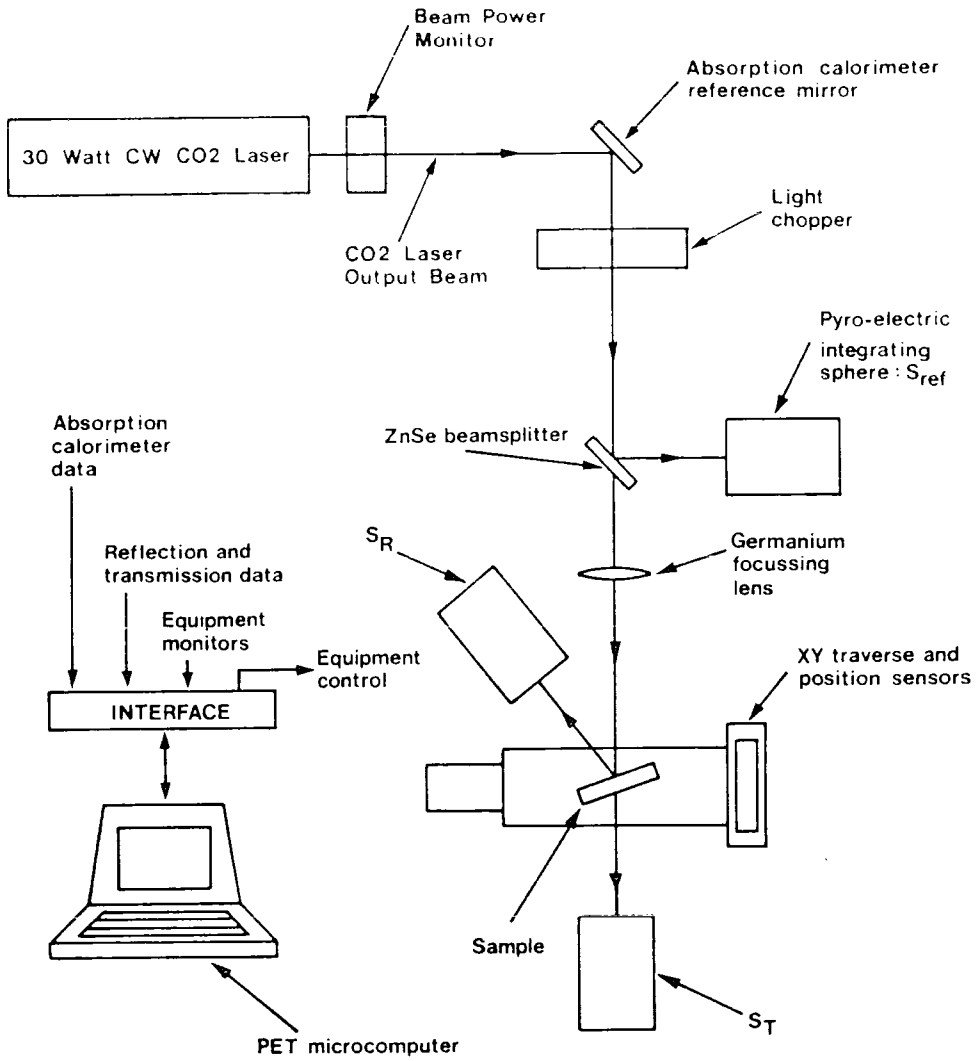

Schematic diagram of the apparatus used to measure absorption coefficients at 10–11μm

FIGURE 6.32/1

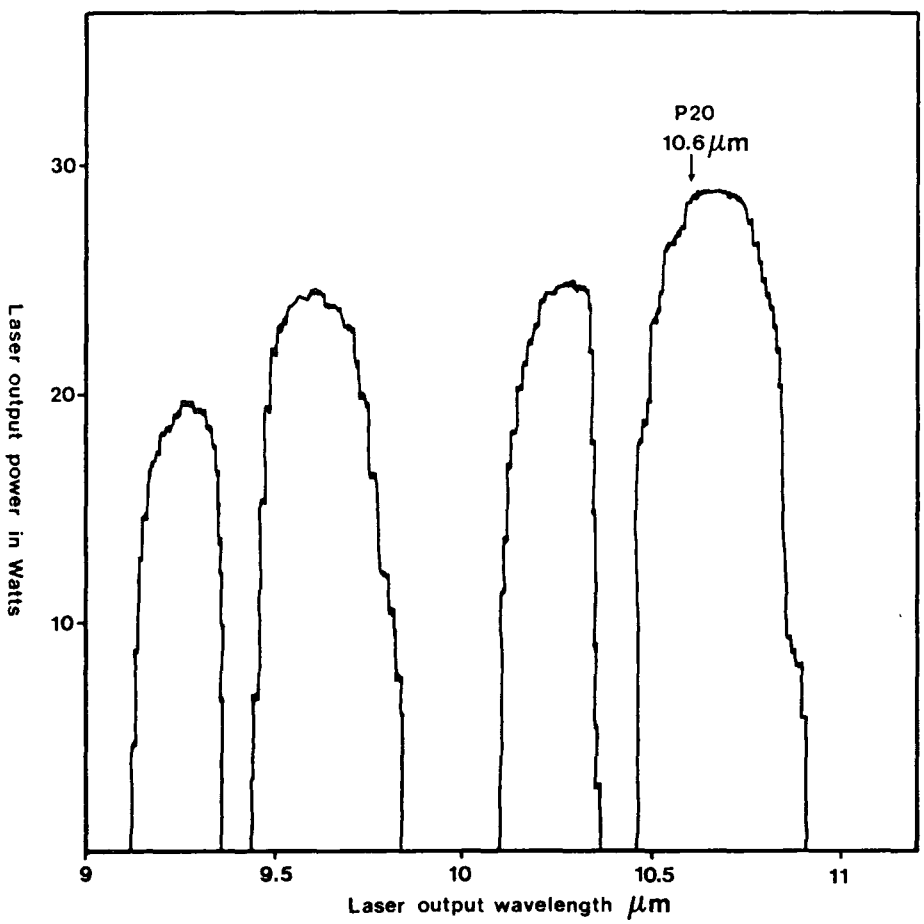

Tuning characteristic of 30 Watt cw laser used for absorption measurements

FIGURE 6.32/2

The methods employed to measure temperature changes in window samples can be understood by reference to Figure 6.32/3. The circuit shown in this figure consists of a Wheatstone bridge, the imbalance signal of which is amplified and then taken to an analogue-to-digital converter. The Wheatstone bridge was made up of four separate arms. Two of these lay in the absorption unit itself (Figure 6.32/1) and consisted of a high stability resistor R_{HS} and a pair of series-connected potentiometers used to bring the bridge into balance. The remaining two arms of the Wheatstone bridge were provided by thermistor pairs embedded in the brass holders containing the sample and the sample reference. The latter component was mounted to one side of the laser-beam path and in close proximity to the sample. Any fluctuations in ambient temperature were hence cancelled out, allowing the bridge circuit to remain balanced. The circuit shown in Figure 6.32/3 was duplicated to provide a reference channel, which was used to monitor the power of the incident laser-beam. Temperature changes of less than 10^{-4}°K could be detected using this arrangement, and linearity over the range of temperature rises encountered was better than 1% as long as the bridge circuits were near balance. The outputs from both bridge circuits were amplified and then taken to separate analogue-to-digital converters. The resulting data were fed into a PET 4032 microcomputer via a MINICAM general purpose interface unit. The temperatures of both the sample and reference could be monitored continually using this arrangement, allowing data to be stored and post-processed to provide absorption coefficients in the manner described in the previous section (6.31).

The experimental method was as follows. Using the PET control features, the laser was first tuned to the desired wavelength. A window sample was cleansed in an appropriate solvent and accurately weighed before being placed in the sample holder. The system was allowed to thermalise until the cooling curves of both the sample and the reference were flat, indicating that they had reached thermal equilibrium with the environment. With the PET regularly sampling the temperature of both components, the laser was switched on for a period of between 0.5 and 40 seconds. The choice of exposure time depended on the laser power and the sample and reference channel sensitivities as determined by the amplifier gains. Sampling was then continued until the cooling curves of both components had stabilised, yielding a result similar to the one shown in Figure 6.31/1 in the preceeding section. A typical window sample with an absorption coefficient of 0.02 cm-1 would show a temperature rise of about 50 mK.

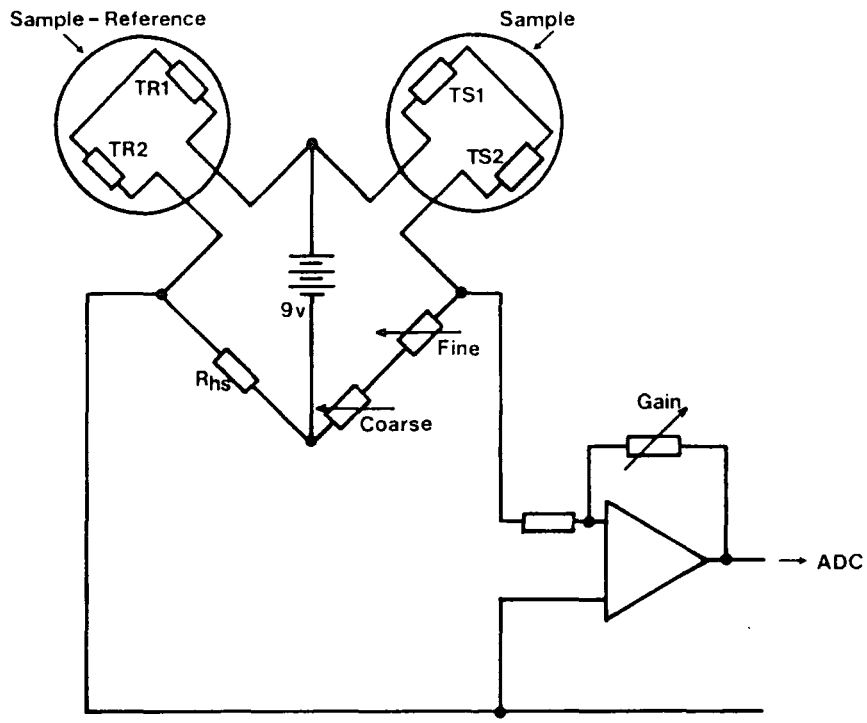

Circuit diagram of temperature-sensor arrangement. TR1, TR2, TS1 and TS2 are miniature bead thermistors embedded in the reference and sample holders R_{hs} is a high stability resistor in the Wheatstone bridge.

FIGURE 6.32/3

A brass disc coated on one face with 3M Nextel Matt Black paint and measured as being 96% absorbing at 10.6 μm by the National Physical Laboratory, Teddington, was used as the calibration standard. The disc was simply substituted for the sample in the apparatus and a procedure identical to that described above followed. A calculation based on the ratio of the reference and sample temperature rises yielded a calibration factor (section 6.312) which, because it incorporated both the absorption coefficient of the copper reference mirror and its thermal capacity, meant that these parameters did not have to be measured directly.

This apparatus provided a relatively rapid, extremely accurate and consistent method of measuring absorption coefficients of window and mirror samples at values as low as 10^{-6} cm^{-1}.

6.33 Results

Using the tuning facility provided by the apparatus (Section 6.32) the absorption coefficients of several samples of CVD ZnSe were measured at wavelengths between 9.15 and 10.91 μm. The results are shown in Figure 6.33/1. No power law was detectable (Figure 6.33/2) owing to the restricted range [17]. The calorimeter, however, proved to be invaluable when used to verify results provided by a Perkin Elmer IR spectrophotometer which was operating in enhanced gain mode at AWRE, Aldermaston. The subject of this investigation was a solid block of CVD ZnSe 2.88 x 2.54 x 2.9 cm^3, provided by the Raytheon Corp., USA (see Figure 6.33/3). This sample contained the Zn-H species as indicated by the dip in the IR transmission spectrum shown in Figure 6.2/19. However, the peak at about 890 cm^{-1} was unexpected. Also shown in Figure 6.2/19 is the tuning range of the CW30TX laser, which allowed a verification to be made of the transmission peak. As can be seen from the results in Figure 6.33/2(a) no such dip in the absorption spectrum occurred, indicating that the peak in 6.2/19 was introduced by the Perkin Elmer system operating at its sensitivity limit.

The solid block of Raytheon ZnSe yielded interesting results when its absorption coefficient was measured along the three axes normal to the sample faces (Figure 6.33/3). The values obtained showed the absorption coefficient to be anisotropic.

(1) CVD/1

β (cm^{-1})	w/number (cm^{-1})	λ (μm)
0.021	928	10.78
0.026	953	10.49
0.032	971	10.30
0.032	981	10.19
0.032	1033	9.68
0.034	1086	9.21

(2) CVD/2

β (cm^{-1})	w/number (cm^{-1})	λ (μm)
0.0139	928	10.78
0.0167	953	10.49
0.0183	971	10.30
0.0244	1033	9.68
0.0347	1086	9.21

(3) CVD/3

β (cm^{-1})	w/number (cm^{-1})	λ (μm)
0.008	928	10.78
0.012	953	10.49
0.019	981	10.19
0.019	1033	9.68
0.017	1064	9.21

ABSORPTION VERSUS WAVELENGTH TABULATION FOR CVD ZnSe SAMPLES

FIGURE 6.33/1

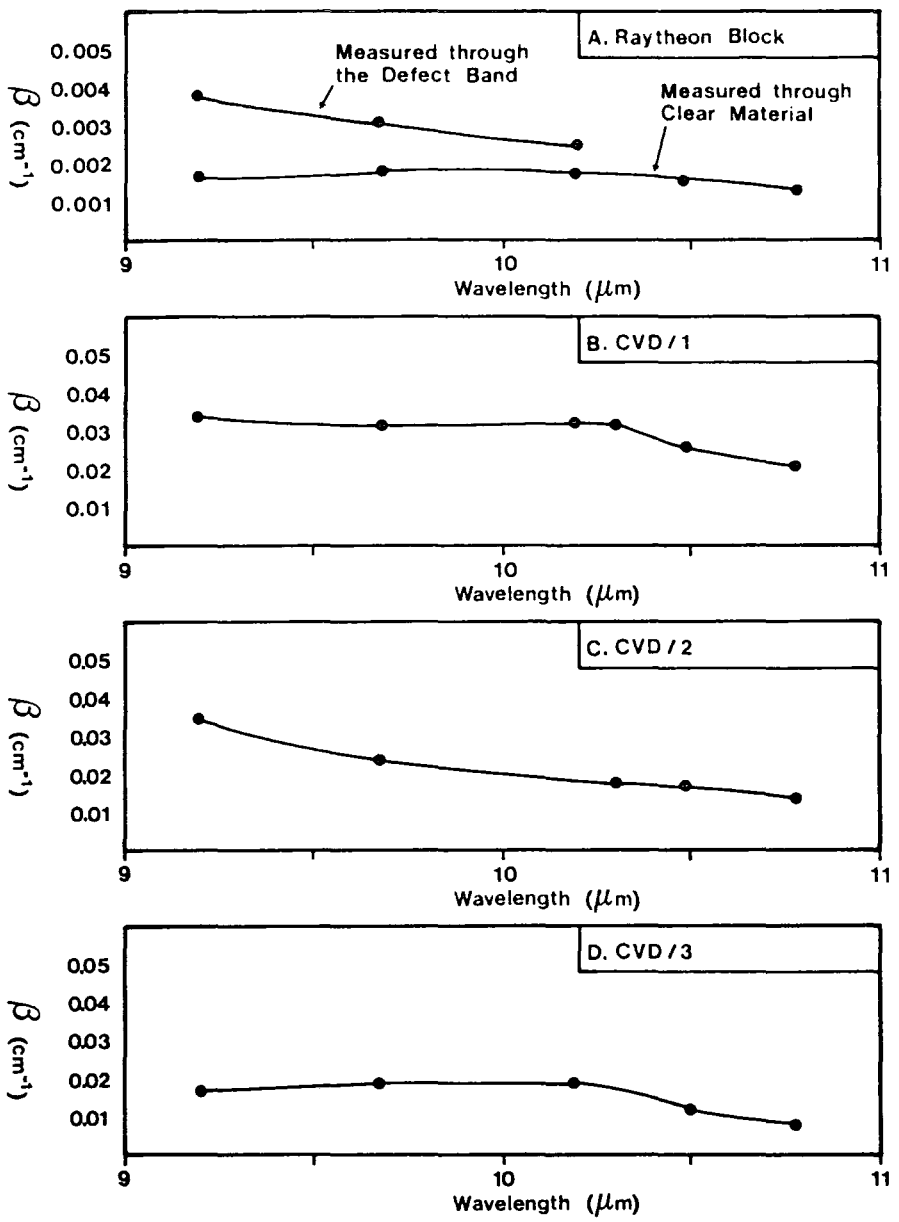

Dependence of absorption on wavelength for the CVD material

FIGURE 6.33/2

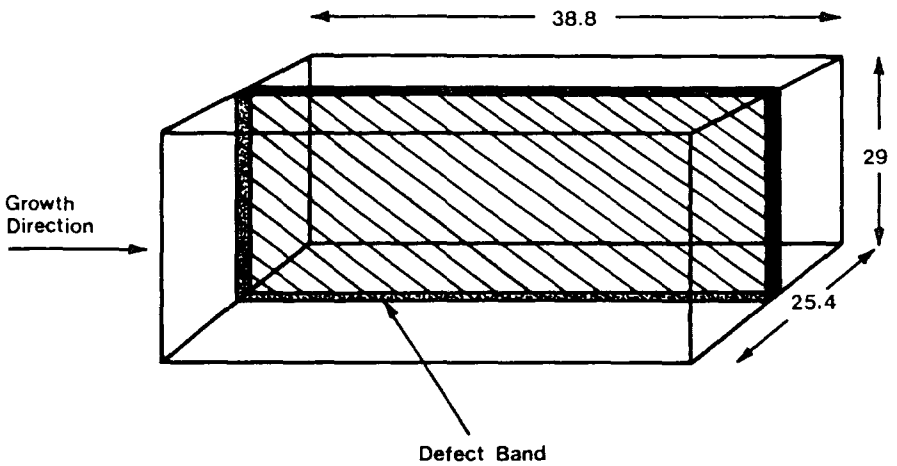

Axis Length	Absorption (%)	Absorption Coeff. (cm^{-1})
38.8mm	0.64	0.0017
29.0mm	0.97	0.0033
25.4mm	0.98	0.0038

Absorption results from the block of Raytheon ZnSe and a drawing of the block showing the defect band

FIGURE 6.33/3

When the sample was viewed whilst it was held up to the light, a thin, diffuse band was observed in the plane indicated by Figure 6.33/3. The shortest optical path length (2.54 cm) yielded the largest absorption coefficient. It seems probable therefore, that this anomaly may be explained by the defect band having a large absorption at 10.6 μm. This hypothesis is supported by the evidence in Figure 6.33/2(a) where the absorption coefficient of the sample is plotted as the wavelength is varied. The absorption increased by up to a factor of two when the laser beam was shifted from the clear path to the one passing through the defect band. The results can also be explained by supposing that the grains are formed during growth such that they are columnar [23] in the direction of growth (Figure 6.33/3). If this were the case, radiation propagating along the 3.88cm axis would encounter substantially fewer gain boundaries and would hence be scattered less. This would result in a much shorter optical path length and a lower absorption than would be the case for the other two axes.

Four CVD ZnSe samples were examined in the SEM at the GEC Hirst Research Centre, and the intensity of the CL emission at 630 nm [3] measured in each case. The values are recorded in Figure 6.33/4 alongside values obtained for the 10.6 μm absorption coefficient. The latter quantity was plotted against the 633 nm band intensity (Figure 6.33/5), the result indicating that the two quantities might be connected. This could be achieved via the free carrier absorption mechanism [17,24].

6.34 Discussion

The grain boundary structure in CVD ZnSe has been shown to have a very strong effect on the electrical properties of the material. The boundaries can be observed in the EBIC mode of the SEM to behave as if they were two Schottky barriers back-to-back, causing samples to exhibit a high DC resistivity. The AC resistivity was shown to decrease by approximately two orders of magnitude when measured at 200 KHz. The formation of the potential barriers is thought to be due to the segregation of impurity at the grain boundary sites during the liquid-zinc annealing process, which is used to lower the resistivity of as-grown ZnSe. High resistivity samples which did not undergo annealing did not

SAMPLE	B(cm^{-1}) @10.6 μm	633 nm band intensity (arbitrary units)
CVD/1	0.03	100
CVD/2	0.02	8.4
CVD/3	-	-
CVD/4	0.018	3.9
CVD/5	0.005	1.0

COPPER-RED LUMINESCENCE INTENSITY TABULATED AGAINST ABSORPTION COEFFICIENT FOR CVD ZnSe SAMPLES

FIGURE 6.33/4

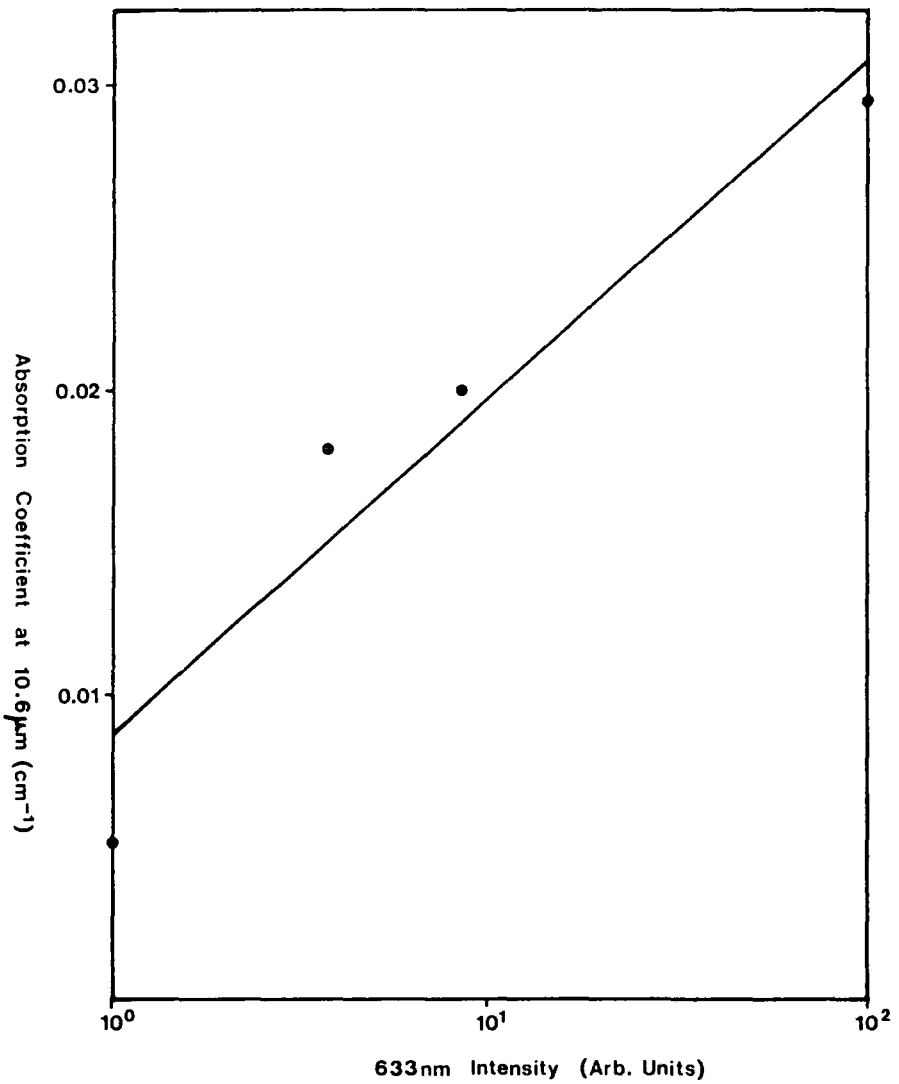

Absorption coefficient of CVD ZnSe as a function of 633nm band cathodoluminescence intensity.

FIGURE 6.33/5

show EBIC contrast at the grain boundaries, indicating that conduction processes were still bulk-limited in this case. The grain boundary contrast observed in the EBIC mode of the SEM has been shown to be photosensitive. When illuminated with a 12W tungsten lamp, the contrast was increased by a substantial amount showing the barrier to be lowered. This indicates that the grain boundaries are largely responsible for the photoconductive properties of CVD ZnSe.

Cathodoluminescence studies made in the SEM revealed the presence of an emission band at 630 nm. This is thought to be the well-known Cu-red band in ZnSe. Photographs of the CL image showed that this band, together with the edge-emission (bandgap transitions) band at 465 nm were suppressed at the grain boundaries. The suppression of the Cu-red band could be due to an absence of copper at the grain boundaries. This explanation seems unlikely to be correct since copper is present in reasonably high concentrations (Figure 6.2/18), and grain boundaries are expected to act as sinks for this impurity. Moreover, an absence of copper does not provide an adequate explanation for the suppression of the edge-emission band. Instead it is thought that the Zn-H species found to be present in the CVD samples is responsible. During the annealing process, the hydride would migrate through the crystal and segregate to the grain boundaries, where it would act as a luminescence-killer agent in a manner similar to some transition elements such as Fe, Co and Ni. The Cu-red band has indeed been shown to be quenched in the presence of Zn-H [6] supporting this view.

CVD ZnSe is becoming increasingly important as an infrared window material in 10.6 μm laser systems. An extremely important parameter associated with any laser optic is the absorption coefficient. For a window operating in the transparent regime this factor is often strongly related to the free carrier density. For this reason the effect of impurities incorporated into the substrate material has been the subject of serious study recently [17]. Laser absorption measurements were carried out on a number of CVD ZnSe samples at the GEC Hirst Research Centre, Wembley where a sensitive calorimeter had been set up. Measurements were made as a function of wavelength. No distinct exponential dependence manifested itself in the limited tuning range available, although, in each case, the

absorption increased with increasing frequency indicating that the bandgap absorption tail was perhaps the dominating process in this wavelength region.

The examination of a large block of CVD ZnSe procured via AWRE from the Raytheon Corp, USA provided some interesting results. The value measured along the longest axis was 3.6 x 10^{-4} cm^{-1} (assuming the usual surface absorption of ~0.25% per surface) which was 5.25 times less than the value measured along the shortest axis. The reason for this anisotropy was not clear. It can be explained if it is assumed that the grains grow in a highly asymmetric columnar fashion along the growth direction (Figure 6.33/3). If this were the case the optical path length of the laser radiation would be increased by scattering to a greater extent along the short axes of the block. However the picture is made more complex by the presence of a defect plane in the sample, which absorbed strongly in the 10.6 μm region.

It was shown that the cathodoluminescence studies mentioned earlier could be linked to the absorption coefficient of CVD ZnSe (Figure 6.33/5). Samples exhibiting a higher Cu-red band intensity had a higher absorption coefficient at 10.6 μm. This result can be explained in terms of a free-carrier absorption mechanism as outlined by Dutt et al [24]. The link already established [6] between Zn-H content and 630 nm Cu-red intensity allows the supposition to be made that the hydride species concentration influences the absorption coefficient. The greater the Zn-H content in a given sample, the lower the absorption coefficient becomes, until a plateau value is reached.

The relationship between the Cu-red band intensity and the absorption coefficient requires further investigation. In particular the effect of incorporating other luminescence-killer elements, such as Fe, Co and Ni should be studied.

CHAPTER SIX - REFERENCES

1 K L Lewis and J Hill, Proc 7th Int Conf on Chem Vap Deposition, (1980), 629

2 G J Russell, M J Robertston, B Vincent and J Woods, J Mat Sci, 15, (1980), 939

3 G Jones and J Woods, J LUM, 9, (1974), 389

4 H G Lipson, Appl Opt 16, (11), (1977), 2902

5 Aslam-Khan M, Proc Roy Soc, 80A, (1962), 599

6 G J Russell, P Waite and J Woods, Inst Phys Conf Ser No 60: Section 7, (1981), 371

7 P A Miles, Appl Opt 16, (11), 2891

8 D L Stienwatt and R F Potter, Optical Properties of III-V Compounds, Semiconductors and Semimetals, 3, (1973), 71

9 J P Dakin and W A Gambling, J Opto-Electronics, 5, (1973), 335

10 L C Nistor, S V Nistor, V Teoderescu, Eva Cojocuru and I N Mihailescu, Appl Opt 18, (20), (1979), 3517

11 H B Rosenstock, J Appl Phys, 50, (1), (1979), 102

12 A I Branstein and M Branstein, J Vac Sci Techl, 8, 412

13 G F Sherman and G F Frazier, Opt Engineering, (1975)

14 M Hass and B Bendow, Appl Opt 16, (11), (1977), 2882

15 F Urbach, Phys Rev 92, (1953), 1324

16 G J Burrell and B Ellis, Semiconductor opto-electronics, Butterworth, London, (1973)

17 K L Lewis and G S Arthur, Boulder Damage Symposium, NBS Special Publication 669, (1982), 86

18 B Jensen, J Phys Solids, 34 (1973), 2235

19 Enrique Bernal G, Appl Opt 14, (2), (1975), 314

20 R Gibbs and K L Lewis, J Phys E Sci Instrum, 11, (1978), 304

21 R Gibbs and R M Wood, Damage in laser components at 10.6 μm, Second Annual Report, No 16,204C, (1975)

22 T T Saito, A B Callender and L B Simmons, Appl Opt 14, (3), (1975), 721

23 J Foley, S K Sharma and R M Wood, 12th Symp on Opt Materials for High Power Lasers, NBS Special Publication 620, (1981)

24 B V Dutt, O K Kim and W G Spitzer, J Appl Phys, 48, (1977), 2110

CONTENTS

7 CONCLUSIONS

7.1 SUMMARY

7.11 CVD material
7.12 Durham-grown material

7.2 SUGGESTIONS FOR FUTURE WORK

7 CONCLUSIONS

7.1 SUMMARY

The main aim of the work described in this thesis was to investigate and characterise the deep levels in zinc selenide samples grown by two different techniques (Chapter 3). In addition, the grain boundary structure of the CVD material was studied in detail since it was found to play an important role in the determination of the electrical properties.

The techniques used to characterise the deep centres were thermally stimulated luminescence (TSL), thermally stimulated conductivity (TSC) and deep level transient spectroscopy (DLTS). The first two techniques were conducted on as-grown samples with resistivities varying between 10^9-10^{13} ohm-cm, whereas the DLTS measurements required Schottky barrier devices to be fabricated from samples which had been annealed in liquid zinc to reduce the resistivity to about 10-100 ohm-cm.

7.11 CVD material

Initial attempts to perform TSC measurements on the CVD samples proved unsuccessful. The decay of the photocurrent due to the initial trap-filling excitation was much slower than with the Durham-grown material. This was traced to the electrically active nature of the grain boundaries, which were studied using the EBIC mode of a scanning electron microscope in Zn-annealed samples. The results obtained from this work showed that the grain boundaries could be accurately represented as two Schottky barriers arranged back-to-back. Since the grain size was approximately 20-100 microns, there were typically many hundreds of these barriers in a single sample which caused the DC resistivity to remain high even when the sample was annealed in liquid zinc. These findings were supported by AC resistivity measurements which showed the conductivity was about two orders of magnitude greater at a frequency of 200 kHz.

The mechanism to explain the formation of the potential barriers is not completely understood. The grain boundaries almost certainly act as

'sinks' for impurities incorporated during the growth process. Cathodoluminescence studies revealed that both the edge emission at 465 nm and the copper-red band centred on 630 nm were suppressed at the grain boundaries, indicating that non-radiative recombination (luminescence killer) centres were located there. Infra-red transmission measurements also showed that a zinc hydride (ZnH) species was present in all of the CVD-grown sample studied. Measurements performed at AWRE, Aldermaston related the concentration of the ZnH species to the intensity of the copper-red emission. It was found that the Cu-red band intensity decreased as the concentration of ZnH increased, which implied that this species was the one responsible for quenching the cathodoluminescence at the grain boundaries.

Absorption coefficients at 10.6 microns were measured in four different CVD-grown samples and the results plotted against the intensity of the 630 nm Cu-red band intensity. The absorption coefficient was shown to increase as the copper-red band intensity increased. This result can also be related to the influence of the ZnH content on the Cu-red luminescence intensity mentioned above. Hence, the absorption coefficient of the CVD material at 10.6 microns decreases as the concentration of the ZnH impurity increases. A mechanism for achieving low absorption laser windows might therefore be to introduce an impurity such as the ZnH species or another known luminescence 'killer' such as Fe, Co or Ni during growth. The presence of these recombination centres would thus reduce the carrier concentration in the conduction band which would result in a lower free carrier absorption. It should be noted that strict limits on other impurities such as Al, Na, Cu, Li, Ga, In etc., would also have to be observed in order to attain absorption coefficients below 10^{-3} cm^{-1}. This might involve annealing the sample to remove impurities such as Cu, and to help diffuse the 'killer' impurity away from the grain boundaries and into the grains.

TSL was performed on the CVD-grown samples CVD/1 and CVD/2. In the former sample, two traps at 0.10 eV and 0.28 eV were found, although the 0.10 eV levels might correspond to a trap distribution above this value. The 0.10 eV level is attributed to the sodium acceptor, and this has also been identified using photoluminescence excitation (PLE) [6.17]. The

origin of the 0.28 eV level is not clear, but DLTS measurements detected electron traps at 0.27 eV in the same material in a concentration of 1.36×10^{14} cm^{-3}. It is thought that these traps may be due to a lattice vacancy, or a vacancy-impurity complex.

CVD/2 was found to contain a level at 0.20 eV by TSC and TSL, showing it to be different from CVD/1. There is not enough data available for speculation as to the origin of these traps.

Sample CVD/1 exhibited a sudden quenching of the free-carrier lifetime at 100°K which decreased the TSC signal to such an extent that the apparatus could hardly measure the detrapping of the deeper levels. The activation energy of the quenching was calculated to be 0.11 eV from steady state photoconductivity measurements. This might indicate that the 0.10 eV levels found by the TSC measurements and ascribed to the Na acceptor significantly alter the recombination kinetics as they empty of holes.

It was observed during the TSC and TSL work undertaken on the CVD material that the detrapping of levels occurred at higher temperatures than with Durham-grown ZnSe for traps of similar thermal ionisation energy. This observation was supported by the computer modelling work, which indicated that the attempt-to-escape frequencies of traps in CVD material were probably about two orders of magnitude lower than those found for the traps in Durham-grown samples.

7.12 Durham-grown material

The Durham-grown ZnSe was taken from three boules: 345, 388 and 400. Boule 388 was undoubtedly doped with high levels of copper during growth, but the other two were thought to be relatively free of this impurity. Samples from boule 388 yielded a total of five traps at 0.16, 0.23, 0.26, 0.45 and ~0.06 eV. Traps were measured in boule 400 at 0.17, 0.27 and 0.43 eV, showing good agreement with the 0.16, 0.26 and 0.45 eV traps in boule 388. DLTS analysis of samples from boule 388 revealed electron traps at 0.14, 0.23 and 0.62 eV, in concentrations of 3×10^{13} cm^{-3},

2×10^{14} cm^{-3} and 3×10^{14} cm^{-3} respectively. The capture cross-sections were all close at about 2×10^{-18} cm^2. Samples from boule 400 also yielded electron traps at between 0.41-0.44 eV and at 0.31 eV when studied using the DLTS technique.

It is suggested that the levels at 0.16-0.17 eV and 0.26 eV are the same as those observed by Kosai [1.23] at 0.17 and ~0.30 eV. The traps at approximately 0.26-0.30 eV are hence ascribed to a vacancy-impurity complex. As far as the electron traps observed at 0.23 eV in samples from boule 388 are concerned, no firm indications of the defect responsible have been found in the literature to date. The electron traps at 0.14-0.17 eV have also been observed by other workers [1.23,1.33] although there has been no speculation as to the identity of the impurity or defect responsible. Electron traps at 0.41-0.45 eV have also been reported elsewhere [1.26], and traps at 0.42 eV were found in ZnSe:In grown at Durham and analysed independently [5.14], however no suggestions relating to the identity of the impurity of defect responsible have been put forward. These traps might be hole traps, which would explain why they were not observed when DLTS measurements were performed on the same material. The electron traps at about 0.6 eV found in samples from boule 388 may be the same as those found by Kosai [1.23] in LPE-grown ZnSe, although once again no speculations were given as to the identity of this level.

A single Schottky barrier sample was obtained from boule 345 for TSL analysis. This sample yielded traps at 0.30, 0.60 and 0.70 eV. The 0.30 eV traps were associated with a shallower level, or levels, which caused initial calculations of the ionisation energy to be inaccurate. Unfortunately these shallower levels could not be analysed independently due to the interference of the 0.30 eV traps. The 0.30 eV traps are thought to be the same as the 0.26-0.30 eV levels discussed above. The 0.60 eV levels may correspond to the self-activated centre reported frequently [1.19,1.32,1.33], or it might be an electron trap corresponding to those observed in samples from boule 388. The third set of traps at 0.70 eV were unique to this material. Oidwai and Woods [1.32] referred to acceptors observed at 0.67 eV which they ascribed to the presence of copper, however Christianson and Wessels [1.27] have suggested that a hole

trap found by them at 0.71 eV might in fact be due to a native defect.

A Schottky barrier sample from boule 388 was studied using the DLTS apparatus under different conditions of biassing and temperature. The transients produced were plotted out and compared. The results indicated that the device could probably be described as an MIS structure, however the DTLS peaks observed in the sample were not due to interface states, since the concentration profile study showed that the traps were present in the bulk of the material.

7.2 SUGGESTIONS FOR FUTURE WORK

Most of the present work involved the characterisation of defect and impurity levels within the forbidden gap of ZnSe. Initially the methods of TSC and TSL were used to good effect in discovering the number of traps in the various samples and giving a fair idea of the energy position. However, the nature of the TSC and TSL anaysis is not ideal since there are a great many parameters governing the peak shape and the position of the peak maximum. The technique of DLTS was still relatively new when the experimental work reported in this thesis was done, however it provided a means of accurately ascertaining the energy position, the concentration profile, and the capture cross-section of impurity and defect levels .

In the DLTS measurements described in Chapter 5, only majority carriers could be detected due to the nature of the experiment, however optical DLTS (ODLTS), where the filling pulse is provided by a light source such as a pulsed dye-laser, allows both types of trap to be detected. A future work program should use this technique to enable all the traps in a sample to be detected. Other obvious improvements to the apparatus would include provision for logging capacitance transients as a function of temperature, thus enabling analyses to be undertaken in a single thermal scan, and the inclusion of a temperature-controlled cryostat such that transients could be plotted out at any temperature in the range 4-400°K.

Although the DLTS technique provides a very powerful tool for the characterisation of semiconductors, the aim should be to analyse trapping levels to find the ten parameters discussed in Chapter 1, namely: optical and thermal emission rates for electrons and holes, optical and thermal capture rates for electrons and holes, the energy position, and the concentration. This would require the use of additional characterisation methods, but it would provide a greater chance for the impurity or defect to be identified.

In addition, a future work programme might attempt a comparative study of ZnSe doped with various elements such as In, Ga, Al, N, P, Cl, F, Cu, Li, Na etc., using transient capacitance techniques to provide the characterisation data. In particular the investigation of the role of zinc and selenium vacancies could be pursued along the same lines as Besomi and Wessels [1.26], who related the measured concentration of several trapping levels to the Zn/Se ratio used during growth.

The CVD material could be further studied by characterising the grain boundaries in terms of barrier height, the energy position of traps, and the capture cross-section. This could be achieved by using techniques such as the method of laser-induced photo-conductivity [1].

CHAPTER 7 - REFERENCES

1 E Poon, E S Yang, H L Evans, W Hwang, and R M Osgood, Jr., Appl. Phys. Lett., 42, (3), (1983), 285

APPENDIX 1 DERIVATION OF EXPRESSIONS FOR THE TSC AND TSL INTENSITIES

The simple insulator model described in Section 4.2.1 can be used to derive expressions for the TSC and TSL intensities as a function of time with no simplifications as follows:

The Kinetic equations governing the system in 4.2/1 are:

$$\frac{dn_1}{dt} = -\gamma n_1 + \beta n_c (N_1 - n_1) \qquad \text{A1-1}$$

$$\frac{dn_c}{dt} = \frac{dn_1}{dt} - \alpha n_c n_R \qquad \text{A1-2}$$

and $$n_R = n_c + n_1 \qquad (N_2=0) \qquad \text{A1-3}$$

from A1-3, differentiating with respect to time gives:

$$\frac{dn_1}{dt} = \frac{dn_R}{dt} - \frac{dn_c}{dt} \qquad \text{A1-4}$$

By substituting the value for n_1 obtained from A1-3, and the expression for dn_1/dt obtained from A1-4 into equations A1-1 and A1-2 we have:

from A1-1 $$\frac{dn_R}{dt} - \frac{dn_c}{dt} = -\gamma (n_R - n_c) + \beta n_c (N_1 - n_R + n_c) \qquad \text{A1-5}$$

and from A1-2 $$\frac{dn_c}{dt} = -\frac{dn_R}{dt} + \frac{dn_c}{dt} - \alpha n_c n_R \qquad \text{A1-6}$$

Equation A1-6 can be further simplified to give:

$$n_c = 1 \frac{1}{\alpha n_R} \frac{dn_R}{dt} \qquad \text{A1-7}$$

This expression is then differentiated with respect to time, to yield

$$\frac{dn_c}{dt} = \frac{1}{\alpha n_R^2} \cdot \frac{dn_R}{dt}^2 - \frac{1}{\alpha n_R} \cdot \frac{d^2 n_R}{dt^2} \qquad \text{A1-8}$$

The terms n_c and dn_c/dt derived above can now be removed from A1-5 by direct substitution giving

$$\frac{dn_R}{dt} + \frac{1}{\alpha n_R}\frac{d^2n_R}{dt^2} - \frac{1}{\alpha n_R^2}\left(\frac{dn_c}{dt}\right)^2 = -\gamma n_R - \frac{\gamma}{\alpha n_R}\frac{dn_R}{dt} - \frac{\beta}{\alpha n_R}\frac{dn_R}{dt}\,N_1 - n_R - \frac{1}{\alpha n_R}\frac{dn_R}{dt}$$

multiplying through by n_R, rearranging, and substituting $\delta = \beta/\alpha$ gives the expression for TSL intensity as:

$$\frac{dn_R}{dt} = -\frac{\gamma_R n^2 + \alpha^{-1}\frac{d^2 nR}{dt^2}}{n_R(1-\delta) + \delta N_1 + \alpha^{-1}(\gamma - (1+\delta)(n_R)^{-1}.dn_R/dt)} \qquad \text{A1-9}$$

and from A1-7 and A1-9 the corresponding equation for TSC can be found

Results A1-9 and A1-7 can be simplified by applying the assumptions 4.2-16 and 4.2-18. How this is achieved is demonstrated by the following argument.

Beginning with the Kinetic equations A1-1, A1-2 and A1-3, we add the two assumptions:

$$\frac{dn_c}{dt} << \frac{dn_1}{dt} \qquad \text{A1-10}$$

and $$n_c << n_1 \qquad \text{A1-11}$$

Using A1-3 with A1-11 we can write

$$n_R = n_1 \qquad \text{A1-12}$$

Differentiating A1-12 with respect to time we have

$$\frac{dn_R}{dt} = \frac{dn_1}{dt} \qquad \text{A1-13}$$

Substituting A1-13 into A1-12, and taking A1-10 into consideration gives

$$\frac{dn_R}{dt} = -\alpha n_C n_R \qquad \text{A1-14}$$

Substituting A1-13 into A1-1 gives

$$\frac{dn_R}{dt} = -\gamma n_1 + \beta n_C (N_1 - n_1) \qquad \text{A1-15}$$

Using A1-12 in A1-15 yields the expression

$$\frac{dn_R}{dt} = -\gamma n_R + \beta n_C (N_1 - n_R) \qquad \text{A1-16}$$

Now equation A1-14 can be substituted into A1-16 to give

$$n_C n_R = \frac{\gamma n_R}{\alpha} - \delta n_C N_1 + \delta n_C n_R \qquad \text{A1-17}$$

where $\delta = \beta/\alpha$ again.

Rearrangement to make n_C the subject gives the TSC expression as

$$n_C = \frac{\gamma n_R}{\alpha (n_R + \delta N_1 - \delta n_R)} \qquad \text{A1-18}$$

The result for the TSL intensity is arrived at by eliminating the term n_C from equations A1-14 and A1-16. Both of these expressions are therefore rearranged to make n_C the subject and then equated to give

$$\frac{\frac{dn_R}{dt} + \gamma n_R}{\beta (N_1 - n_R)} = -\frac{\frac{dn_R}{dt}}{\alpha n_R} \qquad \text{A1-19}$$

Simple rearrangement is now possible, to render dn_R/dt as the subject

$$\frac{dn_R}{dt} = -\frac{\gamma n_R^2}{(n_R(a-\delta) + \delta N_1} \qquad \text{A1-20}$$

which is the simplfiied expression for the TSL intensity.